CATALYTIC CONVERSION OF METHANE INTO ALKANES AND OXYGENATES AND DEACTIVATION OF HYDRODEOXYGENATION CATALYSTS

A Dissertation
Presented to
The Academic Faculty

by

Chukwuemeka Okolie

In Partial Fulfillment
of the Requirements for the Degree
Doctor of Philosophy in the
School of Chemical & Biomolecular Engineering

Georgia Institute of Technology
December 2017

CATALYTIC CONVERSION OF METHANE INTO ALKANES AND OXYGENATES

AND DEACTIVATION OF HYDRODEOXYGENATION CATALYSTS

Approved by:

Dr. Carsten Sievers
School of Chemical & Biomolecular Engineering
Georgia Institute of Technology

Dr. Pradeep Agrawal
School of Chemical & Biomolecular Engineering
Georgia Institute of Technology

Dr. Carson Meredith
School of Chemical & Biomolecular Engineering
Georgia Institute of Technology

Dr. Ryan P. Lively
School of Chemical & Biomolecular Engineering
Georgia Institute of Technology

Dr. Thomas Orlando
School of Chemistry & Biochemistry
Georgia Institute of Technology

Date Approved: 11/13/2017

To my family, friends and my advisor, Dr. Carsten Sievers. None of this would have been possible without you all.

ACKNOWLEDGEMENTS

I would like to thank my research advisor, Dr. Carsten Sievers, for taking a chance on me accepting me into his research group and for providing me with guidance, resources and direction that enabled me to grow as an independent researcher. Your mentorship, advice, sincerity and unconditional patience has helped me grow significantly as a researcher throughout my graduate school career and they are immensely appreciated. I also want to thank Dr. Sievers for providing me many opportunities to conduct research with several external collaborators throughout my time in his research group which has provided me a great platform for the next stage of my career as a researcher. I would like to also thank my thesis committee, Dr. Pradeep Agrawal, Dr. Carson Meredith, Dr. Ryan Lively and Dr. Thomas Orlando for their support, guidance, and encouragement at several milestones of my PhD career. I would also like to thank Eli Stavitski of Brookhaven National laboratories for his guidance and support in learning, running and analyzing x-ray adsorption spectroscopy which was very impactful in my research. The efforts of Libor Kovarik of Pacific Northwest National laboratories is greatly appreciated. Libor's efforts in microscopy were very important for understanding several characteristics of the catalysts that were used in my research. Matthew Yung of National Renewable Energy laboratories is also greatly appreciated for his efforts and guidance in completing the last chapter of this Ph.D. thesis. Financial support from American Chemical Society Petroleum Research Fund, Department of Energy Basic Energy Sciences and the National Renewable Energy laboratories is greatly appreciated.

I would like to thank the group members of Dr. Sievers research group, especially, Jessica Rogers, Guo Shiou Foo, Mariana V. Rodrigues Yasmeen Belhsiene, Yimeng Lyu and Jungseob So. Jessica and Guo Shiou provided guidance and intellectual support that was critical

to my progression as a researcher. I am immensely fortunate to have had the opportunity to work with such intelligent researchers and I am a better researcher because of their efforts. I appreciated the experimental support I received from Mariana Rodrigues, Yimeng Lyu and Yasmeen Belhsiene. Memories from the long nights I spent in the lab with Jungseob So fixing IR spectroscopy instruments will never be forgotten. Friendship and emotional support from Sireesha Aluri, Lisa Wiest, Michael Stellato, Jason Lee, Qandeel Almas and Andrew Tricker will be forever cherished.

I would like to thank those who supported my research efforts behind the scenes. Leslie Schlag and Kysten Riley for helping me process countless expense and travel reports, Jerry Nunn for helping me find the root of many issues with the fume hoods, Hank (Major) White for always checking in on me during late nights in the lab, Shanell Riley for shipping several chemical samples on my behalf, Kevin Guger for fixing multiple computers for me, Ashley Elayne for helping me fabricate reactor tubes, and Mary Williams at the RBI front desk for always ensuring that I receive my packages in a timely manner.

To my parents, I have modelled my life from yours and that is what has led me this far in life. Your inspiration, support and encouragement have seen me through the highs and lows of my Ph.D. career. To my sisters, you will always be the number 2 women in my life right below mom of course. Thank you for all your encouragement and support through every step of this journey. To the best friend in the world, Desayo Ajisegiri, your friendship means everything to me and your high expectations from me have kept me on track at very low moments of my Ph.D. career. To Lloyd Williams, thank you for all your kind words of encouragement throughout my residency at the Renewable Bio-Products Institute building.

TABLE OF CONTENTS

Page

ACKNOWLEDGEMENTS iv

LIST OF TABLES xi

LIST OF SCHEMES xii

LIST OF FIGURES xiii

LIST OF SYMBOLS AND ABBREVIATIONS xxii

SUMMARY xxiv

CHAPTER

1 Introduction 1

1.1 Catalytic Utilization of Natural Gas for the Production of Chemicals and Fuels 1

1.2 State of the Art of Catalytic Synthesis of Alcohols 4

1.3 Strategy for Improved Catalytic Systems for Methane Activation and Conversion to useful Fuels and Chemicals 5

1.4 Biomass as an Alternative Source for Energy and Chemical Production 6

1.5 Limitations of Hydrodeoxygenation Processes 9

1.6 Objectives and Organization 10

2 Non-Oxidative Coupling of Methane to Ethane, Ethylene and Aromatics over Nickel on Ceria-Zirconia 13

2.1 Background 13

2.2 Experimental 17

2.2.1 Materials 17

2.2.2 Catalyst Synthesis 17

2.2.3 Catalyst Characterization 18

2.2.4 In-Situ IR Spectroscopic Studies on Surface Reactions of Methane 22

2.2.5 In-Situ FTIR Spectroscopic Study during Reaction with Methane at 450 °C over NiO/CZ 22

2.2.6 Reactivity Studies 23

2.3 Results and Discussion 24

2.3.1 Structural and Textural Properties of the Catalysts 24

2.3.2 Reactivity towards Non-Oxidative Coupling of Methane 26

2.3.3 Strategies for Improved Performance 36

2.4 Conclusions 37

3 Conversion of Methane to Methanol and Ethanol over Nickel Oxide on Ceria-Zirconia Catalysts in a Single Reactor 39

3.1 Background 39

3.2 Experimental 41

3.2.1 Materials 41

3.2.2 Catalyst Synthesis 41

3.2.3 Characterization 42

3.2.4 In-Situ IR Spectroscopic Studies on Surface Reactions of Methane 46

3.2.5 Operando Transmission FTIR Spectroscopic Studies 46

3.2.6 Reactivity Studies 47

3.2.7 Verification of Alcohols in the Product Stream 48

3.2.8 Elementary Reactions for the Conversion of Methane to Alcohols 49
3.3 Results and Discussion 49
3.4 Conclusions 59
4 Optimization of Active Sites of NiO/CZ to Improve Methane Conversion to Alcohols 60
4.1 Background 60
4.2 Experimental 63
4.2.1 Materials 63
4.2.2 Catalyst Synthesis 64
4.2.2.1 Dry Impregnation (DI) 64
4.2.2.2 Strong Electrostatic Adsorption (SEA) 65
4.2.2.2.1 Point of Zero Charge Study 65
4.2.2.2.2 Catalyst Preparation 65
4.2.2.3 Co-Precipitation (CP) 66
4.2.3 Characterizations 66
4.2.4 Reactivity Studies 67
4.3 Results 69
4.3.1 NiO/CZ_SEA Synthesis Optimization 69
4.3.1.1 Determination of Point of Zero Charge 69
4.3.2 Characterization of NiO/CZ Catalysts Prepared by DI, SEA and CP 71
4.3.2.1 Structural and Textural Properties of Catalysts Prepared using Different Synthesis Techniques 71
4.3.2.2 Lewis Acidic Characteristics and Dispersion of Nickel Oxide on Catalysts 74

4.3.3 Performance of Catalysts Prepared by Different Synthesis Techniques 76
4.4 Discussion 80
4.4.1 Structure and location of NiO on Ceria-Zirconia 80
4.4.2 Catalyst Performance and Carbon Deposit 84
4.5 Conclusions 87
5 Understanding the Role of "Roadblocks" in Catalyst Deactivation during Hydrodeoxygenation of Pyrolysis-Oil Model Compounds 89
5.1 Background 89
5.2 Experimental 91
5.2.1 Materials 91
5.2.2 Catalyst Synthesis 92
5.2.3 Characterization 93
5.2.4 Adsorption of Catechol Roadblocks on HDO catalysts 95
5.2.5 Thermal Gravimetric Analysis 95
5.2.6 Catalytic Performance 95
5.3 Results 97
5.3.1 Catalyst Characterization 97
5.3.2 Temperature-Programmed Reaction of Adsorbed Catechol to Roadblocks 102
5.3.3 Analysis of OH Groups by FTIR Spectroscopy 104
5.3.4 Reactivity for HDO of Anisole 107
5.4 Discussion 109
5.4.1 Adsorption of Bidentate Catecholate Roadblocks 109

5.4.2 Accessibility of Active Sites Upon Blocking with Catechol 112

5.4.3 Catalyst Deactivation during HDO of Anisole on Catalysts with Roadblocks 119

5.5 Conclusions 123

6 Final Conclusions and Recommendations 126

APPENDIX A: SUPPLEMENTARY INFORMATION FOR CHAPTER 2 132

APPENDIX B: SUPPLEMENTARY INFORMATION FOR CHAPTER 3 137

APPENDIX C: SUPPLEMENTARY INFORMATION FOR CHAPTER 4 165

APPENDIX D: SUPPLEMENTARY INFORMATION FOR CHAPTER 5 167

REFERENCES 178

VITA 204

LIST OF TABLES

Page

Table 2.1 Physicochemical properties of ceria-zirconia based catalysts 24

Table 2.2 Thermodynamic data for gas phase non-oxidative methane reactions 27

Table 4.1 Physicochemical properties of catalysts 72

Table 5.1 Nitrogen Physisorption and Hydrogen Chemisorption Results 97

Table 5.2 TGA results showing percentage of catechol remaining on the roadblocked samples after heating 103

Table 5.3 FTIR Spectra Characteristics of the OH groups in HBEA and ZSM-5 Zeolites 106

Table 5.4 Pore diameters in zeolite supports 116

Table A.1 FTIR spectra characteristics for methane activation over NiO/CZ 132

Table B.1 Lewis acid sites concentration and metal oxide dispersion on catalysts 136

LIST OF SCHEMES

Scheme 2.1 Mechanism for the formation of aromatics and coke in methane aromatization 28

Scheme 5.1 Interaction of catechol on acidic HDO catalysts 112

Scheme 5.2 Major reaction pathway for HDO of anisole over bifunctional Pt/HBEA catalyst 121

LIST OF FIGURES

Page

Figure 1.1 Schematic representation of several catalytic processes for the conversion of methane into useful fuels and chemicals 2

Figure 1.2 Share of bioenergy in the world primary energy mix 7

Figure 2.1 XRD patterns of ceria-zirconia based catalysts 25

Figure 2.2 EDX maps of 2 wt.% NiO/CZ 26

Figure 2.3 (a) Conversion of methane over NiO/CZ at different temperatures (b) Selectivity of carbon products over NiO/CZ at 500 ^{o}C (c) 450 ^{o}C (d) 350 ^{o}C (e) Yields of hydrogen at different temperatures 30

Figure 2.4 In-situ XANES of NiO/CZ during exposure to methane at 450 ^{o}C (a) Ce L_3-edge (b) Ni K-edge 32

Figure 2.5 (a) TEM of spent NiO/CZ catalyst after reaction with methane at 450 ^{o}C for 8 h. (b) X-ray photoelectron spectra in the C1s region of NiO/CZ after 4 h of methane exposure at 450 ^{o}C 33

Figure 2.6 (a) Amount of carbon deposit on spent catalysts after reaction at different temperatures measured from CHN analysis vs. TPO using TG Analysis (b) Raman spectra of spent catalysts after reaction at different temperatures 34

Figure 2.7 Subtracted in-situ FTIR spectra during exposure of 2 wt.% NiO/CZ to methane at 450 ^{o}C 36

Figure 3.1 Difference IR spectra of products from CH_4 on selected catalysts at 473 K 51

Figure 3.2 HAADF images and corresponding EDX maps of Ni for (a) 2 wt.% NiO/CZ (b) 2 wt.% NiO/SiO_2 (c) 5 wt.% NiO/CZ. The scales in the Ni EDX maps correspond to the integrated signal from the ionization peak of Ni(K) 53

Figure 3.3 In-situ XANES spectra: (a) Ce L_3-edge during reaction of CH_4 over NiO/CZ at 723 K (b) Ni K-edge during reaction of CH_4 over NiO/CZ at 723 K (c) Ni K-edge during exposure to H_2O at 723 K 55

Figure 3.4 Conversion of methane and O_2 and yields of products formed during reactions of methane, steam and oxygen in a packed bed reactor setup at 723 K and 1 atm over 2 wt.% NiO/CZ. Yields of carbon-containing products are calculated on a carbon atom basis. A space velocity of 3000 h^{-1} of reactant gas diluted in nitrogen was used 57

Figure 4.1 Mechanism of Electrostatic Adsorption as Proposed by J.R. Regalbuto 70

Figure 4.2 Experimental PZC data fit with theoretical model. Adjustable parameters, PZC = 7.9. Adjustable theoretical model parameters; difference between pK_1 and pK_2 (ΔpK) = 6.0, Number of charged sites (N_s) = 8 OH.nm^{-2} at 25 ^oC 71

Figure 4.3 (a) XRD pattern of NiO/CZ catalysts prepared using different synthesis techniques (b) the corresponding magnification of the (111) diffraction lines of ceria at 28.9˚ shown in (a)73

Figure 4.4 (a) FTIR spectra of pyridine on catalysts at 150 ˚C showing adsorption on Lewis acid sites (band at 1445 cm^{-1}) (b) Concentration of Lewis acid sites on catalysts prepared using

different synthesis techniques with 2 wt.% nickel. Numbers in bracket represent dispersion of nickel oxide measured from the amount of pyridine adsorbed 75

Figure 4.5 (a) FTIR spectra of pyridine on NiO/CZ_CP catalysts at 150 ˚C showing adsorption on Lewis acid sites (b) Concentration of Lewis acid sites on NiO/CZ_CP catalysts with different Ni loading 76

Figure 4.6 Reactivity results of catalysts during reactions with of methane, steam and oxygen in a packed bed reactor setup at 450 ˚C and 1 atm. (a) conversion of methane over 2NiO/CZ prepared from different techniques (b) alcohol selectivities over 2NiO/CZ prepared from different techniques (c) conversion of methane over NiO/CZ_CP with different Ni loading (d) yields of alcohol over NiO/CZ_CP as a function of Ni loading 78

Figure 4.7 Carbon content on catalyst from reaction with methane (a) Carbon deposit on 2NiO/CZ prepared from different techniques calculated from C balance during reaction run (b) weight of carbon deposit on spent 2NiO/CZ prepared from different techniques as determined from CHN analysis (c) carbon deposit on NiO/CZ_CP with different loadings of NI calculated from C balance during reaction run (d) weight of carbon deposit on spent NiO/CZ_CP catalysts with different Ni loadings as determined from CHN analysis 80

Figure 4.8 Lattice parameter of fluorite cubic structure of ceria as a function of Ni loading 83

Figure 4.9 Specific activity (Conversion/μmol Ni) (a) catalysts prepared using different synthesis techniques with 2 wt.% nickel (b) catalysts prepared using co-precipitation with different weight loadings of nickel 85

Figure 5.1 N_2 adsorption and desorption isotherms of HBEA and HZSM-5 series: comparison between (a) fresh HBEA, Pt/HBEA and HBEA_RB (b) fresh Pt/HBEA and Pt/HBEA_RB, (c) fresh Ga/HZSM-5 and Ga/ZSM-5_RB 98

Figure 5.2 Horvath-Kowazoe microporous distribution for HBEA and HZSM-5 series: (a) fresh samples and roadblock Pt/HBEA, (b) fresh Ga/ZSM-5 and Ga/ZSM-5_RB 99

Figure 5.3 FTIR Spectra during temperature programmed desorption at 3E-8 bar following CO adsorption on Pt/HBEA reduced at 450 °C 100

Figure 5.4 Concentration of (a) Lewis acid sites and (b) Brønsted acid sites of Blank Catalysts and Catalysts with Roadblocks. Numbers in parenthesis represent fraction of acid sites in roadblock catalysts to acid sites in blank catalysts 102

Figure 5.5 FTIR spectra of catechol adsorbed on HDO catalysts at various temperatures (a) Pt/HBEA (b) Ga/ZSM-5 104

Figure 5.6 FTIR Spectra showing OH region of catalysts activated at 400 ^{o}C with and without catecholate roadblocks (a) HBEA and Pt/HBEA (b) ZSM-5 and Ni/ZSM-5 (c) ZSM-5 and Ga/ZSM-5 106

Figure 5.7 Conversion of anisole on fresh HDO catalysts compared to catalysts with catecholate roadblocks (a) Pt/HBEA (b) HBEA (c) Ga/ZSM-5 108

Figure 5.8 Yield of deoxygenated products on fresh HDO catalysts compared to catalysts with catecholate roadblocks (a) Pt/HBEA (b) HBEA (c) Ga/ZSM-5 109

Figure 5.9 Fraction of accessible active sites on HDO catalysts after blocking with catechol. Accessibility (x/x_o) was measured by dividing the amount of measured sites after the introduction of catechol by the amount of sites measured before the introduction of catechol 119

Figure A.1 Difference IR spectra of products from methane at different temperatures on (a) CZ (b) NiO/CZ 133

Figure A.2 Selectivities of heavy aromatics over NiO/CZ (a) 500 °C (b) 450 °C (c) 350 °C 134

Figure A.3 TPO of spent NiO/CZ after reaction with methane at different temperatures 135

Figure A.4 Peak fitting of Raman spectra of spent catalysts after reaction at (a) 500˚C (b) 450 ˚C and (c) 350 ˚C 136

Figure B.1 FTIR spectra of pyridine on catalysts at 423 K showing adsorption on Lewis acid sites (band at 1445 cm^{-1}) 138

Figure B.2 XRD patterns of ceria-zirconia based catalysts 139

Figure B.3 XRD pattern of NiO/CZ and NiO/SiO_2 and the NiO-free supports 140

Figure B.4 Difference IR spectra of products from CH_4 at different temperatures on (a) CZ (b) 2 wt.% CoO/CZ (c) 2 wt.% NiO/CZ (d) 2 wt.% NiO/SiO_2 (e) FeO_x/CZ (f) PdO/CZ (g) Al_xO_y/CZ

Figure B.5 Subtracted operando IR spectra during reaction of methane, oxygen and steam over 2 wt.% NiO/CZ with a steam to carbon ratio of 1 and oxygen to carbon ratio of 0.2 at 723 K 143

Figure B.6 Subtracted in-situ FTIR spectra during exposure of 2 wt.% NiO/CZ to 5% methane in inert at 723 K 144

Figure B.7 Subtracted operando IR spectra during reaction of methane, oxygen and steam over 2 wt.% NiO/SiO_2 with a steam to carbon ratio of 1 and oxygen to carbon ratio of 0.2 at 723 K 145

Figure B.8 Additional EDX maps of 2 wt.% NiO/CZ collected on JEOL ARM Centurion EDX detector 146

Figure B.9 Additional maps of 5 wt.% NiO/CZ as acquired on JEOL ARM with Centurion EDX detector 147

Figure B.10 Additional maps of 2 wt.% NiO/SiO_2 as acquired on JEOL ARM with Centurion EDX detector 148

Figure B.11 TEM of 2 wt.% NiO/CZ after reaction with methane, steam and O_2 at 723 K for 8 h with a steam to carbon ratio of 1 and oxygen to carbon ratio of 0.2 149

Figure B.12 XPS after in-situ treatment of 2 wt.% NIO/CZ with methane at 723 K (a) Ce 3d (b) Ni 2p 150

Figure B.13 Deconvolution of $3d_{5/2}$ peaks of Ce after exposure of 2 wt.% NiO/CZ to CH_4 for 4 h at 723 K 151

Figure B.14 C 1s XPS after in-situ treatment of 2 wt.% NiO/CZ and 5 wt.% NiO/CZ with methane at 723 K for 4 h 152

Figure B.15 In-situ XANES derivative spectra: Ni K-edge during exposure to H_2O at 723 K 153

Figure B.16 Yields of aromatic products formed during reactions of methane, steam and oxygen in a packed bed reactor setup at 723 K and 1 atm over 2 wt.% NiO/CZ with a steam to carbon ratio of 1 and oxygen to carbon ratio of 0.2 154

Figure B.17 Conversion of methane and yields of products formed during reaction in a packed bed reactor setup at 723 K and 1 atm over 2 wt.% NiO/CZ (a) in the absence of O_2 (b) in the absence of steam 155

Figure B.18 Conversion of syngas and yields of products formed during reaction in a packed bed reactor at 723 K and 1 atm over 2 wt.% NiO/CZ (a) without steam (b) with steam to CO ratio of 1 156

Figure B.19 Conversion of methanol and syngas and yields of products formed during reaction in a packed bed reactor at 723 K and 1 atm over 2 wt.% NiO/CZ 157

Figure B.20 Conversion of (a) methanol and yields of products formed during reaction in a packed bed reactor at 723 K and 1 atm over 2 wt.% NiO/CZ (b) methanol and steam with steam to carbon ratio of 1 158

Figure B.21 (a) Conversion of methane and yields of products formed during reaction in a packed bed reactor setup at 573 K and 1 atm over 2 wt.% NiO/CZ with a molar O_2:CH_4 ratio of 0.2 and H_2O:CH_4 ratio of 1.0 (b) yields of aromatic products 159

Figure B.22 (a) Conversion of methane and yields of products formed during reaction in a packed bed reactor setup at 723 K and 1 atm over 5 wt.% NiO/CZ with a molar O_2:CH_4 ratio of 0.2 and H_2O:CH_4 ratio of 1.0 (b) yields of mono and multi-ring aromatics 160

Figure B.23 (a) Conversion of methane and yields of products formed during reaction in a packed bed reactor setup at 723 K and 1 atm over 2 wt.% NiO/SiO_2 with a molar O_2:CH_4 ratio of 0.2 and H_2O:CH_4 ratio of 1.0 (b) yields of aromatic products 161

Figure B.24 Analysis of effluent stream of the packed bed reactor to verify the formation of products (a) ^{13}C NMR spectrum of liquid condensate (b) mass spectrum of effluent stream 162

Figure B.25 ^{1}H NMR of liquid condensate from reaction run at National Renewable Energy Lab for methane conversion in the presence of steam and oxygen at 723 K over 2 wt.% NiO/CZ 163

Figure B.26 Temperature inside the reactor during full reaction run as seen in Figure 3.4 over NiO/CZ 164

Figure C.1 Conversion of methane and O_2 and yields of products formed during reactions of methane, steam and oxygen in a packed bed reactor setup at 450 °C and 1 atm over (a) 10NiO/CZ_CP (b) 6NiO/CZ_CP (c) 4NiO/CZ_CP (d) 2NiO/CZ_CP 165

Figure C.2 Conversion of methane and O_2 and yields of products formed during reactions of methane, steam, and oxygen in a packed bed reactor setup at 450 °C and 1 atm over 2NiO/CZ_SEA 166

Figure D.1 TGA of blank and roadblocked catalysts in air (a) Pt/HBEA (b) ZSM-5 (c) Ni/ZSM-5 (d) Ga/ZSM-5 167

Figure D.2 TGA of blank and roadblocked catalysts in nitrogen (a) Pt/HBEA (b) ZSM-5 (c) Ni/ZSM-5 (d) Ga/ZSM-5 168

Figure D.3 First order deactivation profile of catalysts during HDO of anisole (a) Pt/HBEA (b) HBEA (c) Ni/ZSM-5 (d) Ga/ZSM-5 169

Figure D.4 Yields of products during HDO of anisole over Pt/HBEA_Blank (a) deoxygenated products (b) oxygenated products 170

Figure D.5 Yields of products during HDO of anisole over Pt/HBEA_RB (a) deoxygenated products (b) oxygenated products 171

Figure D.6 Yields of products during HDO of anisole over HBEA_Blank (a) deoxygenated products (b) oxygenated products 172

Figure D.7 Yields of products during HDO of anisole over HBEA_RB (a) deoxygenated products (b) oxygenated products 173

Figure D.8 Yields of products during HDO of anisole over Ni/ZSM-5_Blank (a) deoxygenated products (b) oxygenated products 174

Figure D.9 Yields of products during HDO of anisole over Ni/ZSM-5_RB (a) deoxygenated products (b) oxygenated products 175

Figure D.10 Yields of products during HDO of anisole over Ga/ZSM-5_Blank (a) deoxygenated products (b) oxygenated products 176

Figure D.11 Yields of products during HDO of anisole over Ga/ZSM-5_RB (a) deoxygenated products (b) oxygenated products 177

LIST OF SYMBOLS AND ABBREVIATIONS

OCM	Oxidative Methane Coupling
NOCM	Non-Oxidative Methane Coupling
ACS	American Chemical Society
ICP-AES	Inductively Coupled Plasma-Atomic Emission Spectroscopy
UHP	Ultra-High Purity
BET	Brunauer-Emmett-Teller
BJH	Barrett-Joyner-Halenda
XRD	X-Ray Diffraction
XANES	X-Ray Absorption Near Edge Structure
XPS	X-ray Photoelectron Spectroscopy
MS	Mass Spectrometry
GC	Gas Chromatograph
CHN	Carbon Hydrogen Nitrogen
TGA	Thermogravimetric Analysis
TPO	Temperature Programmed Oxidation
STEM	Scanning Transmission Electron Microscopy
HAADF	High Angle Annular Dark Field

EDX	Energy-Dispersive X-ray Spectroscopy
FTIR	Fourier Transform Infrared
FID	Flame Ionization Detector
TCD	Thermal Conductivity Detector
WGS	Water Gas Shift
SEA	Strong Electrostatic Adsorption
DI	Dry Impregnation
CP	Co-Precipitation
PZC	Point of Zero Charge
LAS	Lewis Acid Site
BAS	Brønsted Acid Site
NMR	Nuclear Magnetic Resonance
MCT/A	Mercury Cadmium Telluride Antimonide

SUMMARY

The colossal and growing demands for power and chemicals around the world makes it inevitable to rely on cheap, abundant or renewable sources for meeting these demands. As the world population increases and nations undergo further industrialization, the primary energy and chemical usage will increase. Currently, the majority of the world's fuels and chemicals are derived from coal and crude oil. Not only is their availability finite but also predictions indicate that these sources will result in increased atmospheric carbon dioxide and may result in increased average earth temperatures and extreme weather phenomena. Methane serves as an excellent resource for meeting these growing demands due to its abundance. Alternative energy sources could also play a major role in meeting the projected energy demand in the future in a sustainable and environmentally friendly manner. Currently, methane steam reforming is the most common way of utilizing methane for the production of fuels and chemicals but this process is highly energy intensive and expensive. Direct routes for the conversion of methane to useful fuels and chemicals at reasonable conditions is therefore more desirable from an economic perspective.

The direct synthesis of fuels and chemicals from methane and alternative sources is therefore an important area of research. However, there is still a long road of research and experimenting before any catalyst or process for the direct conversion of methane to fuels and chemicals can be commercialized. Also, there is a significant lack of understanding of catalytic processes and pathways of catalysts deactivation during the production of fuels and chemicals from alternative sources. The purpose of this dissertation is to design and optimize catalysts for the conversion of methane into useful chemicals like hydrocarbons and alcohols as well as utilize

different experimental techniques to elucidate deactivation of catalysts during the upgrading of fuels from alternative sources.

The first study focuses on the conversion of methane into higher hydrocarbons and hydrogen under non-oxidative conditions. It is demonstrated in this work that methane can be converted at steady state to ethane, aromatics and hydrogen up to its thermodynamic limit at temperatures of 350 ^{o}C to 500 ^{o}C. At 450 ^{o}C and 500 ^{o}C, traces of ethylene are also produced. NiO on ceria-zirconia (NiO/CZ) is used for methane activation and coupling to form these hydrocarbon products. Two domains of Ni particles are available on the surface of ceria-zirconia which lead to the formation of different types of hydrocarbons. Bigger Ni particles with sufficient surface sites are responsible for the aromatization of methane. Carbon deposits or strongly adsorbed aromatics are also formed when these Ni sites which leads to a progressive reduction in aromatic yields during the reaction. Smaller Ni particles which lacks the surface sites for aromatization are responsible for the formation of ethane and ethylene. On these sites, activated methane groups couple into higher alkyl chains which can be desorbed as ethane and in the cases of high temperatures (450 °C and 500 °C), ethane can undergo further dehydrogenation into ethylene. These Ni sites which are very small in size do not suffer from coking like the larger Ni particles and hence, they remain active throughout the reaction.

In the second study, the thermodynamic barrier of activating methane in a non-oxidative environment is overcome by introducing oxygen as an oxidizing agent. It is demonstrated that the catalyst consisting of small nickel oxide clusters supported on ceria-zirconia (NiO/CZ) can convert methane to methanol and ethanol in a single steady state process at 450 °C using oxygen as an abundantly available oxidant. The presence of steam ensures that alcohols are obtained rather than carbon dioxide as the product of catalytic combustion. The unusual activity of the

catalyst is attributed to the synergy between the small Lewis acidic NiO clusters and the redox-active ceria-zirconia support, which also stabilizes the small NiO clusters.

In the third study, NiO/CZ prepared by dry impregnation, strong electrostatic adsorption and co-precipitation is investigated. This is done in order to obtain the optimum catalyst comprising of nickel oxide and ceria-zirconia for the conversion of methane to alcohols in a single reactor. It is demonstrated that the activity of this catalyst is highly affected by the method of preparation used for synthesis. The activity of this catalyst is attributed to the synergy between the small Lewis acidic NiO clusters and the redox-active ceria-zirconia support. Hence, the activity is improved by reducing the particle size of Lewis acidic NiO clusters on the surface. Strong electrostatic adsorption which is used as an alternative synthesis technique leads to strong metal support interaction which reduces the agglomeration of NiO during calcination. This leads to a catalyst with more highly dispersed NiO clusters and improved methane reactivity compared to the catalyst prepared using traditional impregnation. Co-precipitation, another synthesis technique used, leads to catalysts with NiO incorporated in the ceria lattice. However, the fraction of NiO which are accessible for reaction are well-dispersed leading to high alcohol selectivities. For optimum formation of surface Lewis acidic NiO clusters using this synthesis technique, a 6 wt.% nickel loading is determined as optimum.

The fourth study investigates the deactivation of catalyst by strongly adsorbed surface species during Hydrodeoxygenation of a bio-oil model compound. The effect of these species on the performance of BEA and MFI type zeolites is investigated in this study. Catecholate species are formed when catechol is introduced to the catalyst. Due to the large kinetic diameter of catechol relative to the pore sizes of BEA and MFI structures, most of these species remain on the external surface of the zeolite. Although these species are adsorbed on the surface, they block

the pore mouths of the zeolite and restrict access to active sites inside the zeolite framework. Other sites on the external surfaces of the zeolites are affected even more greatly. The metal sites deposited on the zeolites using the conventional wet impregnation followed by calcination and reduction are larger than the zeolite pores and reside on the external surface of the zeolite, mainly inside defect sites where silanol nests form or on some surface acidic hydroxyl groups. Although catechol-derived species do not directly poison these metal sites, they adsorb at the perimeter of these metal sites and can form a blanket coverage of the metals. These catecholate species formed appear to restrict access of the reactants to the active sites both inside the pores and on the external surfaces of the zeolite, leading to a deactivation of the catalyst. Several analytical techniques are used to monitor the effects of these catecholate species – roadblocks – on the accessibility of active sites and the performance of the catalysts.

CHAPTER 1

INTRODUCTION

1.1 Catalytic Utilization of Natural Gas for the Production of Chemicals and Fuels

The recent discoveries of shale gas deposits in North America and methane hydrates in the sediments of ocean floors opens up new opportunities for its utilization as a source of important chemicals and fuels.[1] Methane comprises the most abundant compound in natural gas. Several different processes based on catalysis and reaction engineering have been proposed for the conversion of methane into useful fuels and chemicals (Figure 1.1). The processes can be grouped into two major types. The first one consists of indirect routes, in which methane is converted into synthesis gas (syn-gas) either by partial oxidation or by steam or dry reforming at temperatures of 800 °C to 1000 °C.[2-5] Syn-gas produced from the reforming step can undergo further processing into useful chemicals and fuels such as diesel fuel, gasoline, methanol, dimethyl ether, lower α-olefins, paraffins, and higher alcohols. The second type of processes involves direct conversion of methane without the initial production of syn-gas. Specifically, oxidative coupling[6-9] and non-oxidative coupling[10-13] processes can directly convert methane into higher hydrocarbons while partial oxidation can be used to convert methane into oxygenates.[9, 14-15]

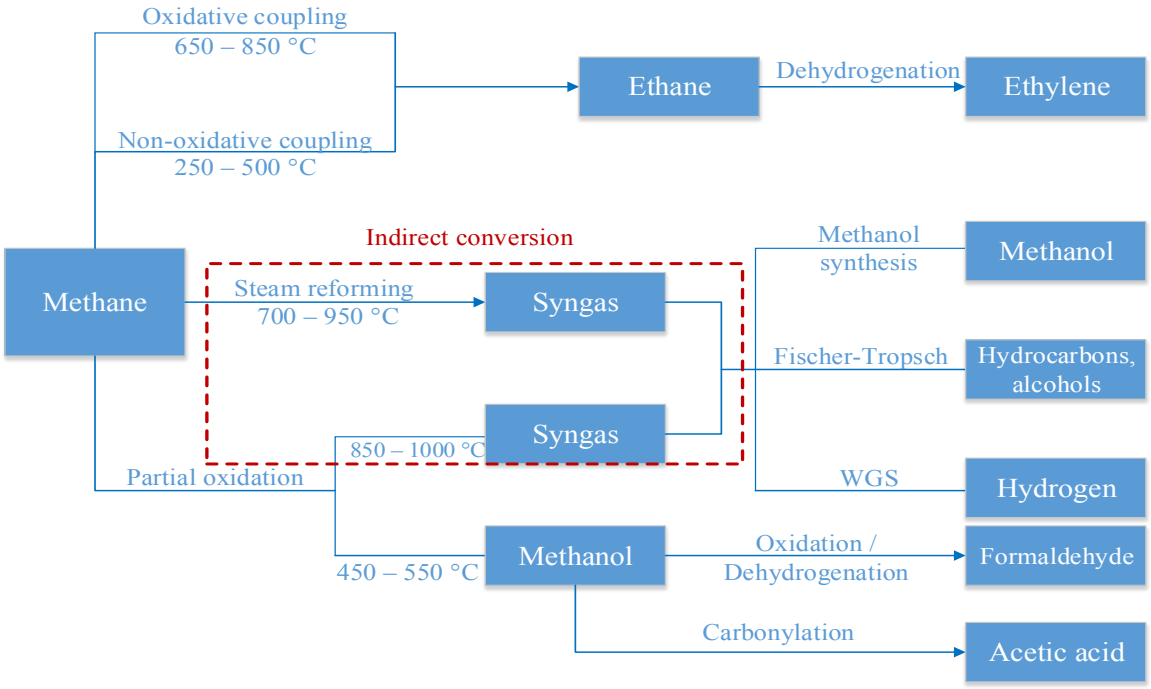

Figure 1.1 Schematic representation of several catalytic processes for the conversion of methane into useful fuels and chemicals.

The conversion of methane using the indirect route has already been commercialized. Several large facilities are operational including the Sasol plants near Johannesburg in South Africa, the PetroSA plant at Mossel Bay, the Shell Middle Distillate Synthesis plant in Malaysia, the Oryx gas-to-liquid plant in Qatar, and the gas-to-liquid plant in Nigeria.[16] However, due to the high energy requirements for the reforming step, the conversion of methane to syn-gas and the compression of syn-gas typically accounts for about 60-70% of the capital cost to operate the plant. Moreover, this technique limits the utilization of remote and inconveniently located natural gas fields, which accounts for a significant percentage of the world's natural gas reserve.

A great amount of incentive therefore still exists for the development of processes for direct conversion of methane to important fuels and chemicals without syn-gas as an intermediate. One widely pursued strategy has focused on the direct catalytic conversion of

methane to C_{2+} hydrocarbons in an oxidative environment, or as commonly referred to in the literature, oxidative coupling of methane (OCM). The best single-pass ethylene yield reported so far from this process is approximately 25%, which is deemed insufficient for industrial application of this process.[9] A major setback in this process is that, oxygen in the mix further oxidizes hydrocarbon products into carbon dioxide and water, decreasing the selectivity of hydrocarbons at high methane conversion. Research efforts shifted direction to removing the oxidant in OCM processes as a means of preventing the oxidation of hydrocarbon products in a process commonly referred to as non-oxidative coupling of methane (NOCM).[10-13] This reaction is thermodynamically unfavorable affording very limited conversion of methane. However, due to the absence of an oxidant, the selectivities to C_{2+} hydrocarbons are very high. To overcome the thermodynamic limitations in a single-pass reactor, the catalyst could be incorporated in a membrane that can selectively remove hydrogen and promote the forward reaction. Another highly attractive route for efficient utilization of natural gas involves transformation of methane into liquid oxygenates or alcohols.[9] Methanol has been studied as a major desired product from this reaction because it is a more energy-dense derivative of methane which will significantly reduce transportation costs and also because it is a highly desirable precursor to a number of commodity chemicals such as formaldehyde and acetic acid[9] as well as highly important fuels like olefins and gasoline.[9] The production of ethanol from methane is also very highly attractive because it is even more valuable than methanol as a very important medical solvent as well as a highly desired fuel.[17-19] Unfortunately, this direct approach of alcohol synthesis from methane is not yet competitive with indirect reforming via synthesis gas.

1.2 State of the Art of Catalytic Synthesis of Alcohols

The conventional route for the catalytic synthesis of methanol utilizes synthesis gas and carbon dioxide as the primary feedstock. The synthesis gas used is typically obtained by steam reforming of methane at high temperatures over Ni-based catalysts[20] or by gasification of coal.[21] The reforming route results in a hydrogen-rich syn-gas which is then converted to methanol. The gasification products are usually poor in hydrogen composition; an H_2 to CO fraction between 0.45 and 1 is usually obtained in this process.[21] In both cases, the syn-gas product also contains CO_2, which at low optimum concentration is required for high conversion of syn-gas to methanol.[22] Processes for the synthesis of methanol are divided into two. The first process is performed at low temperature and pressure (250 °C and 5-10 MPa) over copper-based catalysts that contain ZnO and an oxide support e.g. $Cu/ZnO/Al_2O_3$ or $Cu/ZnO/Cr_2O_3$. The other process is performed at high temperature and pressure (400 °C and 10-20 MPa) over copper-free catalysts that comprises of zinc oxide and chromite (ZnO/Cr_2O_3).[22-24] The reaction occurs by sequential hydrogenation of CO or CO_2.

Following the synthesis of methanol from syn-gas, intensive research centered on the development of catalysts and processes for shifting the synthesis away from solely methanol and into higher alcohols particularly C_2-C_4 alcohols. ZnO/Cr_2O_3 catalysts promoted by alkali were used in certain processes to produce a mixture of higher alcohols. These processes however, were very non-selective and formed large amounts of hydrocarbons.[22] The catalysts were later improved by using a heavy alkali ion dopant and higher alcohol selectivity and yields were obtained.[25-27] In general, these processes are performed at temperatures around 400 ^oC and pressures around 10 MPa. It was later found that low temperature copper-based, zinc oxide-containing catalysts promoted by heavy alkali were more active and selective than the copper-

free catalysts for higher alcohols synthesis forming primarily C_2 to C_4 alcohols in addition to methanol.[28-30] The proposed routes for C-C bond formation include methanol and CO homologation and CO insertion into metal-carbon bonds. More recently, ethanol formation from methanol and syngas was also reported over Cu/SiO_2 catalysts at atmospheric pressure.[31] While these processes are promising, they are only applicable with conventional feedstocks and hence alcohol synthesis directly from methane is still desirable for utilizing unconventional feedstocks.

1.3 Strategy for Improved Catalytic Systems for Methane Activation and Conversion to useful Fuels and Chemicals

The activation of methane for upgrading into target products presents scientific difficulties. Due to the perfect symmetry of methane, it is the least reactive of all hydrocarbons, with very high C-H bond energies of 438.8 kJ/mol.[9] Energy intensive conditions that can be used to overcome this activation limitation, often lead to deeper activation of methane in which all the C-H bonds are destroyed. Selectively activating methane is therefore an intrinsically difficult problem in catalysis, requiring both highly active and highly selective catalytic systems. Methane monooxygenase in methanotrophic bacteria catalyzes the selective oxidation of methane to methanol under ambient conditions.[32] Inspired by methane monooxygenases, supported phthalocyanine complexes of Fe, Cu and Co have been investigated as a means of mimicking the chemistry of these enzymes.[33-35] A major setback with these systems is that the reaction did not occur in a conventional catalytic cycle, in which all elementary reactions occur under the same conditions.

In other studies, strong Lewis acidic sites were suggested as a means of activating methane at rather mild conditions (100-150 °C) to form surface methyl groups.[36-37] These highly reactive Lewis acid sites are formed when alumina is calcined at high temperature. In this case,

the methyl groups that were formed remained on the surface rather than engaging in any catalytic turnovers. Nevertheless, this illustrates the potential of Lewis acid sites as parts of a bifunctional catalysts.

Steam methane reforming is the method most widely utilized by industry to activate methane and produce syngas. Ceria-zirconia mixed oxides have been heavily explored for this process on account of their improved redox properties. Due to their high oxygen storage capacity with rapid formation and elimination of oxygen vacancies, much research focus has been dedicated to ceria and ceria-zirconia systems as oxygen carriers in steam methane reforming.[38] The role of zirconia is to enhance both surface and bulk oxygen mobility and reactivity.[38] In addition to this strong redox capability of ceria-zirconia, it can also efficiently activate oxygen through a so-called multiple exchange mechanism.[39] These abilities make ceria-zirconia a very effective oxidation catalyst. Ceria-zirconia oxides also typically serves as active supports for group 8, 9 and 10 metal nanoparticles, which are catalytically active for the activation of methane.[38] The combination of highly redox material for oxidation and components for methane activation, which could be Lewis acidic clusters of group 8, 9 and 10 metal oxides should therefore provide a very efficient material for the conversion of methane into useful chemicals and fuels.

1.4 Biomass as an Alternative Source for Energy and Chemical Production

Crude oil which is currently the major source of energy is a finite resource. Based on the current rate of consumption of crude oil and progressively increasing demand, it is expected to be depleted in 40 years.[40] As a result, alternative and renewable sources for energy is a big area of research. Biomass energy is a large renewable source with the potential of making a significant contribution to the continued supply of energy after the depletion of fossil fuel

sources. Currently, biomass energy contributes 10-14% (Figure 1.2)[41] of the world primary energy, including about 3% of energy for transportation around the world. It also has the potential to contribute up to 30-40% in 2050, by tapping the large volumes of unused residues and wastes.[41] Sources of biomass that could play a major role in this expansion include conventional crops with careful consideration of land availability and food demand. In the medium term, lignocellulosic crops could be produced which could provide the bulk of the biomass resource. In longer term, aquatic biomass could also contribute significantly.[41] Many countries, developed and developing, have promoted the generation of energy from biomass by providing financial incentives and instrumented policies.

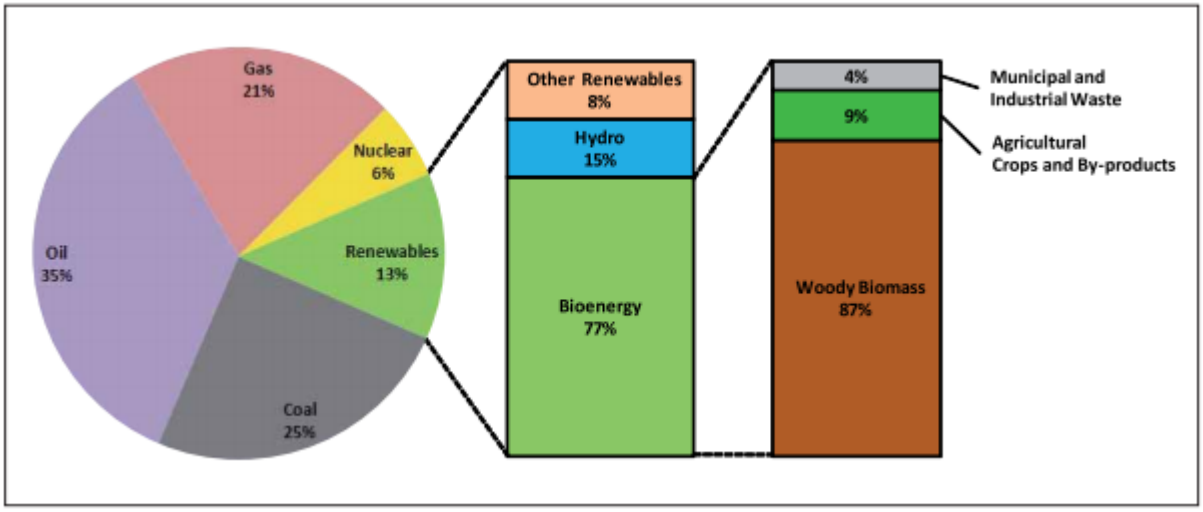

Figure 1.2 Share of bioenergy in the world primary energy mix.[41]

Several routes exist which can be used to convert biomass feedstock into a final energy product. Several technologies have been developed based on the different physical and chemical composition of the biomass feedstock, and to the energy service required which are typically heat, power of transport fuel. The direct combustion of biomass for the production of heat is one of the major application of bioenergy throughout the world. This application is also often cost-

competitive with fossil fuel alternatives.[41] Different technologies are in place or are under development for the production of electricity from biomass. Co-combustion in coal-based power plants is the most cost-effective use of biomass for power generation. Biomass conversion plants, including municipal solid wastes (MSW) combustion plants, are already in successful operation on a commercial scale. Other processes for the conversion of biomass includes gasification in which syngas can be produced from biomass, pyrolysis which produces bio-oils, and hydrolysis to produce sugar monomers.[41] Ultimately, the production of bioenergy will progressively increase in bio-refineries where transport biofuels, power, heat, chemicals and other marketable products could all be produced simultaneously from a mixture of biomass feedstocks.

In the conversion of biomass, gases are typically the main products which could then undergo further processing. However, liquids and solids are also products from biomass conversion. Different parameters such as temperature, heating rate and residence time define the distribution of different types of products during thermochemical treatment.[42] Conditions such as short residence times, fast heating rates and moderate temperatures (fast pyrolysis) usually lead to the production of bio-oils.[43] Solid fuel and char production are favored in slow pyrolysis. Bio-oil production from biomass in fast pyrolysis has emerged as the more attractive option due to their high selectivities of up to 70%.[43] Bio-oil are typically very viscous with low volatility and heating value which makes them poor fuels. They are also corrosive and polymerizes with time. This is all due to the high oxygen content of bio-oils typically around 35-40%.[44] Upgrading of bio-oils to bio-fuels is therefore required to eliminate oxygenated groups and improve the thermal and chemical stabilities, heating values, and volatility of bio-oils. Hydrodeoxygenation (HDO), in which excess hydrogen is used to remove oxygenated functional groups from bio-oils in the form of water, is an evolving technology for the upgrading of bio-oils.[45]

1.5 Limitations of Hydrodeoxygenation Processes

Although HDO is a very attractive process for upgrading bio-oils, because it requires rather moderate temperatures and pressures, it also has some limitations. The design and selection of an effective catalyst for performing the reaction has proven to be non-trivial. Since HDO is a very similar process to hydrodenitrogenation (HDN) and hydrodesulphurization (HDS), early work studied sulfided NiMo and CoMo catalysts for HDO because they showed high activity for HDN and HDS.[46] However, they showed very limited activity for HDO. Also, hydrogen sulfide which is very toxic, must be added into the feedstock to maintain their activity. Several other catalysts have been investigated as a means to overcome the problems presented by HDN and HDS catalysts. Many supported metal catalysts and bimetallic catalysts were tested and displayed activity in HDO reaction.[47-48] However, these catalysts require a very high hydrogen pressure. Subsequently, metal-impregnated zeolite catalysts were investigated for HDO reactions because of its strong acidity, crystalline structure and uniform pore size, and showed very good activity under atmospheric pressure.[49] Jones et al reported high reactivity for HDO of phenol over Pt/HY, Pt/HBEA and Pt/HZSM-5.[50] Resasco et al reported higher catalytic activity of bifunctional Pt/HBEA than monofunctional Pt/SiO_2 and HBEA for HDO of anisole.[51] Horacek et al used Pt/HBEA for HDO of model compounds of bio-oil.[52] The authors reported that HBEA exhibited a particularly high catalytic activity for HDO of large bio-oil compounds because of its large pores comprising of 12 rings. Lee et al. reported that the acidity of the zeolite support affected the catalytic activity of a bifunctional Rh catalyst for HDO of guaiacol.[53] The authors showed in this study that a decrease in the Si/Al ratio in Pt/HY led to an increase in the conversion of guaiacol.

Although, major insights have been presented for optimizing HDO catalysts, a major problem that still exists in HDO catalysis is deactivation. Catalyst deactivation typically occur through poisoning by nitrogen species or water, sintering of the catalyst, deposition of metal (specifically alkali metals) or coking.[54] The extent of these different pathways for catalyst deactivation is dependent on the catalyst in use, but carbon deposition has proven to be a general problem and the most significant pathway for catalyst deactivation.[54-55] Coke is principally formed on HDO catalysts through polymerization and polycondensation on the catalyst surface, forming polyaromatic species. These polyaromatic species block the active sites on the catalyst.[55] Coke formation increases with increasing acidity of the catalyst (both Lewis and Brønsted acid sites. The Lewis acid sites bind species to the catalyst while the Brønsted sites donate protons to the compounds to form carbocations which are believed to be responsible for coking.[55] This constitute a problem since acid sites are part of a bifunctional catalyst for HDO reactions.

1.6 Objectives and Organization

The overall objective of this work is to develop and optimize a catalyst for the efficient utilization of unconventional natural gas resources as well as provide insight on the pathways of deactivation of highly active zeolite catalyst during Hydrodeoxygenation of bio-oils. The development of an efficient catalyst for the conversion of stranded methane resource will have both an economic and environmental impact. Currently natural gas associated with oil during petroleum drilling are often vented and flared. This is not only a waste of a valuable resource, but methane and CO_2 emissions contribute to greenhouse gases. Understanding the pathway for catalyst deactivation during HDO reactions will be essential to further optimize the existing processes and will provide insight to enable the rational design of the new generation of catalysts for upgrading bio-oils.

In Chapter 2, a catalyst comprising of nickel oxide and ceria zirconia (NiO/CZ) was developed and used for activating methane and converting methane to higher hydrocarbons and aromatics at low temperatures not exceeding 500 °C and under a non-oxidative environment. Due to the thermodynamic constraints of this reaction, the conversion of methane is highly limited at low temperatures. However, this catalyst shows great potential for industrial application for the conversion of methane into higher hydrocarbons and aromatics if the catalysts are incorporated into membranes that can selectively remove hydrogen and drive the thermodynamic reaction in the forward direction to improve methane conversion.

In Chapter 3, the thermodynamic limitations were eliminated and the production of oxygenates was facilitated on the same catalyst (NiO/CZ). Steam was used to facilitate the hydrolysis of surface groups that form on the catalyst upon the activation of methane and oxygen was co-fed to convert surface hydrogen to water providing a thermodynamic driving force. In addition to alcohols, carbon dioxide and hydrogen and small amounts of aromatics are formed as by-products. Importantly, the formation of alcohols occurs at 450 °C in steady state with a turnover frequency of at least 50 h^{-1}. This is a significant improvement from previous studies, in which a high-temperature calcination step was required for every turnover.

In Chapter 4, the effect of preparation methods on the performance of NiO/CZ towards the production of alcohols was studied. Strong electrostatic adsorption (SEA) which was used as an alternative synthesis technique led to strong metal support interaction which reduces the agglomeration of NiO during calcination. This in turn led to a catalyst with more highly dispersed NiO clusters and improved reactivity than the catalyst prepared using traditional impregnation. Co-precipitation was also used as another unique synthesis technique which after optimizing the amount of nickel loading, presented a catalyst will improved methane reactivity.

In Chapter 5, the effect of strongly adsorbed “roadblocks” on zeolitic catalysts during HDO of bio-oils was studied. In this study, catecholate “roadblocks” were deliberately introduced into the catalyst. Physicochemical characterization and reactivity studies were then performed on the catalysts with roadblocks as a means of gaining insight on the effect of “roadblocks” as a pathway for deactivation during HDO reactions.

CHAPTER 2

NON-OXIDATIVE COUPLING OF METHANE TO ETHANE, ETHYLENE AND AROMATICS OVER NICKEL ON CERIA-ZIRCONIA

2.1 Background

The world is continuing its reliance on raw hydrocarbon feedstock supply, especially with the discovery of increasingly abundant sources of natural gas in shale and offshore gas fields. Methane, which is the main constituent of natural gas, is therefore an excellent raw material for the production of fuels and chemicals.[3, 56-70]

Methane is a very stable molecule with four equivalent C-H bonds, which each have bond energies of 438.8 kJ/mol each.[9] The C-H bonds in methane are stronger than the ones in the possible products (hydrocarbons or oxygenates), which means that the products will be more reactive than methane.[9] Consequently, controlling the selectivity of methane conversion is a much bigger challenge than achieving high reactivity. Also, kinetics constraints on the reaction, in which all four C-H bonds of methane are destroyed, such as methane reforming into synthesis gas or methane decomposition into carbon and hydrogen, are much easier to overcome than the reactions in which only one or two of the C-H bonds are broken under either oxidative or non-oxidative conditions.[13] This has significantly hindered major breakthroughs in research efforts on the direct conversion of methane. The most challenging problems associated with the direct conversion of methane arise from both kinetics and thermodynamics. High temperatures are required for activating methane, and at such conditions, radical reactions in the gas phase in which methane is completely oxidized to syngas and carbon dioxide are dominating.[3]

The use of methane as a feedstock has been extensively studied.[3, 56-70] Several different processes based on catalysis and reaction engineering have been proposed and reported which

can be grouped into two. The first one consists of indirect routes, in which methane is reformed into synthesis gas, which is further converted into useful chemicals and fuels like alkanes and oxygenates.[3, 56-58] The second type of process involves a direct conversion of methane into C_2 hydrocarbons and oxygenates without the production of syn-gas as an isolated intermediate.[9, 59, 65-66, 70] Today, all large-scale commercial processes for natural gas conversion are performed through the indirect route.[3, 56, 58, 65, 68] Some of the large volume products from synthesis gas are methanol and longer chain hydrocarbons, which are produced through Fischer-Tropsch synthesis.[71-72] Over the past years, several commercial plants for Fischer-Tropsch synthesis (FTS) were built.[73] While this approach is in principle feasible for upgrading methane, of the initial methane reforming step is extremely energy intensive and FTS plants require large capital investment and a significant scale to be economically viable.[71] In particular, this limits the utilization of remote and inconveniently located natural gas fields, which accounts for a significant percentage of the world's reserve, as previously mentioned.

A great amount of incentive therefore still exists to develop processes for direct conversion of methane to value-added products without synthesis gas as an intermediate. For a direct conversion of methane to higher hydrocarbons, two main reaction pathways have been considered in the literature which are done either in the presence or absence of an oxidant. The earlier which is done in the presence of an oxidant and commonly referred to as oxidative coupling of methane (OCM) was highly investigated in the mid-1980s to the mid-1990s.[13, 74] This reaction, although thermodynamically favorable, suffers from selectivity issues. No catalyst has been able to reach a C_{2+} yield higher than 25% and selectivity to C_{2+} higher than 80%, which are the descriptors for industrial application of OCM.[13] Over-oxidation of methane to syngas and CO_2 is responsible for low selectivity to C_{2+}. Research effort therefore shifted gears to

investigate the production of higher hydrocarbons from methane in the absence of oxygen. The so called non-oxidative coupling of methane (NOCM) is being investigated as a means to this end.[10, 12, 75-77] This reaction pathway shows great promise because oxidizers are absent, hence, high selectivities to products can potentially be attained. However, due to the absence of an oxidant, this reaction suffers greatly from thermodynamics showing enormously positive Gibbs free energy and in turn affording limited conversions of methane.

Various attempts to accomplish the NOCM reaction used classical and ill-defined heterogeneous catalysts in multistep processes: (i) methane dissociation on Ru or Pt particles by chemisorption (and stepwise surface carbon-carbon bond formation) and (ii) liberation of products by hydrogenation.[12, 76] Due to the thermodynamic constraints of NOCM, a number of researchers used very high temperatures (> 800 °C) to perform a direct conversion of methane to higher alkanes and aromatics.[10, 75] Isolated iron sites embedded in a silica matrix[10] and molybdenum oxide nanostructures in zeolites[75] were found to be the active sites for this reaction. However, the energy requirements for such processes are substantial, and it is challenging to avoid agglomeration of a highly dispersed active phase at such high temperatures. Another study demonstrated a direct coupling of methane into ethane at low temperatures up to its thermodynamic limit using silica-supported tantalum hydride.[77] In this study, the authors proposed a mechanism that involves a C-H bond activation of methane over Ta-H followed by dehydrogenation of $-CH_3$ to $=CH_2$ and $\equiv CH$.[77] It was proposed that both carbene and carbyne species are able to activate another molecule of methane by a σ-bond metathesis process,[78] which leads to the formation of a methyl-methylidene intermediate. Finally, a migratory insertion of the methyl group onto the carbene ligand as shown by a previous study,[79] leads to the formation of ethyl groups. This ethyl groups can then be displaced by methane via σ-bond metathesis,

releasing ethane and consequently forming another methyl group. The catalyst was prepared by a grafting technique under H_2 treatment at 250 °C. This synthesis technique is rather complex. The complexity of synthesis coupled with the unpredictable trend in tantalum price,[80] makes this material not very desirable for the preparation of industrial catalysts. Moreover, a steady decline in methane conversion was observed affording only a limited turnover number. Therefore, the development of a catalyst with commercial viability for non-oxidative coupling of methane still presents major opportunities. The thermodynamic constraints can be addressed from a process improvement in which the catalyst is incorporated in a membrane reactor that can selectively remove hydrogen under reasonable reaction conditions in which the membranes are stable. Some research efforts have already been invested in this direction.[12, 81]

Catalysts comprising of nickel particles on doped ceria support have been extensively used in the literature for the purpose of methane activation and reforming reactions.[38, 82-84] This is because ceria-zirconia serves as active supports for group 8, 9 and 10 metal nanoparticles.[38] These metal nanoparticles in turn act as catalytically active phase for the activation of C-H bonds of hydrocarbons.[38] A study that tested for the effect of ceria to zirconia ratio on the performance of $Ni/Ce_xZr_{1-x}O_2$ towards methane steam reforming revealed that higher thermal stability, higher redox properties and smaller Ni crystallite size were some of the important descriptors for the catalyst performance towards methane conversion.[85]

In this study, nickel oxide supported on ceria-zirconia was used for methane activation and subsequent coupling to higher hydrocarbons and aromatics at temperatures not exceeding 500 ˚C. A continuous production of ethane up to its thermodynamic limit was observed over 2 wt.% nickel oxide on ceria zirconia. Some ethylene and aromatics were also continuously produced.

2.2 Experimental

2.2.1 Materials

Cerium (III) nitrate hexahydrate (99% trace metals basis), zirconyl (IV) oxynitrate hydrate (99% trace metals basis), nickel (II) nitrate hexahydrate, and ammonium hydroxide (A.C.S. regent grade, 28–30% NH_3content) were purchased from Sigma Aldrich. Silica (99.8% purity) was purchased from Sigma Aldrich. Gases (methane, nitrogen, carbon monoxide, and hydrogen) with ultra-high purity (UHP Grade 5) were purchased from Airgas. Dry air for calcination was generated in our labs using a Parker Balston Gas Generator 1000. Deionized water was obtained from a Barnstead NANOpure ultrapure water system which was purified to 18.2 MΩ/cm.

2.2.2 Catalyst Synthesis

The ceria zirconia support was prepared by coprecipitation of the precursors of ceria and zirconia.[86-87] Cerium nitrate hexahydrate and zirconyl nitrate hydrate were dissolved in deionized water to form a 0.1 M solution. The coprecipitation was modified by adding the 0.1 M precursor solution drop-wise to an aqueous ammonium hydroxide solution while stirring continuously. The precipitate was then filtered, rinsed with deionized water, and dried in an oven overnight at 373 K. The catalyst was then calcined for 4 h in 200 mL/min zero grade air at 450 ^{o}C with a ramp rate of 5 ^{o}C/min. The co-precipitation material was comprised of Ce (0.83) and Zr (0.17) as determined by ICP-OES and is referred to as CZ in this thesis. Nickel oxide clusters was deposited on the CZ support using conventional dry impregnation or pore volume impregnation.[88] The metal content chosen was 2 wt.%. For this purpose, the nickel precursor was dissolved in deionized water equal to the pore volume of the ceria zirconia support, as

determined by nitrogen physisorption. The resulting solution was added dropwise to the support and collected in a beaker at room temperature. It was mixed thoroughly for 30 minutes, dried at 100 ^{o}C for 5 h and then calcined for 4 h at 450 ^{o}C with a ramp rate of 10 ^{o}C/min.

2.2.3 Catalyst characterization

Nitrogen physisorption measurements of the prepared samples were taken using a Micromeritics ASAP 2020 physisorption analyzer. The catalysts were degassed at 200 ^{o}C for 4 h prior to measurement. Surface areas and pore volumes were calculated based on the BET method[89] and BJH method[90], respectively.

To determine the amount of ceria, zirconia, and nickel on the catalyst, ceria zirconia and NiO on ceria zirconia were sent to Galbraith Laboratories for inductively coupled plasma-atomic emission spectroscopy (ICP-AES) analysis.

X-ray diffraction patterns were obtained using a Phillips X'Pert diffractometer equipped with an X'celerator module using Cu Kα radiation. Diffractograms were collected at incident angles from $2\theta = 5$ to 90° with a step size of 0.0167°.

Pyridine adsorption followed by FTIR spectroscopy was performed using a Nicolet 8700 FTIR spectrometer with an MCT/A detector. Each spectrum was recorded with 64 scans at a resolution of 4 cm^{-1}. Each sample was pressed into a translucent self-supported wafer and loaded into a vacuum FTIR transmission cell. The sample was activated at 450 ^{o}C for 1 h under high vacuum and cooled to 150 ^{o}C. A background spectrum was taken. The chamber was dosed with 0.10 mbar of pyridine for 30 mins or until adsorption equilibrium of pyridine was reached. Subsequently, the cell was evacuated for 1 h to remove physisorbed pyridine and a spectrum was taken. To determine the strength of acid sites, the sample was heated to 250 ^{o}C, 350 ^{o}C and 450 ^{o}C for 1 h, and a spectrum was taken at 150 ^{o}C. After each experiment, the density of the wafer

was determined by using a circular stamp of 6.35 mm to cut a disc of specific size from the wafer. The concentration of Lewis and Brønsted acid sites were determined by the Beer-Lambert law using the integral of the peaks at 1445 cm^{-1} and 1540 cm^{-1}, respectively. Extinction coefficients were used as reported by Tamura et al.[91]

In-situ XANES Ce L_3-edge and Ni K-edge were collected at beamline 9-BM-C at the Advanced Photon Source of Argonne National Laboratories (Proposal GUP-43235). A Si(1 1 1) double monochromator was used to select the beam energy for all measurements. The beam size was 800 x 1000 μm. Samples were pressed into wafers and placed in a cubic reactor. The beam was internally calibrated with a metallic cerium reference foil for Ce L_3-edge and a metallic nickel reference foil for Ni K-edge. Spectra were then collected in fluorescence mode. A spectrum was first taken of each of the fresh samples. The samples were then activated in helium at 450 ^oC for 1 h in the cubic reactor while continuously taking spectra. The gas was then switched to 5% methane and balance helium and spectra were taken continuously. Separate experiments were performed under the same conditions for both Ce L_3-edge and Ni K-edge.

In-situ XANES experiments with steam were performed in the same reactor and at the same conditions. Helium was used to bubble steam into the reactor while continuous XANES spectra were taken at the Ni K-edge.

XPS measurements were performed with a Physical Electronics Quantera Scanning X-ray Microprobe. This system uses a focused monochromatic Al Kα X-ray (1486.7 eV) source for excitation and a spherical section analyzer. The instrument has a 32 element multichannel detection system. The 83 W X-ray beam focused to 100 μm diameter was rastered over a 1.1 mm x 0.1 mm rectangle on the sample was used for the analysis. The X-ray beam is incident normal to the sample and the photoelectron detector is at 45° off-normal. High energy resolution spectra

were collected using a pass-energy of 69.0 eV with a step size of 0.125 eV. For the Ag 3d5/2 line, these conditions produced a FWHM of 1.07 eV. The sample experienced variable degrees of charging. Low energy electrons at ~1 eV, 20μA and low energy Ar^+ ions were used to minimize this charging. The 2 wt. % NiO/CZ catalyst powders were pressed into 4 mm x 1 mm diameter holes machined into a custom 13 mm diameter SS sample stub designed for use with a custom modified ULVAC PHI XPS sample platen. The custom sample platen and sample stub including the fresh catalysts were placed into the XPS vacuum introduction system and pumped to <1x10-7 Torr using a turbomolecular vacuum pumping system prior to introduction into the XPS spectrometer ultrahigh vacuum system. The spectrometer vacuum system pressure was maintained at <1x10-9 Torr during analysis and pumped using a series of sputter ion and turbomolecular vacuum pumps. After XPS analysis of the fresh catalysts, the sample stub was transferred to an attached catalytic reaction side chamber also pumped by a series of sputter ion and turbomolecular vacuum pumps. The sample stub was then transferred from the catalytic side chamber into an attached high vacuum tube furnace. The pressure of the tube furnace was increased ~760 Torr using 5% methane/He at a flow rate of 100 SCCM. The catalyst was heated to 450 ^oC at a rate of 10 ^oC/minute and held for 1 hour. This procedure was repeated with a wait time of 4 hours at 450 ^oC in 5% methane/He flow. After the catalyst was cooled to room temperature, the gas was quickly removed using a turbomolecular vacuum pump attached to the tube furnace. The stub was then transferred into the UVH catalytic chamber and then into the XPS spectrometer vacuum for analysis.

Quantification was performed using standard sensitivity factors contained in the ULVAC-PHI, Inc. MultiPak V9.5.0.8 version date of 10-30-2013 software. Peak area intensities required for quantification were calculated after applying a Shirley background subtraction. These

quantification results include the instrument transmission function, source angle, and asymmetry corrections. Typical XPS analysis depth for ceria based materials using inelastic mean free path calculation is up to 3 nm depending on the kinetic energy of the detected electron.[92] The majority of the electrons detected are coming from the first atomic layer.

EDX map was collected with a Scanning Transmission electron microscopy (STEM) (FEI Titan 80-300). The FEI Titan is equipped with CEOS GmbH double-hexapole aberration corrector for the probe-forming lens, which allows imaging with sub Angstrom resolution in STEM mode. EDX mapping was performed with FEI ChemiSTEM^{R}, which comprise of four symmetrically arranged windowless silicon drift detectors (SDD) with solid angle of ~0.8 sr. Acquisition and evaluation of the spectra was performed with Bruker Espirit software package. In general, the STEM sample preparation involved mounting powder samples on copper grids covered with lacey carbon support films, and then immediately loading them into the STEM airlock to minimize an exposure to atmospheric O_2..

The carbon loading on the spent catalysts was determined using a TA instruments SDT Q600 TGA. An empty alumina crucible was used to tare the TGA before each analysis. Individual samples were then loaded on the crucible and put in the TGA for analysis. The samples were ramped to 800 ^{o}C at 20 ^{o}C/min in a 100 mL/min flow of dry air. Spent catalysts were also sent to Atlantic Microlab for CHN analysis. Raman spectroscopy was also performed on the spent catalysts. For this purpose, the samples were loaded on microscope slides. The microscope was then focused on the sample region of interest at 20x resolution. Using a WITEC spectrometer with a 532 nm laser, the structural fingerprint of the samples were measured to determine the molecules present. Three individual measurements were then taken with an integration time of

10 seconds each which were averaged. A smooth function was used to remove noise and/or interference.

2.2.4 In-situ IR Spectroscopic Studies on Surface Reactions of Methane

Methane activation over ceria zirconia and nickel oxide supported on ceria zirconia was investigated by in-situ FTIR spectroscopy. The catalysts were pressed into self-supported wafers and introduced to a custom made high vacuum cell with ZnSe windows. A cryogenic pump and a turbo pump were used to evacuate the cell to 10^{-6} mbar. Each wafer was activated in high vacuum at 450 ^{o}C for 1 h and cooled to 50 ^{o}C. Then, it was exposed to 530 mbar of CH_4 for 1 h. The methane in the cell was then removed with the cryogenic pump, and a spectrum was collected immediately. The wafer was also contacted with methane at 100 ^{o}C, 150 ^{o}C, 200 ^{o}C and 250 ^{o}C following the same procedure as used at 50 ^{o}C. After the experiments, the cell was evacuated for 3 h at 250 ^{o}C and spectra were collected.

2.2.5 In-Situ FTIR Spectroscopic Study during Reaction with Methane at 450 ^{o}C over NiO/CZ

50 mg of the catalyst was pressed into a circular self-supported wafer with a diameter of 2 cm. The wafer was loaded into the sample holder, and it was assembled as part of the FTIR cell together with the cell body and heating block. The cell was built based on a design reported in the literature.[93] The assembled FTIR cell was placed into a Nicolet 8700 FTIR spectrometer. Each spectrum was recorded with 64 scans at a frequency of one per minute for 8 h during exposure to 10% methane and balance inert at 25 ccm total flow rate (to make up a space velocity of 3000 h^{-1}) at 450 ^{o}C and atmospheric pressure. The effluent line was connected to a Hiden HPR-20 QIC mass spectrometer to monitor the signal of the product stream over time.

2.2.6 Reactivity Studies

Reactivity experiments for the non-oxidative coupling of methane were performed in a packed bed reactor. The studies were performed using 200 mg of catalyst sieved to 75 μm. Catalyst samples were activated in-situ at 450 ^{o}C in nitrogen for an hour prior to reactivity studies. A space velocity of 3000 h^{-1} of reactant gas diluted in nitrogen (5% methane) was employed. A 100 ccm total flow rate of gas was used. The reactor was connected to an online Bruker 450-GC refinery gas analyzer (RGA) and a Hiden HPR20 mass spectrometer. The RGA is equipped with two TCD detectors and a FID. One TCD is used for analysis of hydrogen and the second for analysis of permanent gas mixtures (including methane). The FID channel allows for identification of methane and higher hydrocarbons. The TCD for hydrogen gas analysis uses a Molsieve 5A column while the TCD for permanent gas analysis uses a Molsieve 13x and Hayseep Q columns in series. The column to the FID is a BR-1. The GC was calibrated for all reactant and product gases by flowing 3-4 known amounts of the gas in question at the same temperature used in the reaction and monitoring the peak areas. Product gas was sampled at 20 minutes intervals using the RGA. The following definitions were used:

Conversion: $X_R[\%] = \frac{F_{CH4,in} - F_{CH4,out}}{F_{CH4,in}}$ x 100

C Product Selectivity: $Y_p\,[\%] = \frac{\nu_p \cdot F_{p,out}}{F_{CH4,in} - F_{CH4,out}}$ x 100

H_2 yield: $[\%] = \frac{F_{H2,out}}{2.F_{CH4,in}}$ x 100

Where ν_p is the number of carbon atoms in the compound and F_x is the molar flow rate of the gas in question.

2.3 Results and Discussion

2.3.1 Structural and Textural Properties of the Catalysts

The fraction of ceria and zirconia as determined by ICP-OES (Table 2.1) were 0.83 and 0.17 respectively. The actual content of nickel on ceria-zirconia (NiO/CZ) as determined by ICP-OES was 1.96 wt.% which is very close to the nominal value.

Table 2.1 Physicochemical properties of ceria-zirconia based catalysts.

Catalyst	Abbreviation	Metal loading (wt. %)[a]	Surface area ($m^2 \cdot g^{-1}$)[b]	Average pore diameter (Å)[c]	Pore volume ($cm^3 \cdot g^{-1}$)[d]	LAS Conc. ($\mu mol.g^{-1}$)[e]	Dispersion[f]
$Ce_{0.83}Zr_{0.17}O_2$	CZ	N/A	85	66	0.097	3	N/A
$NiO/Ce_{0.83}Zr_{0.17}O_2$	NiO/CZ	1.96	78	69	0.098	80	0.26

[a] Elemental analysis determined from ICP-OES at Galbraith laboratories
[b] Calculated from N_2 physisorption data using the BET equation
[c] Calculated from N_2 physisorption BJH adsorption data
[d] Calculated from N_2 physisorption BJH desorption cumulative pore volume
[e] Determined by pyridine adsorption followed by FTIR spectroscopy
[f] Dispersion of metal oxide on CZ determined from pyridine adsorption on Lewis acidic metal oxide followed by FTIR spectroscopy

The X-ray diffraction pattern of ceria-zirconia and nickel oxide supported on ceria-zirconia contained four prominent diffraction peaks associated with the (111), (200), (220), and (311) planes (Figure 2.1).[94-98] As in our previous work, all peaks in the diffractogram were attributed to the cubic fluorite phase of ceria-zirconia, indicating that no crystalline impurities were present.[87, 99] The narrowness of the peaks of ceria-zirconia indicates that the ceria-zirconia is a solid solution, not separate ceria and zirconia-rich phases. No peaks representative of the additional metal oxides were seen on the XRD patterns of the supported metal oxide catalysts. This means that the nickel oxide clusters on ceria-zirconia were very small and well dispersed. The crystallite sizes calculated by the Scherrer equation were approximately 8 nm for pure CZ as well as NiO/CZ. The concentration of Lewis acid sites (LAS) on CZ as determined by pyridine

adsorption followed by FTIR spectroscopy was very low (2.9 μmol.g^{-1}), whereas a concentration of 80 μmol.g^{-1} was observed for the catalyst with additional nickel oxide clusters, indicating that the nickel oxide clusters are Lewis acidic.[100] The characteristic band of pyridinium ions protonated on Brønsted acid sites was not observed for either sample.

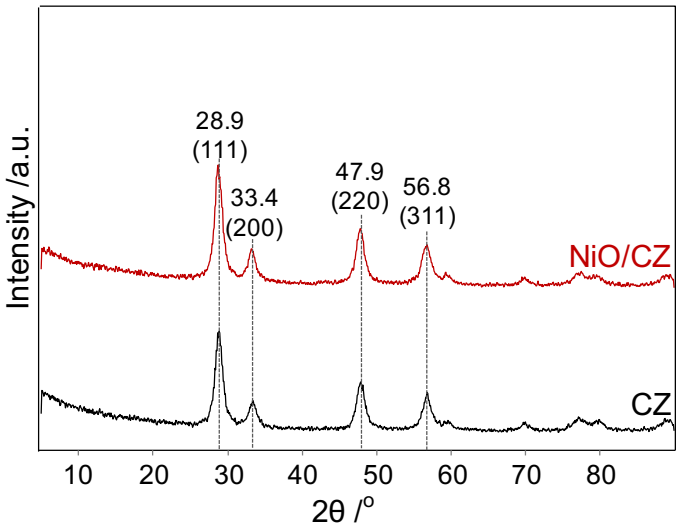

Figure 2.1 XRD patterns of ceria-zirconia based catalysts

The EDX maps of NiO/CZ revealed small and well dispersed NiO particles on ceria-zirconia (Figure 2.2). Specifically, NiO mainly exists as clusters below the detection limit of ~2-3 nm. The size of smaller particles cannot be determined reliably due the limitated stability of NiO clusters under high electron beam currents of modern EDX detectors. Nevertheless, the apparent uniform distribution of Ni signals indicates well-dispersed NiO particles on the entire surface of the ceria-zirconia support, indicating that NiO clusters may be significantly smaller and that cluster containing only a few Ni atoms may be present. In addition to the small particles of NiO, some larger particles up to 10 nm were observed. It is suggested that ceria stabilizes very small, well-dispersed nickel oxide clusters, which are capable of activating methane.[100] Previous

studies showed that pure ceria can stabilize similar non-metallic Pt and Au species, which are very active for water-gas shift reactions.[101]

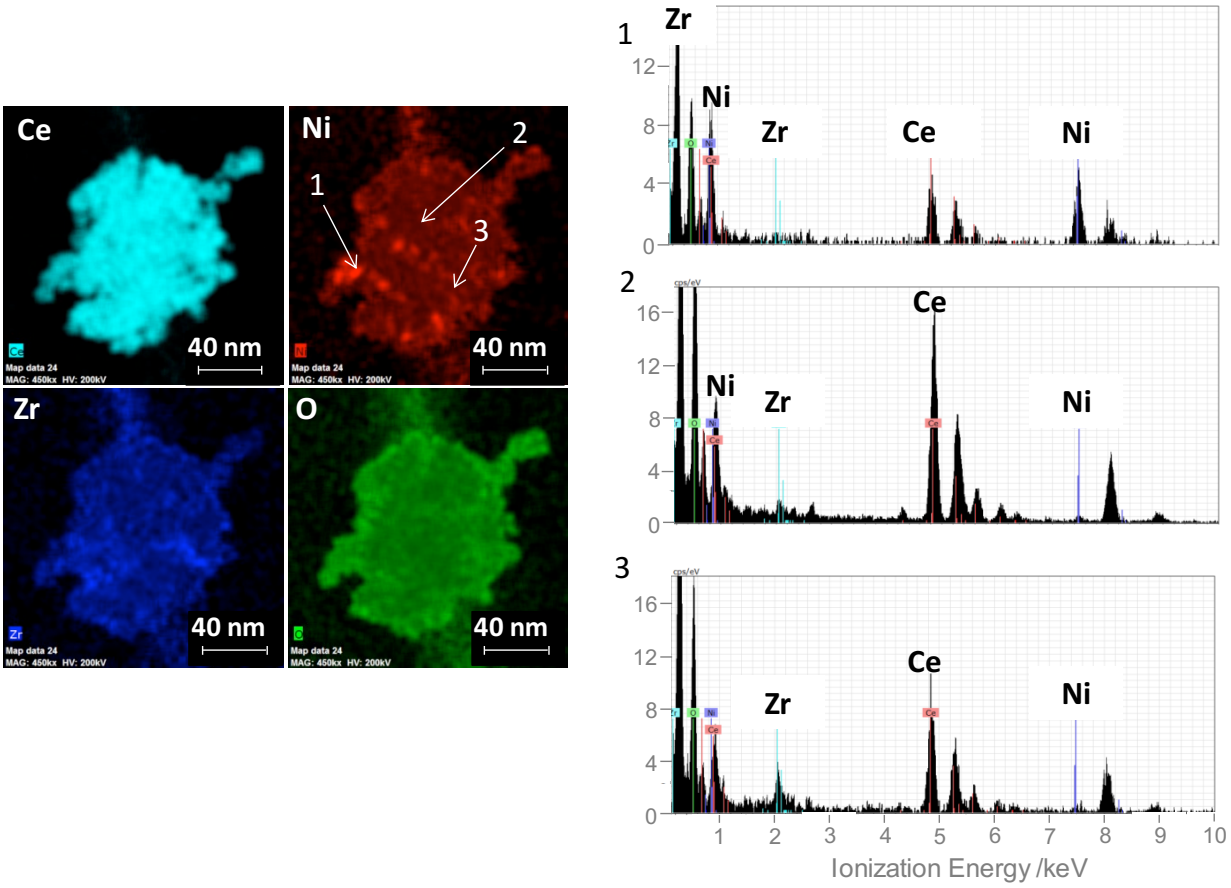

Figure 2.2 EDX maps of 2 wt.% NiO/CZ and spectra showing ionization peaks corresponding to different elements.

2.3.2 Reactivity towards Non-Oxidative Coupling of Methane

Previous studies showed that methane can be activated over NiO/CZ to form surface methyl groups which can be further coupled to higher alkyl groups on the surface.[102] Based on this, it was hypothesized that higher hydrocarbons could be formed from methane over this catalyst. It was observed that these surface alkyl groups formed on NiO/CZ can be removed in high vacuum at 250 ^{o}C within 1 h (Figure A1). A similar desorption step should occur more readily at higher

temperatures. However, the formation of higher alkanes (e.g., ethane) is thermodynamically limited (Table 2.2).

After activation in nitrogen, the conversion of methane at 350 – 500 °C initially increased with increasing time on stream. At 450 and 500 °C it reached a maximum at 0.6% and 1.2%, respectively (Figure 2.3a). The conversion then declined and approached the thermodynamic limit for the conversion of methane to ethane (Table 2.2). Specifically, the conversions of methane after 480 min at 500 ^{o}C, 450 ^{o}C and 350 ^{o}C were 0.39 ± 0.01%, 0.26 ± 0.04% and 0.11 ± 0.02%, respectively, which is slightly lower than the equilibrium conversion for the reaction of methane to ethane.

Table 2.2 Thermodynamic data for gas phase non-oxidative methane reactions.

	ΔG° /kJ.mol^{-1}			X_{CH4} /%		
Reaction	350 ^{o}C	450 ^{o}C	500 ^{o}C	350 ^{o}C	450 ^{o}C	500 ^{o}C
$2CH_4 \leftrightarrow C_2H_6 + H_2$	76	77	78	0.13	0.32	0.45
$2CH_4 \leftrightarrow C_2H_4 + 2H_2$	137	126	121	0.00026	0.0038	0.011
$2CH_4 \leftrightarrow C_2H_2 + 3H_2$	241	220	209	8.59E-09	1.30E-06	9.83E-06
$CH_4 \leftrightarrow C + 2H_2$	26	18	14	6	13	20
$6CH_4 \leftrightarrow C_6H_6 + 9H_2$	335	303	288	1.83E-12	2.18E-11	3.78E-10
$6CH_4 + 4.5O_2 \leftrightarrow C_6H_6 + 9H_2O$	-1592	-1583	-1579	100	100	100

X_{CH4} represents equilibrium conversion of methane

The increase in methane conversion at the beginning is probably due to activation of the catalyst by reduction of big NiO particles to metallic Ni (vide infra). The maximum of methane conversion in the earlier stages of the reactions at 450 and 500 °C is attributed to conversion of methane into carbonaceous deposits, which were quantified based on the carbon balance (Figure

2.3 b-d). The yield of hydrogen also went through a maximum in a similar fashion as the conversion of methane (Figure 2.3e), indicating that dehydrogenation of methane occurred as part of the formation of solid carbonaceous deposits (Table 2.2 Line 4). Several studies have suggested the formation of carbon nanotubes/nanofibers by methane dehydrogenation over Ni based catalysts around 450 ˚C.[103-105] Based on the particle size of NiO/Ni, it is suggested that in the beginning of the reaction, the formation of the solid carbonaceous deposits can occur on Ni particles that are big enough for them to assemble. An aromatic ring has a diameter of 0.45 nm, but the minimum domain size for aromatization might be even larger than that.[106] The formation of aromatic products alongside the carbonaceous deposits is attributed to the coupling of methane derivatives during dehydrogenation (Scheme 2.1) coupled with an oxidation reaction to provide a thermodynamic driving force (Table 2.2 Lines 5 and 6). The redox active CZ support supplies oxygen for this purpose.

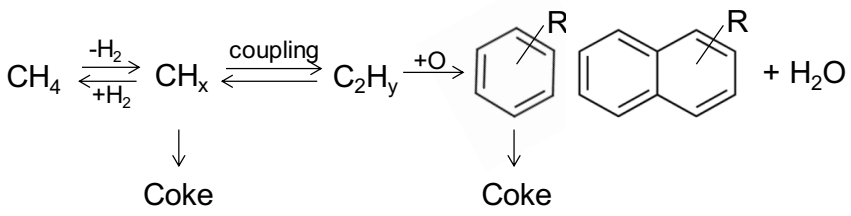

Scheme 2.1 Mechanism for the formation of aromatics and coke in methane aromatization.[107]

At 350 ^{o}C, the conversion of methane did not go through a maximum but continuously approached 0.12%, which is the thermodynamic limit for the conversion of methane to ethane in the absence of an oxidant (Table 2.2, Line 1). Previous studies showed that the reduction of surface ceria in CZ starts around 300 ^{o}C,[87] but at 350 ^{o}C, only a very small fraction of cerium at the surface was reduced. Hence, the amount of oxygen released at this temperature was significantly smaller than the amount released at 450 ^{o}C and 500 ^{o}C. As seen in Figure 2.3d, the

selectivity to aromatics at 350 ˚C was very low compared to 450 ^{o}C (Figure 2.3c) and 500 ˚C (Figure 2.3b) further indicating that reduction of ceria to supply oxygen under methane environment is very limited at this temperature.

The carbon containing products of the reactions at 500 ^{o}C, 450 ^{o}C and 350 ^{o}C were ethane, benzene, toluene and traces of ethylene (at 500 ^{o}C and 450 ^{o}C) and some heavier aromatics such as ethylbenzene, styrene, isopropyl benzene and n-propyl benzene. At the start of the reaction, aromatics were the main products. The selectivities to these aromatic products continuously declined, while the selectivity to ethane increased and reached 81% at 500 ^{o}C, 83% at 450 ^{o}C and 97% at 350 ^{o}C, all on a carbon atom basis. The selectivity to ethylene also increased during the reaction and reached 4.4% at 500 ^{o}C and 1.5% at 450 ^{o}C. No ethylene was observed at 350 ^{o}C. The yields of hydrogen at steady state was higher in the order of 500 ^{o}C > 450 ^{o}C > 350 ^{o}C, which is expected due to the endothermic nature of dehydrogenation reaction. The ratios of ethylene and hydrogen to ethane formed at 450 °C and 500 °C were slightly below the ratios expected under thermodynamic control. The decreasing selectivities of ethane coupled with an increase in the selectivity of ethylene at higher temperatures indicates that ethane is either undergoing a dehydrogenation reaction to form ethylene or that the surface species are undergoing dehydrogenation before desorption to form ethylene.

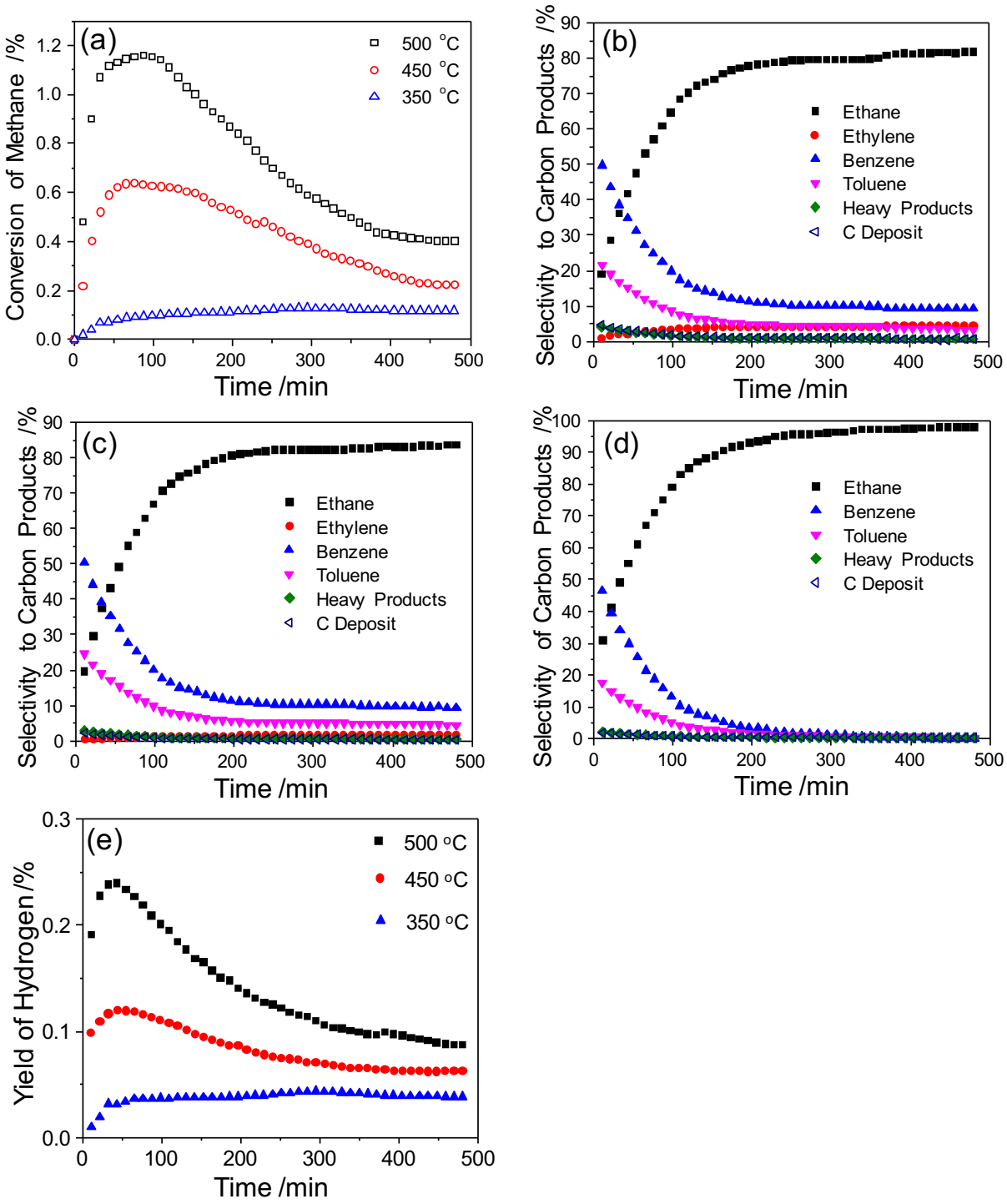

Figure 2.3 (a) Conversion of methane over NiO/CZ at different temperatures (b) Selectivity of carbon products over NiO/CZ at 500 °C (c) 450 °C (d) 350 °C (e) Yields of hydrogen at different temperatures

In-situ XANES spectroscopy was used to probe the oxidation states of ceria and nickel during 5 h of exposure to methane at 450 °C in the absence of any oxidant (Figure 2.4). No shifts of the ceria or nickel edges were observed during activation in nitrogen. The continuous shift of the position of the Ce L_3 edge to lower energy in the first four hours indicated a reduction of some Ce^{4+} species to Ce^{3+} (Figure 2.4a). The position and white line intensity at the Ni K edge remained unchanged for the first 4 h of exposure to methane, indicating that oxidation state of nickel oxide remained approximately constant (Figure 2.4b). Although, big NiO particles seem to reduce during this time frame, it is not observed on XANES since only very few of these big NiO particles exist. The white line then disappeared within 30 min, and the edge position shifted to lower energy, which shows that nickel oxide was reduced to metallic nickel. The combined observations from the Ce L_3 and Ni K edges indicate that easily reducible ceria at or near the surface can supply oxygen to NiO clusters to keep them oxidized until the active oxygen species in CZ are depleted.[102] During the surface reduction with methane, oxygen atoms are removed and steam is formed. Hence, the reduction of ceria and eventually nickel oxide at the initial stage of the reaction supplies oxygen, which drives methane aromatization (Table 2.2, Line 6) from derivatives of methane dehydrogenated species (Scheme 2.1).

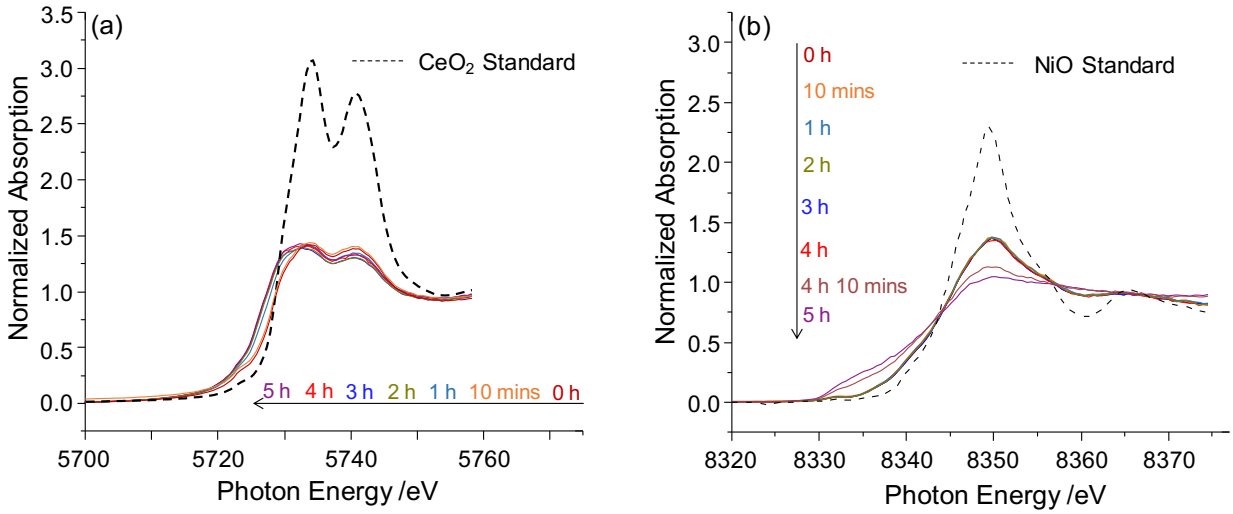

Figure 2.4 In-situ XANES of NiO/CZ during exposure to methane at 450 ^{o}C (a) Ce L_3-edge (b) Ni K-edge.

TEM images of spent catalyst revealed the presence of shells and pockets of graphitic carbon covering Ni domains around 5 nm and greater (Figure 2.5a). However, these graphitic carbon deposits were absent in the parts of the ceria-zirconia matrix where big Ni particles were not detected confirming that big Ni particles were responsible for the formation of carbonaceous deposits and that small Ni domains were not deactivated by coke throughout the reaction.

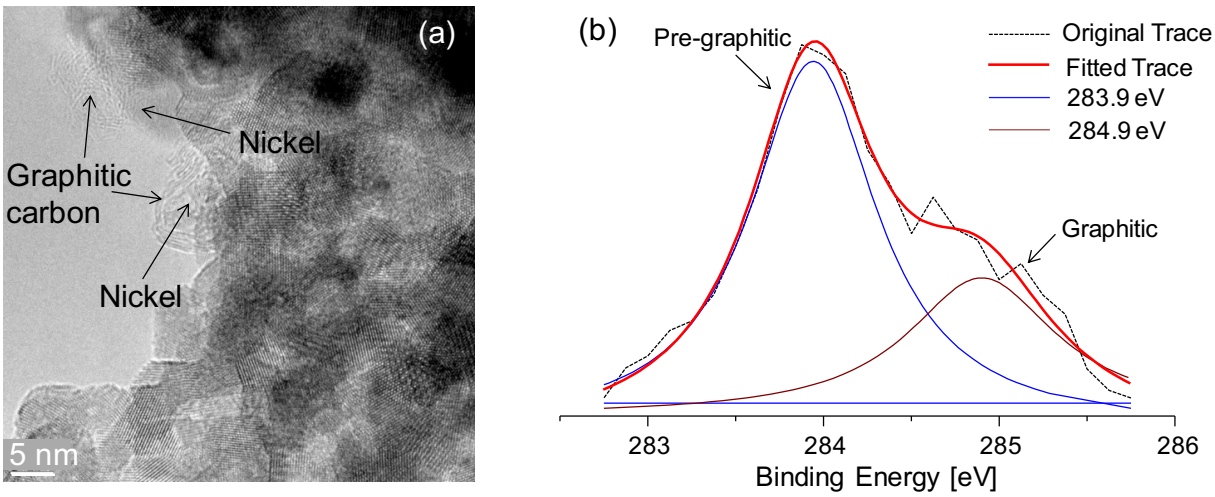

Figure 2.5 (a) TEM of spent NiO/CZ catalyst after reaction with methane at 450 ^{o}C for 8 h. (b) X-ray photoelectron spectra in the C1s region of NiO/CZ after 4 h of methane exposure at 450 ^{o}C.

To further confirm different types of carbonaceous deposits, catalysts were analyzed by C1s XPS after reacting with methane for 4 h (Figure 2.5b). The XP spectrum showed a C=C peak at 284.9 eV indicating that carbon must be deposited in graphitic form.[108-109] Another peak at 283.9 eV was also observed. The lower C1s binding energy of this carbon material compared to that of graphitic carbon suggests that it may be a hydrogen-poor sp-type of pre-graphitic carbon.[110] No carbon containing oxygen was detected. CHN analysis of the spent catalyst revealed that 3.3 wt.%, 4.6 wt.% and 7.6 wt.% of carbon and hydrogen deposits were formed during the reactions at 350 ^{o}C, 450 ^{o}C and 500 ^{o}C, respectively, which was in good agreement with TPO in a thermogravimetric analyzer (Figure 2.6). The Raman spectra of the spent catalysts (Figure 2.6b) showed bands at 1350 and 1590 cm^{-1} which represents "D" (disorder) and "G" (graphite) peaks respectively.[111-112] However, these bands were deconvoluted to obtain detailed structural information (Figure A.3). The two bands were fitted with four Lorentzian-shaped bands (D1, D2, D4 and G) at ν = 1350, 1600, 1210 and 1575 cm^{-1}, respectively and one

Gaussian-shaped band (D3) at 1530 cm^{-1}.[113-114] These components are assigned as graphene edges, graphene sheets, polyenes, graphitic carbon and amorphous carbon respectively. It has been suggested that the ratio $I_{D1}/(I_G + I_{D1} + I_{D2})$ is a measure of the degree of graphitization of carbonaceous materials in which I is the integral of the fitted peak.[114] The intensity ratio of the bands $I_{D1}/(I_G + I_{D1} + I_{D2})$ increased from 0.67 at 350 °C to 0.71 at 450 °C and 0.73 at 500 °C, which shows that the coke became less graphitic with increasing temperature. The amount of graphitic carbon deposit increased when the reaction was run at higher temperatures in agreement with the CH and TPO results.

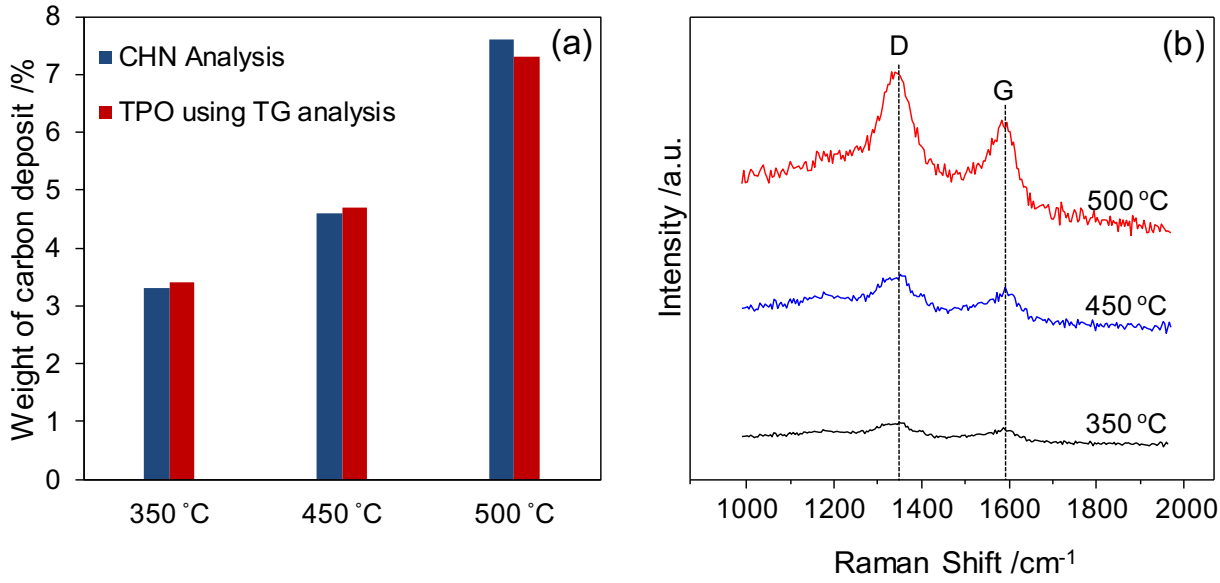

Figure 2.6 (a) Amount of carbon deposit on spent catalysts after reaction at different temeperatures measured from CHN analysis vs. TPO using TG Analysis (b) Raman spectra of spent catalysts after reaction at different temperatures.

IR spectroscopy was used to elucidate the surface reactions during exposure of NiO/CZ to methane at 450 °C (Figure 5.7, Table A.1). The bands of CH_3 (2957 and 2871 cm^{-1}) and CH_2 stretching vibrations (2921 and 2853 cm^{-1}) appeared in the first hour on stream and did not

change significantly afterwards.[115] This shows that methane is readily converted to surface alkyl groups over NiO/CZ. While previous studies of methane activation over Lewis acidic γ-Al_2O_3 showed the formation of surface methyl groups,[116] the observation of bands of CH_2 stretching vibrations implies that higher alkyl groups were present on the surface of NiO/CZ. The presence of CH_3 and CH_2 deformation peaks between 1490 and 1440 cm^{-1} confirmed this conclusion.[115]

Several peaks corresponding to C=C bonds of aromatics and graphitic coke were also seen between 1653 cm^{-1} and 1502 cm^{-1}. The peaks representing aromatic C=C vibrations grew throughout the 12 h period of contact with methane at 450 ^oC, but the growth was relatively limited compared to their intensity after 1 h. The increase of the intensities of these peaks indicates that the surface coverage increased throughout the 12 h and did not entirely reach saturation. It is suggested that some of these aromatic species desorb from the surface in the form of benzene, toluene and traces of heavier aromatics, such as styrene, ethylbenzene and propylbenzene, as seen on the reactivity results (Figure 2.3). A peak around 1580 cm^{-1} is also observed which is assigned to graphitic coke.[117-118] The intensity of this peak increased slowly and approached an asymptotic limit. This indicates that surface coverage of graphitic coke approached saturation within the first hour on stream. This confirms the observation on the TEM images of the spent catalyst in which only certain domains of the catalysts were covered with graphitic coke. These domains which comprise of big Ni particles of around 5 nm as seen in (Figure 2.5a) are responsible for the formation of graphtic carbon deposits. The rest of the catalyst where these big Ni particles are absent are free from deactivation by coking.

To sum up the observations from the IR spectra coupled with the reactivity results and the characterization of NiO/CZ after exposure to methane, it appears that the two types of active Ni species on the CZ support play different roles for methane conversion. Aromatization of

methane is not possible on Ni domains that are smaller than an aromatic ring (i.e., 0.45 nm), but the actual minimum domain size might be even somewhat larger. As a result, at least some of these sites form higher alkyl chains, which desorbs as ethane or ethylene. In the case of the bigger Ni domains, further C-C coupling steps coupled with an oxidation reaction results in the formation of aromatics such as benzene, toluene and traces of styrene, ethylbenzene and propylbenzene. Solid carbon deposits are also formed on these big Ni domains and eventually deactivate these sites. The production of aromatics gradually declines as the big Ni domains are covered by coke and oxygen from ceria is depleted. At this point, the smaller Ni domains make up the majority of the active sites, and the reaction pathway towards the formation of ethane and ethylene becomes dominant.

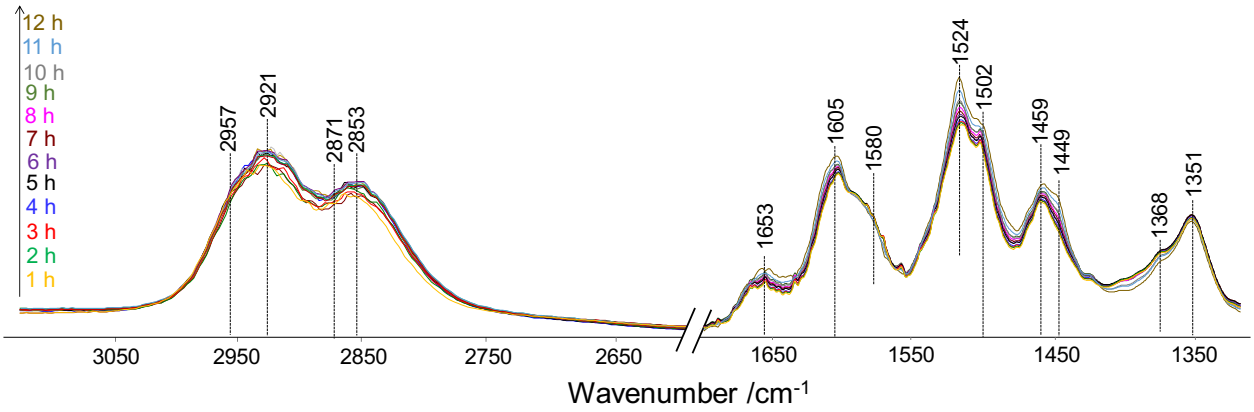

Figure 2.7 Subtracted in-situ FTIR spectra during exposure of 2 wt.% NiO/CZ to methane at 450 ^{o}C

2.3.3 Strategies for Improved Performance

The present contribution shows that Ni/CZ is capable of activating methane at low temperatures and coupling surface methyl groups to ethane. However, this endothermic reaction is thermodynamically limited to 0.45% conversion at 500 °C (Table 2.2). To improve the

conversion to an acceptable level for industrial application without increasing the operating temperatures, these catalysts could be incorporated into membranes that can selectivity remove hydrogen to drive the reaction in the forward direction. Several studies in the literature have successfully demonstrated the use of such membranes on systems with either catalysts that are significantly more expensive than and not as active as the catalyst in this study or for non-oxidative methane aromatization at high temperatures (700 – 800 ˚C).[12, 81]

2.4 Conclusions

Nickel particles on ceria zirconia catalysts are active for the conversion of methane into ethane, ethylene and aromatics such as benzene, toluene, ethylbenzene, styrene and propylbenzene. The nickel sites are responsible for the activation of methane. Coupling of activated methane groups resulted in the formation of different products. Two domains of Ni particles are present on CZ which play different roles in the conversion of methane based on their particle size. Bigger Ni particles which are greater than 0.45 nm is responsible for the formation of carbonaceous deposits because they have enough surface sites for them to assemble. Aromatics are also formed on these sites due to coupling with an oxidation reaction during the reduction of CZ. Smaller Ni particles which are smaller than a benzene ring (0.45 nm) and down to isolated Ni atoms are not involved in the formation of carbonaceous deposits. Activated methane group couple into higher alkyl chains which are desorbed from the catalyst surface as ethane. In cases in which the temperature was high enough, ethane is either able to undergo further dehydrogenation to form ethylene or the surface alkyl groups dehydrogenate before desorption. The catalyst was able to perform this reaction for 8 h with no clear signs of a complete deactivation because coking was restricted and selective on the catalyst surface. This study therefore presents an efficient and cheap catalyst for converting methane into useful hydrocarbons in the absence of an oxidant at

reasonably low temperatures up to the thermodynamic limit. The high stability of the catalyst at the reaction condition potentially makes it an important part of a membrane reactor for improving methane conversion. By selectively removing hydrogen from the reaction mix, the membrane reactor can potentially improve the yields of useful products from methane in a non-oxidative environment.

CHAPTER 3

CONVERSION OF METHANE TO METHANOL AND ETHANOL OVER NICKEL OXIDE ON CERIA-ZIRCONIA CATALYSTS IN A SINGLE REACTOR

3.1 Background

The availability of methane from conventional and unconventional reserves has revolutionized the world's energy mix in recent years.[119] In conventional processes, methane is reformed into syngas,[120] which can be used for methanol synthesis[121] or be converted to higher hydrocarbons by Fischer-Tropsch synthesis.[122] Unfortunately, these processes are only economical on large scales, and reforming requires high temperatures (typically > 1100 K). Since transporting gas over long distances is economically challenging, many natural gas reserves are "stranded", and methane is often flared on site rather than used in a productive way. In addition to the loss of a valuable resource, this practice results in greenhouse gas emissions.[123] Catalytic processes that could enable conversion of methane to liquid products in a single reactor have enormous potential to enable more effective use of stranded gas reserves. This situation has led to intense interest in converting methane to value-added chemicals and fuels.[9-10, 15, 64, 124-126]

The conventional route for methanol production uses $Cu/ZnO/Al_2O_3$, ZnO/Cr_2O_3 or similar catalysts at 30-350 bar.[121 127] The reaction occurs by sequential hydrogenation of CO or CO_2. Synthesis of ethanol and higher alcohols was reported over Rh, Mo, and modified Fischer–Tropsch or methanol synthesis catalysts and typically also requires elevated pressure.[128] The proposed routes for C-C bond formation include methanol and CO homologation and CO insertion into metal carbon bonds. Ethanol formation from methanol and syngas was also reported over Cu/SiO_2 catalysts at atmospheric pressure.[31]

An interesting route for methane activation that might avoid the economy of scale of established routes is direct partial oxidation into oxygenates like methanol, formic acid and formaldehyde or methanol precursors such as methyl bisulphate.[9] In nature, bacterial methanotrophs convert methane to methanol with metalloenzymes, such as methane monooxygenases.[32] Soluble monooxygenase contains a carboxylate bridged diiron center, whereas a dicopper cluster has been proposed as the active site of particulate monooxygenase.[14] While monooxygenases enable an interesting path for methane conversion, they only have limited potential for large scale industrial processes. Inspired by methane monooxygenases, supported phthalocyanine complexes of Fe, Cu, and Co have been investigated.[33-35] In other studies, methane was converted to methanol over small metal oxide clusters in zeolites, such as bis(μ-oxo) dicopper complexes in Cu/ZSM-5.[15, 129-134] However, prohibitively expensive oxidants like tert-butyl hydroperoxide,[33] H_2O_2,[15] or N_2O[135] had to be used in many of these studies to generate reactive oxygen species. In other studies, the "catalyst" was reactivated by calcination before it was able to undergo the next turnover.[132, 136] Thus, the reaction did not occur in a conventional catalytic cycle, in which all elementary reactions occur under the same conditions.

Methane can also be activated at rather mild temperatures (373 – 423 K) by strong Lewis acid sites that are formed when alumina is calcined at high temperature.[36-37] However, in many cases, the methyl groups remained on the surface rather than engaging in catalytic turnovers. Nevertheless, this illustrates the potential of Lewis acid sites as components of bifunctional catalysts.

In this study, we developed a catalyst that is capable of converting methane to alcohols at steady state and moderate temperatures in a single reactor. Steam was necessary to release the

alcoholic products, and O_2 acted as an oxidant. This catalyst combines Lewis acid sites with a redox-active ceria-zirconia (CZ) support to enable catalytic turnovers. Additionally, coupling and/or methanol homologation reactions occur, to form ethanol, which is more valuable than methanol.

3.2 Experimental

3.2.1 Materials

Cerium (III) nitrate hexahydrate (99% trace metals basis), zirconyl (IV) oxynitrate hydrate (99% trace metals basis), nickel (II) nitrate hexahydrate, iron (III) nitrate nonahydrate, palladium (II) nitrate hydrate, aluminum (III) nitrate nonahydrate, cobalt (II) nitrate hexahydrate and ammonium hydroxide (A.C.S. regent grade, 28–30% NH_3content) were purchased from Sigma Aldrich. Silica (99.8% purity) was purchased from Sigma Aldrich. Gases (methane, nitrogen, carbon monoxide, hydrogen and oxygen) with ultra-high purity (UHP Grade 5) were purchased from Airgas and dry air for calcination was generated in our labs using a Parker Balston Gas Generator 1000. Methanol (99.9% purity) was purchased from Sigma Aldrich. Deionized water was obtained from a Barnstead NANOpure ultrapure water system which was purified to 18.2 MΩ/cm.

3.2.2 Catalyst synthesis

The ceria zirconia support was prepared by coprecipitation of the precursors of ceria and zirconia.[86-87] Cerium nitrate hexahydrate and zirconyl nitrate hydrate were dissolved in deionized water to form a 0.1 M solution. The coprecipitation was modified by adding the 0.1 M precursor solution drop-wise to an aqueous ammonium hydroxide solution while stirring continuously. The precipitate was then filtered, rinsed with deionized water, and dried in an oven overnight at 373

K. The catalyst was then calcined for 4 h in 200 mL/min zero grade air at 723 K with a ramp rate of 5 K/min. The co-precipitation material comprised of Ce (0.83) and Zr (0.17) as determined by ICP-OES and is referred to as CZ in the manuscript. Metal oxide clusters of Ni, Fe, Pd, Co and Al were deposited on the CZ support using conventional dry impregnation or pore volume impregnation.[88] The metal content chosen was 2 wt.% in all cases. For this purpose, the metal precursor in question was dissolved in deionized water equal the pore volume of the ceria zirconia support, as determined by nitrogen physisorption. The resulting solution was added dropwise to the support, collected in a beaker, at room temperature. It was mixed thoroughly for 30 minutes, dried at 373 K for 5 h and then calcined for 4 h at 723 K with a ramp rate of 10 K/min. For reference, a sample with the same concentration of NiO on commercial SiO_2 support was prepared using the same approach. As another reference sample, 5 wt.% Ni was also deposited on to CZ using the same synthesis approach as with other materials.

3.2.3 Characterization

Nitrogen physisorption measurements of the prepared samples were taken using a Micromeritics ASAP 2020 physisorption analyzer. The catalysts were degassed at 473 K for 4 h prior to measurement. Surface areas and pore volumes were calculated based on the BET method[89] and BJH method,[90] respectively.

To determine the amount of ceria, zirconia, and nickel on the catalyst, ceria zirconia and NiO on ceria zirconia were sent to Galbraith Laboratories for inductively coupled plasma-atomic emission spectroscopy (ICP-AES) analysis.

X-ray diffraction patterns were obtained using a Phillips X'Pert diffractometer equipped with an X'celerator module using Cu Kα radiation. Diffractograms were collected at incident angles from $2\theta = 5$ to 90° with a step size of 0.0167°.

Pyridine adsorption followed by FTIR spectroscopy was performed using a Nicolet 8700 FTIR spectrometer with an MCT/A detector. Each spectrum was recorded with 64 scans with a resolution of 4 cm^{-1}. Each sample was pressed into a translucent self-supported wafer and loaded into a vacuum FTIR transmission cell. The sample was activated at 723 K for 1 h under high vacuum and cooled to 423 K. A background spectrum was taken. The chamber was then dosed with 0.10 mbar of pyridine for 30 mins or until adsorption equilibrium of pyridine was reached. Subsequently, the cell was evacuated for 1 h to remove physisorbed pyridine and a spectrum was taken. To determine the strength of acid sites, the sample was heated to 523 K, 623 K and 723 K for 1 h, and a spectrum was taken at 423 K. After each experiment, the density of the wafer was determined by using a circular stamp of 6.35 mm to cut a disc of specific size from the wafer. The concentration of Lewis and Brønsted acid sites were determined by the Beer-Lambert law using the integral of the peaks at 1445 cm^{-1} and 1540 cm^{-1}, respectively. Extinction coefficients were used as reported by Datka et al.[137]

In-situ XANES spectra at the Ce L_3-edge and Ni K-edge were collected at beamline 9-BM-C at the Advanced Photon Source of Argonne National Laboratories (Proposal GUP-43235). A Si (1 1 1) double monochromator was used to select the beam energy for all measurements. The beam size was 800 x 1000 μm. Samples were pressed into wafers and placed in a cubic reactor. The beam was internally calibrated with a metallic cerium reference foil for Ce L_3-edge and metallic nickel reference foil for Ni K-edge and spectra were collected in fluorescence mode. A spectrum was first taken of each of the fresh samples. The samples were then activated in helium at 723 K for 1 h in the cubic reactor while continuously taking spectra. The gas was then switched to 5% methane and balance helium and spectra were taken continuously. Separate experiments were performed under the same conditions for both Ce L_3-edge and Ni K-edge.

In-situ XANES experiments with steam were performed in the same reactor and at the same conditions. Helium was used to bubble steam into the reactor while continuous XANES spectra were taken at the Ni K-edge.

XPS measurements were performed with a Physical Electronics Quantera Scanning X-ray Microprobe. This system uses a focused monochromatic Al Kα X-ray (1486.7 eV) source for excitation and a spherical section analyzer. The instrument has a 32 element multichannel detection system. The 83 W X-ray beam focused to 100 μm diameter was rastered over a 1.1 mm x 0.1 mm rectangle on the sample used for the analysis. The X-ray beam is incident normal to the sample and the photoelectron detector is at 45° off-normal. High energy resolution spectra were collected using a pass-energy of 69.0 eV with a step size of 0.125 eV. For the Ag 3d5/2 line, these conditions produced a FWHM of 1.07 eV. The sample experienced variable degrees of charging. Low energy electrons at ~1 eV, 20μA and low energy Ar^+ ions were used to minimize this charging. The 2 and 5 wt.% NiO/CZ catalysts powder was pressed into a 4 mm x 1 mm diameter holes machined into a custom 13 mm diameter SS sample stub designed for use with a custom modified ULVAC PHI XPS sample platen. The custom sample platen and sample stub including the fresh catalysts was placed into the XPS vacuum introduction system and pumped to <1x10-7 Torr using a turbomolecular vacuum pumping system prior to introduction into the XPS spectrometer ultrahigh vacuum system. The spectrometer vacuum system pressure is maintained at <1x10-9 Torr during analysis and pumped using a series of sputter ion and turbomolecular vacuum pumps. After XPS analysis of the fresh catalysts the sample stub was transferred to an attached catalytic reaction side chamber also pumped by a series of sputter ion and turbomolecular vacuum pumps. The sample stub was then transferred from the catalytic side chamber into an attached high vacuum tube furnace. The pressure of the tube furnace was

increased ~760 Torr using 5% methane/He at a flow rate of 100 SCCM. The catalyst was heated to 723 K at a rate of 10 K/minute and held for 1 hour. This procedure was repeated with a wait time of 4 hours at 723 K in 5% methane/He flow. After the catalyst was cooled to RT the gas was quickly removed using a turbomolecular vacuum pump attached to the tube furnace. The stub was then transferred into the UVH catalytic chamber and then into the XPS spectrometer vacuum for analysis.

Quantification was performed using standard sensitivity factors contained in the ULVAC-PHI, Inc. MultiPak V9.5.0.8 version date of 10-30-2013 software. Peak area intensities required for quantification were calculated after applying a Shirley background subtraction. These quantification results include the instrument transmission function, source angle, and asymmetry corrections. Typical XPS analysis depth from inelastic mean free path calculations is up to 3 nm depending on the kinetic energy of the detected electron. The majority of the electrons detected are coming from the first atomic layer.

The EDX map was collected with aberration corrected Scanning Transmission Electron Microscope (STEM) (JEOL JEM-ARM200F) operated at 200 kV. The electron-optics column incorporates CEOS GmbH double-hexapole aberration corrector for the probe-forming lens, which allows imaging with ~0.8 nm resolution in scanning transmission electron microscopy (STEM) mode. The presented images were acquired on HAADF detector with beam convergence of 27.5 mrad and collection angle of 68-280 mrad. Elemental analysis was performed using Energy Dispersive X-ray Spectroscopy (EDX) using high collection angle SSD. (~0.7srad, JEOL Centurio). Acquisition and evaluation of the spectra was performed by NSS Thermo Scientific software package. In general, the STEM sample preparation involved

mounting powder samples on copper grids covered with lacey carbon support films, and then immediately loading them into the STEM airlock to minimize an exposure to atmospheric O_2.

Spent catalysts were sent to Atlantic Microlab for CHN analysis.

3.2.4 In-situ IR spectroscopic studies on surface reactions of methane

Methane activation over different catalysts was investigated by in-situ FTIR spectroscopy. The catalysts were pressed into self-supported wafers and introduced into a custom made high vacuum cell with ZnSe windows. A cryogenic pump and a turbo pump were used to evacuate the cell to 10^{-6} mbar. Each wafer was activated in high vacuum at 723 K for 1 h and cooled to 323 K. It was then exposed to 530 mbar of CH_4 for 1 h. The methane in the cell was then removed with the cryogenic pump, and a spectrum was collected immediately. The wafer was also contacted with methane at 373 K, 423 K, 473 K and 523 K following the same procedure as used at 323 K.

3.2.5 Operando transmission FTIR spectroscopic studies

50 mg of the catalyst was pressed into a circular self-supported wafer with a diameter of 2 cm. The wafer was loaded into the sample holder, and it was assembled as a part of the FTIR cell together with the cell body and heating block. The cell was built based on a design reported in the literature.[93] The assembled FTIR cell was placed into a Nicolet 8700 FTIR spectrometer. Each spectrum was recorded with 64 scans at a frequency of one per minute for 8 h during exposure to 5% methane and balance inert at 25 ccm total flow rate (to make up a space velocity of 3000 h^{-1}) at 723 K and atmospheric pressure, and also at standard reaction condition similar to the case for the packed bed reactor (see below in reactivity studies). All lines were heated to 393

K to prevent condensation of steam. The effluent line was connected to a Hiden HPR-20 QIC mass spectrometer to monitor the signal of the product stream over time.

3.2.6 Reactivity Studies

Reactivity experiments for the coupling and selective oxidation of methane were performed in a packed bed reactor using a steam to carbon ratio of 1 and an oxygen to carbon ratio of 0.2. The studies were conducted using 200 mg of catalyst sieved to 75 μm. Catalyst samples were activated in-situ at 723 K in nitrogen for an hour prior to reactivity studies in all the reactivity experiments. A space velocity of 3000 h^{-1} of reactant gas diluted in nitrogen (5% CH_4) was employed. A 100 ccm total flowrate of gas was used. The reaction temperature was 723 K (unless specified otherwise) and pressure was atmospheric. In experiments with methanol and syngas, the total flowrate was kept the same at 100 ccm and carbon monoxide comprised 5% of the stream. The methanol to CO ratio was 1 and the H_2 to CO ratio was 2. In the experiment with just methanol, a 5% methanol gas in nitrogen reactant stream was used and the reaction was ran for 8 h at 723 K. Reactivity of syn-gas over NiO/CZ was also conducted in the presence and absence of steam. A 100 ccm total flow rate was employed with 5 % CO and an H_2 to CO ratio of 2. In the case where steam was present in the stream, a CO to steam ratio of 1 was employed. The reactor was connected to an online Bruker 450-GC refinery gas analyzer (RGA) and a Hiden HPR20 mass spectrometer. The RGA is equipped with two TCD detectors and an FID. One TCD is used for analysis of hydrogen and the second for analysis of permanent gas mixtures (including methane). The FID channel allows for identification of methane and higher hydrocarbons as well as alcohols. The TCD for hydrogen gas analysis uses a molsieve 5A column, the TCD for permanent gas analysis uses a Molsieve 13x and Hayseep Q columns in series, and the column to the FID is a BR-1. The GC was calibrated for all reactant and product

gases by flowing 3-4 known amounts of the gas in question at the same temperature used in the selective oxidation reaction (723 K) and monitoring the peak areas. Product gas was sampled at 20 minute intervals using the RGA. The mass spectrometer equipped with a Faraday detector was used for hydrogen and steam analysis by monitoring the signal at m/z of 2 and 18 respectively in continuous Multiple Ion Detection (MID) mode. The mass spectrometer was also used for oxygen analysis by monitoring the signal at m/z of 32, 31 and 46. The following definitions were used:

Conversion: $X_R[\%] = \frac{F_{R,in} - F_{R,out}}{F_{R,in}}$ x 100

C Product Yield: $Y_p\,[\%] = \frac{F_{p,out}}{\nu_p \cdot F_{CH4,in}}$ x 100

H_2 Yield: $Y_{H2}\,[\%] = \frac{F_{H2,out}}{(2.F_{CH4,in} + F_{H2O,in})}$ x 100

Where ν_p is the normalized stoichiometric coefficient and F_x is the molar flow rate of the gas in question.

3.2.7 Verification of alcohols in the product stream

In order to verify the formation of methanol and ethanol, the effluent stream of the reactor was connected to a cold trap set at a temperature of 273 K. ^{13}C NMR was then performed on the condensate. For this purpose, a Bruker Advance III-400 spectrometer was used. Deuterated D6-DMSO was used as the lock solvent in a sealed 1 mm capillary as an external standard. Quantitative data were collected with ^{13}C decoupling using 30˚ pulse angle with a scan time of 2 sec and delay time of 1 sec between scans. The number of scans collected was 512 through TopSpin 3.0 software and processed using MestReNova NMR software by Mestrelab Research S. L.

2 wt.% NiO/CZ was also sent to the National Renewable Energy Laboratories for testing and products analysis from ^{1}H NMR also verified the presence of methanol and ethanol as products of methane conversion in the presence of steam and oxygen at 723 K.

3.2.8 Elementary reactions for the conversion of methane to alcohols

To obtain reasonable yields of alcohols, it is necessary to couple activation and coupling of methane with an oxidation reaction as in reactions 3 and 4.

$$CH_4 + H_2O \leftrightarrow CH_3OH + H_2 \qquad \Delta G_{723\ K} = 124.7\ kJ/mol \qquad (1)$$

$$2CH_4 + H_2O \leftrightarrow C_2H_5OH + 2H_2 \qquad \Delta G_{723\ K} = 181.4\ kJ/mol \qquad (2)$$

$$CH_4 + H_2O + 1/2O_2 \leftrightarrow CH_3OH + H_2O \qquad \Delta G_{723\ K} = -87.0\ kJ/mol \qquad (3)$$

$$2CH_4 + H_2O + O_2 \leftrightarrow C_2H_5OH + 2H_2O \qquad \Delta G_{723\ K} = -190.8\ kJ/mol \qquad (4)$$

3.3 Results and Discussion

The CZ support with a molar CeO_2:ZrO_2 ratio of 83:17 was obtained by co-precipitation following a procedure published before.[87, 99] Al_2O_3, CoO_x, FeO_x, PdO, and NiO clusters on CZ were prepared by dry impregnation of nitrate precursors. The loading was 2 wt.% (on a metal basis) in all cases. The desired Lewis acidic metal oxide clusters were obtained by calcination at 723 K. NiO/SiO_2 with the same Ni loading and NiO/CZ with 5 wt.% Ni were prepared as reference samples.

The concentration of acid sites on each catalyst was determined by pyridine adsorption followed by FTIR spectroscopy. Only the characteristic band of pyridine on Lewis acid sites (LAS) (1445 cm^{-1}) was observed, while none of the spectra contained the characteristic peak of pyridinium ions on Brønsted acid sites (1540 cm^{-1}) (Figure S1). Pure CZ had a low

concentration of LAS (2.9 μmol.g^{-1}), whereas significantly higher values of 80±4 μmol.g^{-1} were measured for the samples with additional metal oxide clusters except for Al_2O_3/CZ (Figure B.1b). This analysis shows that 26% of the Ni atoms in 2 wt.% NiO/CZ are involved in forming a Lewis acid site (Table B.1).

The ability of the Lewis acidic catalysts to activate methane was probed by in-situ IR spectroscopy. All samples were activated in vacuum at 723 K. After 1 h of exposure to 530 mbar of methane at 323 K and evacuation for 1 min, CZ only retained a small amount of physisorbed methane as indicated by a small peak at 3014 cm^{-1} (Figure B.4a). At temperatures between 373 and 523 K, no stable surface species were observed. This shows that CZ does not have sufficient Lewis acidity for methane activation. On catalysts with additional metal oxide clusters, peaks corresponding to asymmetric and symmetric CH_3 stretching modes were observed around 2957 and 2875 cm^{-1}, respectively, starting at 373 – 423 K (Figure 3.1 and B4b-g). The intensity of the peaks varied between catalysts with different supported metal oxide clusters, but they were observed for all the samples used in this study. In agreement with previous work on methane activation on γ-Al_2O_3,[37] we conclude that methane is activated and that surface methyl or methoxy groups are formed. In case of NiO/CZ and FeO_x/CZ, additional bands were observed around 2921 and 2851 cm^{-1} (Figure 3.1 and Figure B4e). These peaks are attributed to asymmetric and symmetric CH_2 stretching modes, respectively.[138] The presence of these bands indicates that surface methyl groups are coupled to longer alkyl or alkoxy chains. Methane activation was also studied on NiO/SiO_2 to probe the role of the CZ support in the activation and coupling of methane. Only the peaks of methyl groups were observed, but no CH_2 groups were formed. This shows that CZ plays a direct or indirect role in enabling the formation of alkyl chains with more than one carbon atom.

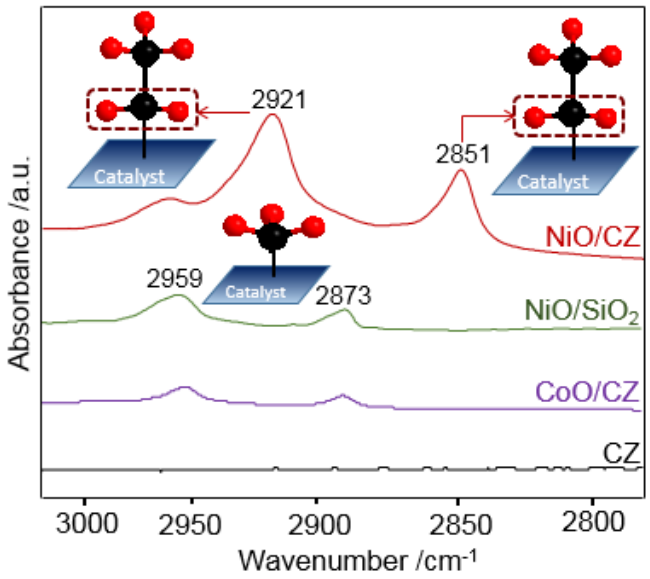

Figure 3.1 Difference IR spectra of products from CH_4 on selected catalysts at 473 K

Based on these results, we hypothesized that CZ stabilizes very small, well-dispersed NiO or FeO_x clusters that are capable of activating and coupling methane at low temperatures. Previous reports showed that similar non-metallic Pt and Au species can be stabilized by pure ceria and that these species are highly active as part of water-gas-shift catalysts.[101] To verify our hypothesis, EDX maps and X-ray diffractograms of NiO/CZ, NiO/SiO_2, and were obtained. The EDX maps of NiO/CZ with 2 wt.% Ni showed the presence of well-dispersed Ni on the entire surface of the CZ support (Figure 3.2a and B.8). The exact size distribution of the Ni clusters cannot be quantified by EDX mapping due to the detectability-stability limits. Nevertheless, it can be concluded that they should be present as NiO clusters below ~2-3 nm in size. In addition to the well dispersed NiO, several larger particles (up to 10 nm) were also occasionally observed. In contrast, the EDX map of NiO/SiO_2 only revealed Ni in the form of larger particles of 10 – 25 nm (Figure 3.2b). An increase of the Ni loading on CZ to 5 wt.% also resulted in the formation of larger NiO clusters (Figure 3.2c). In agreement with these results, the X-ray diffractogram of NiO/CZ only contained peaks corresponding to CZ, whereas diffractions of NiO crystallites were

observed for NiO/SiO_2 (Figure B.3). This shows that the concentration of crystalline particles in 2 wt.% NiO/CZ is below the detection limit for XRD. It is suggested that the high dispersion of NiO on CZ is one prerequisite for the unique activity of these species. In addition, CZ could alter the net charge of the supported NiO clusters or provide interfacial active sites.

Further insight into the synergy between the NiO clusters and the CZ support was obtained by probing the oxidation state of Ni and Ce with in-situ XANES experiments (Figure 3.3). When NiO/CZ was exposed to a flow of 4% methane in helium at 723 K, the Ce L3-edge shifted to lower energy over the course of 4 h (Figure 3.3a), indicating reduction of the CZ support. After 4 h, no further shift of the Ce L3-edge could be observed. The final edge position and the line shape with two maxima, which is typical for Ce 4+, indicated that the majority of Ce atom remained in an oxidation state of 4+ with a small contribution from Ce 3+.[139-140] The relatively low white line intensity is attributed to strong Ce fluorescence absorption by ceria matrix. Complementary XPS experiments showed that 49% of the Ce atoms within 3 nm from the surface were reduced to Ce 3+ upon exposure to CH_4 for 4 h at 723 K (Figure B.13). Thus, it is suggested that the reduction of CZ at 723 K is mostly limited to surface sites, whereas the bulk essentially remains oxidized.[87, 140]

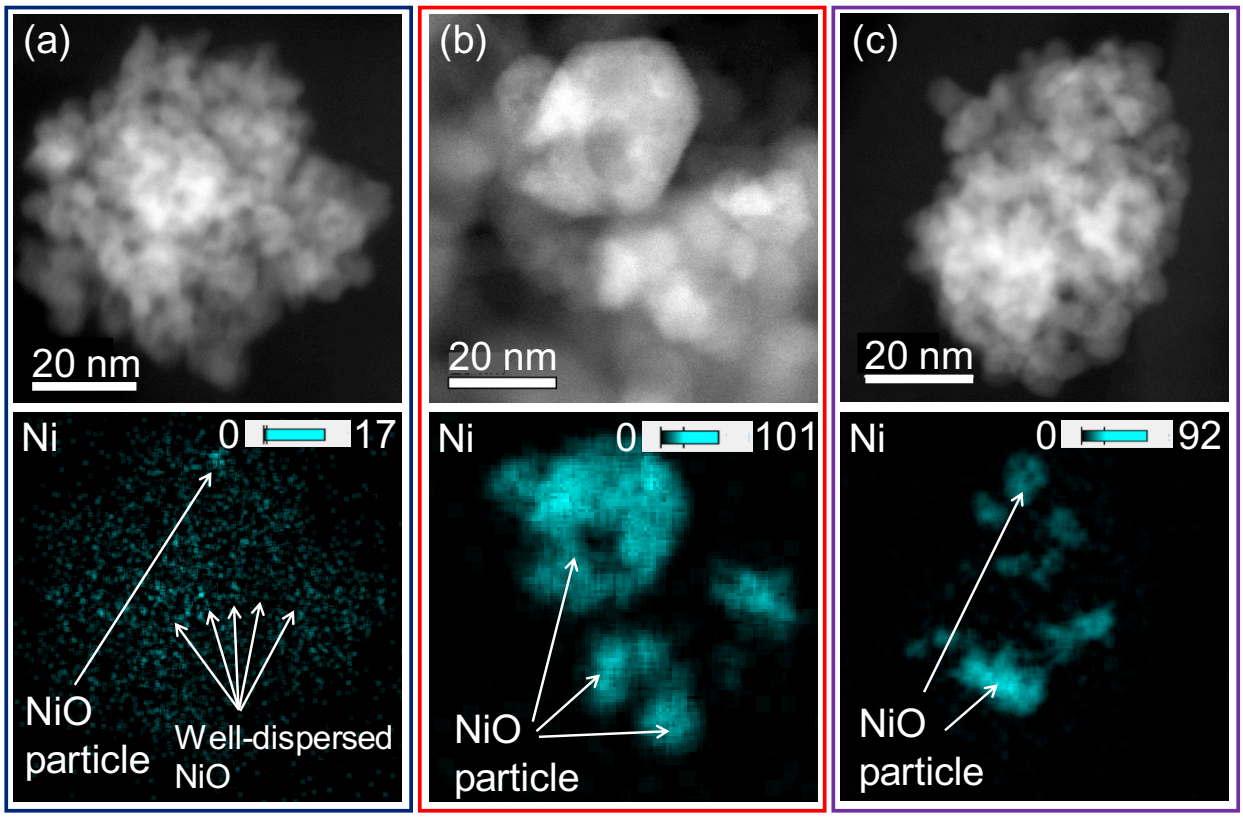

Figure 3.2 HAADF images and corresponding EDX maps of Ni for (a) 2 wt.% NiO/CZ (b) 2 wt.% NiO/SiO_2 (c) 5 wt.% NiO/CZ. The scales in the Ni EDX maps correspond to the integrated signal from the ionization peak of Ni(K)

The spectrum at the Ni K-edge did not change in the first 4 h, while the reduction of CZ was proceeding (Figure 3.3b). However, a reduction of the white line intensity and a shift of the edge to higher energy occurred within 30 minutes once the reduction of Ce stopped. This shows that NiO clusters are readily converted to metallic Ni when they are present on a reduced CZ surface. Together, the changes of the Ce L3-edge and Ni K-edge indicate that CZ can act as an oxygen reservoir that can supply a certain amount of oxygen to NiO clusters to keep them in the oxidized state. Importantly, CZ has been reported to efficiently activate oxygen even at room temperature via a so-called multiple exchange mechanism.[39] The combined abilities of activating

oxygen and transferring activated oxygen species to the supported particles, such as the NiO clusters in this study, make CZ an effective component of bifunctional oxidation catalysts.[141-142]

In addition to studying the redox behavior of NiO/CZ, we used in-situ XANES to probe the interaction of steam with the supported NiO clusters, since in previous studies the formation of metal hydroxides prevented selective oxidation of methane over CuO_x and FeO_x clusters in steady state.[132, 136] No changes were observed at the Ni K-edge when NiO/CZ was exposed to steam at 723 K for 4 h (Figure 3.3c) indicating that the NiO clusters are not converted into hydroxides under these conditions. The derivative of the spectrum provides even clearer evidence for the absence of hydroxyl species (Figure B.15). While the white line of the $Ni(OH)_2$ standard showed two distinct maxima, this feature was not observed for the NiO standard or the NiO/CZ catalyst after exposure to steam at 723 K. Thus, it is safe to conclude that NiO clusters are stable in this environment.

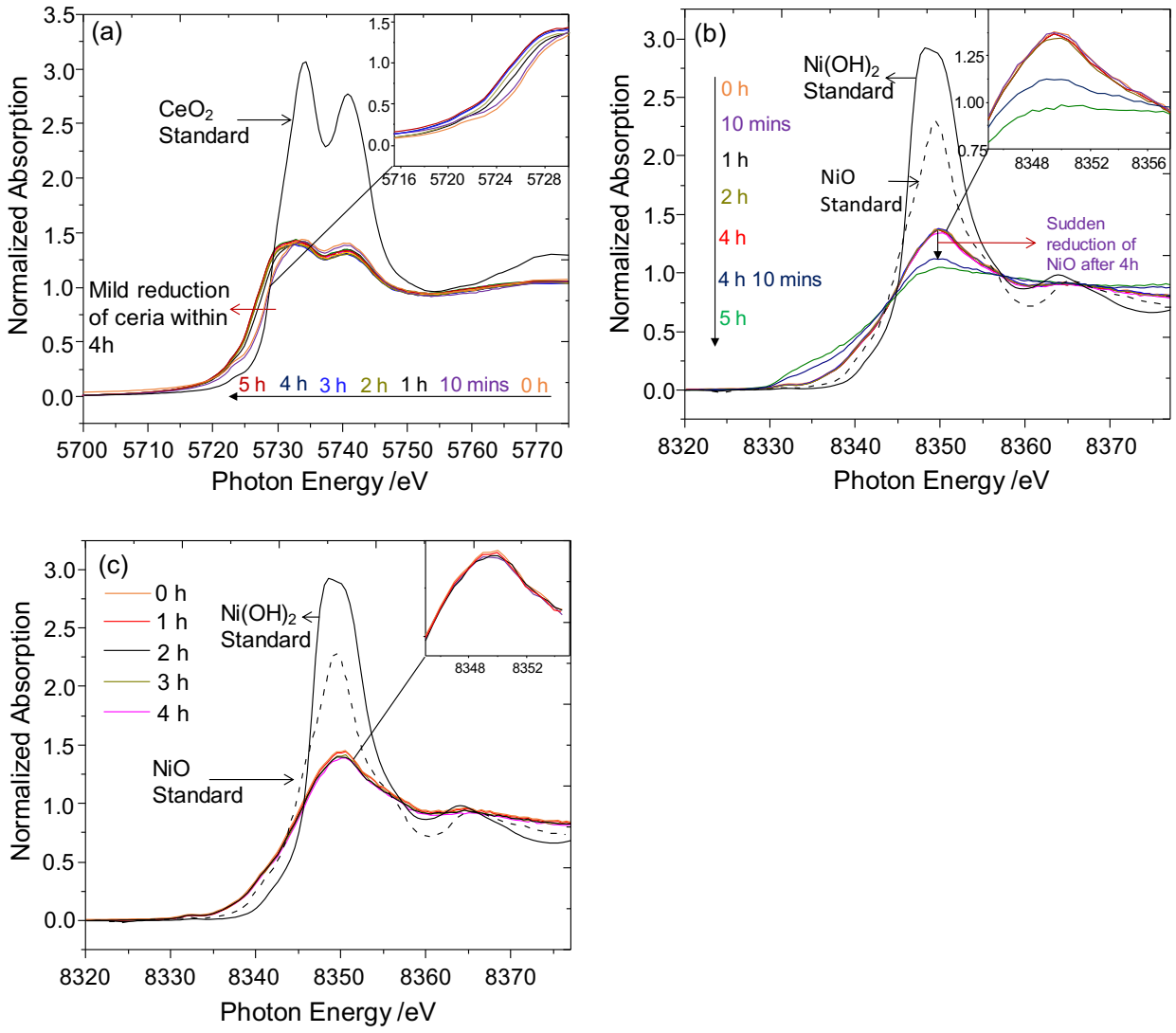

Figure 3.3. In-situ XANES spectra: (a) Ce L_3-edge during reaction of CH_4 over NiO/CZ at 723 K (b) Ni K-edge during reaction of CH_4 over NiO/CZ at 723 K (c) Ni K-edge during exposure to H_2O at 723 K

Based on the observation of higher alkyl or alkoxy chains on NiO/CZ (Figure 3.1) and the characterization of this material, we hypothesized that methanol and higher alcohols can be formed over these catalysts. It was shown that steam can hydrolyze surface methoxy species to form methanol [134]. However, this elementary reaction needs to be coupled with a selective oxidation step to make the process thermodynamically feasible (see appendix B). Thus, the

conversion of methane over 2 wt.% NiO/CZ was studied in a packed bed reactor at 723 K with a feed steam-to-carbon ratio of 1.0, an O_2 to carbon ratio of 0.2, and a balance of nitrogen (Figure 3.4). The initial methane conversion was 18%. It declined to 15% over the first 3 h on stream, but no further changes were observed after that. If one assumed that every Ni atom of the catalyst constitutes an active site, the conversion of 15% would correspond to a turnover frequency of 50 h^{-1}. Methanol, ethanol, and CO_2 were observed as the main carbon containing products along with hydrogen. The ethanol and methanol yields reached 3.7% and 2.9% on a C atom basis, respectively. This corresponds to a cumulative alcohol selectivity of up to 43%, and an ethanol selectivity of 24% on a C atom basis. The formation of methanol and ethanol was confirmed by NMR spectroscopy (Figures B.24a and B.25) and MS (Figure B.24b). The production of methanol and ethanol throughout the reaction remained almost constant. No products with three or more carbon atoms were observed under the conditions applied here. The conversion and selectivity to ethanol are comparable to the performance of typical catalysts for conversion of syngas to ethanol.[143] The formation of H_2 and CO_2 can be attributed to oxy-reforming or a sequence of steam reforming and the water-gas-shift reaction, but oxidation of other surface species could also contribute to the formation of CO_2.

In the initial stage of the reaction, 2.6% of the carbon atoms entering the reactor remained unaccounted for in the product stream and 1.5% were converted to aromatics (Figure 3.4). Within 5 h, the fractions of unaccounted carbon and aromatics decreased to 0.23% and 0.14%, respectively, and remained at approximately this level for the remaining 3 h of the reaction. Previous reports indicated that coking is typical for Ni particles that have a certain minimum size.[144-145] Thus, it is suggested that carbonaceous deposits are formed on the few large NiO clusters (Figure 3.2a). Some aromatic precursors of these deposits are desorbed instead of being

permanently deposited. Once the larger particles are covered, the formation of deposits and aromatics almost ceases. In contrast, the well-dispersed NiO clusters remain accessible and active. CHN analysis of the spent catalyst indicated the presence of 2.9 wt.% of carbon deposits.

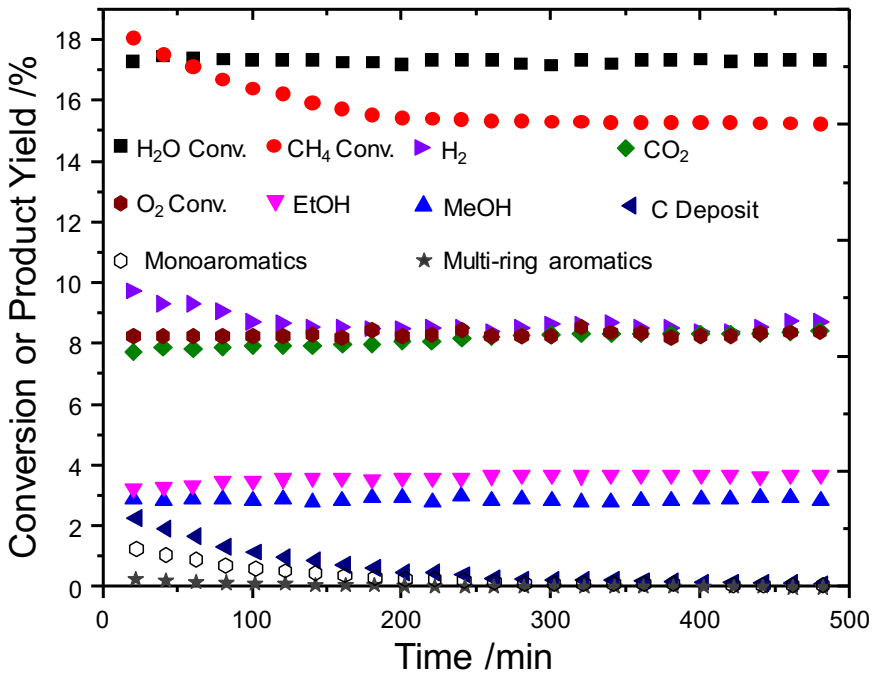

Figure 3.4 Conversion of methane and O_2 and yields of products formed during reactions of methane, steam and oxygen in a packed bed reactor setup at 723 K and 1 atm over 2 wt.% NiO/CZ. Yields of carbon-containing products are calculated on a carbon atom basis. A space velocity of 3000 h^{-1} of reactant gas diluted in nitrogen was used

Further evidence for this scenario was obtained when methane was converted under identical conditions over 2 wt.% NiO/SiO_2 and 5 wt.% NiO/CZ, which contained larger NiO particles. Over 2 wt.% NiO/SiO_2, the initial conversion was 15%, but the catalysts deactivated completely over the course of 6 h (Figure B.23a). The amount of deposited carbon on the spent catalyst as determined by CHN analysis was 5.8 wt.%, which is significantly higher compared to 2 wt.% NiO/CZ. Only CO and CO_2 were observed as carbon-based products over this catalyst,

which demonstrates further that the synergy between NiO and CZ plays a critical role in the production of alcohols. The initial conversion over 5 wt.% NiO/CZ was 23%, but it declined to 13% within 5 h (Figure B.22a), and the cumulative alcohol selectivity was only around 30%. These observations show that 5 wt.% NiO/CZ contains fewer small NiO clusters that are active for sustained production of alcohol than 2 wt.% NiO/CZ.

To illustrate the function of steam, 2 wt.% NiO/CZ was used in a reaction with a feed that only contained methane and O_2 in N_2 (Figure B.17b). The conversion dropped from 17% to 14% over the first 3 h on stream and remained constant for the rest of the experiment. CO_2 was the only carbon containing product detected. This shows that steam is necessary to obtain alcohols, whereas the combustion of methane dominates in the absence of steam in the feed. With a feed containing only methane, steam and nitrogen, the initial methane conversion was 2% and some alcohols were formed (Figure B.17a). However, the catalytic activity ceased within about 4 h, which correspond to the time at which the reduction of Ce stopped during the in-situ XANES experiment under similar conditions.

The observations described above show that NiO clusters can activate methane, similar to the one in previous reports of methane activation on other types of Lewis acidic sites.[36-37] In the case of sufficiently large clusters, carbonaceous deposits are formed, and the clusters are deactivated. The CZ support appears to stabilize NiO clusters that are sufficiently small to avoid this deactivation path. In the presence of steam, the surface species can be hydrolyzed and desorbed as alcohols. Based on the in-situ XANES results (Figure 3.3a and 3.3b) and well-documented activity of CZ for activating O_2,[39] it is suggested that the active oxygen species required for the selective oxidation reaction originate on CZ. However, the exact origin of O atoms in the products will be the subject of future studies. A reference experiment showed that

methanol formation over NiO/CZ is also possible from syngas and steam (Figure B.18b), but CO was not completely converted.

The strong peaks of alkyl or alkoxy groups with two or more carbon atoms in in-situ IR spectra (Figures 3.1 and B.5) seems to point at a reaction path involving coupling of surface alkyl or alkoxy species. In a reference experiment, ethanol was formed from a mixture of methanol and syngas at the same temperature and pressure (Figure B.19). This indicates that homologation might be an alternative reaction path,[128] but the observation of residual CO in this experiments (as opposed to the absence of CO in the product stream from methane conversion) indicates that homologation is less likely to be the dominant reaction path.

3.4 Conclusions

In summary, the present results show that the unique synergy between small NiO clusters and redox-active CZ results in a catalyst that can convert methane to methanol and ethanol in a single reactor. To the best of our knowledge, this is the first report of a single-reactor conversion of methane to ethanol. Unlike in studies of many other materials based on supported metal oxide clusters, all parts of the catalytic cycle occur at the same temperature with a turnover frequency of at least 50 h^{-1}.

CHAPTER 4

OPTIMIZATION OF ACTIVE SITES OF NiO/CZ TO IMPROVE METHANE CONVERSION TO ALCOHOLS

4.1 Background

Methane, which constitutes the main component of natural gas, is an excellent raw material for the production of fuels and chemicals.[9, 33, 64, 124-125, 146-147] This is because of the abundant availability of methane reserves especially with recent discoveries of shale gas deposit in North America and methane hydrates in ocean floors which represent at least twice the amount of carbon in other known sources of fossil fuels.[1] However, large amounts of natural gas are located in remote areas and because shipping gas is not economically feasible and liquefaction or building pipelines is technically challenging and prohibitively expensive, these gas reserves are considered "stranded".[147-150] As a result, a lot of natural gas by-products from oil wells in remote locations are vented or flared. Conversion of methane to liquid products under reasonable reaction conditions is therefore a highly desirable option as an alternative for utilizing "stranded" methane resources and can be an entry point for the production of value-added chemicals. However, such reactions have proven to be challenging to perform.[10, 147-149, 151]

An important catalytic route that is being explored for utilizing methane feedstock is a direct partial oxidation of methane into oxygenates like methanol, formic acid and formaldehyde or methanol precursors such as methyl bisulphate.[9] A direct conversion of methane to methanol has been investigated as the most attractive solution because methanol is less reactive than other oxygenates and could be transported in pipelines. Also, methanol is a highly desirable precursor to chemicals such as acetic acid[152] as well as ethylene and propylene via MTO chemistry.[153-154] Higher alcohols such as ethanol was also recently shown to be produced alongside methanol

from methane in a single reactor at low temperature over 2 wt.% NiO supported on ceria-zirconia (NiO/CZ).[100] This is an advantageous process because higher alcohols are even more energy dense than methanol and can also be used for the production of important chemicals through dehydration[155-156] and oligomerization.[156-158] Also, ethanol is a very important medical solvent as well as a highly important fuel.

Catalyst of NiO/CZ that was used in the previous study for the conversion of methane to methanol and ethanol was prepared using dry impregnation method. This method of synthesis was utilized in the previous study because catalyst synthesis on industrial scales are usually implemented using impregnation method. In dry impregnation (DI), the metal precursor is dissolved into a solution which is just sufficient to fill up the pore volume of the support.[159-160] This method is advantageous because no filtration step is required and hence, no metal is lost during synthesis. A major drawback with this method is that the metal precursor is deposited by precipitation during drying.[161] As a result of this method of metal deposition, a very weak interaction between the support and the metal is most often achieved. There is very little control over the deposition of the metal which often results in the formation of larger metal oxide particles and low dispersion of the metals or metal oxides.[159-160, 162]

As a result of the drawbacks of impregnation methods of catalyst synthesis as discussed in the previous paragraph, much research effort has been dedicated to the fundamentals of catalyst synthesis. Several synthesis techniques have been proposed with the aim of providing a much better control of the deposition of metals and metal oxides on catalysts support.

Strong electrostatic adsorption (SEA) is one of several other synthesis techniques that has been proposed and proven to be both reproducible and leads to catalysts with smaller metal oxide or metal particles and higher dispersion than catalysts prepared by impregnation methods.[162-170]

This technique is a special case of wet impregnation in which the final pH is set to the pH range in which the electrostatic interaction is strongest.[167] The deposition of metal particles by SEA therefore involves mainly electrostatic interactions between the metal precursor and the support. This strong electrostatic adsorption limits the degree of agglomeration of metal oxides during calcination of the sample following impregnation.

Another synthesis technique that is very commonly used in the literature for the synthesis of metal oxide catalysts is co-precipitation.[171-175] This method produces a "mixed" precipitate comprising of two or more insoluble species that are simultaneously removed from solution. Chemical precipitation is generally not a controlled process in terms of solid phase nucleation and growth processes. Therefore, solids obtained by chemical precipitation typically have a wide particle size distribution and uncontrolled particle morphology and a high degree of agglomeration during calcination. However, several protocols have been recommended in using this synthesis technique to obtain a narrow particle size distribution. These requirements involve a high degree of supersaturation in alkaline solution, a uniform spatial concentration distribution inside the precipitation reactor and a uniform growth time for all particles or crystals. If these protocols are observed when carrying out catalyst synthesis by co-precipitation, catalysts with well dispersed metal or metal oxide particles can potentially be obtained.

In this study, different synthesis techniques were used to prepare NiO/CZ with the aim of obtaining an optimum dispersion of NiO particles on CZ. This bi-functional catalyst of NiO/CZ was recently shown to be capable of converting methane to alcohols at steady state in a single reactor.[100] The process occurs at moderate temperatures using O_2 as an oxidant. The activity of this catalyst depends on the Lewis acidity of well-dispersed NiO clusters as well as the redox activity of the CZ support. Detailed characterization of the catalyst material revealed that the

particle size of NiO on CZ plays an important role in the selectivity of methane to alcohol. Based on this observation, an optimization of the performance of this catalyst is performed from a synthesis perspective with the aim of increasing the dispersion of NiO on the CZ support. Strong electrostatic adsorption (SEA) was used to deposit NiO on CZ in which a net surface charge is introduced on the CZ support, which is opposite to the charge of the metal complex and lead to a strong interaction between the metal complex and the support. Co-precipitation (CP) was also used as a means to prepare NiO/CZ. Since CP is a bulk synthesis technique and only a fraction of NiO particles end up as accessible Lewis acidic sites on the surface, several catalysts with different loading of Ni were also prepared to find the optimum loading. The performance of the newly synthesized catalysts was compared with the performance of the catalyst prepared using dry impregnation in the previous study.

4.2 Experimental

4.2.1 Materials

Cerium (III) nitrate hexahydrate (99% trace metals basis), zirconyl (IV) oxynitrate hydrate (99% trace metals basis), nickel (II) nitrate hexahydrate, silica (99.8% purity), ammonium hydroxide (A.C.S. regent grade, 28–30% NH_3 content) and sodium hydroxide (ACS reagent, ≥ 97.0%) were purchased from Sigma Aldrich. Hydrogen chloride and sodium hydroxide (A.C.S. reagent grade) from Sigma were used as pH adjustors in catalyst synthesis using strong electrostatic adsorption (SEA). Gases (methane, nitrogen, carbon monoxide, carbon dioxide and hydrogen) with ultra-high purity (UHP Grade 5) were purchased from Airgas. Dry air for calcination was generated in our labs using a Parker Balston Gas Generator 1000. Deionized water was obtained from a Barnstead NANOpure ultrapure water system which was purified to 18.2 MΩ/cm.

4.2.2 Catalyst Synthesis

The catalysts were synthesized using three different synthesis technique namely; dry impregnation (DI), strong electrostatic adsorption (SEA) and co-precipitation (CP).

4.2.2.1 Dry Impregnation (DI)

The ceria zirconia support was first prepared by coprecipitation of the precursors of ceria and zirconia.[176] For this purpose, cerium nitrate hexahydrate and zirconyl nitrate hydrate were dissolved in deionized water to form a 0.1 M solution. The coprecipitation was modified by adding the 0.1 M precursor solution drop-wise to an aqueous ammonium hydroxide solution while stirring continuously. The precipitate was then filtered, rinsed with deionized water, and dried in an oven overnight at 100 ^{o}C. The catalyst was then calcined for 4 h in 200 mL/min zero grade air at 450 ^{o}C with a ramp rate of 5 ^{o}C/min. The co-precipitation material was comprised of Ce (0.83) and Zr (0.17) as determined by ICP-OES and is referred to as CZ in the manuscript. Nickel oxide clusters were deposited on the CZ support using dry impregnation or pore volume impregnation (reference). The nickel content impregnated was 2 wt.%. Nickel (II) nitrate hexahydrate was dissolved in deionized water equal to the pore volume of the ceria zirconia support, as determined by nitrogen physisorption. The resulting solution was added dropwise to the CZ support collected in a beaker at room temperature. It was then mixed thoroughly for 30 minutes, dried at 100 ^{o}C for 5 h and then calcined for 4 h at 450 ^{o}C with a ramp rate of 10 ^{o}C/min. The catalyst was then analyzed by ICP-OES using a Perkin Elmer Optima 3000 DV. The catalyst prepared using this technique is represented as 2NiO/CZ_DI in this manuscript.

4.2.2.2 Strong Electrostatic Adsorption (SEA)

The ceria zirconia support was first prepared using the same technique as with dry impregnation.

4.2.2.2.1 Point of zero charge study

To determine the point of zero charge (PZC) of the ceria zirconia support, pH solutions ranging from 0.5 to 12.97 were prepared using HCl or NaOH. High surface loading of CZ was used for this study. The exact mass of CZ used corresponded to a surface loading (S.L.) of 1000 $m^2.L^{-1}$. The support was contacted with the pH solutions, shaken for an hour in a rotary shaker, and then the final pH was then measured. A glass bodied Mettler Toledo pH probe was employed for all pH measurements. The pH meter was calibrated using standard buffer solutions at the start of every experiment. The experiments were conducted using 50 mL polypropylene bottles at room temperature.

4.2.2.2.2 Catalyst preparation

CZ was weighed in a polypropylene bottle and dissolved in a solution of deionized water to make up a surface loading of 1000 $m^2.L^{-1}$. The nickel content used was also 2 wt.%. Nickel (II) nitrate hexahydrate corresponding to 2 wt.% loading was added to the aqueous solution of ceria zirconia and the pH was adjusted to 9.5 using HCl or NaOH. The solution was then placed in a rotary shaker. The pH of the impregnating solution was re-adjusted to 9.5 every 30 minutes over a period of 4 hours at which time the deposition of all the nickel in the solution had occurred. The catalyst was then filtered using 45 μm nylon syringe filters, dried overnight at 100 ^oC and calcined for 4 h at 450 ^oC with a ramp rate of 10 ^oC/min. The catalyst was then analyzed

by ICP-OES using a Perkin Elmer Optima 3000 DV. The catalyst prepared using this technique is represented as 2NiO/CZ_SEA in this manuscript.

4.2.2.3 Co-Precipitation (CP)

NiO/CZ catalysts were prepared by co-precipitation method with different weight loading of Ni (2 wt.%, 4 wt.%, 6 wt.% and 10 wt.%). Cerium nitrate hexahydrate, zirconyl nitrate hydrate and nickel (II) nitrate hexahydrate were dissolved in deionized water to form a 0.1 M solution. The coprecipitation was modified by adding the 0.1 M precursor solution drop-wise to an aqueous sodium hydroxide solution while stirring continuously following a procedure reported in the literature.[171] The precipitate was then filtered, rinsed with deionized water, and dried in an oven overnight at 100 ^{o}C. The catalyst was then calcined for 4 h in 200 mL/min zero grade air at 450 ^{o}C with a ramp rate of 5 ^{o}C/min. The composition of the co-precipitation materials were determined using ICP-OES at Galbraith National Lab and are reported in Table 4.1. The catalyst prepared using this technique is represented as xNiO/CZ_CP in this manuscript. Where x is the weight loading of nickel used.

4.2.3 Characterizations

Nitrogen physisorption measurements of the prepared samples were taken using a Micromeritics ASAP 2020 physisorption analyzer. The catalysts were degassed at 200 ^{o}C for 4 h prior to measurement. Surface areas and pore volumes were calculated based on the BET method[89] and BJH method,[90] respectively.

To determine the amount of ceria, zirconia, and nickel on the catalyst, ceria zirconia and NiO on ceria zirconia were sent to Galbraith Laboratories for inductively coupled plasma-atomic emission spectroscopy (ICP-AES) analysis.

X-ray diffraction patterns were obtained using a Phillips X'Pert diffractometer equipped with an X'celerator module using Cu Kα radiation. Diffractograms were collected at incident angles from 2θ = 5 to 90° with a step size of 0.0167°.

Pyridine adsorption followed by FTIR spectroscopy was performed using a Nicolet 8700 FTIR spectrometer with an MCT/A detector. Each spectrum was recorded with 64 scans at a resolution of 4 cm^{-1}. Each sample was pressed into a translucent self-supported wafer and loaded into a vacuum FTIR transmission cell. The sample was activated at 450 ^{o}C for 1 h under high vacuum and cooled to 150 ^{o}C. A background spectrum was taken. The chamber was dosed with 0.10 mbar of pyridine for 30 mins or until adsorption equilibrium of pyridine was reached. Subsequently, the cell was evacuated for 1 h to remove physisorbed pyridine and a spectrum was taken. To determine the strength of acid sites, the sample was heated to 250 ^{o}C, 350 ^{o}C and 450 ^{o}C for 1 h, and a spectrum was taken at 150 ^{o}C. After each experiment, the density of the wafer was determined by using a circular stamp of 6.35 mm to cut a disc of specific size from the wafer. The concentration of Lewis and Brønsted acid sites were determined by the Beer-Lambert law using the integral of the peaks at 1445 cm^{-1} and 1540 cm^{-1}, respectively. Extinction coefficients were used as reported by Tamura et al.[91]

4.2.4 Reactivity studies

Reactivity experiments for the oxidation of methane over the catalysts prepared were performed in a packed bed reactor using a steam to carbon ratio of 1 and an oxygen to carbon ratio of 0.2. The studies were conducted using 200 mg of catalyst sieved to 75 μm. Catalyst samples were activated in-situ at 723 K in nitrogen for an hour prior to reactivity studies in all the reactivity experiments. A space velocity of 3000 h^{-1} of reactant gas diluted in nitrogen (5% CH_4) was employed. A 100 ccm total flowrate of gas was used. The reaction temperature was

450 ^{o}C and pressure was atmospheric. The reactor was connected to an online Bruker 450-GC refinery gas analyzer (RGA) and a Hiden HPR20 mass spectrometer. The RGA is equipped with two TCD detectors and an FID. One TCD is used for analysis of hydrogen and the second for analysis of permanent gas mixtures (including methane). The FID channel allows for identification of methane and higher hydrocarbons as well as alcohols. The TCD for hydrogen gas analysis uses a molsieve 5A column, the TCD for permanent gas analysis uses a Molsieve 13x and Hayseep Q columns in series, and the column to the FID is a BR-1. The GC was calibrated for all reactant and product gases by flowing 3-4 known amounts of the gas in question at the same temperature used in the selective oxidation reaction (723 K) and monitoring the peak areas. Product gas was sampled at 20 minute intervals using the RGA. The mass spectrometer equipped with a Faraday detector was used for hydrogen and steam analysis by monitoring the signal at m/z of 2 and 18 respectively in continuous Multiple Ion Detection (MID) mode. The mass spectrometer was also used for oxygen analysis by monitoring the signal at m/z of 32, 31 and 46. The following definitions were used:

Conversion: $X_R[\%] = \frac{F_{R,in} - F_{R,out}}{F_{R,in}}$ x 100

C Product Yield: $Y_p\,[\%] = \frac{F_{p,out}}{\nu_p \cdot F_{CH4,in}}$ x 100

H_2 Yield: $Y_{H2}\,[\%] = \frac{F_{H2,out}}{(2.F_{CH4,in} + F_{H2O,in})}$ x 100

Where ν_p is the normalized stoichiometric coefficient and F_x is the molar flow rate of the gas in question.

4.3 Results

4.3.1 NiO/CZ_SEA synthesis optimization

4.3.1.1 Determination of point of zero charge

At the point of zero charge (PZC), the support surface has a net neutral charge. At pH values below the PZC, the surface of the support is positively charged or protonated and favors the adsorption of anionic species. When the pH value is above the PZC of the metal oxide support, the surface is negatively charged or deprotonated. This favors the electrostatic adsorption of cationic species. In this study, CZ was used as the support and NiO was deposited on CZ using a precursor of nickel (II) nitrate hexahydrate which is cationic. In order to determine the appropriate conditions to deposit Ni^{2+} on the metal oxide support via strong electrostatic adsorption, it is therefore important to determine the point of zero charge of the support of CZ. The plateau as seen in Figure 1 represents the PZC of CZ. It exists because the number of surface OH groups is significantly greater than the quantity of OH^- ions initially present in solution.[173] This enables CZ to buffer the solution at its PZC. An intuitive picture of this surface chemistry is depicted in Figure 1. The PZC of CZ in this study was found to be around a pH of 7.9. This value was determined by plotting an x=y line across the pH plot and looking for its point of interception with the data points that constitute the plateau in Figure 2. Details of the theoretical model applied to the PZC plot can be found in the literature.[163-164, 177-178] Two parameters of the model are adjustable based on the support used; the total number of charged sites N_s and the difference between pK_1 and pK_2 (ΔpK). For ceria, these values can be readily found in the literature; $N_s = 8$ OH.nm^{-2} and $\Delta pK = 6$.[164]

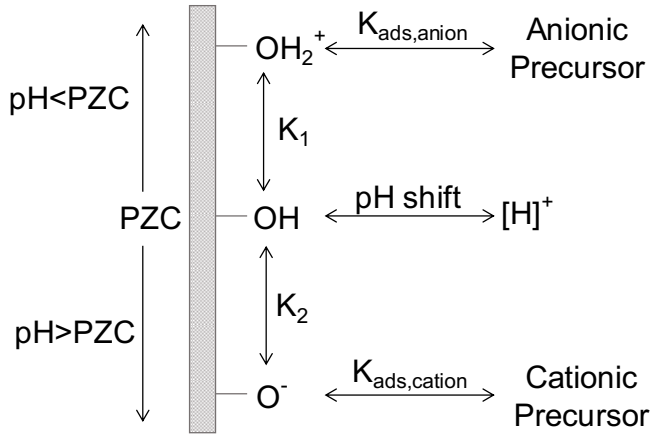

Figure 4.1 Mechanism of electrostatic adsorption as proposed by J.R. Regalbuto.[167]

It should be noted that ideally, an anionic precursor of Ni should be used since the PZC of CZ is on the high side.[159] However, for this study, it is important to maintain the same Ni precursor (nickel (II) nitrate hexahydrate) that was used to prepare similar catalysts using other synthesis techniques which this catalyst will ultimately be compared with. Also, nickel (II) nitrate hexahydrate is the nickel precursor generally selected to prepare oxide-supported catalysts, due to its low cost, high solubility in water and decomposition at moderate temperatures.[179] To facilitate electrostatic adsorption using the cationic precursor of nickel (II) nitrate hexahydrate, the net surface charge of the support needs to be negative (or at a pH above the PZC of 7.9). In this study a pH of 9.5 was used to ensure that the surface of CZ is negatively charged and also that precipitation does not occur. The amount of Ni uptake by this method (as well as other synthesis techniques) were determined by ICP-OES analysis as seen in Table 4.1.

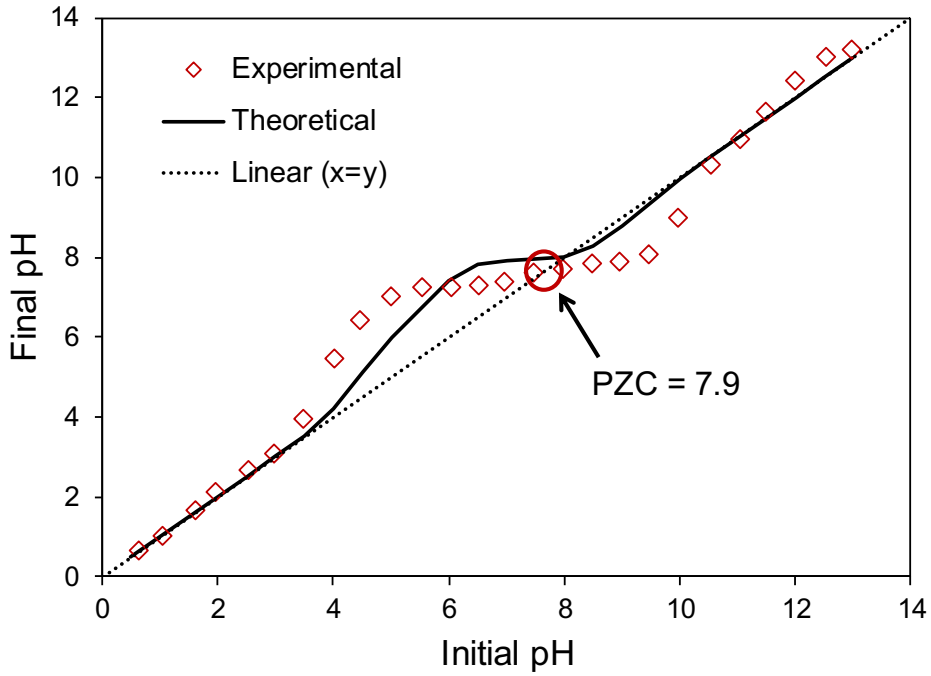

Figure 4.2 Experimental PZC data fit with theoretical model. Adjustable parameters, PZC = 7.9. Adjustable theoretical model parameters; difference between pK_1 and pK_2 (ΔpK) = 6.0, Number of charged sites (N_s) = 8 OH.nm^{-2} at 25 ^{o}C.[164]

4.3.2 Characterization of NiO/CZ catalysts prepared by DI, SEA and CP

4.3.2.1 Structural and textural properties of catalysts prepared using different synthesis techniques

Table 4.1 shows the results from elemental analysis and N_2 physisorption. From elemental analysis, it was found that 2NiO/CZ_DI contained 1.96 wt.% nickel and 2NiO/CZ_SEA contained 1.95 wt.% nickel. The catalysts prepared using co-precipitation with different nickel loading, which are referred to as 2NiO/CZ_CP, 4NiO/CZ_CP, 6NiO/CZ_CP and 10NiO/CZ_CP contained 1.93, 3.97, 5.91 and 9.94 wt.% nickel respectively. The molar ratio of ceria to zirconia on each of the catalyst prepared were also determined by elemental analysis and

reported in Table 4.1. The surface area and pore volume of the catalysts as determined by N_2 physisorption are also reported in Table 4.1. The BET surface area of all the samples with nickel oxide are within ±8% of the CZ sample without nickel oxide. The samples prepared by DI and SEA had BET surface area slightly lower than that of pure CZ while the BET surface areas of the samples prepared by CP with nickel loading ≥ 4 wt.% were slightly higher than that of pure CZ. The BJH desorption pore volumes of samples prepared by CP were slightly lower than samples prepared by DI and CP as well as pure CZ sample. Pyridine adsorption measurements found dispersions of 31% for 2NiO/CZ_SEA and 25% for 2NiO/CZ_DI.

Table 4.1 Physicochemical properties of catalysts

Catalysts	Ceria : Zirconia[a]	Ni content (wt.%)[a]	BET surface area ($m^2.g^{-1}$)[b]	Pore volume ($cm^3.g^{-1}$)[c]
CZ	83:17	N/A	85.1	0.097
2NiO/CZ_DI	83:17	1.96	78.1	0.098
2NiO/CZ_SEA	83:17	1.95	77.8	0.098
2NiO/CZ_CP	84:16	1.93	83.2	0.078
4NiO/CZ_CP	84:16	3.97	85.2	0.075
6NiO/CZ_CP	83:17	5.91	87.1	0.072
10NiO/CZ_CP	84:16	9.94	89.5	0.070

The phase structures of the catalysts prepared using different synthesis techniques were analyzed by x-ray diffraction (Figure 4.3a). All samples showed major contributions around 28˚, 33˚, 47˚, 56˚, 59˚, 69˚, 76˚ and 79˚, which can be indexed to (111), (200), (220), (311), (222), (400), (331), and (420) of the face-centered cubic (fcc) fluorite-type structure of ceria, respectively.[180-181] Previous studies showed that the most intense peak for pure ceria and pure

zirconia were found at similar diffraction angles.[87] A ceria and zirconia mixture in separate phases would therefore result in one broad peak that could be deconvoluted into two peaks corresponding to contributions from ceria and zirconia respectively. The narrowness of the peaks of ceria-zirconia indicates that the ceria-zirconia is a solid solution, not separate ceria and zirconia-rich phases. By closely comparing the (111) diffraction peaks for the fluorite structure as seen in Figure 4.3b, it is seen that the position of the catalysts prepared using CP shifted to the left with increasing Ni loading but remained nearly unchanged for catalysts prepared using DI and SEA. In addition to the fcc fluorite peaks for ceria structure, some weak diffraction peaks were observed at 2θ equals 37.5°, 43.5° and 63° on some catalysts. These peaks correspond to (111), (200) and (220) crystal planes of face-centered cubic NiO respectively.[180, 182] The peaks linked with NiO phases were present in 10NiO/CZ_CP and a very minor contribution is also seen on the diffraction trace of 6NiO/CZ_CP.

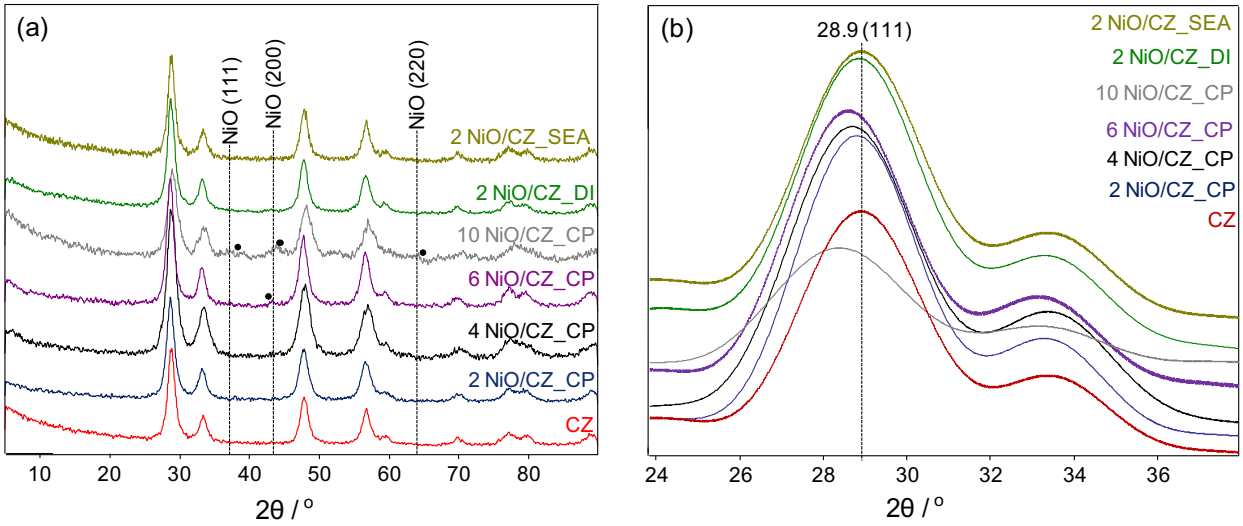

Figure 4.3 (a) XRD pattern of NiO/CZ catalysts prepared using different synthesis techniques (b) the corresponding magnification of the (111) diffraction lines of ceria at 28.9˚ shown in (a).

4.3.2.2 Lewis acidic characteristic and dispersion of nickel oxide on catalysts

The FTIR spectra of NiO/CZ prepared using different synthesis techniques (DI, SEA and CP) after pyridine adsorption only showed bands at 1445 cm^{-1}, which is characteristic of Lewis acid sites (LAS) (Figure 4.4a). Bands at 1540 cm^{-1} corresponding to pyridinium ions protonated on Brønsted acid sites (BAS) were not seen (Figure 4.4a). The concentration of Lewis acid sites on the catalysts prepared using DI, SEA and CP with 2 weight percent metal loading were 86, 105 and 30 $\mu mol.g^{-1}$ respectively. The difference in the LAS concentration of these samples which have the same metal oxide concentrations indicates that the metal oxides were dispersed differently on each of these catalysts. The LAS concentration is highest on the catalyst prepared using SEA followed by DI and then CP. Since most of the NiO particles adsorb on the surface of CZ on the catalysts prepared by SEA and DI,[159] the dispersion of metal oxide on these catalysts were calculated from the amount of pyridine adsorbed. The dispersion of nickel oxide on NiO/CZ_SEA and NiO/CZ_DI were 0.31 and 0.25 respectively. It must be noted that these dispersions reported are lower limits because it may not be possible to adsorb pyridine on two adjacent Lewis acid sites because of the molecular size of pyridine. The hypothesis behind the SEA approach to catalyst preparation is that monolayer adsorption of metal complexes on surface charge via strong electrostatic adsorption prevents agglomeration during calcination and lead to small well-dispersed metal oxide particles.[167] Therefore, it is not surprising that SEA synthesis technique resulted in a catalyst (NiO/CZ_SEA) with higher dispersion of nickel oxide compared to the catalyst prepared using traditional dry impregnation (NiO/CZ_DI). The catalyst prepared using CP showed a significantly lower concentration of LAS than the other catalysts as seen in Figure 4.4b. In this technique, only the fraction of nickel that remains on the surface will adsorb pyridine leading to a smaller measured concentration of LAS on this sample. The

dispersion of this sample (NiO/CZ_CP) can also not be measured from pyridine adsorption as was the case with catalysts prepared using DI and SEA.

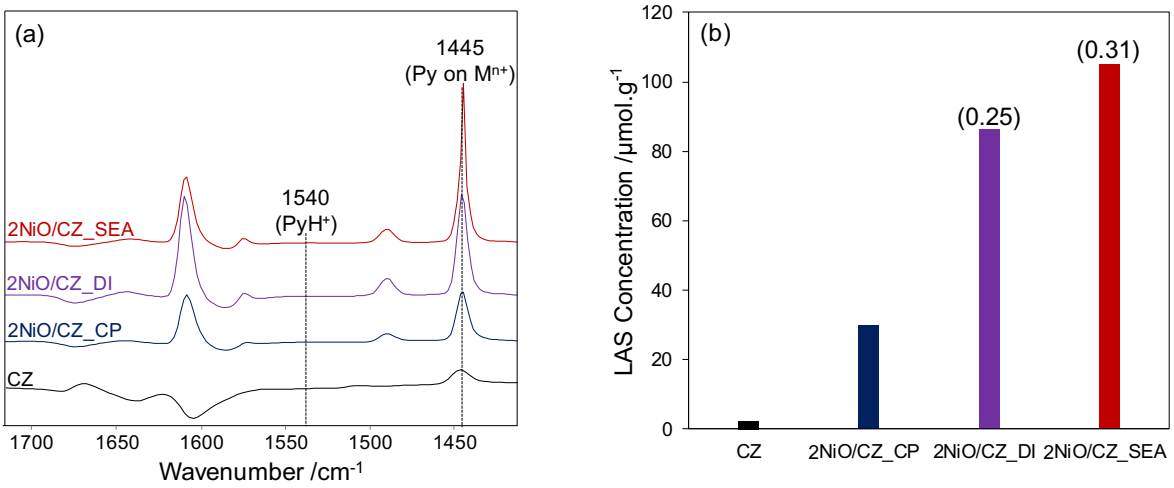

Figure 4.4 (a) FTIR spectra of pyridine on catalysts at 150 ˚C showing adsorption on Lewis acid sites (band at 1445 cm^{-1}) (b) Concentration of Lewis acid sites on catalysts prepared using different synthesis techniques with 2 wt.% nickel. Numbers in bracket represent dispersion of nickel oxide measured from the amount of pyridine adsorbed.

Several catalysts with different weight loading of Ni was prepared using CP to determine the optimum loading of Ni on CZ using this synthesis technique. Pyridine adsorption followed by FTIR spectroscopy was also used to determine the concentration of acid sites on these catalysts. Like the other catalysts, these catalysts only showed IR bands corresponding to Lewis acid sites with no contribution from Brønsted acid sites on the IR spectra (Figure 4.5a). The concentration of Lewis acid sites increased with increasing loading of Ni as seen in Figure 4.5b.

The concentration of Lewis acid sites on 2NiO/CZ_CP, 4NiO/CZ_CP, 6NiO/CZ_CP and 10NiO/CZ_CP were 30 µmols, 35 µmols, 66 µmols and 68 µmols respectively.

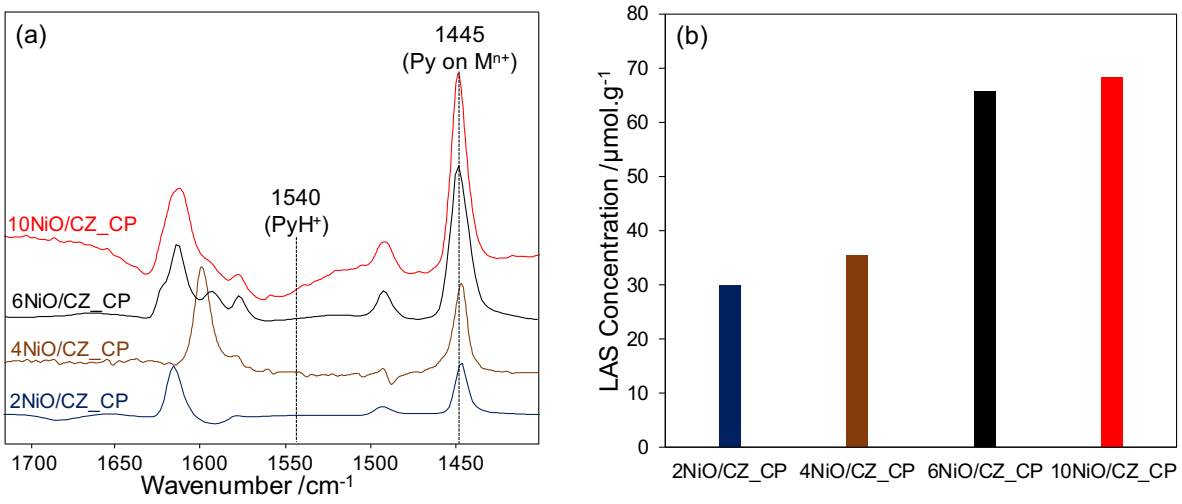

Figure 4.5 (a) FTIR spectra of pyridine on NiO/CZ_CP catalysts at 150 ˚C showing adsorption on Lewis acid sites (b) Concentration of Lewis acid sites on NiO/CZ_CP catalysts with different Ni loading

4.3.3 Performance of catalysts prepared using different synthesis techniques

The initial conversion of methane was about 20% for 2NiO/CZ_SEA, 18% for 2NiO/CZ_DI and 14% for 2NiO/CZ_CP, respectively (Figure 4.6a). For 2NiO/CZ_SEA, the methane conversion decreased and stabilized around 18%, while 2NiO/CZ_DI deactivated and stabilized around 15% and 2NiO/CZ_CP stabilized around 12% over the 8 hours of the reaction run (Figure 4.6a). Methanol, ethanol, carbon dioxide and traces of aromatics comprised the carbon containing products formed. (Figure C.1). The selectivity of alcohols (methanol and ethanol) formed over 2NiO/CZ_SEA was 39% initially and increased and stabilized over 47% during the duration of the reaction as seen in Figure 4.6b. For 2NiO/CZ_DI, the selectivity to

alcohols starts around 34% and increases slightly and stabilized around 43% after 5 hours of reaction. When the reaction was performed over 2NiO/CZ_CP, the selectivity to alcohols starts around 39% and increases slightly and stabilized around 47% during the duration of the reaction.

The weight loading of Ni on catalysts prepared using CP was varied in order to find the optimum loading using this synthesis technique. 4, 6 and 10 wt.% NiO/CZ were prepared for this purpose. When the reaction was run over 4NiO/CZ_CP for 8 hours, the initial conversion of methane was 18%. The conversion of methane gradually decreased and attained a steady state methane conversion of 15% after 4 hours of reaction as seen in (Figure 4.6c). For 6NiO/CZ_CP, the initial conversion of methane was over 20%. The conversion of methane decreases and stabilized around 17% after 4 hours of reaction. 10NiO/CZ_CP resulted in an initial methane conversion over 26%. This conversion decreased quite rapidly and stabilized around 17% after 6 hours of reaction. The measure of catalytic performance as a result of an increase in Ni loading was deduced from the yields of alcohols formed over each of the catalyst used. The yields of alcohols over catalysts prepared from co-precipitation with Ni loadings of 2, 4, 6 and 10 wt.% were 5.6%, 6.7%, 7.1% and 5.5% respectively as seen in Figure 4.6d which indicates that 6 wt.% Ni loading is optimum for the preparation of this catalyst using co-precipitation.

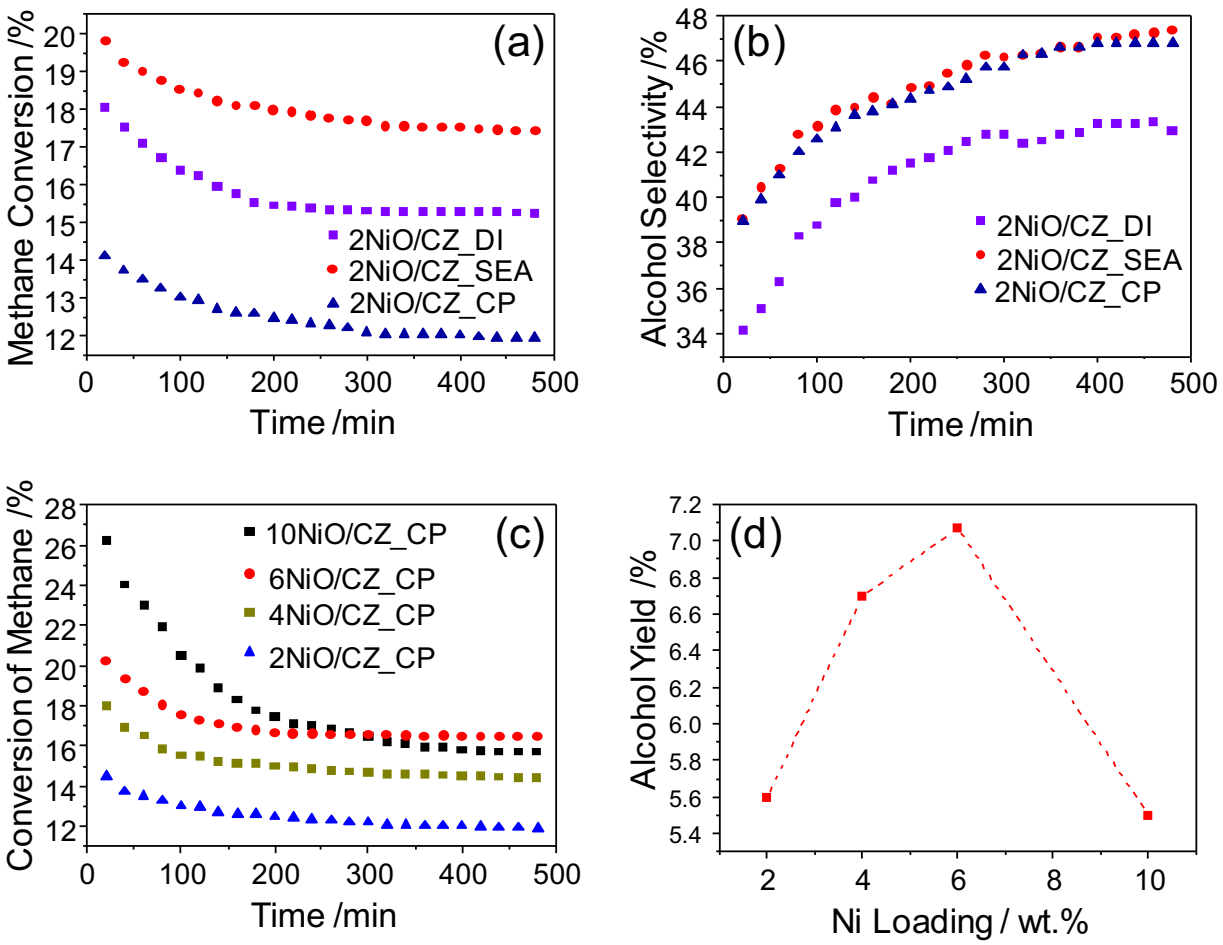

Figure 4.6 Reactivity results of catalysts during reactions with of methane, steam and oxygen in a packed bed reactor setup at 450 ˚C and 1 atm. (a) conversion of methane over 2NiO/CZ prepared from different techniques (b) alcohol selectivities over 2NiO/CZ prepared from different techniques (c) conversion of methane over NiO/CZ_CP with different Ni loading (d) yields of alcohol over NiO/CZ_CP as a function of Ni loading

The amount of carbon deposit was measured by performing a carbon balance on the carbon containing products during the reaction. On 2NiO/CZ_SEA, 2% of carbon was initially deposited on the catalyst. The deposition of carbon reduced and stopped after 6 hours of reaction as seen in Figure 4.7a. The reaction over 2NiO/CZ_DI showed an initial carbon deposit of 2.6%

which decreased to around 0.1% during the course of the reaction. 2NiO/CZ_CP showed an initial carbon deposit of 1.5% which slightly decreased and stopped after 6 hours of reaction. An increase in the amount of Ni content on the catalyst prepared using co-precipitation resulted in an increase in the amount of carbon deposit. When the reaction was run over 4NiO/CZ_CP, the amount of carbon deposit was 3% initially and it decreased over the course of 6 hours until no additional carbon was deposited. The reaction run over 6NiO/CZ_CP resulted in an initial carbon deposit of 3.5% which decreased within 6 hours until only little traces of carbon was being deposited. Over 10NiO/CZ_CP, the initial carbon deposit was slightly over 4% and decreased within 6 hours until only traces carbon was being deposited (Figure 4.7b). CHN analysis of these catalysts after reaction for 8 hours showed that 2NiO/CZ_SEA contained 2.09% carbon, whereas 2.9% carbon was deposited on 2NiO/CZ_DI while 1.87% of carbon was deposited on 2NiO/CZ_CP (Figure 4.7c). 4NiO/CZ_CP, 6NiO/CZ_CP and 10NiO/CZ_CP contained 2.93%, 3.45% and 5.85% of carbon respectively as seen in Figure 4.7d.

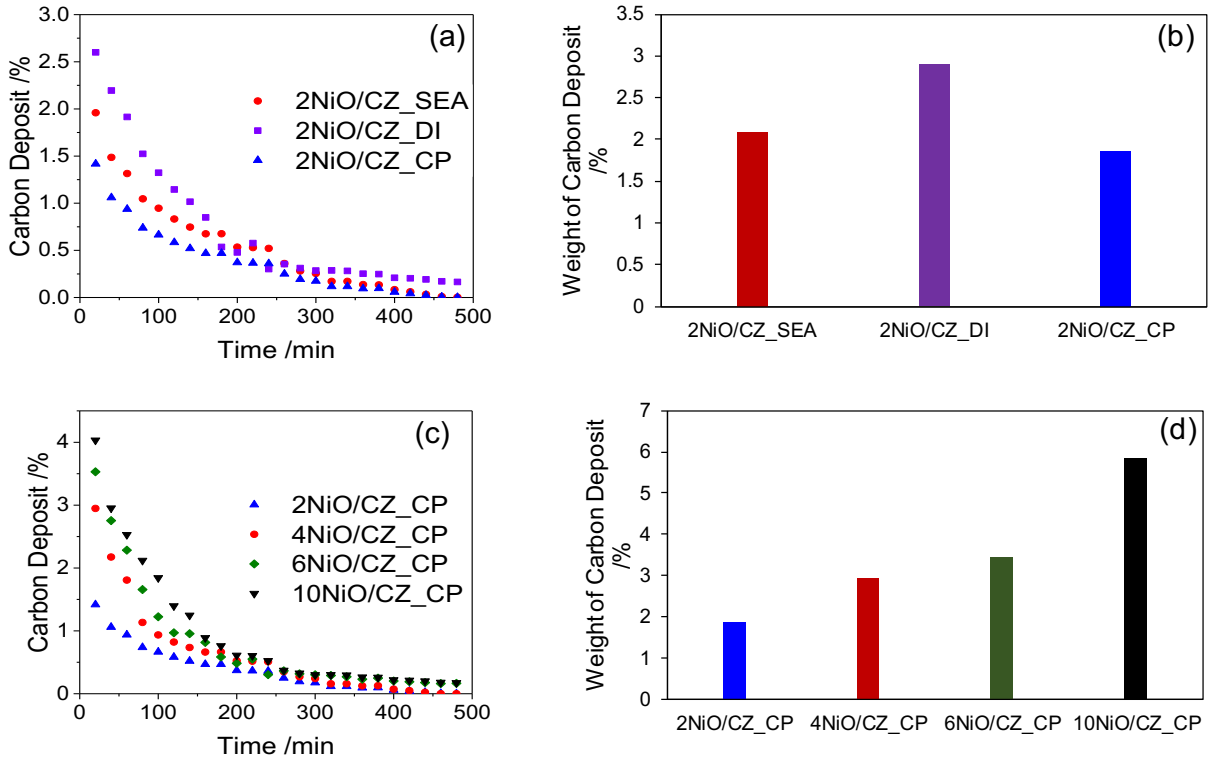

Figure 4.7 Carbon content on catalyst from reaction with methane (a) Carbon deposit on 2NiO/CZ prepared from different techniques calculated from C balance during reaction run (b) weight of carbon deposit on spent 2NiO/CZ prepared from different techniques as determined from CHN analysis (c) carbon deposit on NiO/CZ_CP with different loadings of NI calculated from C balance during reaction run (d) weight of carbon deposit on spent NiO/CZ_CP catalysts with different Ni loadings as determined from CHN analysis

4.4 Discussion

4.4.1 Structure and location of NiO on Ceria-Zirconia

Several studies have shown that the activity of supported metal or metal oxide catalysts depends strongly on the method of catalyst preparation.[183] Several phenomena have been highlighted as reasons for this influence of catalyst preparation method on its activity. Strong

metal-support interaction[183-184] and the effect of the particle size of the metal or the metal oxide[183, 185] are considered to be of paramount importance. Several studies have shown that on a ceria support, Ni can exist in two forms. NiO phases on the ceria surfaces which is usually predominant when the catalyst is prepared using impregnation technique[180, 182, 186] or as Ni^{2+} ions incorporated into the ceria lattice which happens when precipitation or other bulk synthesis technique is employed for the catalyst synthesis.[180, 182] The extent of Ni^{2+} incorporation into the ceria lattice in the catalysts used in this study were measured from x-ray diffraction analysis of the catalysts. As seen on Figure 4.3b, an enlargement of the (111) peak of the fluorite lattice of ceria showed some shifts to the left of this peak on some of the catalysts containing Ni compared to pure CZ support. These shifts to the left indicates that some Ni^{2+} were incorporated into the ceria lattice to form a solid solution with the typical cubic fluorite structure for the mixed system.[180, 187-188] These peak shifts were more apparent on the catalysts prepared using CP. The shifts also increased as the Ni content on the CP catalysts were increased indicating that Ni^{2+} were mostly incorporated into the lattice when they catalysts were prepared using CP and only a fraction of Ni are available as surface Lewis acid NiO sites. The lattice parameters of the crystal structure of ceria was calculated on each of the catalysts prepared by using the positions of line (111) on the XRD traces and Bragg's law. The lattice parameter of CZ was calculated to be 0.5348 nm which is very similar to that determined theoretically by Vegard's law (0.5357 nm) and similar to other values reported in the literature.[189-190] While the lattice parameter remained approximately the same for 2NiO/CZ_DI and 2NiO/CZ_SEA compared to CZ without any Ni, the lattice parameter is seen to increase linearly on NiO/CZ_CP with increasing Ni content (Figure 4.8). An increase in the lattice parameter of ceria is often due to the presence of defects and impurities in the lattice structure.[188] In this case, the progressive introduction of Ni^{2+} into the

crystal lattice of ceria-zirconia by co-precipitation, resulted in the linear increase in the lattice parameter with an increasing loading of Ni. When the concentration of Lewis acid sites was compared for catalysts with 2 wt.% Ni prepared using different synthesis techniques, the catalyst prepared by CP showed a significantly lower LAS concentration compared to catalysts prepared using the other two synthesis technique as seen in Figure 4.4. Ni therefore exists in 2 predominant phases on the catalysts prepared using co-precipitation. While some amount of Ni^{2+} is incorporated into the lattice, a fraction of Ni remains on the surface as Lewis acidic NiO. Upon observation of the XRD traces (Figure 4.3a), no NiO diffraction peaks lines were seen for CP catalysts with 2wt.% Ni and 4wt.% Ni suggesting that the nickel oxide is either amorphous or very small and well-dispersed below the detection limit of XRD. The peaks linked to NiO phases had very minor contribution on CP catalyst with 6 wt.% Ni which means that some bigger NiO particles detectable by XRD were formed. NiO phase contribution was even more pronounced on the catalyst with 10wt.% Ni which means that significantly bigger NiO particles were formed on this catalyst (Figure 4.3a). Also, the LAS concentration of 10NiO/CZ_CP is approximately the same as that of 6NiO/CZ_CP which could indicate that in addition to the incorporation of nickel into the ceria-zirconia lattice, a good amount of the additional nickel formed bigger NiO clusters on the surface.

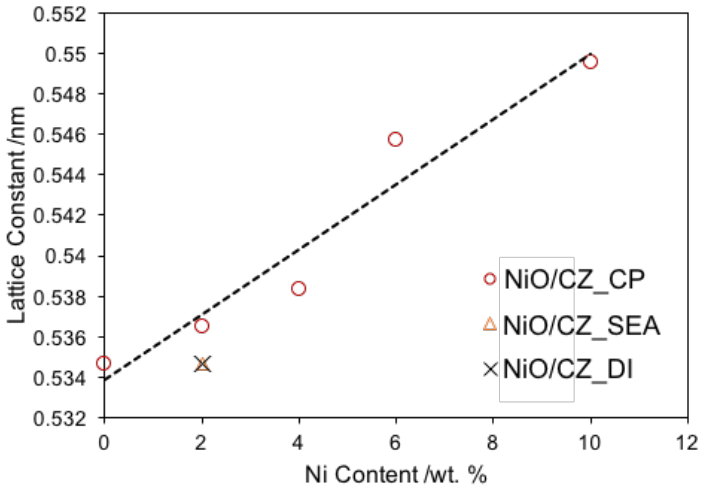

Figure 4.8 Lattice parameter of fluorite cubic structure of ceria as a function of Ni loading

The catalyst prepared using dry impregnation (2NiO/CZ_DI) showed a significantly higher LAS concentration than 2NiO/CZ_CP. Also, the lattice parameter of the cubic structure of ceria on 2NiO/CZ_DI is the same as that of CZ. This indicates that Ni primarily exists on the surface of this catalyst as Lewis acidic NiO as opposed to being incorporated into the crystal lattice of CZ as was the case with the catalysts prepared using co-precipitation. However, it is speculated that the strength of metal support interaction from impregnation technique is not high enough to prevent some agglomeration of NiO particles on the surface during calcination.[167] Therefore, the improvement of the dispersion of NiO on the surface can be attained by using a synthesis technique that promotes a stronger metal support interaction. Nevertheless, ceria was shown to stabilize very small, well-dispersed nickel oxide clusters even using impregnation technique of synthesis for the conversion of methane to alcohols.[102]

In the case of 2NiO/CZ_SEA, the lattice parameter of the cubic structure of ceria upon the introduction of nickel is the same as that of ceria-zirconia without any nickel and the position of the (111) diffraction peak of ceria-zirconia remained the same compared to pure ceria-

zirconia. This confirms that Ni primarily exists on the surface layer as NiO particles and there is significantly minor incorporation into the lattice. This catalyst also showed very high nickel oxide dispersion of 31% compared to 2NiO/CZ_DI which indicates that strong metal support interactions which is introduced by using SEA synthesis technique suppressed the agglomeration of nickel oxide on the surface during calcination. An improvement of metal or metal oxide dispersion on catalytic support has been shown in several literatures when SEA was used rather than impregnation for catalyst synthesis.[167, 191-193]

4.4.2 Catalyst performance and carbon deposit

The effect of the structure and location of nickel species on the catalytic activity was illustrated by the performance of the catalysts prepared using different synthesis technique (DI, SEA and CP) for the conversion of methane to alcohols at 450 °C for 8h using a steam to carbon ratio of 1 and an oxygen to carbon ratio of 0.2. The reactivity of 2NiO/CZ_DI was reported in previous studies.[100] This catalyst showed a cumulative alcohol selectivity of 43% on a C atom basis. Hydrogen, CO_2 and traces of aromatics were also seen as products on this catalyst. In the initial stage of the reaction, 2.6% of the carbon deposits were formed. Within 5h, the deposition of carbon decreased to 0.23% and remained around this level for the remaining course of the reaction. It was suggested from this observation as well as the formation of even more carbon deposit on a catalyst that was intentionally prepared with big NiO clusters that carbonaceous deposits were formed on the larger NiO clusters while the well-dispersed NiO clusters remained active. Therefore, in this study, specific aim was directed at improving the activity of NiO/CZ by using different synthesis techniques to prevent the formation of these larger NiO clusters that are responsible for the formation of carbon deposit.

The catalyst prepared using SEA (2NiO/CZ_SEA) showed improved reactivity compared to 2NiO/CZ_DI. On a specific basis, this catalyst converted more amount of methane and in turn, produced more alcohols. Furthermore, if one analyzes the conversion of methane relative to the moles of nickel present in the catalyst (specific activity), it can be seen that the 2NiO/CZ_SEA sample uses the nickel present more effectively than 2NiO/CZ_DI (Figure 4.9a). This indicates that more nickel present on the catalyst were used for the conversion of methane. The higher dispersion of nickel on 2NiO/CZ_SEA compared to 2NiO/CZ_DI (Figure 4.4b) means that fewer large NiO particles were formed on 2NiO/CZ_SEA. Since these large NiO particles are responsible for the formation of carbon deposit and are inactive for alcohol formation, it is reasonable that less amount of carbon deposit formed on 2NiO/CZ_SEA compared to 2NiO/CZ_DI (Figure 4.7).

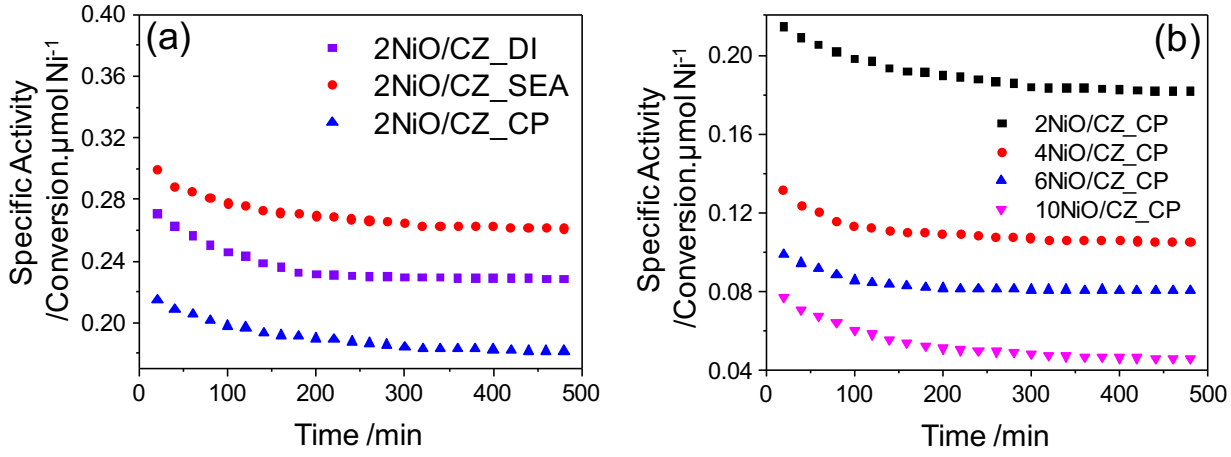

Figure 4.9 Specific activity (Conversion/µmols Ni) (a) catalysts prepared using different synthesis techniques with 2 wt.% nickel (b) catalysts prepared using co-precipitation with different weight loadings of nickel

The catalyst prepared using CP with 2 wt.% nickel loading (2NiO/CZ_CP) showed lower conversion of methane compared to 2NiO/CZ_DI but higher cumulative selectivities to alcohols

(Figures 4.6a and b). The specific activity of this catalyst was lower than that of 2NiO/CZ_DI. These observations indicate that this catalyst although comprises of a higher fraction of active sites for the formation of alcohols compared to 2NiO/CZ_DI, less amount of nickel present on the catalyst were used for the conversion of methane. On this catalyst, some fraction of nickel was incorporated into the lattice of ceria to form a solid solution as have been discussed in the previous section. This phase of nickel is not accessible for the conversion of methane. The high selectivity of alcohol on this catalyst indicates that the fraction of nickel oxide that are accessible on the surface seems to be very well dispersed. The fraction of well-dispersed accessible nickel oxide on catalysts prepared using co-precipitation was therefore improved by increasing the weight loading of nickel. A specific aim was directed towards finding an optimum weight loading that results in the formation of the highest amount of surface nickel oxide for the conversion of methane to alcohols. As the loading of nickel was increased, a decrease in the specific activity was observed for these catalysts (Figure 4.9b). This indicates that a smaller amount of nickel in the catalysts were utilized for methane conversion because more nickel was incorporated into the ceria lattice. However, an increasing activity of the catalyst based on the cumulative yields of alcohols were observed with a maximum at 6 wt.% nickel loading. The yield of alcohols declined when the nickel loading was increased further to 10 wt.% because since the surface area of ceria-zirconia is limited, a large amount of nickel on the surface will result in the formation of larger nickel oxide clusters which was confirmed by the XRD results. The amount of carbon deposited on the catalysts also progressively increased as the nickel loading was increased. The increase in carbon deposit was very significant on the catalyst with 10 wt.% nickel. This confirms that more surface nickel oxide particles were formed as the amount of nickel increased. This formation of more nickel oxide on the surface provided more

active sites for the formation of alcohols until the point where significant amount of big NiO clusters formed which resulted in higher formation of carbon deposits and a decrease in alcohol yields.

4.5 Conclusions

The present results show that preparation methods drastically affect the size and location of nickel in ceria-zirconia. In the case of strong electrostatic adsorption (2NiO/CZ_SEA), where the preparation method leads to strong metal support interactions, the nickel particles are primarily on the surface as Lewis acidic NiO clusters and are very small and well dispersed compared to the catalyst prepared using traditional dry impregnation. This was determined using pyridine adsorption which showed that NiO/CZ_SEA adsorbed more pyridine than 2NiO/CZ_DI. As a result, the activity of the catalyst prepared using SEA in terms of methane conversion and alcohol selectivities was better than the catalyst prepared using DI. On the catalysts prepared using co-precipitation, two different phases of nickel were formed. A fraction was incorporated into the ceria-zirconia lattice to form a solid solution. The rest were available as Lewis acidic NiO clusters on the surface. Because of the incorporation of Ni^{2+} into the ceria-zirconia lattice, a significantly amount of nickel on the catalyst was not utilized for methane conversion. However, the Lewis acidic surface NiO which are accessible on the surface were very dispersed as evidenced by the high cumulative selectivities to alcohols. The optimum loading of nickel that leads to the best amount of well-dispersed surface NiO particles for alcohol formation using co-precipitation was found to be 6 wt.% as this catalyst had the best yield of alcohols. The yield of alcohols decreased when the loading of nickel was increased to 10 wt.% because due to the limited surface area of ceria-zirconia, an increased amount of big NiO clusters

were formed on the surface which led to an increased formation of carbon deposit and a low yield of alcohol.

A broader implication of this work would be to improve the activity of NiO/CZ even further for the conversion of methane to alcohols in a single reactor. This can be achieved through careful preparation of catalyst and characterization at each step of synthesis. A synthesis technique that avoids agglomeration of NiO and leads to very small and well-dispersed particles would in turn lead to a higher activity of the catalyst.

CHAPTER 5

UNDERSTANDING THE ROLE OF "ROADBLOCKS" IN CATALYST DEACTIVATION DURING HYDRODEOXYGENATION OF PYROLYSIS-OIL MODEL COMPOUNDS

5.1 Background

Biomass energy is gaining increased attention as an alternative to depleting fossil fuels because of its renewability.[194] Biomass currently contributes 10-14% of the world's main energy production. This includes 3% of energy for transportation.[195] There is also a potential to increase the contribution to transportation energy up to 30 – 40% by 2050.[196] Therefore, the development of an efficient path for the utilization of biomass as a source of energy is highly important. Flash pyrolysis, which involves a thermochemical decomposition of biomass at elevated temperatures in the absence of oxygen, is an attractive approach for utilizing biomass. Pyrolysis oils which account for 70% of the products from flash pyrolysis of biomass cannot directly be used as a transportation fuel due to their high oxygen content.[43] Upgrading of pyrolysis oil is therefore required to eliminate oxygenated groups and improve the thermal and chemical stabilities, heating values, and volatility of pyrolysis oils. Hydrodeoxygenation (HDO) is an evolving technology for upgrading pyrolysis oils, where the oxygenated functional group is removed as water in the presence of excess hydrogen gas.[45, 194, 197-198]

HDO is a very similar process to and proceeds simultaneously with hydrodenitrogenation (HDN) and hydrodesulphurization (HDS) during hydro processing of liquid fuels.[199-200] As a result, early work studied sulfided NiMo and CoMo catalysts, which showed high activity for HDN and HDS.[201-202] These catalysts, however, displayed limited activity for HDO compared to monometallic or bimetallic Rh based catalyst supported on zirconia.[203] However, during HDO

over sulfided NiMo and CoMo catalysts, sulfides are converted into inactive oxides unless toxic hydrogen sulfide is supplied to keep the catalysts in the active sulfide phase.[204] Learning from these drawbacks of sulfided catalysts, several noble and transition monometallic or bimetallic catalysts were extensively studied for HDO.[47-48, 51, 205-221] In many cases, these catalysts combine the metal functionality with acid sites, which can catalyze oxygen removal by dehydration steps.[209-210, 216, 222] While some of these catalysts require a high hydrogen pressure or convert aromatics to products with saturated rings, they generally display high initial activity in HDO reactions. Particularly, Pt/HBEA displays good activity for HDO of anisole and m-cresol at atmospheric pressure producing deoxygenated aromatics such as benzene, toluene, and xylene.[51, 216, 222] Ga/ZSM-5 has also shown a high initial activity for the upgrading of pine vapors into olefins, aromatic hydrocarbons, naphthalene, alkyl naphthalenes, and alkyl anthracenes.[223] However, zeolite-based HDO catalysts consistently deactivate within a few hours on stream.

Despite the significance of catalyst deactivation in HDO, only few studies investigated deactivation pathways during HDO of model compounds in detail. Coking has been suggested as the most common deactivation path in HDO studies.[224-225] Studies of molybdenum sulfide-based catalysts also showed that various phenolic compounds could adsorb as phenate species on Lewis acid sites and poison the catalyst.[226-228] A recent study used operando FTIR spectroscopy during HDO reactions of several model compounds over Pt/HBEA to elucidate the evolution of carbonaceous surface species.[222] It showed coke formation occurs but that other surface species with lower molecular masses seem to be responsible for most of the deactivation. The formation of strongly chemisorbed catecholate species during HDO of guaiacol over HBEA and Pt/HBEA seemed to be particularly detrimental for catalytic activity. These strongly adsorbed species were suggested to form “roadblocks” at pore mouths or on the external surfaces of the zeolite framework

and consequently restrict the diffusion of reactants and products in and out of the pores since the pore sizes of zeolite BEA are only slightly larger than the reactants. In the case of HZSM-5 catalysts, coke formation was speculated to cause blockage of active sites during upgrading of pyrolysis vapor.[223] However, the effect of roadblocks has not been considered as an alternate deactivation path on HZSM-5 even though they have smaller pore mouths than HBEA and are therefore potentially more susceptible to roadblocks.

In this work, a comprehensive picture of the effect of strongly adsorbed "roadblocks" on the catalyst reactivity during hydrodeoxygenation is provided. This work focuses on Pt/HBEA and Ga/HZSM-5, which have shown high activity for HDO reactions. For a rigorous assessment of their impact, "roadblocks" are deliberately introduced by adsorption of catechol onto the zeolite followed by heat treatment. The accessibility of the micropores of the zeolites, the metal sites on the zeolites and the Lewis and Brønsted acid sites of the zeolites upon the introduction of these catecholate "roadblocks" were studies. Also, the effect on the rate of deactivation of the catalysts due to roadblocks were quantified based on a first order deactivation model.

5.2 Experimental

5.2.1 Materials

Zeolite Beta (CP814E, SiO_2/Al_2O_3 = 25) was purchased from Zeolyst. Ga/ZSM-5 was obtained from the National Renewable Energy Laboratories. Pyrocatechol (≥99%), anisole (>99.7%), and tetraamine platinum (II) chloride hydrate (99.99%), and pyridine, CHROMASOLV Plus, for HPLC (≥99.9%) were purchased from Sigma-Aldrich. Hydrogen and helium (UHP grade 5) were purchased from Airgas. A Barnstead NANOpure ultrapure water system was used to further purify deionized water to 18.2 MΩ/cm.

5.2.2 Catalyst Synthesis

Zeolite Beta (HBEA) was calcined at 550 °C for 4 h. Pt/HBEA was prepared via wet impregnation method of HBEA with a dilute aqueous solution of $Pt(NH_3)_4Cl_2$. The slurry was stirred for 12 h, followed by drying at 110 °C for 12 h. Subsequently, the catalyst was calcined at 420 °C for 4 h. The weight loading of Pt used was 1.3 wt.%. Pt/SBA-15 was prepared as a reference catalyst using the same procedure and weight loading of Pt for the preparation of Pt/HBEA described above. To prepare SBA-15, Pluronic P-123 (24.0 g) was dissolved in distilled water (636 mL) and concentrated HCl (120 mL) in a 2 L Erlenmeyer flask. The solution was stirred for 3 hours at room temperature. Tetraethyl orthosilicate (46.24 g) was added dropwise to the solution. The solution was then stirred continuously for 20 hours at 40 ^{o}C. The mixture was quenched and filtered with copious amounts of distilled water. The resulting white powder was then dried in an oven overnight at 75^{o}C. Afterwards, the sample was put into a calcination oven. To calcine the white powder, it was heated to 200 °C at 1.0 °C min^{-1}, held at that temperature for 2 hours, heated to 550 °C at 1.0 °C min^{-1}, held at that temperature for 6 hours, and finally cooled to room temperature. SBA-15 was calcined again at 550 ^{o}C for 4 h prior to impregnation of Pt. Ga/HZSM-5 was prepared from incipient wet impregnation of HZSM-5 with an aqueous solution containing the Ga nitrate precursors (Aldrich). The weight loading of Ga used was 3.5 wt.%. After impregnation with the metal nitrate aqueous solutions, the catalyst was dried for at least 3 h at 110 ˚C and then heated at 2 K/min to 550 ˚C in air and held for 3 h. Following synthesis, catecholate roadblocks were introduced into the catalysts. The catechol was introduced into the catalysts via incipient wetness impregnation in which pyrocatechol was dissolved in DI water and stirred for 30 minutes to form an aqueous solution before being added dropwise to each of the prepared catalysts collected in a beaker. The slurry was then stirred for 2 h and dried at 100 °C for another 2 h to

remove water. High and low weight loading of catechol were added to Pt/HBEA (Table 2)The sample with high loading comprises of 6.48 wt.% of catechol and is referred to as Pt/HBEA_RBH in this manuscript. The sample with low weight loading contains 1.09 wt.% of catechol and is referred to as Pt/HBEA_RBL. The catecholate loading on this sample is equivalent to 25% of the Lewis acid sites (LAS) concentration. A catecholate weight loading of 2.71% was used in the Ga/HZSM-5 sample and it is referred to as Ga/HZSM-5_RB.

5.2.3 Characterization

Nitrogen physisorption measurements were carried out on a Micromeritics ASAP 2020 physisorption / chemisorption analyzer. The catalysts were degassed at 200 ^{o}C for 4 h prior to measurement. Micropore areas and volumes were calculated on the basis of the t-plot method. H_2 chemisorption was performed in a Micromeritics Autochem II 2920 physisorption/chemisorption analyzer equipped with a TCD detector. The samples were degassed at 100 ^{o}C for 1 h and at 400 ^{o}C for 15 min. The samples were then cooled to 100 ^{o}C and held for 15 min. Next, the samples were reduced under hydrogen flow at 400 ^{o}C for 1 h and evacuated for another hour. The temperature was decreased to 40 ^{o}C, and pulse H_2 chemisorption analysis was performed. A H_2/metal stoichiometry of 0.5 was used to calculate accessible metal sites. To determine the amount of Pt metal deposited, Pt/HBEA was sent to Galbraith Laboratories for inductively coupled plasma-atomic emission spectroscopy (ICP-AES) analysis. Pyridine adsorption followed by FTIR spectroscopy was performed using a Nicolet 8700 FTIR spectrometer with an MCT/A detector. Each spectrum was recorded with 64 scans with a resolution of 4 cm^{-1}. Each sample was pressed into a translucent, self-supported wafer and loaded into a vacuum FTIR transmission cell. The sample was activated at 450 ^{o}C for 1 h under high vacuum followed by a reduction in H_2 at 400 ^{o}C for 1 h. The reduction was carried out in multiple steps. 10 mbar of H_2 was dosed

for 10 mins followed by evacuation for another 5 mins. This procedure was repeated 6 times. The wafer was then cooled to 150 ^{o}C and a background spectrum was taken. The chamber was dosed with 0.10 mbar of pyridine for 30 mins or until adsorption equilibrium of pyridine was reached. Subsequently, the cell was evacuated for 12 h to remove physisorbed pyridine and a spectrum was taken. To determine the strength of acid sites, the sample was heated to 250 ^{o}C, 350 ^{o}C, and 450 ^{o}C for 1 h, and a spectrum was taken at 150 ^{o}C. After each experiment, the density of the wafer was determined by using a circular stamp of 6.35 mm to cut a disc of specific size from the wafer. The concentration of Lewis and Brønsted acid sites were determined by the Beer-Lambert law using the integral of the peaks at 1445 cm^{-1} and 1540 cm^{-1}, respectively. Extinction coefficients were used as reported by Datka et al.[137] CO adsorption followed by FTIR spectroscopy was performed on a self-supported wafer of Pt/HBEA material. The pellet was placed in a custom-made IR transmission cell, pre-heated and reduced in a flow of hydrogen (1 bar) with a heating ramp rate of 5 K/min and dwell time of 1 h at 120 ˚C and 300 ˚C. After reduction, the cell was evacuated to 3E-8 bar and the sample was cooled down to 50 ˚C. The catalyst was then exposed to 10% CO in helium at a static pressure of 0.2 bar for 30 min. In the next step, the sample was evacuated to 3E-8 bar and heated up to 400 ˚C with a ramp of 5 K/min. IR spectra were recorded on a Perkin-Elmer 2000 FT-IR spectrometer with 4 cm^{-1} spectral resolution and 32 scans per spectrum. The background spectra were recorded prior drying/reduction and immediately before CO exposure. During CO-TPD, IR spectra were constantly recorded every 4 min approximately. CHN analysis was performed at Atlantic Microlab, Inc.

5.2.4 Adsorption of catechol roadblocks on HDO catalysts

The adsorption of catechol on the HDO catalysts was observed using a Nicolet 8700 FTIR spectrometer with an MCT/A detector. Each spectrum was recorded with 64 scans at a resolution of 4 cm^{-1}. HBEA, Pt/HBEA and Ga/ZSM-5 loaded with catechol equal to 10% of their pore volumes were pressed into self-supported wafers and each loaded into a vacuum FTIR transmission cell. The samples were activated at 400 ^{o}C for 1 h under high vacuum (<10^{-6} mbar), heated at 100, 200, 300 and 400 ^{o}C for 1 h, and a spectrum was collected at each temperature. Spectra of blank catalyst samples without catechol were collected and used as subtrahend for difference spectra under the same temperature.

5.2.5 Thermal gravimetric analysis

The loading of catechol on the catalysts was determined using a TA instruments SDT Q600 TGA. An empty alumina crucible was used to tare the TGA before each analysis. Individual samples were then loaded on the crucible and put in the TGA for analysis. The samples were ramped to 800 °C at 10 °C/min in a 100 mL/min flow of dry air. The stability of catechol on the catalysts was also determined in same instrument and conditions under the flow of nitrogen.

5.2.6 Catalytic performance

The catalytic performance of the fresh and roadblock catalysts for the hydrodeoxygenation of anisole were tested in a trickle-bed reactor. A stainless steel tube (0.25 in. outer diameter with a wall thickness of 0.035 in.) was used as the reactor. The reactor was mounted in an insulated furnace. A thermocouple was placed in the middle of the reactor, and it was connected to a Eurotherm 2416 temperature controller. A catalyst bed with a mass of approximately 100 mg was used in all experiments. Quartz wool was placed at both ends of the

catalyst bed to keep the catalyst in place. Anisole was fed into the reactor using a Teledyne ISCO model 500D syringe pump. Each experiment was performed at 400 °C and atmospheric pressure. The catalysts were all reduced in the reactor for 1 h at 400 °C with 80 mL/min of hydrogen flow before anisole was fed. All the lines were heated to 300 °C to prevent condensation. A total hydrogen gas flow rate of 80 mL/min was used during the reaction. The H_2/reactant molar ratio was kept at 50. The weight to feed ratio (W/F) defined as the ratio between the mass of the catalyst and the molar flow rate of the reactant was kept at 0.0259 g_{cat} $(mmol_{feed}.h^{-1})^{-1}$. The products were directly analyzed and quantified online using an Agilent 7890A gas chromatograph equipped with an HP-5 column and a flame ionization detector (FID). The following definitions were used:

Conversion: $X\ [\%] = \frac{F_{A,in} - F_{A,out}}{F_{A,in}}$ x 100

Yield: $Y_p\ [\%] = \frac{F_{p,out}}{F_{A,in}}$ x 100

Selectivity: $S_p\ [\%] = \frac{Y_p}{X}$ x 100

The catalysts' deactivation profiles for anisole were calculated by assuming a first-order decay kinetic model.[229]

For first-order decay, the activity is given by:

$a(t) = \exp(-k_{Deact}.t)$ where $a(t) = C.\ln(\frac{1}{1-x})$

Combining gives:

$$\ln(\ln(\frac{1}{1-x})) = k_{Deact.}\, t + C'$$

Where x is the fractional conversion of anisole at a given time and $k_{Deact.}$ is the first-order deactivation rate constant.

5.3 Results

5.3.1 Catalyst Characterization

Surface area, pore volume, and dispersion were obtained from nitrogen physisorption and hydrogen chemisorption as shown in Table 5.1 below.

Table 5.1 Nitrogen Physisorption and Hydrogen Chemisorption Results

	N_2 physisorption				H_2 chemisorption		
	Fresh		Roadblock		Fresh		Roadblock
Sample	Micropore area (m^2/g)	Micropore volume (cm^3/g)	Micropore area (m^2/g)	Micropore volume (cm^3/g)	Dispersion (%)	Particle size (nm)	Accessible metal sites (%)
HBEA	335	0.160	286	0.137	N.A.*		
ZSM-5	196	0.093	-	-	N.A.*		
SBA-15	-	-	-	-	N.A.*		
1.3 wt.% Pt/HBEA	287	0.138	99	0.046	41	2.7	7.7
1.3 wt.% Pt/SBA-15	-	-	-	-	34	3.3	32
3.1 wt.% Ni/ZSM-5	178	0.085	83	0.039	35	3.2	1.9
3.5 wt.% Ga/ZSM-5	182	0.087	70	0.033	N.A.†		
1.3 wt.% Pt/HBEA‡		-	247	0.117	-	-	16

* Contains no metal
† Non-reducible metal at conditions
‡ Catechol roadblocks added equals 25% of Lewis acid sites in Pt/HBEA

The introduction of metals using wet impregnation caused a loss in micropore volume and surface area (Table 5.1). This observation could indicate that the metal particles occupy a part of the micropore volume or that they restrict access to some pores. Similar trends have been reported in the literature.[230] The micropore volume and surface area further decreased upon the introduction of catechol-derived surface species (i.e., roadblocks). Specifically, only 33% of the micropore volume remained accessible to nitrogen after the introduction of high weight loading of catechol derived species (6.48 wt.%) on Pt/HBEA, 85% of this micropore volume were accessible after the introduction of low weight loading of catechol derived species (1.09 wt.%) and 38% of the

micropore volume remained accessible on Ga/ZSM-5 after the introduction of 2.71 wt.% of catechol.

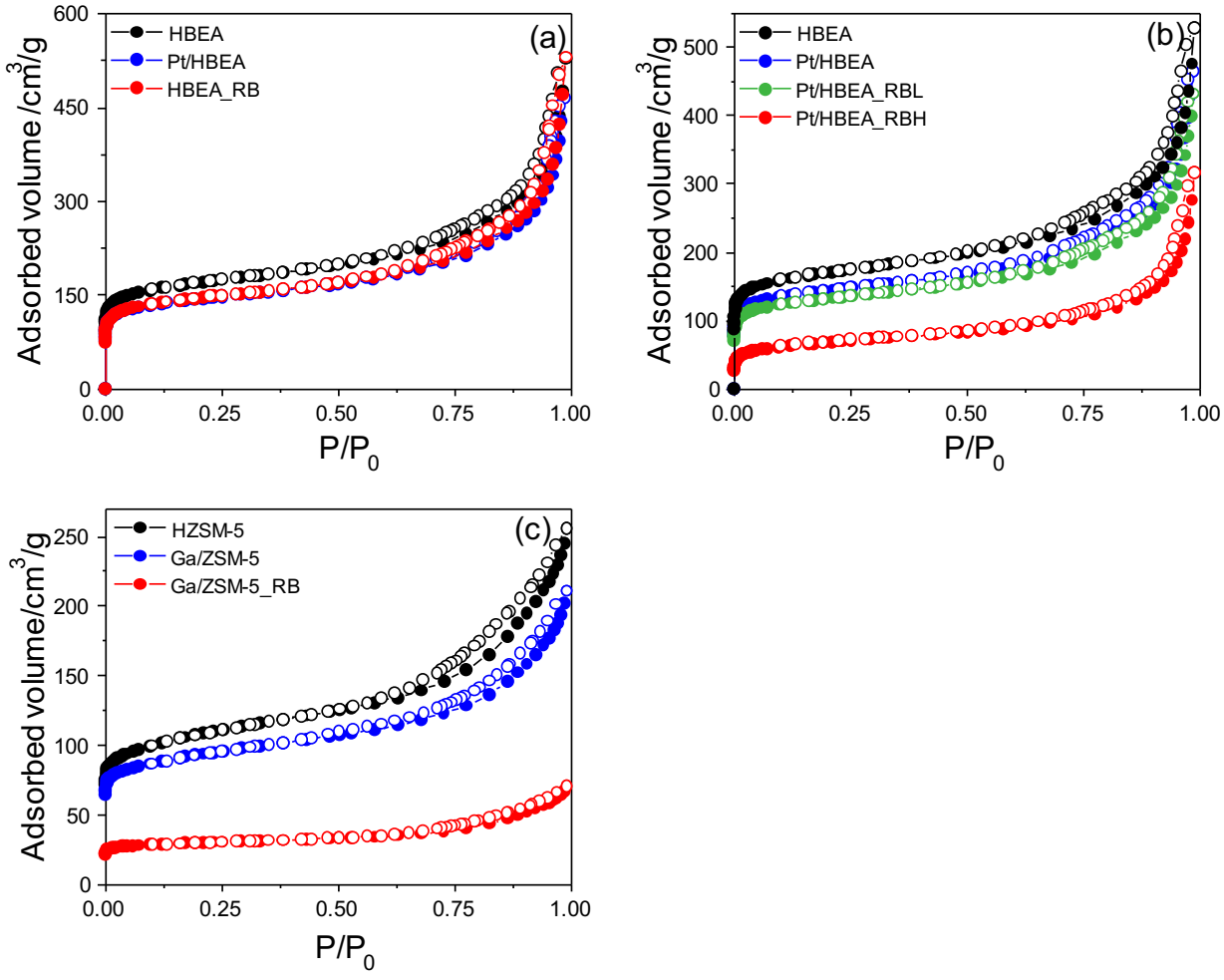

Figure 5.1 N_2 adsorption and desorption isotherms for HBEA and HZSM-5 series: comparison between (a) fresh HBEA, Pt/HBEA and HBEA_RB (b) fresh Pt/HBEA and Pt/HBEA_RB (c) fresh Ga/HZSM-5 and Ga/HZSM-5_RB.

All the nitrogen isotherms (Figure 5.1) were type I, which is characteristic of microporous materials. After introduction of metals and catechol-derived species, there was a clear reduction of micropore volume in low P/P_0 values (Figure 5.1). Upon the introduction of high loading of catechol-derived species in Pt/HBEA (Pt/HBEA_RBH), a significant portion of the micropores

were blocked (Figure 5.1b).The introduction of a reduced amount of catechol on Pt/HBEA (Pt/HBEA_RBL) led to a significant reduction in the amount of micropores that were blocked. The effects of micropore blockage by catechol were even more pronounced in the HZSM-5-based samples, Ga/HZSM-5 (Figure 5.1c).

Figure 5.2 shows the micropore distribution based on the Horvath-Kawazoe method with the Saito-Foley[231-232] model for cylindrical pore geometry that is usually applied for zeolites.[233-235] HBEA-based zeolites (Figure 5.2a) showed a reduction in the amount of micropores with a calculated pore size of 0.65 nm (micropore size very close to reported values in literature[236]). The calculated pore width of the HZSM-5-based zeolites were all around 0.62 nm (similar to literature values[237]). A similar decrease in the amount of micropores was observed for the HZSM-5-based materials upon the introduction of catechol-derived species (Figures 5.2b).

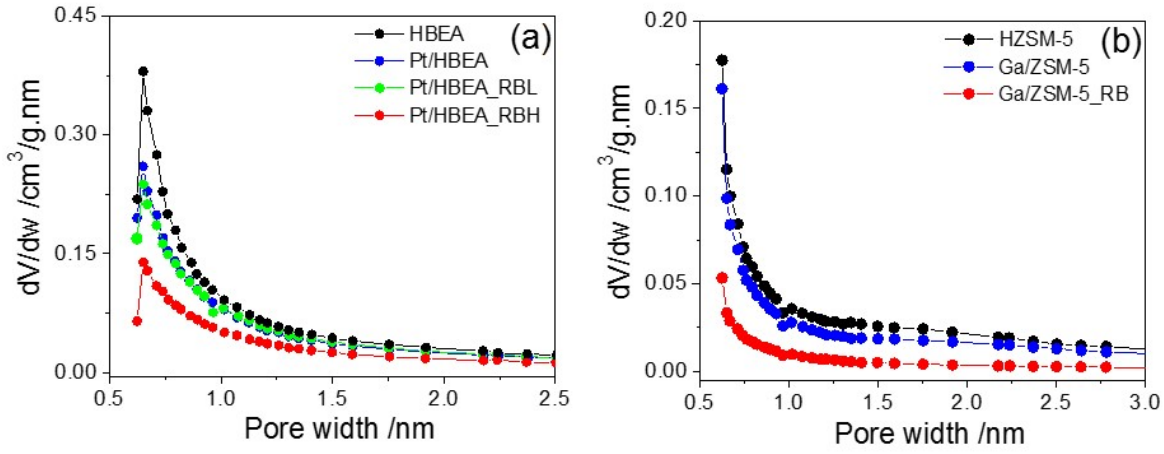

Figure 5.2 Horvath-Kowazoe microporous distribution for HBEA and HZSM-5 series: (a) fresh samples and roadblock Pt/HBEA, (b) fresh Ga/HZSM-5 Ga/HZSM-5_RB.

H_2 chemisorption indicated that the dispersion of metal particles in Pt/HBEA and Pt/SBA-15 were 41% and 34% respectively. The concentration of accessible metal sites in Pt/HBEA and Pt/SBA-15 was reduced to 7.7% and 32.9%, respectively, when high loading of catecholates were

introduced. On Pt/HBEA with low weight loading of catecholates (Pt/HBEA_RBL), 16% of the metal sites remained accessible. GaO_x did not reduce at 450 ^oC. Hence, it was not characterized by hydrogen chemisorption. Also, GaO_x not Ga is the active site on this catalyst.

Figure 5.3 shows the IR spectra obtained after adsorption of CO on Pt/HBEA_Fresh and Pt/HBEA_RB. On Pt/HBEA_Fresh, adsorption of CO resulted in the appearance of an asymmetric band with a maximum at 2080 cm^{-1}. During temperature programmed desorption, this band appeared to shift towards lower frequency and approached 2050 cm^{-1} at 400 °C. On Pt/HBEA_RB, adsorption of CO resulted in a band at 2070 cm^{-1} with significantly lower intensity compared to Pt/HBEA_Fresh. This band also shifted to lower frequency during temperature programmed desorption and was completely removed at 300 °C.

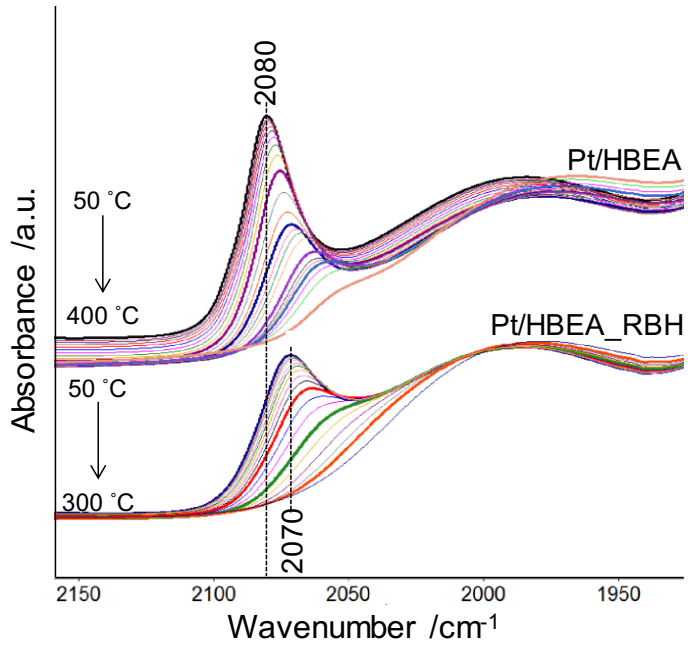

Figure 5.3 FTIR Spectra during temperature programmed desorption at 3E-8 bar following CO adsorption on Pt/HBEA reduced at 450 °C

The concentration of Lewis (LAS) and Brønsted acid sites (BAS) on Pt/HBEA was slightly lower than that of HBEA (Figure 5.4). This could be a result of anchoring of some Pt particles on the peripherals of extra framework alumina[238] that could block some zeolite pore mouths and reduce accessibility of pyridine to acid sites inside the zeolite pores. The concentrations of LAS and BAS sites on Pt/HBEA with catecholate roadblocks decreased compared to fresh Pt/HBEA. Catecholate species have been reported to form on Lewis acid sites,[222, 226, 239-241] which could, in part, result in this decrease in LAS concentration. Adsorption of catechol on some of the BAS could also, in part, account for the decrease in the BAS concentration. Additionally, catecholate roadblocks could be responsible for preventing the diffusion of pyridine into parts of the micropore network of HBEA. The fraction of LAS in Pt/HBEA_RBL that are accessible for pyridine was reduced by about 74% even though the amount of adsorbed catechol was only equivalent to 25% of the LAS concentration. The concentrations of LAS and BAS also decreased significantly for Ga/HZSM-5 with roadblocks compared to the fresh samples. Pt/SBA-15 only had a limited concentration of LAS of 39 $\mu mol.g^{-1}$, which disappeared completely upon the introduction of catechol derived species into the framework. This indicates that these LAS in Pt/SBA-15 are most likely serving as a part of the binding sites for the catechol derived species. Pt/SBA-15 contained no BAS capable of adsorbing pyridine.

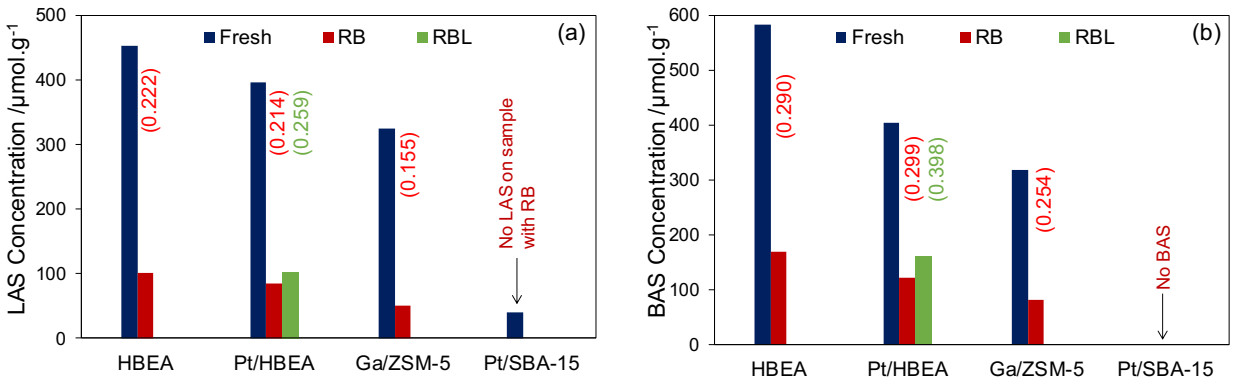

Figure 5.4 Concentration of (a) Lewis acid sites and (b) Brønsted acid sites of Blank Catalysts and Catalysts with Roadblocks. Numbers in parenthesis represent fraction of acid sites in roadblock catalysts to acid sites in blank catalysts.

5.3.2 Temperature-programmed reaction of adsorbed catechol to roadblocks

After the adsorption of catechol on the catalyst materials (Pt/HBEA and Ga/HZSM-5), several peaks were observed (Figure 5.5). The peaks between 1618 and 1450 cm^{-1} are mainly due to the $\nu(C=C)_{ring}$ vibrations of the aromatic ring.[242] The peaks in this region shifted slightly in all materials compared to pure catechol. This can be attributed to the change in aromatic structure due to chemisorption of catechol derivative on a surface as opposed to physisorption in which the molecule remains the same. The δOH peak at 1361 cm^{-1} in the spectrum of pure catechol disappeared when catechol was adsorbed on Pt/HBEA and Ga/HZSM-5 at as low as room temperature and subsequent higher temperatures. This indicates that the hydrogen atom on the phenol had dissociated.[226] At the same time, a peak around 1329 cm^{-1} appeared, which is due to one or more ν(C-O) vibrations.[226] The formation of this new ν(C-O) vibration in additional to the disappearance of the peak at 1361 cm^{-1} again suggest the formation of chemisorbed surface species. Since the δOH peak disappeared entirely, it is safe to assume that the chemisorption occurs by formation of bidentate species. As seen in Figure 5.5, heating up to 400 °C as a means of

removing physisorbed water does not lead to the removal of these surface species. The TGA analysis of catalyst samples loaded with catechol in air showed two peaks (Figure A.1). The first peak around 100 °C represents weight loss due to desorption of water as illustrated by the similarity to the curves of samples not loaded with catechol. A second peak, which starts around 220 °C and ends around 600 °C, is seen only in samples loaded with catechol. We can safely attribute this peak to weight loss from catechol. Upon comparing the weight loss from catechol from TGA when treated in air to the initial loading of catechol on each sample as seen in Table 5.2, we observed a very close correlation.

Table 5.2 TGA results showing percentage of catechol remaining on the roadblocked samples after heating

Catalysts	Catechol Loading (wt.%)	CH Analysis (wt.%)	Mass loss in air (wt.%)	Mass loss in N_2 (wt. %)	Fraction of strongly adsorbed species (%)*
Pt/HBEA_RBH	6.48	5.58	6.25	3.33	47.2
Ga/HZSM-5_RB	2.71	2.08	2.73	1.61	41.0
Pt/HBEA_RBL	1.09	0.94	1.06	0.18	83.0

* Calculated by subtracting the mass loss from surface species under N_2 from the mass loss during TPO in air.

This indicates that catechol was completely removed from each sample around 600 °C upon treatment with air. CH analysis was also used to verify the weight loading of catechol on the zeolites, as seen in Table 5.2. It showed a slightly lower weight loading of catechol in all cases because this analysis does not account for O in catechol. When TGA analysis in a nitrogen environment was performed on these catalysts, weight loss due to catechol significantly decreased compared to weight loss when the samples were treated in air (Table 5.2). This indicates that a significant amount of the catechol-derived surface species remains on the surface of the roadblocked catalysts up to 800 °C.

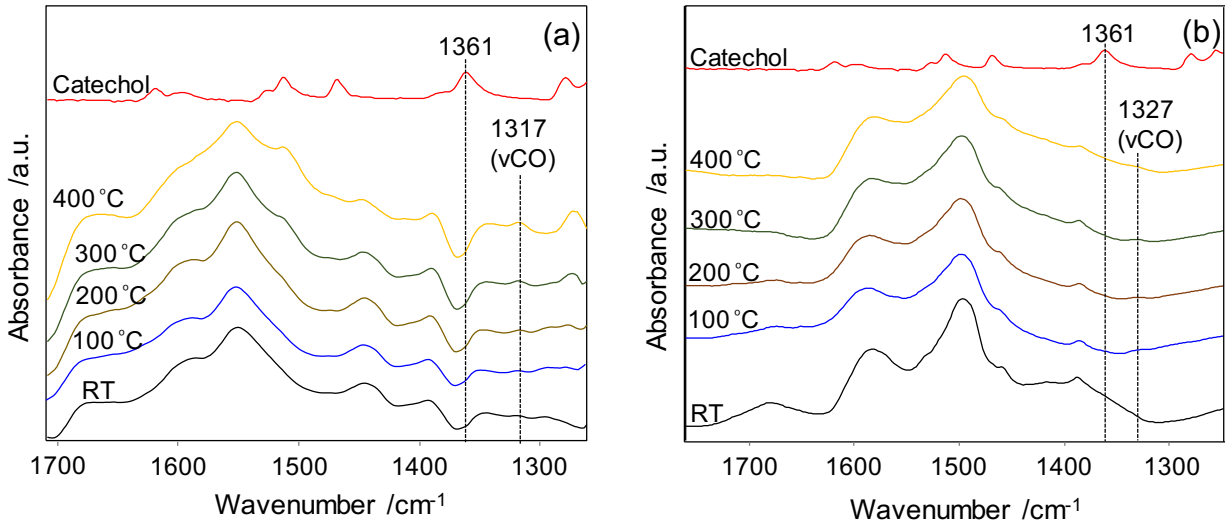

Figure 5.5 FTIR spectra of catechol adsorbed on HDO catalysts at various temperatures (a) Pt/HBEA (b) Ga/ZSM-5.

5.3.3 Analysis of OH groups by FTIR spectroscopy

The FTIR spectra of HBEA based zeolite samples exhibited IR bands at 3777 cm^{-1}, 3743 cm^{-1}, 3663 cm^{-1}, 3643 cm^{-1}, 3607 cm^{-1}, and a broad band around 3429 cm^{-1} (Figure 5.6). Table 5.3 shows band assignments from literature references. The band around 3777 cm^{-1} is common with BEA zeolites, and it is now generally believed to arise from isolated Al-OH species. The band around 3743 cm^{-1} is typically assigned to terminal silanol groups. The band at 3663 cm^{-1} is assigned to Al-OH species from extra framework aluminum, while the band at 3607 cm^{-1} corresponds to acidic bridging hydroxyls. The broad band around 3429 cm^{-1} is attributed to hydrogen bonding OH groups and may include contribution from residual physisorbed water. The IR spectra of activated ZSM-5 based materials show similar bands around 3777 cm^{-1}, 3742 cm^{-1}, 3663 cm^{-1}, 3607 cm^{-1}, and a broad band around 3488 cm^{-1}. The band assignments are similar with the HBEA zeolite sample as shown in Table 5.3.

The peak of free silanol groups at 3743 cm^{-1} reduced in intensity upon the introduction of catechol-derived species on HBEA. The peaks at 3663 cm^{-1}, which represents Al-OH species from extra-framework aluminum and 3607 cm^{-1}, which represents acidic bridging hydroxyls also reduced in intensity or were completely absent on the catalyst with catechol-derived species. Upon introduction of platinum on HBEA, the peak of free silanol groups at 3743 cm^{-1} was completely absent. The peak at 3607 cm^{-1}, which represents acidic bridging hydroxyls, was also completely absent on the catalyst containing platinum. The peak at 3663 cm^{-1}, which represents Al-OH species from extra-framework aluminum, however, did not reduce in intensity due to the introduction of platinum into the zeolite. The fact that similar bands reduced in intensity or were completely absent upon the introduction of platinum and catecholate roadblocks probably means that both the platinum metals and the derivatives of catechol led to the exchange of similar protons of the respective OH groups and are perhaps sitting in close proximity to one another on HBEA zeolites. The Pt and catecholates could either be sitting directly on the OH groups or in their vicinity leading to hydrogen bonding with the OH groups.

On the HZSM-5 zeolite samples, the intensity of the band at 3742 cm^{-1}, which represents silanol groups (Si-OH), is seen to decrease on the sample that contained nickel and gallium. This band is seen to decrease even further after adding catechol-derived species. Other hydroxyl bands around 3663 cm^{-1} (Al-OH) and 3607 cm^{-1} (Si-(OH)-Al) are also affected by both metals and catechol-derived species. Thus similar conclusions can be drawn as with the HBEA catalysts.

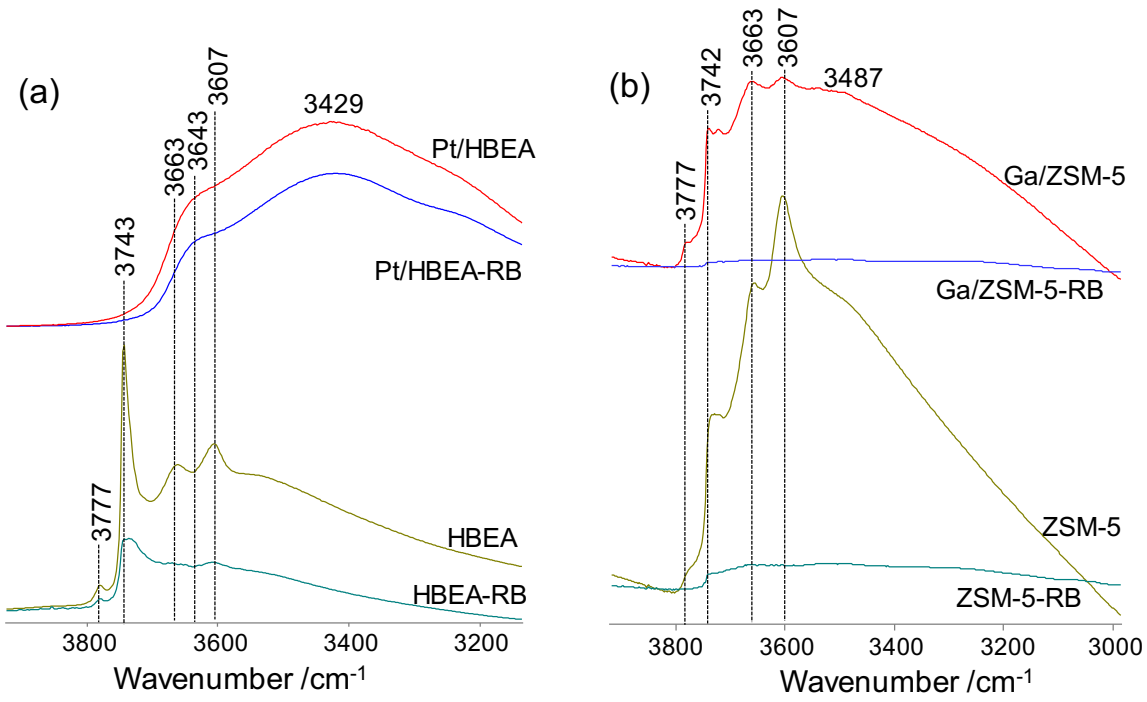

Figure 5.6 FTIR Spectra showing OH region of catalysts activated at 400 ^{o}C with and without catecholate roadblocks (a) HBEA and Pt/HBEA (b) ZSM-5 and Ga/ZSM-5.

Table 5.3 FTIR Spectra Characteristics of the OH groups in HBEA and ZSM-5 Zeolites

Sample	Site	Site Label	Wavenumber	Reference
HBEA	Al-OH species	Al-OH	3782 cm^{-1}	243-245
	Terminal silanol groups	Si-OH	3745 cm^{-1}	243-245
	Internal silanol groups	Si-OH	3740 cm^{-1}	243-245
	Al-OH species arising from extra framework Al	Al-OH	3665 cm^{-1}	243-247
	Acidic bridging hydroxyls	Si-(OH)-Al	3611 cm^{-1}	243-249
	Residual hydroxyls	-	3429 cm^{-1}	250
ZSM-5	Al-OH species	Al-OH	3782 cm^{-1}	243-245
	Silanol groups	Si-OH	3740 cm^{-1}	251
	Al-OH species arising from extra framework Al	Al-OH	3665 cm^{-1}	243-247
	Acidic bridging hydroxyls	Si-(OH)-Al	3610 cm^{-1}	251
	Residual hydroxyls	-	3487 cm^{-1}	250

5.3.4 Reactivity for HDO of Anisole

The initial conversion of anisole over fresh Pt/HBEA was 100%, followed by a slow deactivation to 86% after 8 h on stream (Figure 5.7). The first-order deactivation rate constant was calculated to be 0.109 h^{-1}. Catecholate roadblocks led to a significant drop in the initial activity of the catalyst. For Pt/HBEA with a high catechol loading (Pt/HBEA_RBH), the initial conversion of anisole was only 38%. Pt/HBEA_RBH deactivated even faster with a rate constant of 0.159 h^{-1} as the reaction proceeded and the conversion of anisole was only 19% at the end of the reaction (Figure 5.7a). The reactivity over Pt/HBEA_RBL also decreased significantly compared to fresh Pt/HBEA. The initial anisole conversion was only 49%, which slowly decreased to around 30% by the end of the reaction run. The deactivation rate constant of 0.112 h^{-1} indicated that this catalyst deactivated quicker than the catalyst without catechol but slower than the catalyst with a higher catechol loading. The conversion of anisole over Ga/HZSM-5 started at 97%. This catalysts deactivated more rapidly than Pt/HBEA with first-order deactivation rate constants of 0.154 h^{-1}. The conversions after 8 h was only 68% for Ga/HZSM-5, (Figures 5.7c). The activity of this catalyst also significantly decreased when catechol-derived species were deposited on it. In this case, initial conversions of anisole over Ga/ZSM-5 with roadblocks was only 18%. An even faster deactivation was observed for this catalyst. Ga/HZSM-5_RB deactivated with a rate constant of 0.254 h^{-1} and reached a complete deactivation after only 3.5 h on stream. Overall, Pt/HBEA performed better than Ga/ZSM-5 in terms of anisole conversion during HDO. HDO products over Pt/HBEA included benzene, toluene, and xylene (Figure D.4a). Other oxygenated aromatics including phenol, cresol, methylanisole, and xylenol were also produced (Figure D.4b). Methane was also produced with a higher selectivity of 5% on Pt/HBEA compared to Pt/HBEA_RBH with only 1.7% selectivity to methane. Ga/HZSM-5 produced benzene and toluene and methane as the

only deoxygenated products (Figures D.10a). HBEA was not able to perform a complete deoxygenation of anisole, and the products mainly consisted of oxygenated aromatics like cresol, xylenol, phenol, and methylanisole. Roadblocks on the catalysts also affected the production of deoxygenated products (Figure 5.8). The initial yield of deoxygenated products from Pt/HBEA_RBH, Pt/HBEA_RBL and Ga/HZSM-5_RB decreased by 70%, 61% and 86%, respectively, due to catechol-derived species. Although HBEA was not a good catalyst for the complete deoxygenation of anisole, a small trace of toluene was seen on the fresh catalyst, but it was absent on the catalyst with catechol roadblocks.

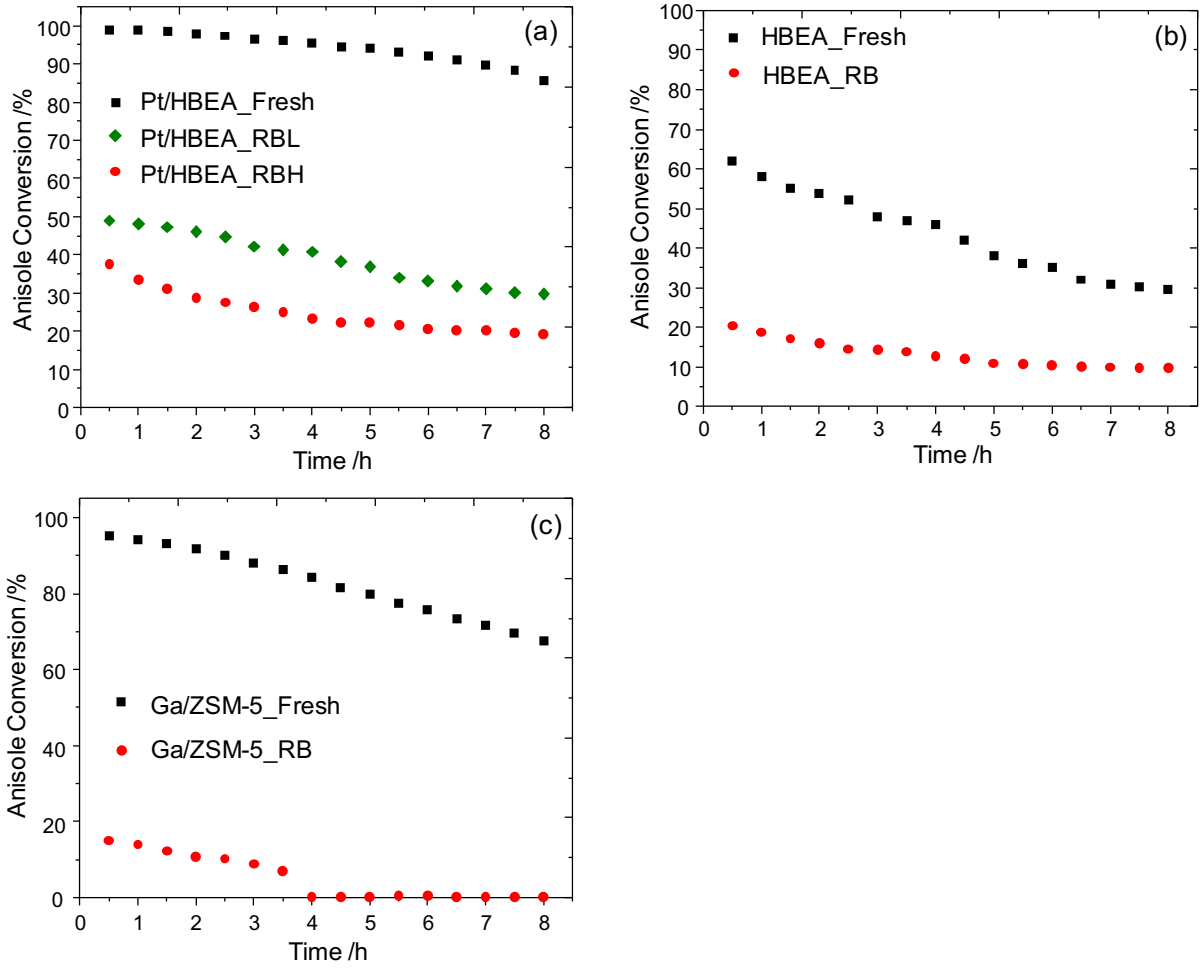

Figure 5.7 Conversion of anisole on fresh HDO catalysts compared to catalysts with catecholate roadblocks (a) Pt/HBEA (b) HBEA (c) Ga/ZSM-5.

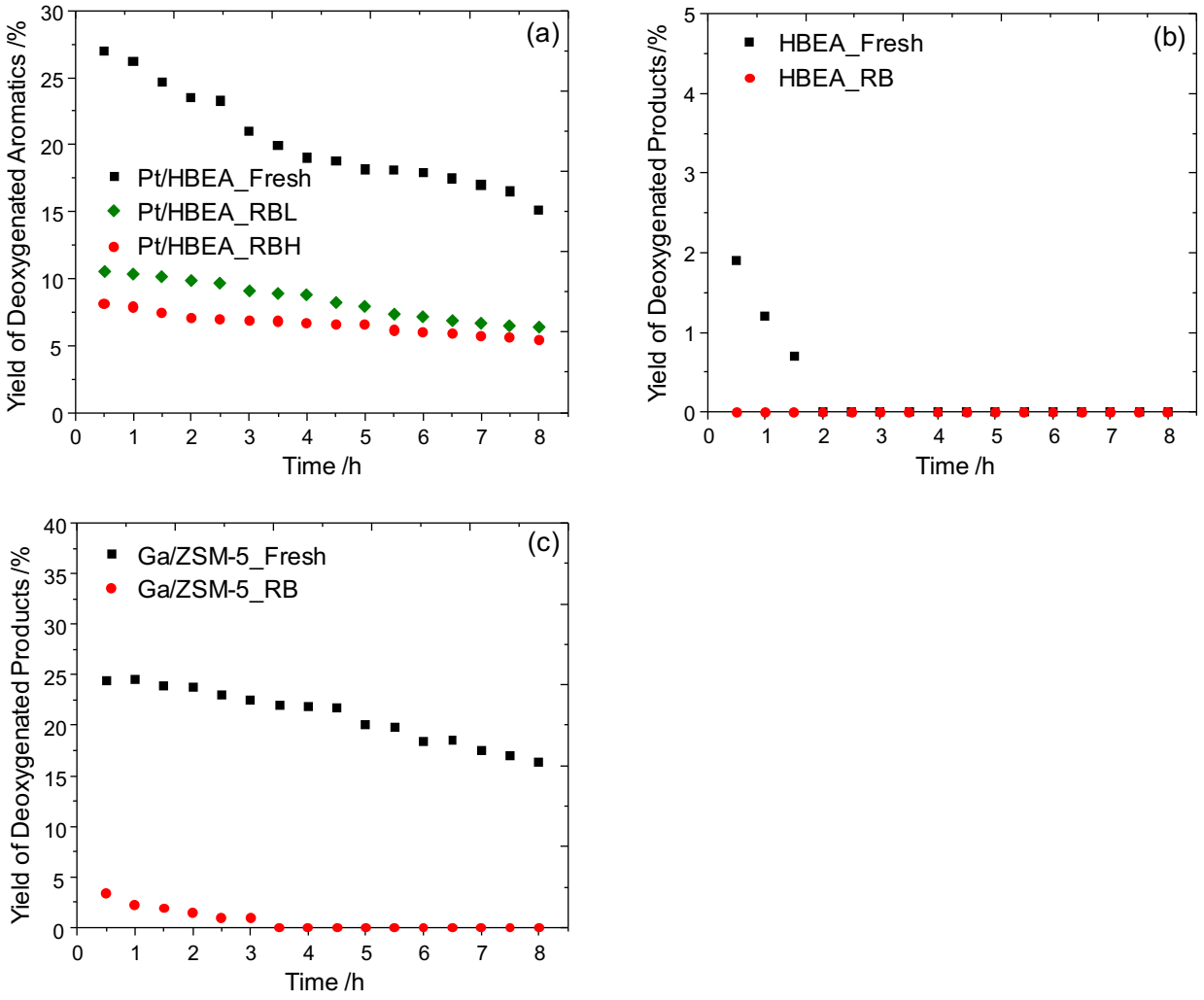

Figure 5.8 Yield of deoxygenated products on fresh HDO catalysts compared to catalysts with catecholate roadblocks (a) Pt/HBEA (b) HBEA (c) Ga/ZSM-5.

5.4 Discussion

5.4.1 Adsorption of Bidentate Catecholate Roadblocks

There are a few reports on the adsorption of catechol on metal oxides. Wang et. al studied the adsorption of catechol on titanium oxide.[252] Catechol first approach the terminal OH group of titanium oxide and forms a physisorbed species. Subsequently, one catechol OH is bound to one Ti atom. From this intermediate, surface species are formed from three alternatives. The first

alternative includes a bidentate mononuclear complex in which a single Ti atom binds coordinatively with two O atoms of catechol. The second possible alternative includes a monodentate binuclear complex in which an adjacent Ti atom has lost an –OH moiety, and can now bind to a catechol –OH moiety. The third involves a bidentate binuclear complex in which the two –OH moieties of the catechol form bonds with two different Ti atoms. Other studies made speculations on the relative stability of these three different structures. Jing et al. using detailed IR and computational studies indicated that the binuclear bidentate complex is the most stable.[240] Guo Shiou et al. studied the adsorption of guaiacol on HBEA using IR spectroscopy and hinted at the formation of a bidentate binuclear catecholate complex.[222]

In this study, TGA analysis of the catalysts loaded with catechol shows that a significant amount of adsorbed catechol remains on the catalysts after heating up to 800 ^{o}C, as seen in Table 5.2. This indicates that catechol-derived species formed are very strongly adsorbed on the catalysts. Such strong adsorption is possible when a bidentate species is formed in which both OH groups of catechol are contributing to its anchorage to the zeolite. Also, the polymerization of catechol during heat treatment could lead to the formation of large polycatechols, which are trapped in the zeolite pores at elevated temperatures. However, this is unlikely on MFI structures because of restricted diffusion of catechol inside the pores to begin with. This means that surface bound catechol-derived species are strongly adsorbed on MFI structures and should also be strongly adsorbed on HBEA surfaces as well. Insights on the mode of adsorption of catechol were derived from IR spectroscopy. The adsorption of catechol on Pt/HBEA led to a significant change in the IR spectrum compared to pure catechol (Figure 5.5a). The peak representative of δ(OH) disappeared, which indicates that the hydrogen atom on the OH group was dissociated. At the same time, a peak appeared around 1317 cm^{-1} starting at 300 ^{o}C, which is due to one or more

ν(C-O) vibrations. The peaks corresponding to $\nu(C=C)_{ring}$ vibrations of the aromatic ring, are also seen to shift slightly compared to pure catechol. The total disappearance of the OH group of catechol coupled with the other bands of catechol still remaining very intense, except for a shift in the $\nu(C=C)_{ring}$ vibrations, indicates the formation of a new aromatic species. The emergence of a new ν(C-O) peak around 1317 cm^{-1} is in agreement with the bonding of the C-O group of the new species with the catalyst after the hydrogen atom is dissociated from catechol. All these characteristics are indicative of the formation of bidentate catecholate species. These species are stable on the surface up to 400 ^{o}C as seen in the IR spectra in Figure 5.5, which means that the adsorption is very strong. Previous reports concluded on the formation of doubly anchored species upon the adsorption of guaiacol on alumina[226] and HBEA[222] and catechol on titanium oxide.[240] The reports of adsorption on metal oxides both suggested that the oxygen atom from the dissociated phenol group is coordinated to a Lewis acid site, while the oxygen atom of the methoxy group is coordinated to a Lewis acid/base interaction forming a bidentate catecholate species. Glycerol has also been shown to adsorb on metal oxides in a similar fashion where phenol groups dissociate and form bidentate species.[253-255] Figure 5.5b also shows similar IR features of the adsorption of catechol on Ga/HZSM-5. These zeolites (HBEA and HZSM-5), however, are made up of defects in the form of silanol nests on the external surface in addition to acid sites. In this case, anchoring of catechol-derived species should be able to occur on the perimeter of these nests as well. The IR spectra of the OH region of the zeolite showed a significant decrease or a complete disappearance in the intensity of the silanol hydroxyl bands between 3740 and 3745 cm^{-1} upon the introduction of catechol. Hence, the formation of strongly adsorbed bidentate species from catechol should be accessible on the external surface in the perimeter of silanol nests. These bidentate or multidentate surface species that form upon the

adsorption of a molecule that has multiple oxygenated functional groups have been reported to adsorb more strongly than monodentate species on γ-alumina, which subsequently slow down the transformation of γ-alumina into boehmite in hot, liquid water.[256-257] It is then very probable that the intended catecholate species remain strongly adsorb on the zeolitic frameworks at HDO reaction conditions mostly on the external surfaces in the perimeters of defect sites.

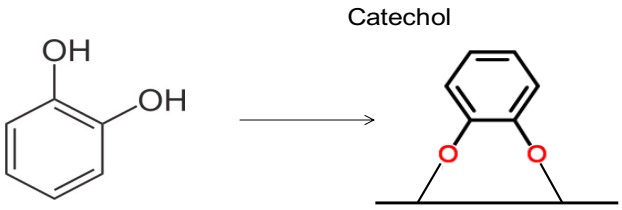

Scheme 5.1 Interaction of Catechol on Acidic HDO Catalysts.

5.4.2 Accessibility of active sites upon blocking with catechol

Zeolites are used in several catalytic processes including petroleum and biomass conversion because of their strong and tunable acidity, their microporous structure allowing molecular traffic control, high reaction surface areas, high thermal stability and their adjustable nature so that they can be tuned for several desired chemical reactants.[258] However, they are highly affected by their intrinsic microporosity as pores are too small to allow diffusion of large biopolymers to the active sites. In an application for the production of aromatics from carbohydrates, it was reported that both Brønsted acid sites and the presence of crystalline pore structure are prerequisite for catalytic activity.[259-260] Small pore zeolites produced mainly oxygenates and cokes as the diffusion of reactants and products is strongly hindered. Hence, the accessibility of reactants is a major area of consideration in zeolite based catalysts.

Hydrodeoxygenation of various bio-oil model compounds have been extensively studied over zeolite based catalysts, and coking has been speculated as the most common route of

deactivation. There is a significant lack of report about the effect of surface species formed by these model compounds on the catalytic activity. A previous study conducted operando FTIR spectroscopy during HDO reactions of several model compounds.[222] In this study, it is suggested that strongly chemisorbed catecholate species are formed on HBEA and Pt/HBEA during HDO of guaiacol. These strongly adsorbed species were suggested to reside on sites not necessarily responsible for the catalyst activity hence they are not poisoning the catalyst instead, they form "roadblocks" on or near the pore mouth of the zeolite framework and consequently restrict the diffusion of reactants and products in and out of the pores since the pore sizes of zeolite HBEA are only slightly larger than the reactants. In this study, we are examining bifunctional or multifunctional catalysts in which several active sites play different roles. On the metal sites, the aromatic rings of reactants are hydrogenated and this is followed by dehydration of the resulting alcohol group on an acid site of the zeolitic support. Hence, accessibility to both these sights are stringent.

H_2 chemisorption was used to probe the accessibility of hydrogen to the metal sites impregnated on the zeolite structures. The average particle size of the metals from hydrogen chemisorption was 2.7 nm for Pt on HBEA. This means that relatively large metal particles were formed from the impregnation technique that was used. These metal particles formed are significantly larger than the pore size of the zeolites, and as a result, a significant amount of the metal sites will remain on the surface of the zeolite. Previous reports of metal sites on microporous zeolites suggest that the impregnation technique of depositing metals results in metal particles on the external surface of the zeolite, as opposed to inside the framework.[51, 261] CO adsorption followed by FTIR spectroscopy on Pt/HBEA provided some insight on the location of Pt on HBEA. Band frequencies between 2082 cm^{-1} and 2056 cm^{-1} were observed. The bands were

relatively easily removed upon temperature programmed desorption and therefore demonstrate the behavior characteristic of CO molecules adsorbed on metal particles which are located on the external surface of the zeolite.[262-263] Thus, they exhibit the typical coverage-dependent shift upon temperature programmed desorption, which is due to elimination of dipole-dipole interaction with decrease in surface coverage.[262] Accessibility of CO to these Pt particles were significantly affected by catecholate roadblocks as indicated by the peak intensity. Also, the position of the CO band began at a lower wavenumber of 2070 cm^{-1} on the catalysts with roadblocks. This indicates that the exposed domains of Pt on this catalysts with roadblocks are smaller compared to the fresh catalyst. Bands at higher frequencies between 2123 cm^{-1} and 2092 cm^{-1}, which are assigned to small or monatomic Pt species that are capable of residing inside the zeolite pores[262, 264] were absent.

The accessibility of metal sites was more severely reduced on the catalysts containing catecholate species compared to other sites located inside the pores of the zeolites. One possible explanation of this reduction in metal site accessibility is that catechol poisons the metal sites by directly adsorbing on them. To investigate this possibility, we used a mesoporous silica support (SBA-15) with the same Pt loading as Pt/HBEA but much larger pore diameters to probe hydrogen adsorption after impregnation with catechol followed by the same heat treatment as for the zeolite samples. After this treatment, 96% of platinum sites in Pt/SBA-15 remained accessible for hydrogen adsorption compared to only 19% of accessible Pt sites on Pt/HBEA after the same deposition procedure for catechol-derived surface species. Pt/SBA-15 had a very limited number of acid sites (Figure 5.4a). The fact that a majority of the Pt sites on SBA-15 still remained accessible after introducing catechol to its framework indicates that the metal sites are not responsible for directly anchoring strongly adsorbed catecholate roadblocks. The adsorption of

catecholate roadblocks was probably significantly affected because of the absence of Lewis acid sites on this material in which case no roadblocks were present. The reasonably big pore mouth of SBA-15 could have also been able to overcome the effect of roadblocks and still allow access of hydrogen to the metal sites if they did indeed form on this material. The reduction of the accessibility of metal sites to hydrogen upon the addition of catechol-derived species must therefore be a result of a different type of coverage, as opposed to direct poisoning.

Catechol is a relatively large molecule of about 4.43 Å, calculated based on the bond lengths of intermolecular atoms as reported by C. J. Brown,[265] and has a kinetic diameter of 5.91 Å, as seen in Table 4. Based on the size and kinetic diameter of catechol compared to the pore sizes of MFI zeolites (Table 5.4), it is suggested that catechol-derived species are mostly sitting on the external surface of the zeolite similar to the metal sites. While catechol should barely be able to diffuse into the pores of HBEA, binding is accessible on the external surface and preferential adsorption of catechol-derived species is likely to happen on the surface before diffusion into the pores. IR spectra of the zeolites after the introduction of catechol showed a significant decrease in the intensities of the bands representing silanol groups and acidic bridging hydroxyl groups similar to what was observed upon the introduction of metals (Figure 5.6). This suggests that, although catechol molecules are not poisoning the metal sites, they are sitting on approximately the same sites on the zeolite surface (most likely in the perimeters of silanol groups). These silanol groups are mostly found in defect sites on the zeolite extraframework.[266] It is suggested that the metals are therefore mostly located inside these defect sites on the external surface of the zeolites. As a result of the introduction of catechol on sites at the perimeter of these defect sites containing metals, a blanket coverage of the metal sites by catechol-derived species becomes very probable.

Table 5.4 Pore diameters in zeolite supports

Zeolite	Maximum diameter of a sphere[a]			
	That can be included (Å)	That can diffuse along (Å)		
		a	b	c
HBEA	6.68	5.95	5.95	5.95
ZSM-5	6.36	4.7	4.46	4.46
Molecule	Kinetic diameter (Å)[b]	Molecule size (Å)		
Catechol	5.91	4.43		

[a] Obtained from International Zeolite Association.[267]

[b]Calculated by assuming that catechol molecule is spherical and correlating its kinetic diameter to its molecular weight as follows ($\sigma = 1.234.(M_w)^{1/3}$)[268]

Upon measuring the concentration of Lewis acid sites after introducing catecholate species onto the zeolite framework, a significant decrease is observed (Figure 5.4a). Previous reports indicate that Lewis acid sites are responsible for the adsorption of catecholate species, as discussed in the previous section.[222, 226] Consequently, extra framework alumina that are Lewis acidic will be poisoned by catechol-derived species. The reference material, Pt/SBA-15, with significantly larger pore mouths also showed a complete decrease in the limited amount of LAS that were present in the blank sample after introducing catechol into the framework. In the case where low loading of catechol species were introduced to Pt/HBEA, the catechol loading was equivalent to, a quarter of the measured amount of Lewis acid sites on Pt/HBEA (Pt/HBEA_RBL), the accessibility of the Lewis acid sites were still greatly affected with only about 26% remaining accessible. This means that in addition to the poisoning of extra framework Lewis acid sites by catechol-derived species, the accessibility of pyridine to the Lewis acid sites in the internal framework of the zeolites was also greatly affected due to the presence of catechol-derived species

near the pore mouth of the zeolite. In this case, both poisoning and roadblocks play important roles in reduced access to the Lewis acid sites during reactions where strongly chemisorbed species could form. The impact of introducing catechol onto the zeolite structures was also seen to affect the BAS concentration but slightly less significantly than the LAS concentration (Figure 5.4b). Although there are no reports in the literature of these sites contributing to the anchorage of catechol derived species, the reduction in intensities of the band at 3610 cm^{-1} upon adding catechol (Figure 5.6) indicates that surface hydroxyls, which are Brønsted acidic, are either poisoned by catechol-derived species or are hydrogen bonded to catechol-derived species in their vicinity. Hence, the decrease in accessibility of these sites is most likely from both a poisoning effect as well as a roadblock effect.

The reduction in the nitrogen adsorbed volume occurred mainly in the micropore region at low values of P/P_0 in the isotherm. The introduction of metals and catechol-derived species reduced the micropore area and volume, but when both were combined, the effect is even worse.

It is known from the literature that HBEA (BEA framework) and HZSM-5 (MFI framework) have three dimensional structures.[269-270] These three-dimensional structures allow the entrance of nitrogen into the pores from multiple channels in different directions when all the channel mouths are not blocked. This avoids a strong decrease in the micropore volume after the introduction of only catechol species or only metals. Hence, the HBEA without metals had a reasonable amount of accessible pore volume even after the introduction of catechol-derived species. Also, when the amount of catechol introduced into the HBEA framework was reduced, (Pt/HBEA_RBL), 85% of the pore volume remained accessible. Although parts of the pore mouths were blocked by small amount of catechol-derived species, the three-dimensional structure of HBEA allowed for the entrance of nitrogen from other channels that were not completely blocked.

Nevertheless, the introduction of both metals and more catechol-derived species on the external surface of the zeolite could block the pore mouths in several directions, causing a complete blockage in some of the micropore channels. As a result of this pore mouth blockage, the accessibility of the micropores to nitrogen was greatly affected, as seen in Figure 5.9. The zeolites´ micropore size relative to the size of catechol as previously discussed also has an effect. HZSM-5 is a 10-ring medium pore size zeolite[269] and HBEA is a 12-ring large pore size[236]. The accessibility of micropores is, therefore, more strongly affected in HZSM-5 structures compared to HBEA, as seen in Figure 5.9. Consequently, the blockage of the pore mouths of the zeolite limits the diffusion of reactants and products into the active sites (Brønsted acid sites) located in the internal framework of the zeolite.

To sum up, several parameters suffer from reduced accessibility upon the introduction of catechol-derived surface species. The metal sites are affected to the greatest extent because the catechol-derived species seem to sit in perimeters of defect sites where the metal sites reside and provide a blanket coverage of the metals. If any small metal sites exist that can reside in the pores, they also experience an additional accessibility restriction because catechol block some of the zeolite pore mouths and restricts access to sites inside the pores. The pores of the zeolites are also affected but not as greatly as the metal sites because HBEA and HZSM-5 are three-dimensional and allows diffusion of probe molecules in different directions. The fraction of exposed acid sites which reside mainly in the pores but are also present on the extra framework are affected to a greater extent than the pores in all cases. The little fraction of these sites that are located on the extra framework of the zeolites are most likely poisoned by catechol and access to the acid sites inside the pore are affected by catecholate roadblocks.

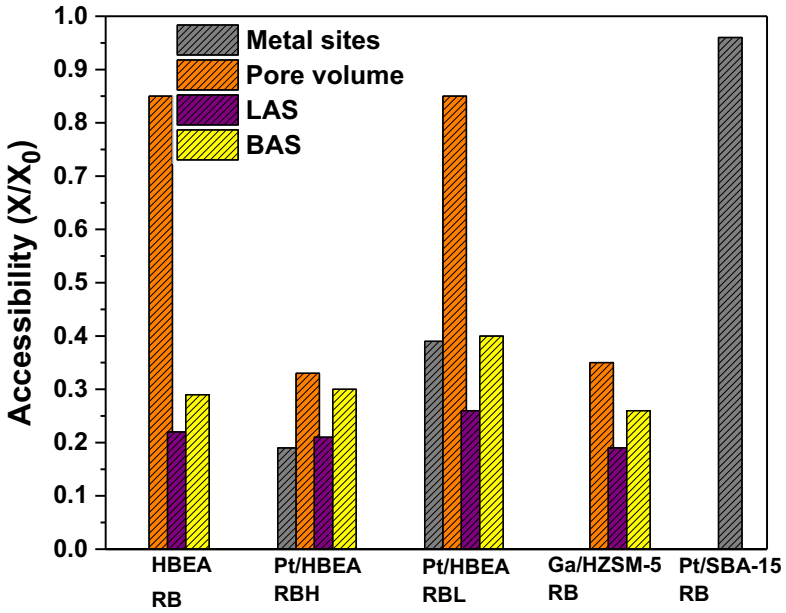

Figure 5.9 Fraction of accessible active sites on HDO catalysts after blocking with catechol. Accessibility (x/x_o) was measured by dividing the amount of measured sites after the introduction of catechol by the amount of sites measured before the introduction of catechol.

5.4.3 Catalyst Deactivation during HDO of Anisole on Catalysts with Roadblocks

Deactivation of HDO catalysts during the reaction is an important problem. Several studies have attributed coking as the most common route for this deactivation. Water has also been attributed to the deactivation of sulfided NiMo catalysts during hydrodeoxygenation.[271] Deactivation by water was reported as a result of competitive adsorption on the active sites or by strong adsorption on the support which leads to partial crystallization of the γ-alumina support into boehmite. The effect of roadblocks has also been presented in the literature as a possible route for the deactivation of catalysts during hydrodeoxygenation. These roadblocks can be more detrimental than coke[222] without directly binding to active sites. A report studied the different extent of catalyst deactivation caused by two different bio-oil model compound feeds (anisole and guiaicol).[217] This report found that bimetallic Pt-Sn on inconel monolithcatalyst is more

severely deactivated by guaiacol than by anisole (or their respective products). This study attributed the rapid deactivation to the strong adsorption of double-functionalized guaiacol and catecholate that remained on the surface and blocked metallic deoxygenation sites. Another recent report from the Sievers group performed a detailed operando study of different bio-oil model compunds during HDO and showed that the strong adsorption of guaiacol derivatives can lead to the formation of roadblocks on Pt/HBEA.[222] A good understanding of the impact of these roadblocks on the performance of zeolites in HDO reactions is, therefore, critical.

In this study, catecholate roadblocks were delibrately deposited on zeolite catalysts to understand the severity of their effect on hydrodeoxygenation reactions. Catechol was used as a precursor for roadblocks instead of guaiacol in order to eliminate the additional complexity that would arise from additional reactions involving the methoxy group in guaiacol. The initial conversion of anisole over Pt/HBEA dropped by 61% with a high catecholate roadblock loading of 6.48 wt.% and by 51% due to lower catechol loading of 1.09 wt.%. The same deoxygenated products were produced over catalysts with and without roadblocks but the yields were significantly reduced on the catalysts with roadblocks. This indicates that only a limited amount of the sites responsible for hydrodeoxygenation were exposed on the catalysts with roadblocks. The simultaneous presence of metal sites and Brønsted acid sites has been reported to be resposnible for the complete HDO of anisole.[51, 222] Hydrogenolysis of the PhO-CH_3 bond has been reported as the preferential step in hydrodeoxygenation of anisole over Pt.[51, 222, 224, 272-273] The Brønsted acid sites in the the HBEA support are responsible for transfering the cleaved CH_3 to an aromatic ring, which results in intra- or intermolecular rearrangements to form transalkylated or dealkylated products (Scheme 5.2).[51, 222, 224]

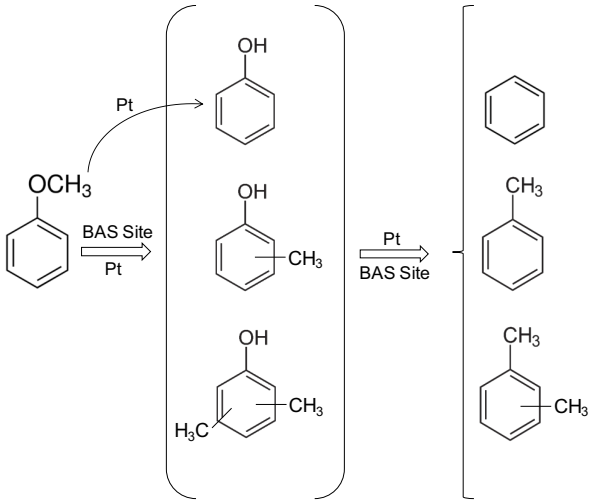

Scheme 5.2 Major reaction pathway for HDO of anisole over bifunctional Pt/HBEA catalyst.

The reduced productivity of HDO products on the catalysts with roadblocks indicates that anisole experienced a restricted access to these active site. On the catalyst surface, access to the Pt sites for hydrogenolysis of the PhO-CH_3 bond is restricted by the catecholate roadblocks. The resulting intermediates after the hydrogenolysis of the PhO-CH_3 bond experience further restrictions by catechol roadblocks to the Brønsted acid sites which are mainly present in the pores of HBEA. In the presence of Pt metal, the dissociated methyl group can also be hydrogenated to form methane. Methane is produced with lower selectivity on Pt/HBEA_RB compared Pt/HBEA which further indicates a restricted accessiblity to the Pt sites for methyl hydrogenation on the catalyst containing catecholate roadblocks. HBEA without Pt sites is not capable of performing a complete deoxygenation of anisole. Major products on this catalyst are oxygenated species (Figure D.6). Pt metal sites are, therefore, essential for the complete deoxygenation of anisole. Several literature studies supports the bifunctionality of Pt and zeolites in HDO reactions.[51, 222] The introduction of catechol reduced the reactivity of the catalysts but did not change the reaction path. The fraction of Pt sites and Brønsted acid sites on Pt/HBEA_RB that were accessible to anisole feed resulted in the same reaction pathway as with

fresh Pt/HBEA. The initial shift in the CO stretching frequencies on Pt/HBEA with roadblocks compared to the fresh catalysts (Figure 5.3) indicates smaller accessible domains of Pt sites on the catalyst with roadblocks. In addition to lower reactivity, the deactivation rate constant of the Pt/HBEA with roadblocks were higher than the fresh Pt/HBEA. This could be attributed to the more rapid coke formation on the catalysts with roadblocks. The blanket coverage of Pt sites on the external surface of the zeolite by catechol-derived species could result in increased coke formation. Previous studies reported that Pt sites are indirectly involved in the suppression of polyaromatics and coke formation. This suppression of coke formation as a result of Pt was attributed to hydrogen spillover.[222] Hydrogen abstraction was reported to be involved in coke formation.[274] In HDO reactions, atomic hydrogen species that are formed on Pt sites could migrate to the HBEA support through spillover and suppress coke formation by encouraging the reverse reaction of hydrogen abstraction. As seen from H_2 chemisorption results, the accessibility of Pt sites to hydrogen is reduced significantly upon the introduction of catechol (Figure 5.9). Hence, the reverse reaction of hydrogen abstraction encouraged by Pt on these roadblocked catalysts is no longer very effective leading to more coke formation. Roadblocks residing near the pore mouths could also lead to entrapment of some anisole that managed to get into HBEA from other channels. Consequently, intermediates may have a higher residence time in proximity to active sites within the zeolite framework and undergo secondary reactions which may include the formation of coke.

Although Ga/HZSM-5 was slightly less active than Pt/HBEA for the hydrodeoxygenation of anisole, it was also very effective for the complete HDO of anisole to products such as benzene, toluene, and xylene, as well as partial HDO to some oxygenated aromatics. However, this catalyst was affected by roadblocks even more severely than Pt/HBEA. In the case of

Ga/HZSM-5, metallic sites are not present since GaO_x hardly reduce below 600 °C[275-276] which is significantly higher than the conditions used in this study. Instead, the GaO_x sites and the Brønsted acid sites are active for HDO. On the GaO_x sites with redox properties, anisole compound probably interacts with oxygen vacancies, and the Ph-OCH_3 bond is preferentially cleaved. Subsequently, the oxygen vacancy is regenerated by reduction with hydrogen. This type of pathway was shown for HDO of oxygenated aromatic compounds over reducible metal oxides like MoO_3,[229] and ceria-zirconia.[99] Several reports have also shown an enhanced performance of HZM-5 catalysts upon incorporation of Ga_2O_3 for hydrogen-based upgrading of pyrolysis vapour.[223, 277] The Brønsted acid sites again are responsible for transalkylated or dealkylated products. Ga/HZSM-5 catalysts generally deactivated faster than Pt/HBEA with or without catechol roadblocks. This is probably because of the absence of metal sites that is believed to suppress coking on this catalyst. Also, as the MFI structure is smaller than BEA structure, accessibility to active sites inside the pores of this catalyst are more severely affected by roadblocks and leads to a complete deactivation of the catalyst within only 3.5 h on stream. In addition to effect caused by roadblocks, GaO_x sites which are Lewis acidic, may also suffer from poisoning by catechol. Hence, strongly chemisorbed species that form during HDO of bulky oxygenated groups could also result in poisoning of important active sites of Ga/HZSM-5 catalysts in addition to serving as roadblocks. Due to this effect of poisoning, reducible metal sites are more desirable than metal oxide sites on zeolite-based HDO catalysts for extended activity.

5.5 Conclusions

Catechol adsorbs strongly at the perimeter of defect sites where metal particle resides on zeolite surfaces forming bidentate catecholate species which are very stable on the catalysts at

elevated temperature. These strongly adsorbed species form “roadblocks” and prevent access of HDO reactants to both active sites on the extraframework of zeolites and in the zeolite pores. Although, these roadblocks are not posioning the metal sites, a blanket coverage of the metals is possible by these catechol-derived species which then prevents their accessibility. Anisole conversion over Pt/HBEA and Ga/HZSM-5 with catecholate roadblocks is seen to decrease dramatically, but the same products are formed. This means that the sites for HDO are not completely blocked but reactivity is heavily affected due to restricted access to the active sites. The reduced accessibility of the metal sites or lack of it also led to more coke formation and consequently, faster catalyst deactivation.

H_2 chemisorption performed to probe the accessible metal sites on blank catalysts and catalysts with roadblocks showed a significant decrease in accessible metal sites due to catechol in Pt/HBEA but not in Pt/SBA-15, a mesoporous silica with limited acid sites. This observation confirms that catechol on the framework is not poisoning the metal site directly but rather, adsorbing on the perimeter of these sites and preventing access to the metal sites on the external surface of the zeolite. Pyridine adsorption followed by FTIR spectroscopy showed a significant drop in the concentration of Lewis and Brønsted acid sites in catalysts blocked with catechol compared to blank catalysts. The drop in LAS concentration is significantly greater than the amount of catechol introduced into the zeolite framework. This was visualized by blocking only 25% of the LAS in Pt/HBEA which resulted in a 74% decrease in LAS. This, again, indicates mass transfer limitations of pyridine to the acid sites in the zeolite pores caused by “roadblocks” sitting on or near the pore mouths of the zeolites.

On the basis of this chapter’s results, it is obvious that coke formation and poisoning are not the only contributing factors to the deactivation of zeolite based catalysts during HDO

reactions. Strongly adsorbed species on the surface of zeolites could form during HDO reactions. These species result in “roadblocks” near the pore mouths of the zeolites causing reduced access of reactants and products in and out of the pore of the zeolite, as well as preventing accessibility to active sites in defects on the external surface of the zeolites. All these lead to an eventual deactivation of the catalysts.

CHAPTER 6

FINAL CONCLUSIONS AND RECOMMENDATIONS

The purpose of this dissertation is to design and optimize catalysts for the conversion of methane into useful chemicals like hydrocarbons and alcohols as well as utilize different experimental techniques to elucidate deactivation of catalysts during the upgrading of fuels from alternative sources. As researchers will continue to seek for effective means for utilizing methane reserves for the production of fuels and chemicals, it is imperative to develop effective catalysts for performing these reactions. Also, a thorough understanding of the reaction kinetics as well as the influence of different active sites will allow effective conversion strategies to be formulated.

In Chapter 2, it was shown that methane can be activated and coupled over NiO/CZ to form ethane, ethylene and aromatics in a non-oxidative environment. Specifically, small Ni domains which do not have enough surface sites for aromatization are active throughout the reaction for the formation of ethane and ethylene, while larger Ni domains lead to the formation of aromatics and coke. However, the conversion of methane to ethane and hydrogen is highly endothermic, and hence, only a very limited conversion of methane can be achieved at low temperatures. To improve the conversion to an acceptable level for industrial application without increasing the operating temperatures, these catalysts could be incorporated into membranes that can selectivity remove hydrogen to drive the reaction in the forward direction. For this purpose, a hydrogen selective membrane with low propensity to catalyze other side reactions can be tested for the continuous separation of hydrogen in the reaction stream and this could lead to methane coupling to ethane and ethylene far beyond the thermodynamic limit.

In Chapters 3 and 4, it was shown that a catalyst comprising of small nickel oxide clusters supported on ceria-zirconia (NiO/CZ) can convert methane to methanol and ethanol in a

single, steady state process at 450 ˚C using oxygen as an abundantly available oxidant. The unusual activity of this catalyst is attributed to the synergy between the small Lewis acidic NiO clusters and the redox active CZ support, which also stabilizes the small NiO clusters. A strong interaction between CZ and NiO will leads to an increase dispersion of NiO clusters. To maximize the performance of the catalyst, different synthesis techniques were used to create a stronger interaction between NiO and CZ, which reduces agglomeration of NiO particles during calcination of the catalyst. This led to catalysts with better dispersion of NiO particles on the CZ support and in turn led to higher catalytic performance in terms of methane conversion and alcohol selectivity. The best catalyst was prepared using strong electrostatic adsorption and had a NiO dispersion of 31%. This means that the dispersion of NiO on CZ might be improved even further. The CZ used in this thesis has a surface area of 85 $m^2.g^{-1}$. Zirconium was used to form a solid solution to reduce the loss in surface area during calcination. Therefore, it would be worthwhile to vary the concentration of zirconium incorporated into the ceria lattice in order to determine the optimum level of zirconium loading required to prevent the loss of surface area of CZ during calcination. Strong electrostatic adsorption should then be used to deposit NiO on this CZ support with potentially higher surface area. The presence of more surface area of CZ will present more sites for the binding of NiO particles and should theoretically increase NiO dispersion. Zirconium also enhances the redox activity of ceria and hence, it is imperative to determine the optimum concentration of zirconia in the ceria matrix.

It was also found in Chapter 3 of this thesis that the presence of steam is required to obtain alcohols rather than carbon dioxide, which is the product of catalytic combustion. It is suggested that steam is required for hydrolysis of the surface species from methane activation to alcohols before the surface species undergoes combustion by oxygen to form CO_2. In this thesis,

an oxygen to steam ratio of 0.2 was used, which led to a CO_2 selectivity of over 50%. Determining the optimum composition of steam and oxygen in the feed will therefore be very important to optimize the process of methane conversion to alcohols and to reduce the formation of CO_2. For this purpose, the reaction should be run at different steam to oxygen ratio, and the products should be examined. In addition to understanding the effect of steam and oxygen on the selectivity to different carbon containing products, an overall understanding of the reaction mechanism will be important to develop strategies for improving the catalyst performance towards the formation of alcohols. For this purpose, it will be important to use operando IR spectroscopy to quantify the amount of surface species and measure the rates for their interconversions. Further insights into the reaction mechanism can be obtained by performing reactivity tests at varying temperatures and partial pressure of different reactant species. Conditions that avoid mass transfer limitations need to be determined in order to perform these reactivity tests so that intrinsic kinetics of the reaction could be obtained. Kinetics parameters, such as activation energy and orders of different reactants, can be obtained from these additional studies, and the plausibility of the reaction mechanism can be tested.

The composition of the product stream from the reaction discussed in Chapter 3 and 4 of this thesis comprises mainly of CH_4, CO_2, O_2, H_2O, CH_3OH and CH_3CH_2OH. In an industrial application, it would be desired to separate these components from the mixture to allow for recycling the unreacted CH_4. The easily condensable products can be separated from the mixture by distillation in the order of increasing boiling points. The methanol with the lowest boiling point could be removed first followed by ethanol and then water. Most importantly, at 15% methane conversion, it would be important to recycle methane. Hence, removing the CO_2 from the gas stream is of utmost importance. Amine scrubbing technology, which was established

over 60 years ago in the oil and chemical industries, could be used here for CO_2 capture from the gas stream following distillation. Commercially, this is the most well-established of the techniques available for CO_2 capture. Other techniques such as the use of solid adsorbents (zeolites and activated carbon) or gas separation membranes could also potentially be used in the future for the separation of CO_2.

In Chapter 5, a rigorous assessment of reactant intermediates which, strongly adsorb and form roadblocks and their impact on the deactivation of zeolite based catalyst during HDO reactions was performed. Phenolics with multiple oxygen-based functional groups can potentially adsorb more strongly on Lewis acid sites or silanol nest peripherals of HDO catalysts and form roadblocks, which lead to a lower reactivity of the catalyst as well as faster deactivation. A two stage process for hydrodeoxygenation could potentially mitigate this problem. A removal of oxygen from molecules with multiple functional groups could be done in the first stage. Different catalysts with high activity for partial HDO could be used in this stage. Ceria-Zirconia catalysts have been reported to be highly active in the partial deoxygenation of guaiacol into phenol without signs of deactivation over 6 days on stream.[99] Also a catalyst comprising of cerium-incorporated into hierarchical HZSM-5 catalysts showed high activity and reduced deactivation in the partial deoxygenation of lignocellulosic biomass into less oxygenated products like furans, ketones and aldehydes.[278] The partially deoxygenated products from the first stage, can then be subsequently deoxygenated completely into benzene and other deoxygenated aromatics in the second stage over Pt/HBEA, Ni/ZSM-5, or Ga/ZSM-5. In addition, catalysts without Lewis acid sites should be considered for HDO as these sites seem to be majorly responsible for the formation of “roadblocks”.

The effects of roadblocks on zeolite based catalysts could also be mitigated by co-feeding water. Several studies have shown positive effects of water on zeolite-catalyzed reactions.[279-282] Although further studies are required to completely unravel the role of water in more details, it is now generally believed that water acts as a sweeping agent, forcing the desorption and diffusion of formed products from the zeolite. It would therefore make sense to use water as a means of removing strongly adsorbed species that forms during HDO of complex reactants with multiple oxygenated groups. This, however, must be done with care as steaming also leads to dealumination of zeolites. Also, polyols have been shown to competitively adsorb on Lewis acid sites even in the presence of water forming strongly chemisorbed multidentate species on γ-Al_2O_3, TiO_2, ZrO_2, CeO_2 and Nb_2O_5.[253-255] However, these studies have not been performed on zeolite-based catalysts in which catechol is potentially also adsorbed on other sites rather than just the Lewis acid sites.

The effects of roadblocks were more prominent in catalysts with small pore diameters. Mesoporous zeolites or catalysts with bigger pore mouths should not be affected by "roadblocks" to the same extent. However, on these catalysts with big pore mouths, the molecules can easily diffuse into the pores and adsorb strongly on Lewis acid sites inside the pores. Hence, mesoporous zeolites without Lewis acid sites should be considered in the development of future generations of HDO catalysts. There are several methods for inducing these mesopores, which include acid treatment of crystalline zeolite, using structure directing agents during synthesis, or templating on a polymer or structured carbon substrate.

In conclusion, this thesis offers a first of its kind conversion of methane to higher hydrocarbons and alcohols (methanol and ethanol) using a cheap catalyst. It also provides insight on catalyst deactivation by strongly adsorbed roadblocks during HDO of pyrolysis oil model

compounds. I hope that researchers would be able to carry-on with the further improvement and optimization of the processes highlighted in this thesis for a more effective production of fuels and chemicals to meet future demands.

APPENDIX A

Supplementary Information for Chapter 2

Table A.1 FTIR Spectra Characteristics for methane activation over NiO/CZ.

Functional group	Group Label	Frequency /cm^{-1}	Reference
asymmetric methyl vibrational stretch	$-CH_3$ asym	2975-2950	37, 115
symmetric methyl vibrational stretch	$-CH_3$ sym	2885-2865	37, 115
asymmetric $-CH_2-$ vibrational stretch	$-CH_2-$ asym	2940-2915	115
symmetric $-CH_2-$ vibrational stretch	$-CH_2-$ sym	2870-2840	115
isolated C=C	$\nu(C=C)_{ring}$	1680-1620	115
asymmetrically substituted aromatics	$\nu(C=C)_{ring}$	1600	115, 283
graphitic coke	$\nu(C=C)_{ring}$	1580-1570	117-118, 284
para-distributed aromatics, 1,2,4-trisubstituted aromatics	$\nu(C=C)_{ring}$	1537-1518	115, 283
Ortho- and meta-disubstituted aromatics, 1,2,3-trisubstituted aromatics	$\nu(C=C)_{ring}$	1507-1504	115, 283
asymmetric methyl deformation vibration	$\delta_{asym}(CH_3)$	1485-1445	115
symmetric methyl deformation vibration	$\delta_{sym}(CH_3)$	1460-1420	115
ethyl deformation vibration	$\delta(CH_2)$	1470-1440	115
methyl groups attached to aromatic rings	$\delta_{asym}(CH_3)$	1390-1370	115, 283
methyl groups attached to aromatic rings	$\delta_{sym}(CH_3)$	1350	115, 283

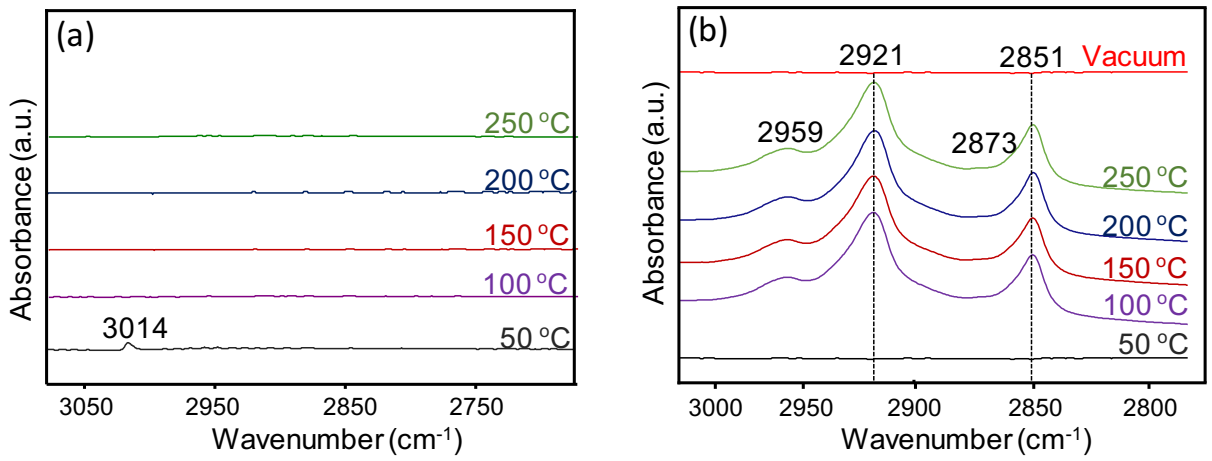

Figure A.1 Difference IR spectra of products from methane at different temperatures on (a) CZ (b) NiO/CZ

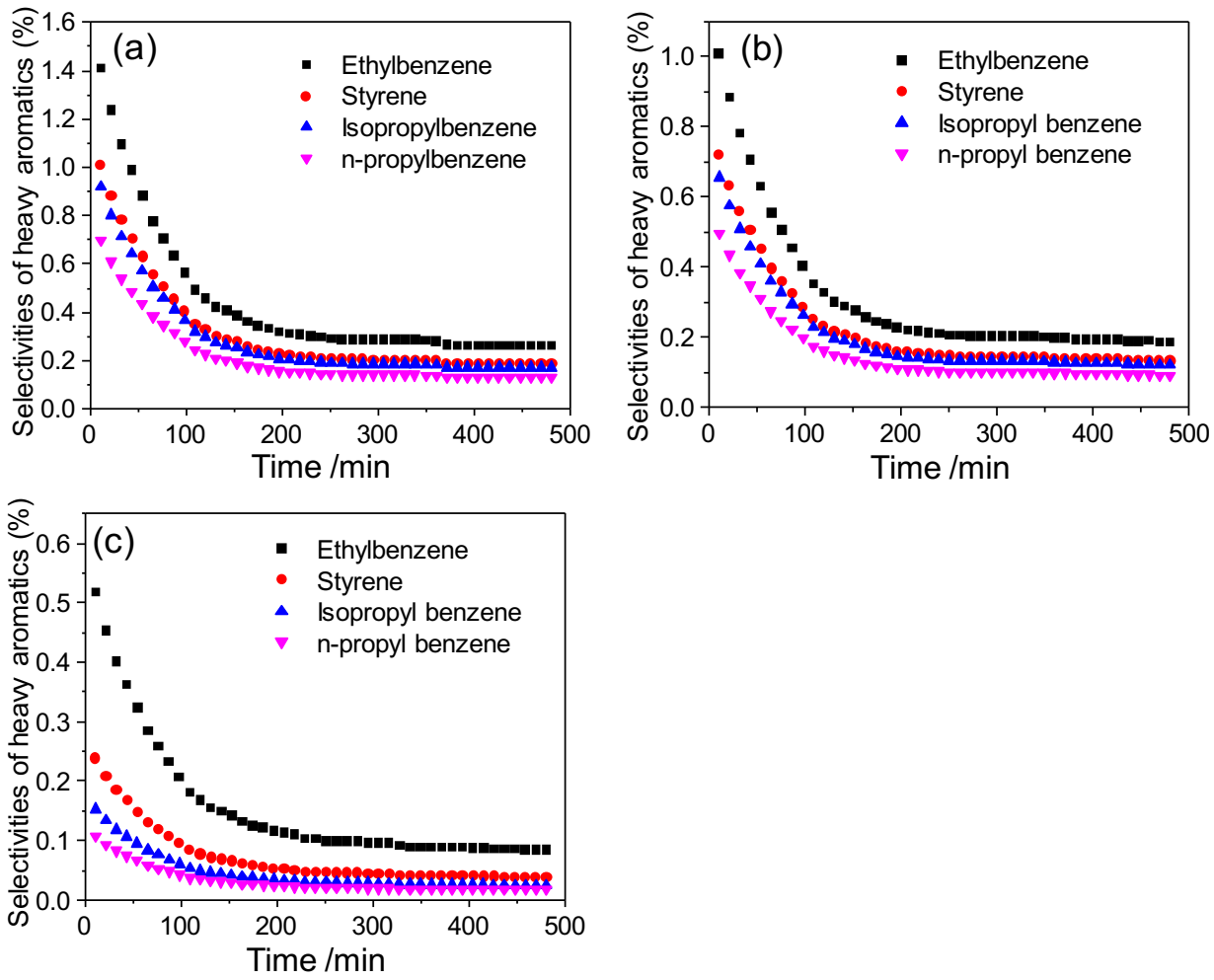

Figure A.2 Selectivities of heavy aromatics over NiO/CZ at (a) 500 ˚C (b) 450 ˚C (c) 350 ˚C

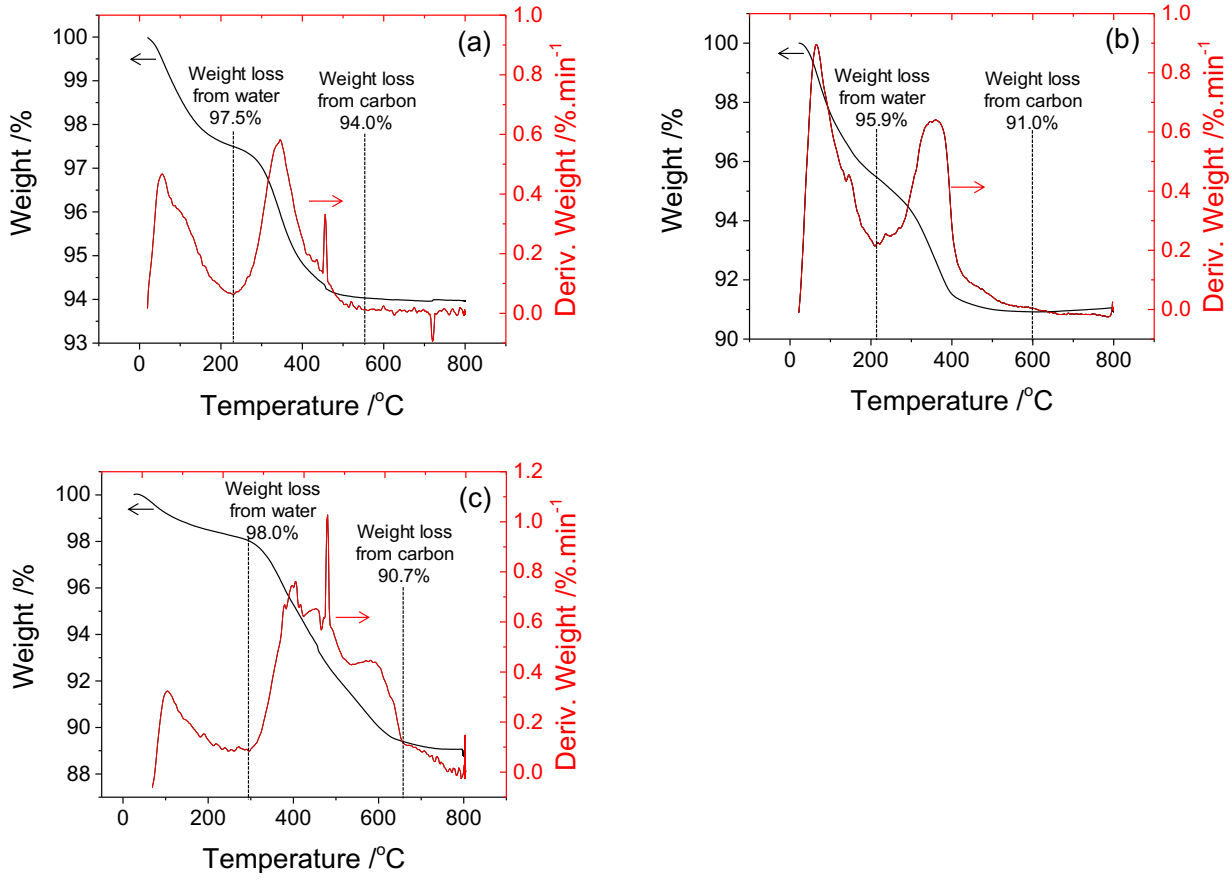

Figure A.3 (a) TPO of spent NiO/CZ after reaction with methane at 350 °C using TGA (b) TPO of spent NiO/CZ after reaction with methane at 450 °C using TGA (c) TPO of spent NiO/CZ after reaction with methane at 500 °C using TGA

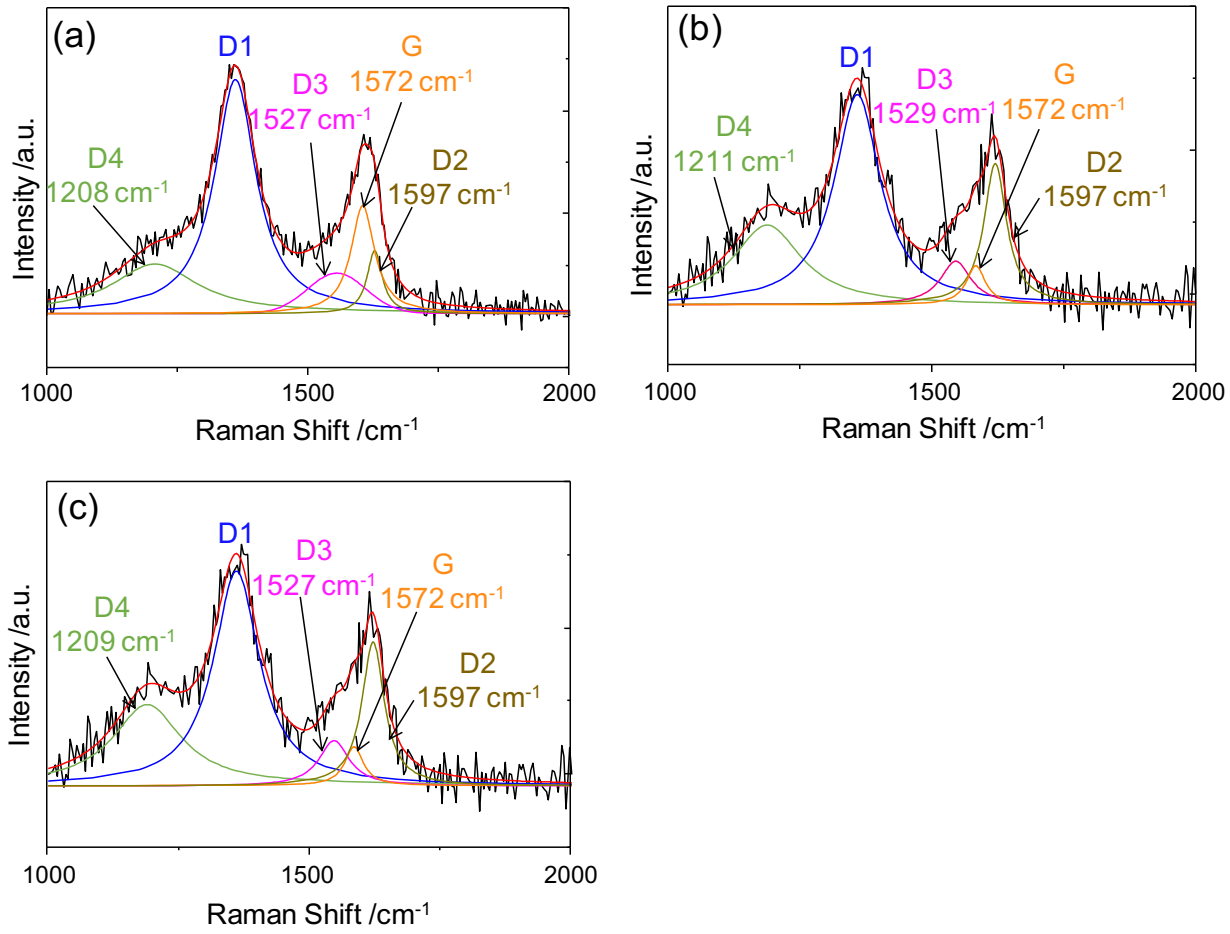

Figure A.4 Peak fitting of Raman spectra of spent catalysts after reaction at (a) 500 ˚C (b) 450 ˚C (c) 350 ˚C.

APPENDIX B

Supplementary Information for Chapter 3

Table B.1 Lewis acid sites concentration and metal oxide dispersion on catalysts.

Catalyst[a]	LAS Concentration (μmol/g)[b]		Dispersion[c]		Metal loading (wt.%)
	Fresh	Spent	Fresh	Spent	
CZ	2.29	N/A	N/A	N/A	N/A
2 wt.% NiO/CZ	86.1	38.5	0.26	0.12	1.96
2 wt.% NiO/CZ‡	79.9	-	-	-	1.96
2 wt.% CoO/CZ	79.8	-	0.24	-	1.97
2 wt.% PdO/CZ	88.2	-	0.44	-	1.94
2 wt.% FeO_x/CZ	78.0	-	0.22	-	1.95
2 wt.% Al_2O_3/CZ	28.9	-	0.04	-	1.91
2 wt.% NiO/SiO_2	38.1	1.9	0.11	0.006	1.98
5 wt.% NiO/CZ	126.5	37.4	0.15	0.04	4.89

a CZ composition as determined by ICP-OES analysis is $Ce_{0.83}Zr_{0.17}$

b Pyridine adsorption followed by FTIR spectroscopy. LAS concentration calculated using Beer's law

c Dispersion of metal oxide on CZ determined from pyridine adsorption on Lewis acidic metal oxide followed by FTIR spectroscopy

2 wt.% NiO/CZ‡ - Sample was exposed to water vapor at 573 K before pyridine adsorption to determine the effect, if any, of the coverage of NiO with OH groups on the Lewis acid site functionality.

B.1 Lewis acidity of catalysts

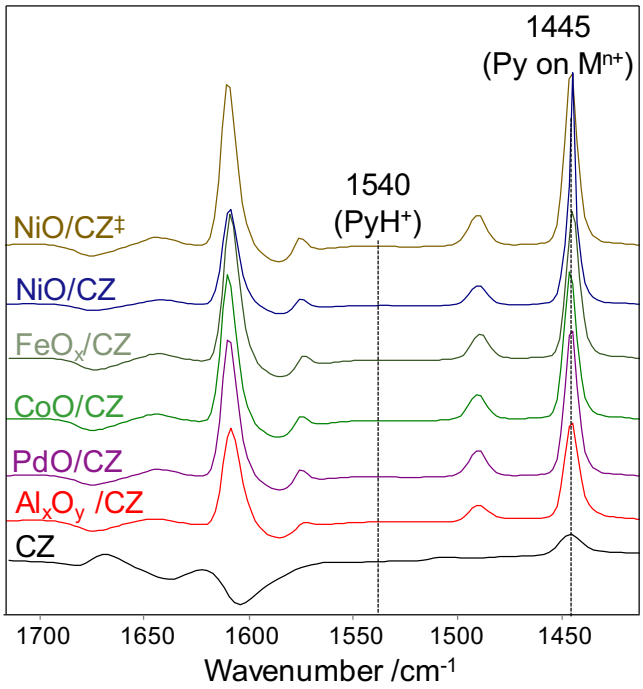

Figure B.1 FTIR spectra of pyridine on catalysts at 423 K showing adsorption on Lewis acid sites (band at 1445 cm^{-1})

The concentration of acid sites on the catalyst materials were quantified using pyridine adsorption followed by FTIR spectroscopy. Pyridine was used because it is a strong base that can distinguish between Brønsted and Lewis acid sites. Characteristic IR bands are obtained for pyridine adsorbed on a Lewis acid site, LAS (around 1445 cm^{-1}) and pyridinium ion (around 1540 cm^{-1}) that is formed when pyridine is protonated on a Brønsted acid site, BAS.[137] Quantifying the amount of adsorbed pyridine from the integral of these vibrational bands was done using the Beer-Lambert's law.

B.2 XRD Patterns of Catalysts

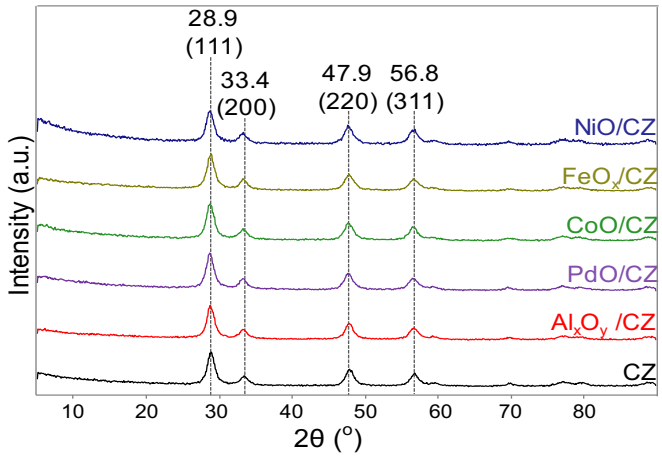

Figure B.2 XRD patterns of ceria-zirconia based catalysts

The X-ray diffraction pattern of ceria-zirconia and metal oxides supported on ceria-zirconia contained four prominent diffraction peaks associated with the (111), (200), (220), and (311) planes, respectively.[86] All peaks in the diffractogram were attributed to ceria-zirconia, indicating that the metal oxide clusters were very small and well dispersed and no crystalline impurities were present. The crystallite sizes calculated by the Scherrer equation were approximately 8 nm for all the materials.

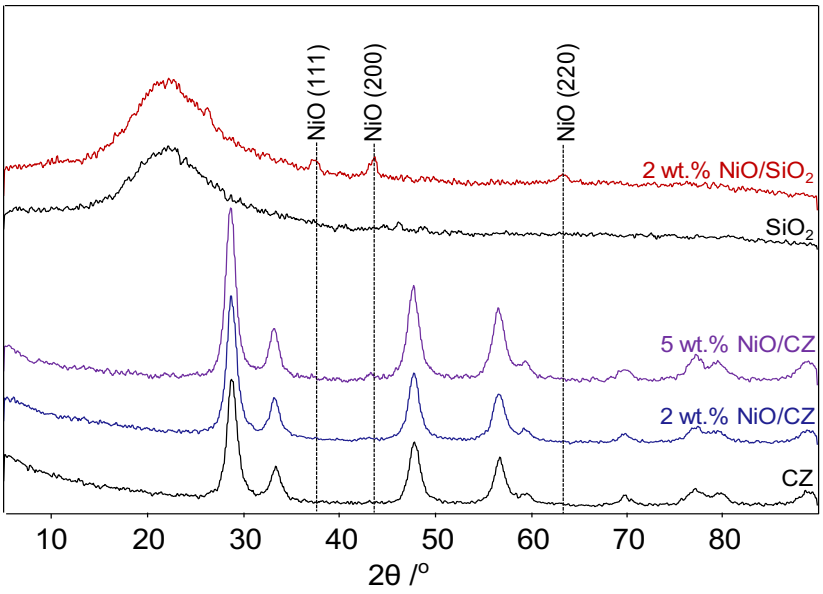

Figure B.3 XRD pattern of NiO/CZ and NiO/SiO_2 and the NiO-free supports. X-ray diffractogram of 2 wt.% NiO/CZ only contained peaks corresponding to ceria-zirconia, whereas diffractions of NiO crystallites were observed for 2 wt.% NiO/SiO_2 and NiO (200) crystallite peak is obvious on the diffractogram of 5 wt.% NiO/CZ. This confirms bigger clusters of NiO on 2 wt.% NiO/SiO_2 and 5 wt.% NiO/CZ compared to 2 wt.% NiO/CZ.

B.4 IR Study of Methane Activation over CZ-based Catalysts

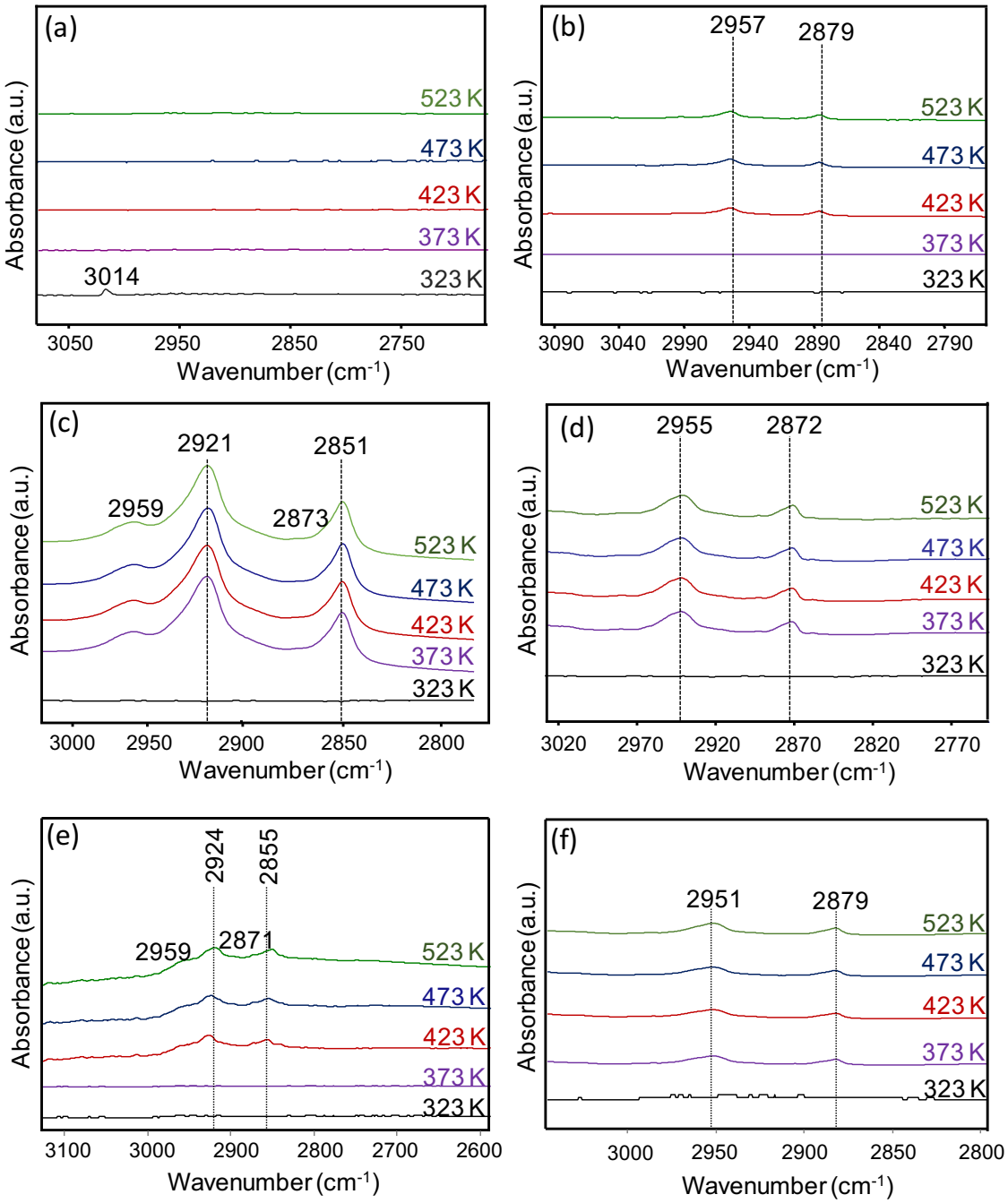

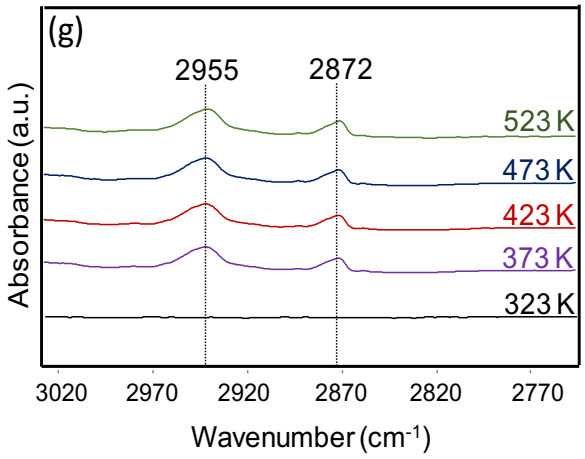

Figure B.4 Difference IR spectra of products from CH_4 at different temperatures on (a) CZ (b) 2 wt. % CoO/CZ (c) 2 wt. % NiO/CZ (d) 2 wt. % NiO/SiO_2 (e) FeO_x/CZ (f) PdO/CZ (g) Al_xO_y/CZ.

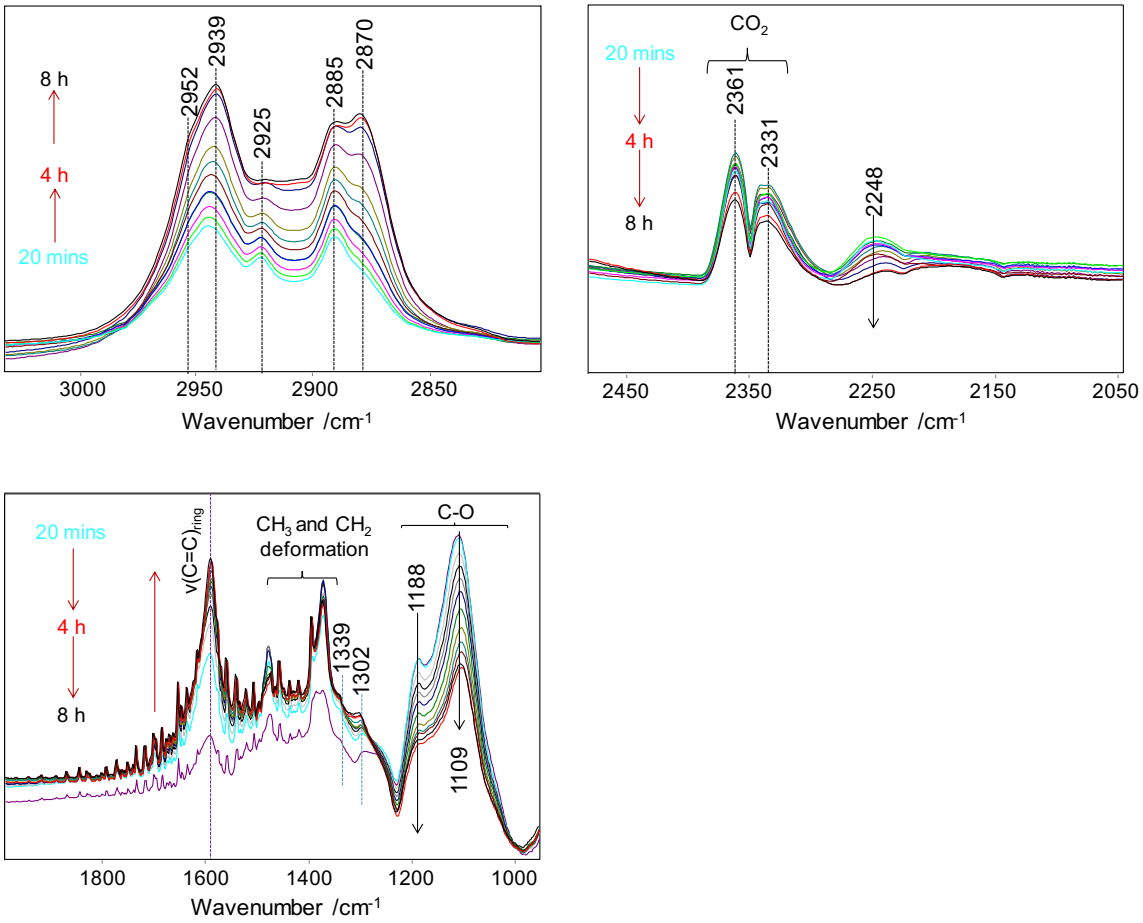

Figure B.5 Subtracted operando IR spectra during reaction of methane, oxygen and steam over 2 wt.% NiO/CZ with a steam to carbon ratio of 1 and oxygen to carbon ratio of 0.2 at 723 K.

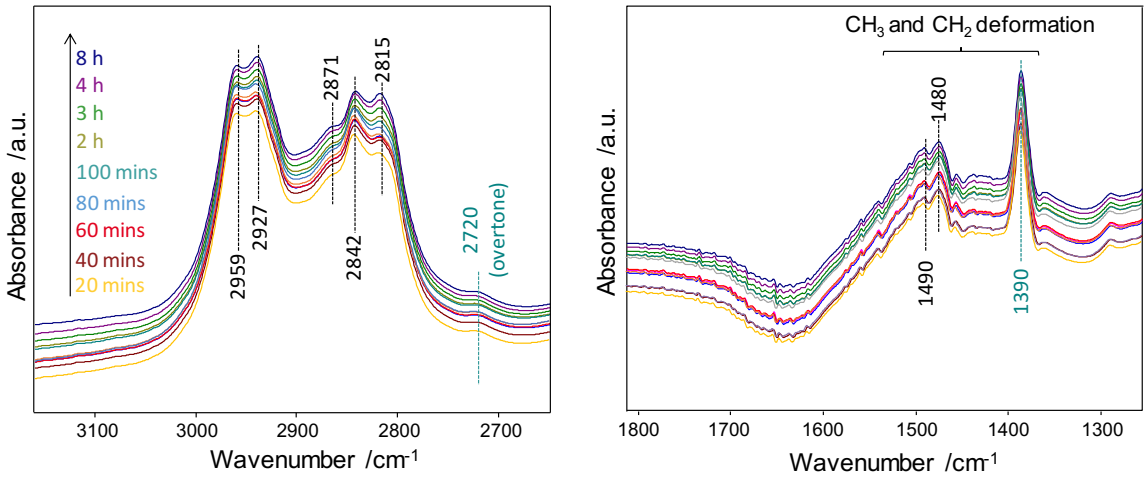

Figure B.6 Subtracted in-situ FTIR spectra during exposure of 2 wt.% NiO/CZ to 5% methane in inert at 723 K.

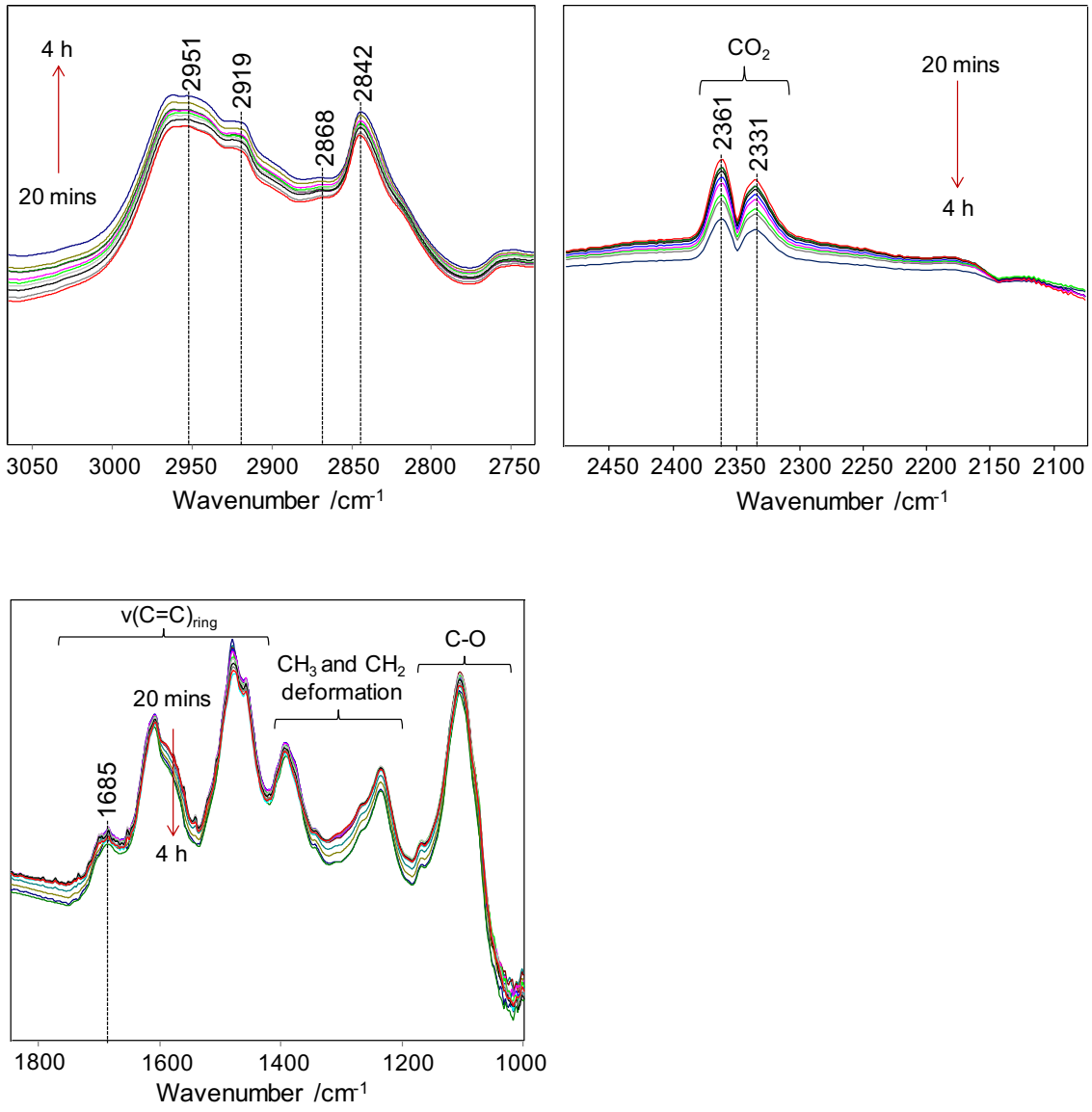

Figure B.7 Subtracted operando IR spectra during reaction of methane, oxygen and steam over 2 wt.% NiO/SiO_2 with a steam to carbon ratio of 1 and oxygen to carbon ratio of 0.2 at 723 K.

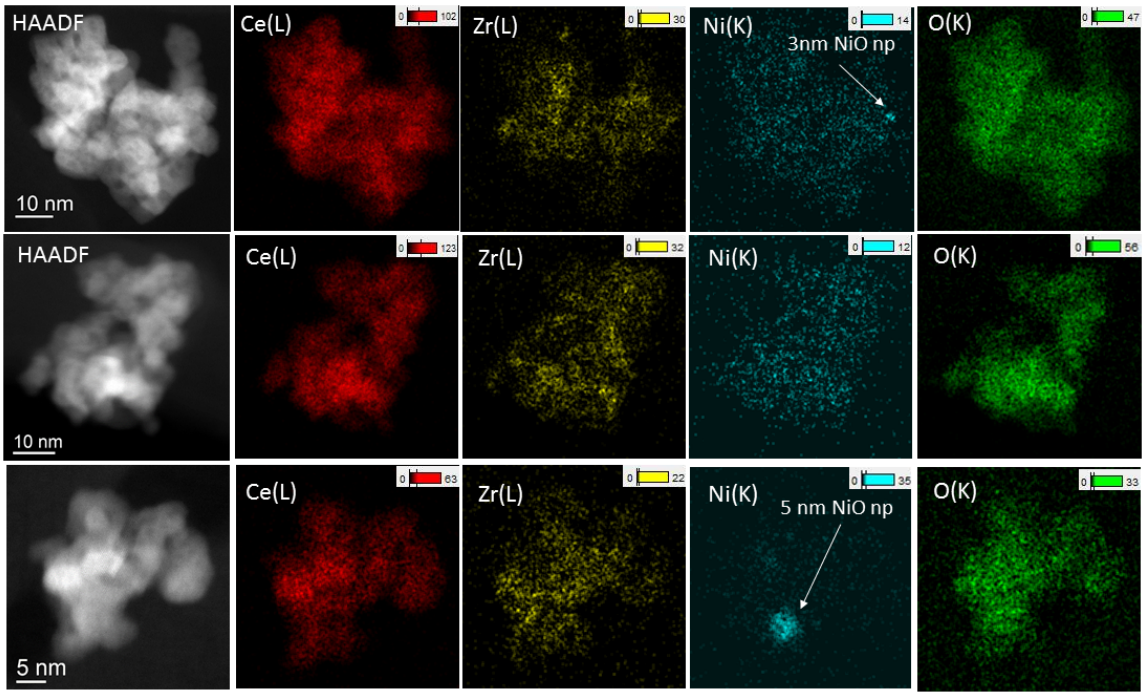

Figure B.8 Additional EDX maps of 2 wt.% NiO/CZ collected on JEOL ARM Centurion EDX detector.

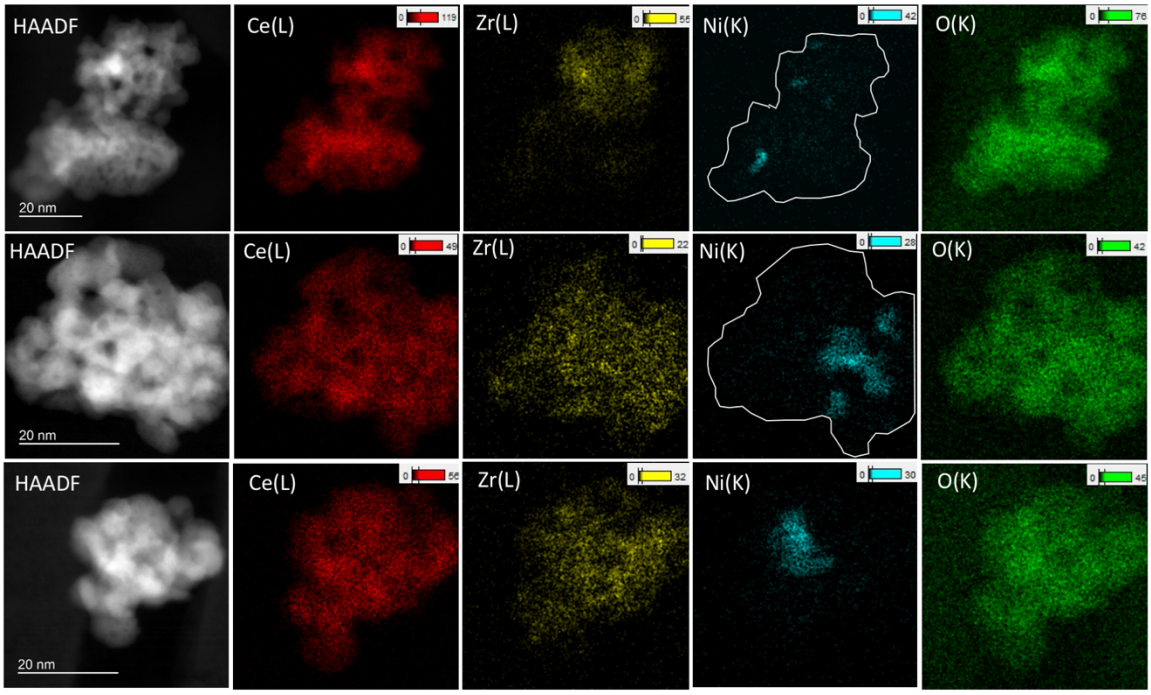

Figure B.9 Additional Maps of 5 wt.% NiO/CZ as acquired on JEOL ARM with Centurion EDX detector.

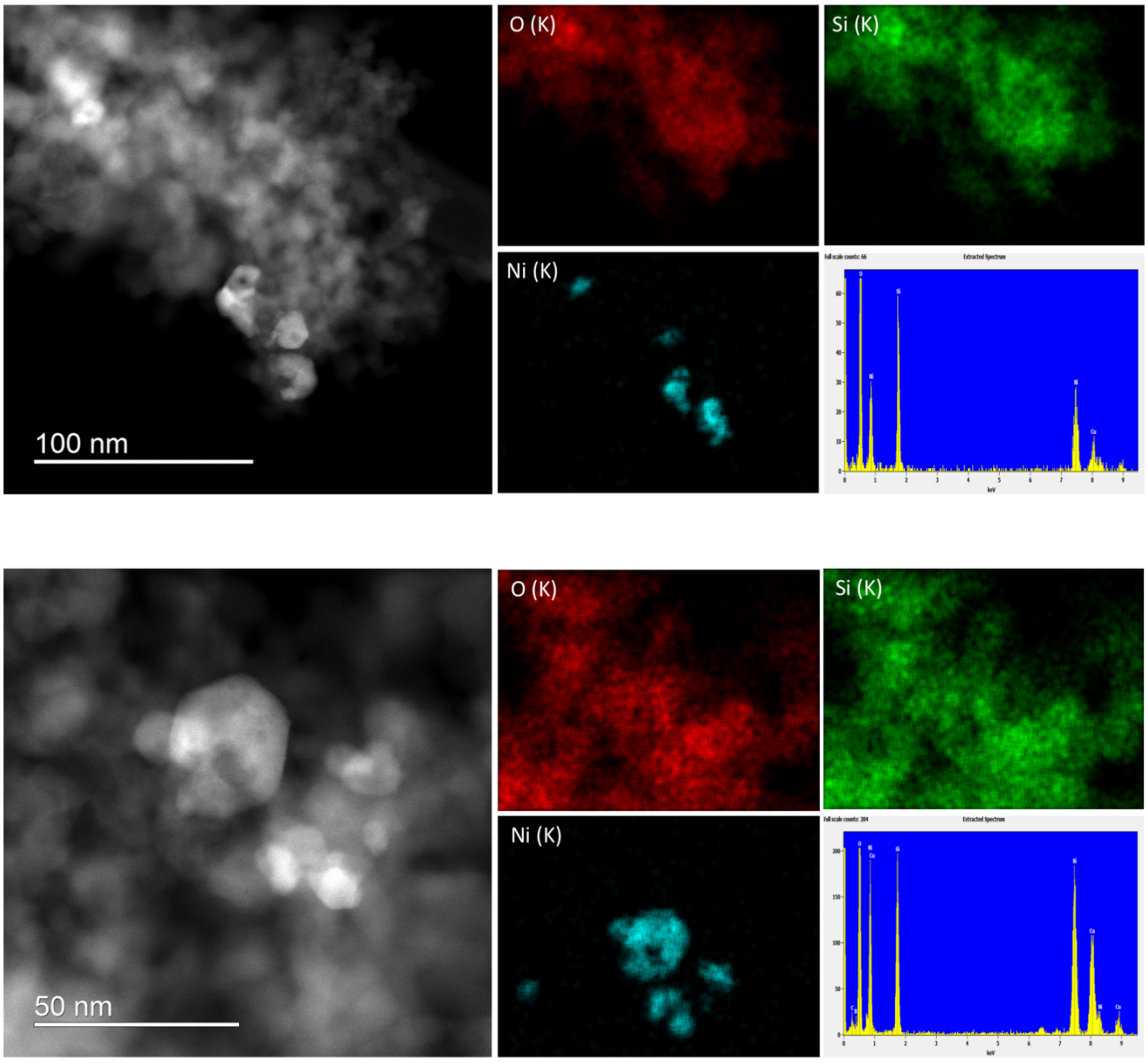

Figure B.10 Additional Maps of 2 wt.% NiO/SiO_2 as acquired on JEOL ARM with Centurion EDX detector.

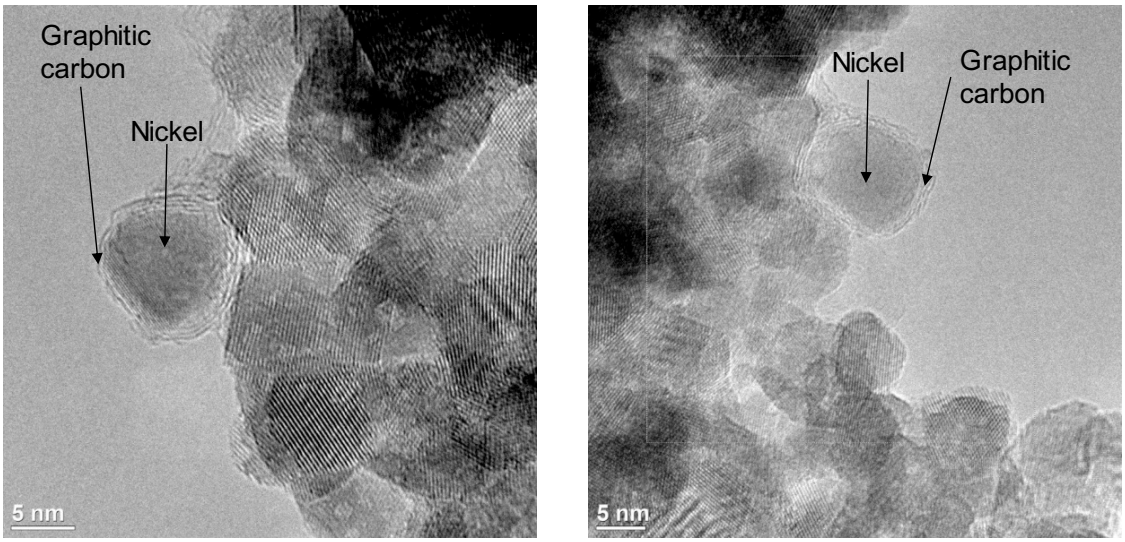

Figure B.11 TEM of 2 wt.% NiO/CZ after reaction with methane, steam and O_2 at 723 K for 8 h with a steam to carbon ratio of 1 and oxygen to carbon ratio of 0.2. Shells and pockets of graphitic carbon were seen covering NiO particles around 5+ nm. CZ matrix where big NiO particles were not seen, were nominally free of carbon.

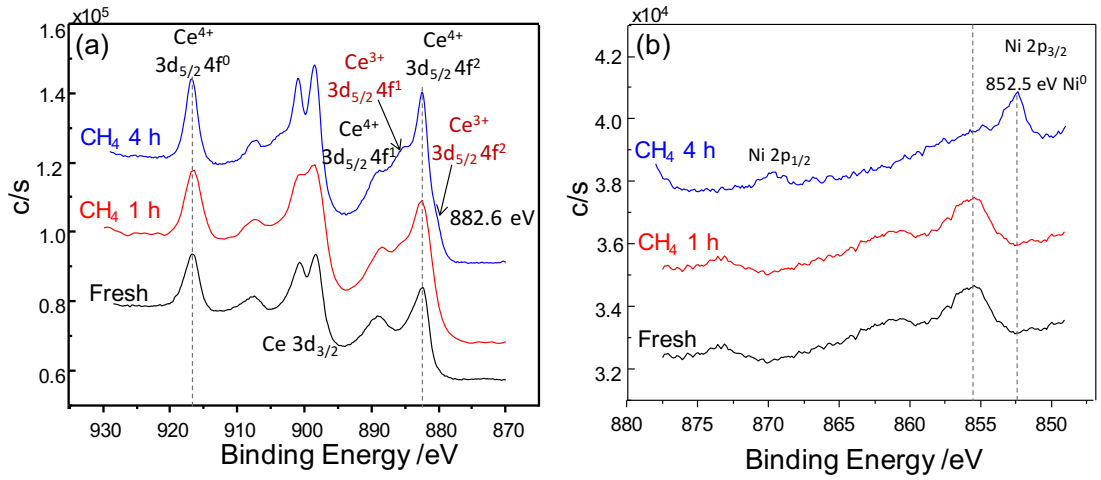

Figure B.12 XPS after in-situ treatment of 2 wt.% NiO/CZ with methane at 723K (a) Ce 3d (b) Ni 2p.

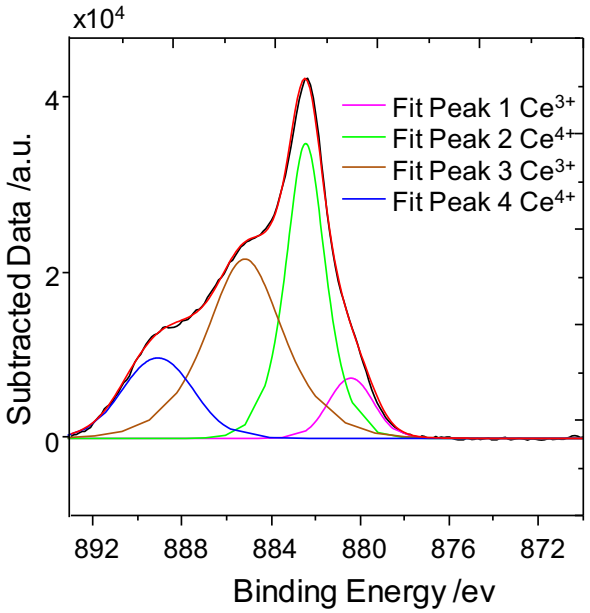

Figure B.13 Deconvolution of $3d_{5/2}$ peaks of Ce after exposure of 2 wt.% NiO/CZ to CH_4 for 4 h at 723 K.

In order to quantify the amount of surface reduction of ceria on 2 wt.% NiO/CZ after exposure to methane for 4 h at 723 K, the fraction of Ce^{3+} formed was measured as follows:

$Ce^{3+} = A_1 + A_3$

$Ce^{4+} = A_2 + A_4$

$[Ce^{3+}] = \frac{Ce^{3+}}{Ce^{3+} + Ce^{4+}}$

Where A_i is the area of the fit peak.

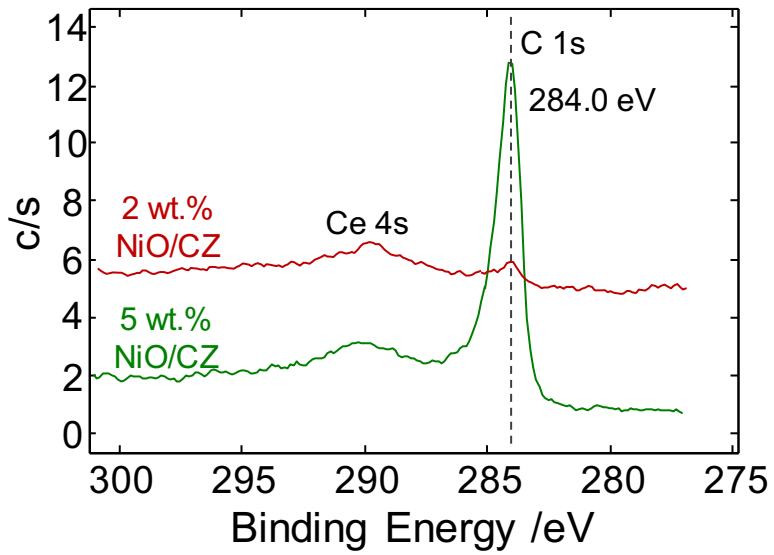

Figure B.14 C 1s XPS after in-situ treatment of 2 wt.% NiO/CZ and 5 wt.% NiO/CZ with methane at 723K for 4h. Peak at 284 eV is assigned to graphtic carbon. Significantly more graphtic carbon is deposited on 5 wt.% NiO/CZ with bigger clusters of NiO particles.

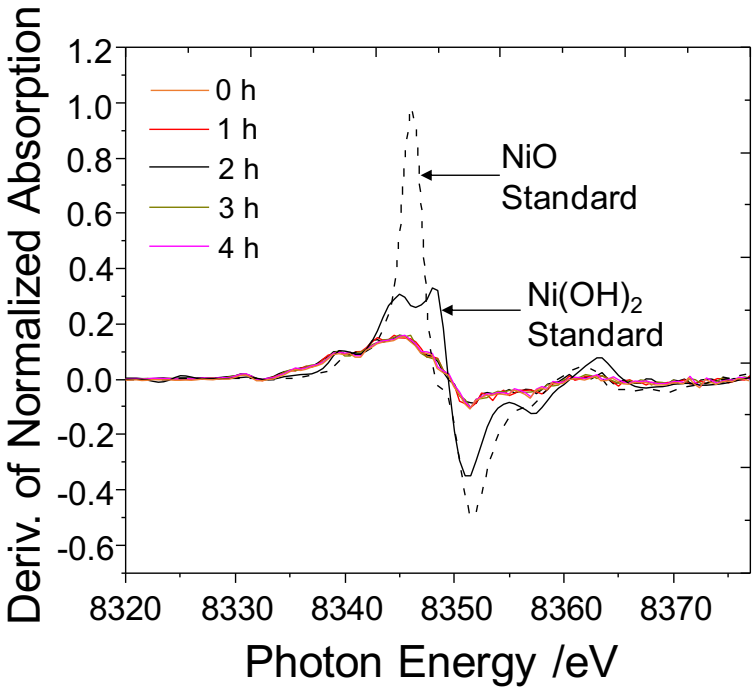

Figure B.15 In-situ XANES derivative spectra: Ni K-edge during exposure to H_2O at 723 K.

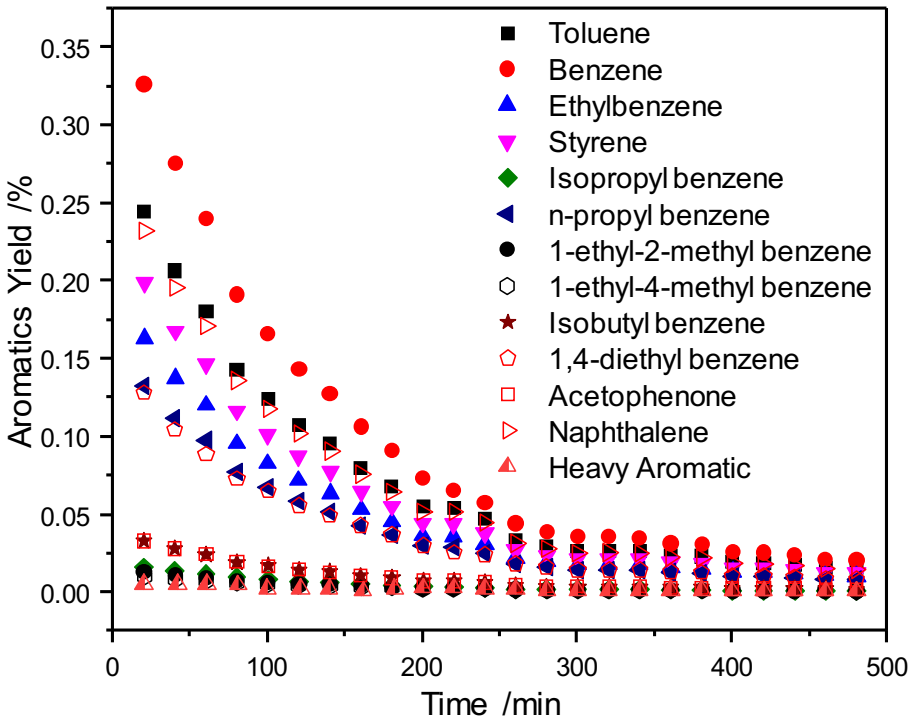

Figure B.16 Yields of aromatic products formed during reactions of methane, steam and oxygen in a packed bed reactor setup at 723 K and 1 atm over 2 wt.% NiO/CZ with a steam to carbon ratio of 1 and oygen to carbon ratio of 0.2.

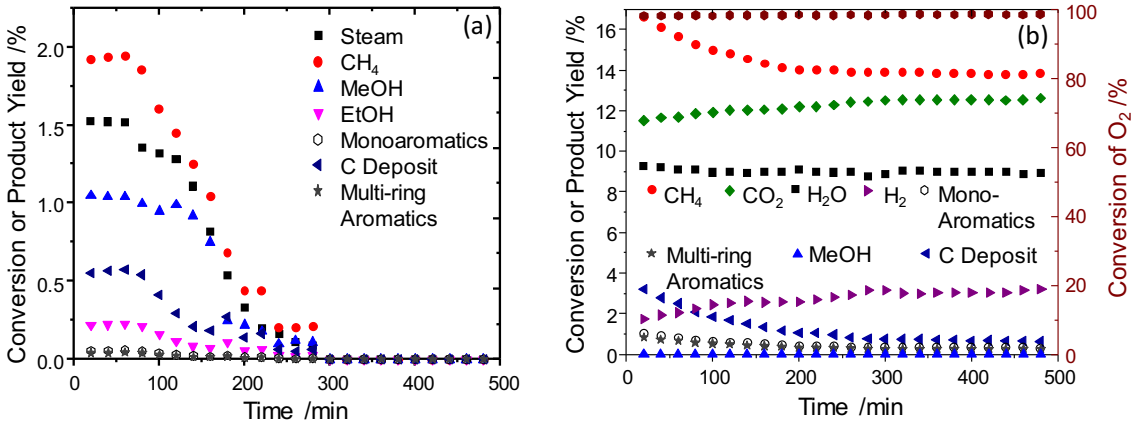

Figure B.17 Conversion of methane and yields of products formed during reaction in a packed bed reactor setup at 723 K and 1 atm over 2 wt.% NiO/CZ (a) in the absence of O_2 (b) in the absence of steam.

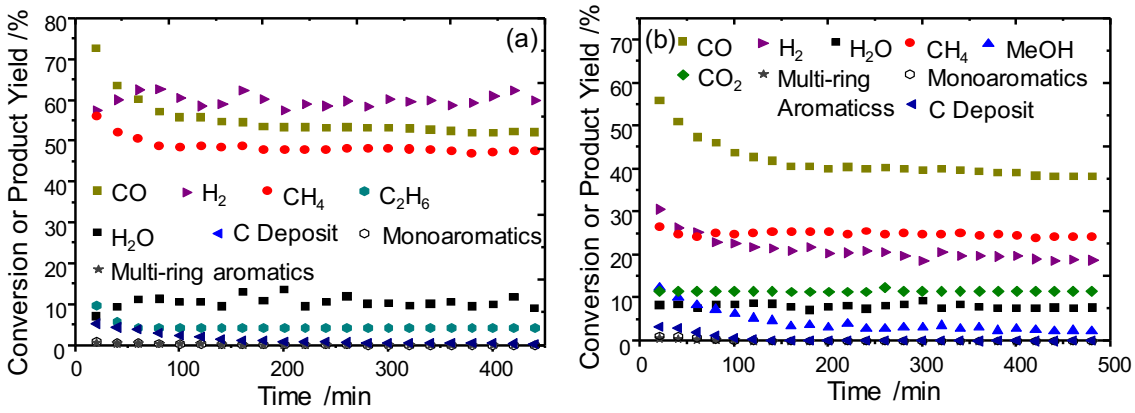

Figure B.18 Conversion of syngas and yields of products formed during reaction in a packed bed reactor at 723 K and 1 atm over 2 wt.% NiO/CZ (a) without steam (b) with steam to CO ratio of 1.

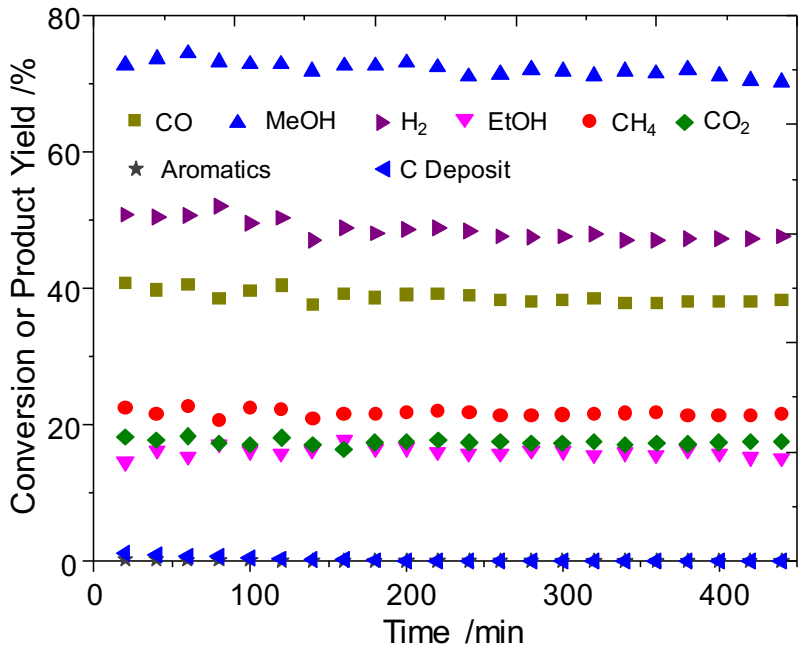

Figure B.19 Conversion of methanol and syngas and yields of products formed during reaction in a packed bed reactor at 723 K and 1 atm over 2 wt.% NiO/CZ.

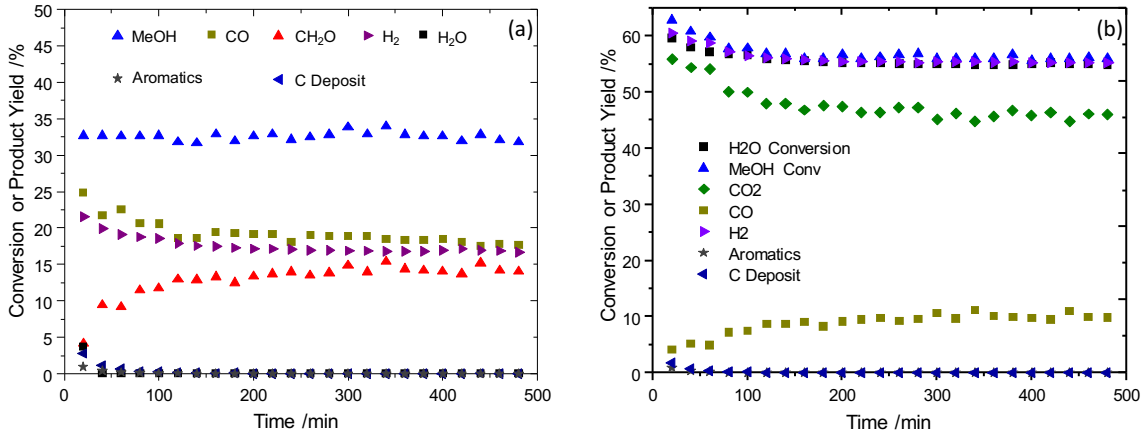

Figure B.20 Conversion of (a) methanol and yields of products formed during reaction in a packed bed reactor at 723 K and 1 atm over 2 wt.% NiO/CZ (b) methanol and steam with steam to carbon ratio of 1.

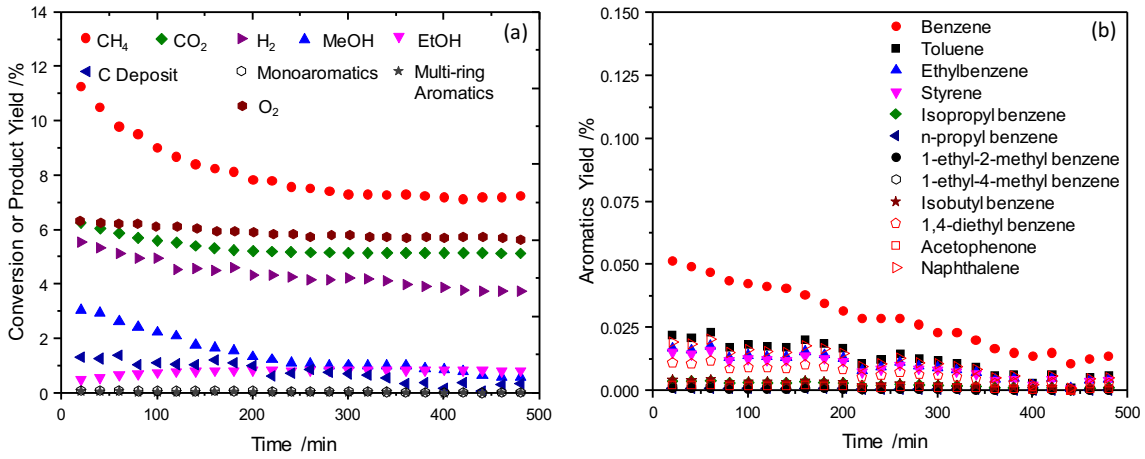

Figure B.21 (a) Conversion of methane and yields of products formed during reaction in a packed bed reactor setup at 573 K and 1 atm over 2 wt.% NiO/CZ with a molar O_2:CH_4 ratio of 0.2 and H_2O:CH_4 ratio of 1.0 (b) yields of aromatic products.

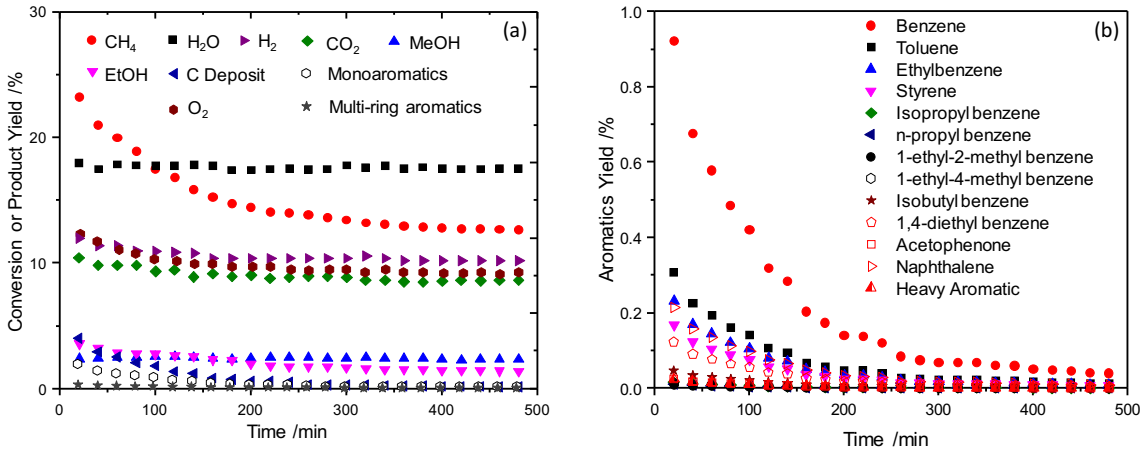

Figure B.22 (a) Conversion of methane and yields of products formed during reaction in a packed bed reactor setup at 723 K and 1 atm over 5 wt.% NiO/CZ with a molar O_2:CH_4 ratio of 0.2 and H_2O:CH_4 ratio of 1.0 (b) Yields of mono and multi-ring aromatics.

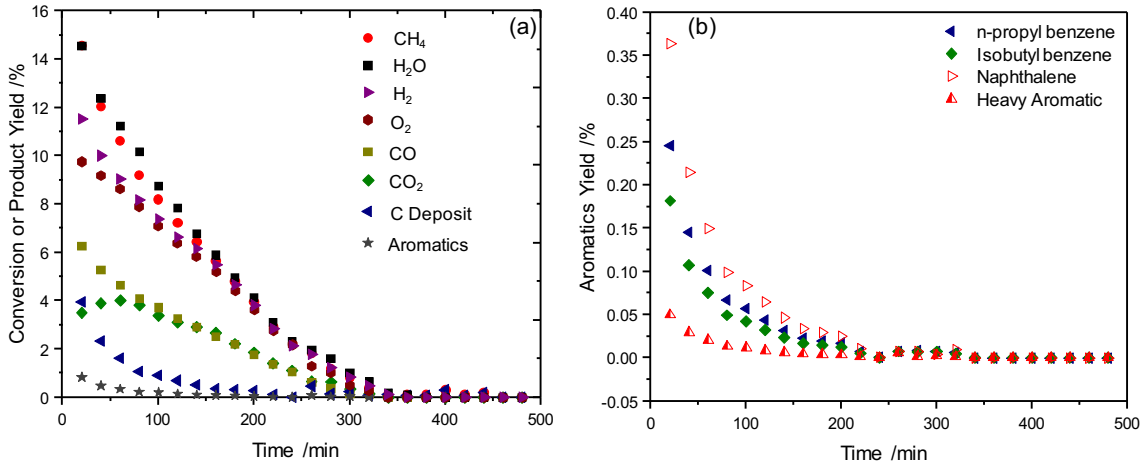

Figure B.23 (a) Conversion of methane and yields of products formed during reaction in a packed bed reactor setup at 723 K and 1 atm over 2 wt.% NiO/SiO_2 with a molar O_2:CH_4 ratio of 0.2 and H_2O:CH_4 ratio of 1.0 (b) yields of aromatic products.

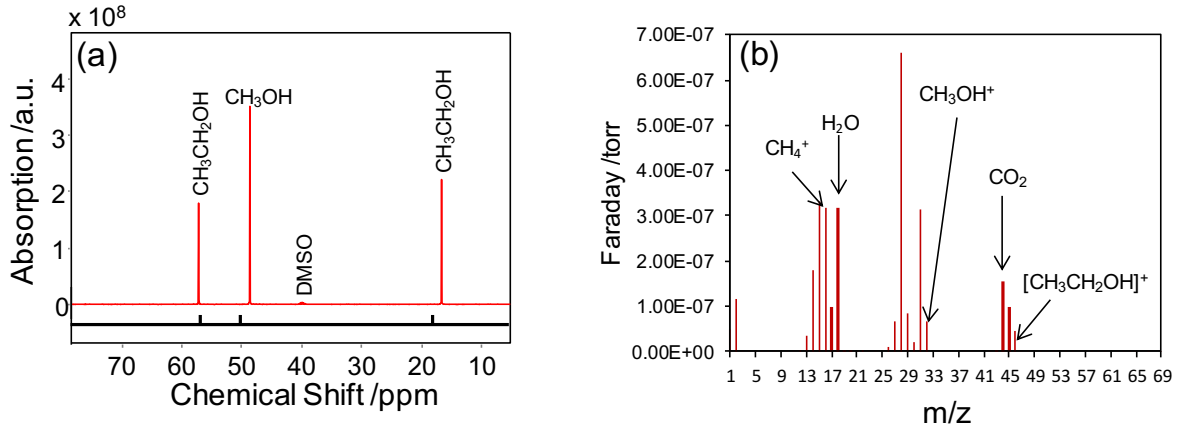

Figure B.24 Analysis of effluent stream of the packed bed reactor to verify the formation of products (a) ^{13}C NMR spectrum of liquid condensate (b) mass spectrum of effluent stream.

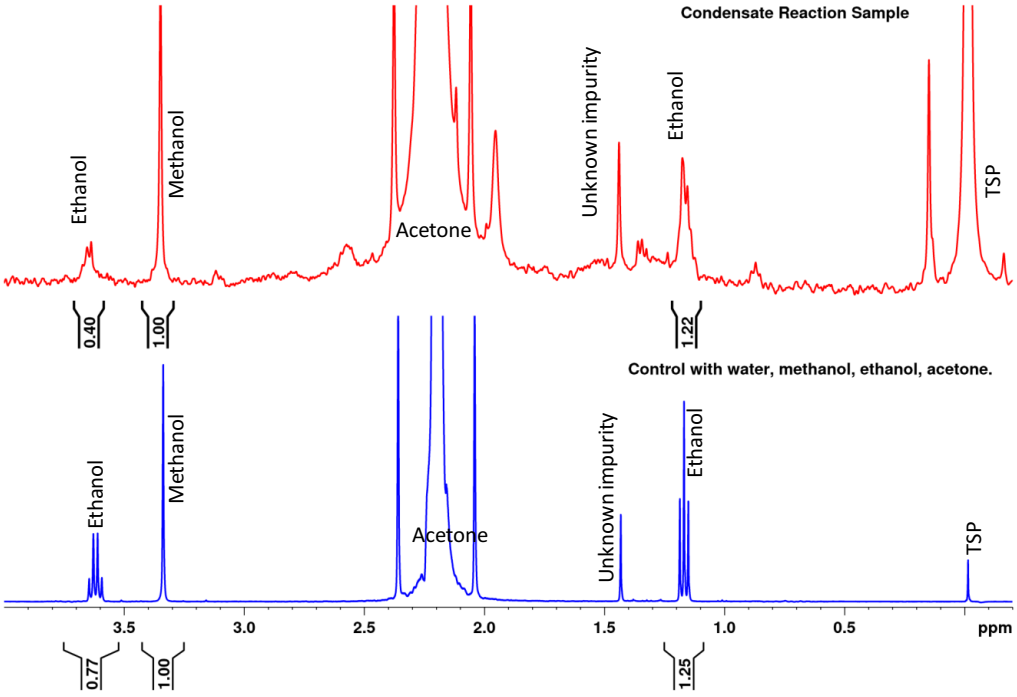

Figure B.25 ^{1}H NMR of liquid condensate from reaction run at National Renewable National Lab for methane conversion in the presence of steam and oxygen at 723 K over 2 wt.% NiO/CZ. Red – NMR of liquid condensate from reaction run, Blue – Control with water, methanol, ethanol and acetone.

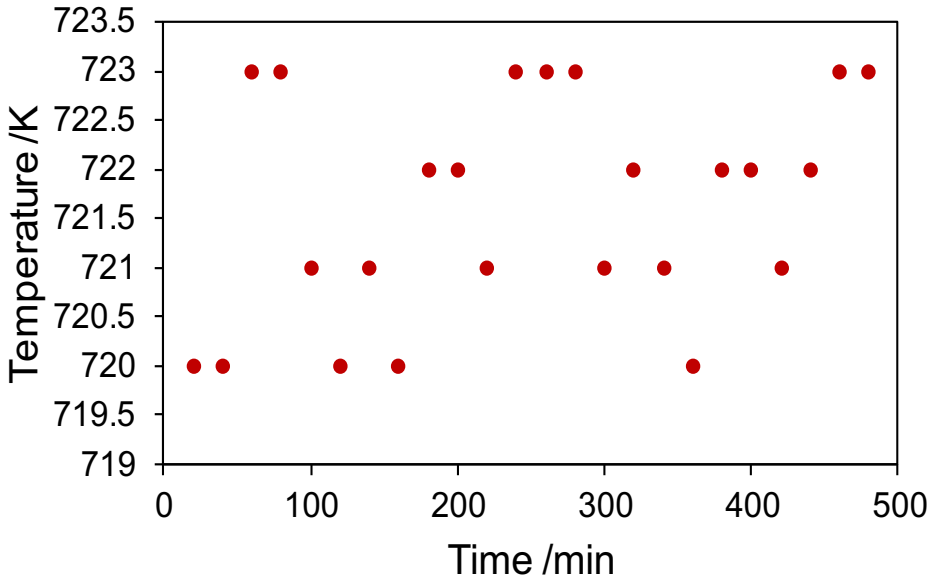

Figure B.26 Temperature inside the reactor during full reaction run as seen in Figure 4 over NiO/CZ.

APPENDIX C

Supplementary Information for Chapter 4

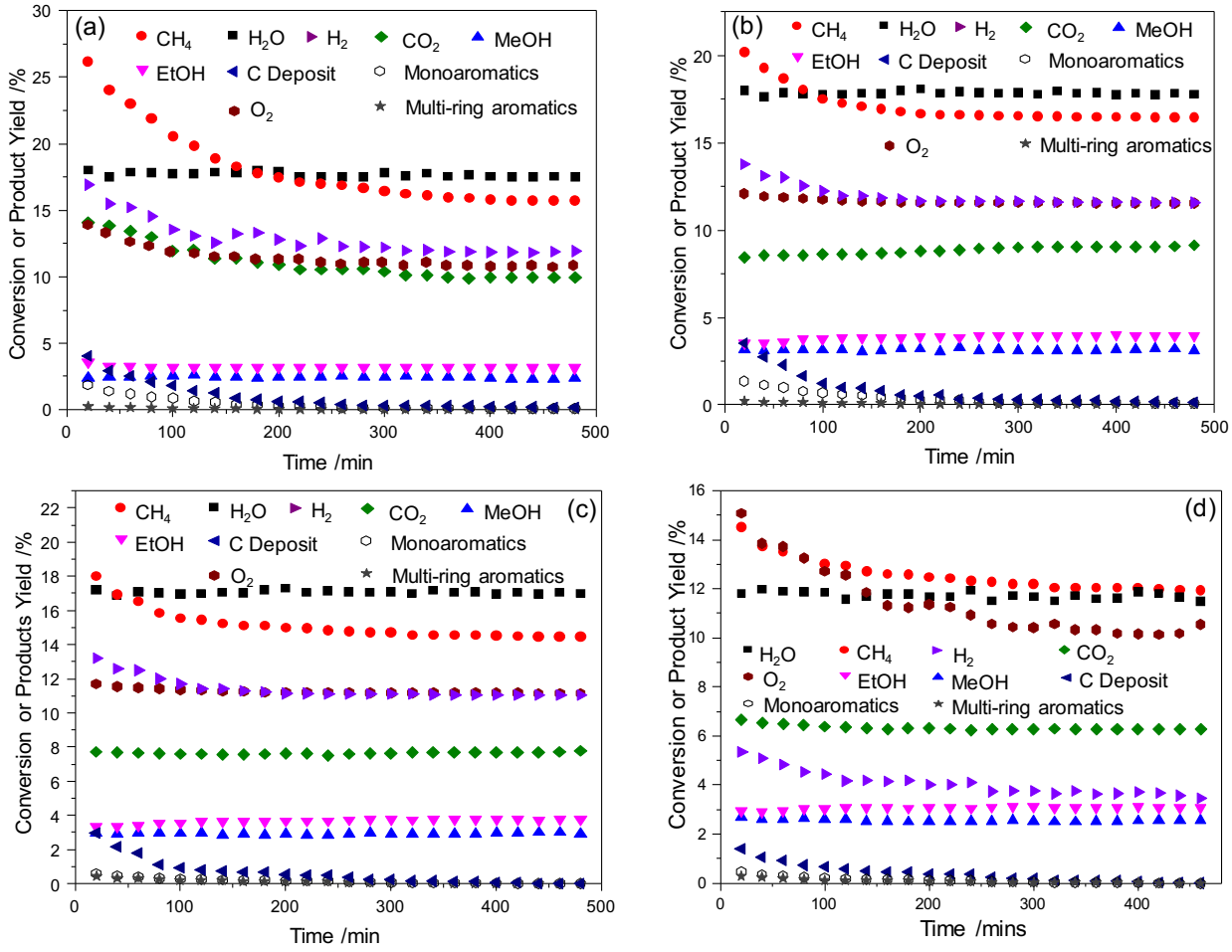

Figure C.1 Conversion of methane and O2 and yields of products formed during reactions of methane, steam, and oxygen in a packed bed reactor setup at 450 ˚C and 1 atm over (a) 10NiO/CZ_CP (b) 6NiO/CZ_CP (c) 4NiO/CZ_CP (d) 2NiO/CZ_CP

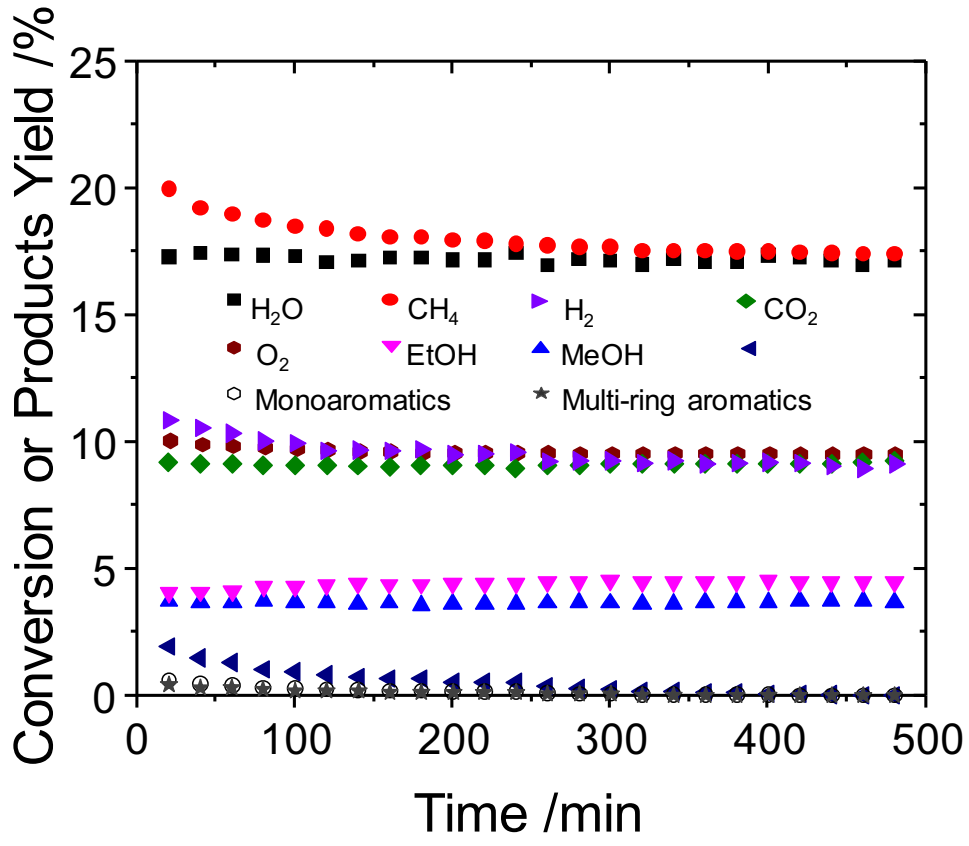

Figure C.2 Conversion of methane and O2 and yields of products formed during reactions of methane, steam, and oxygen in a packed bed reactor setup at 450 ˚C and 1 atm over 2NiO/CZ_SEA

APPENDIX D

Supplementary Information for Chapter 5

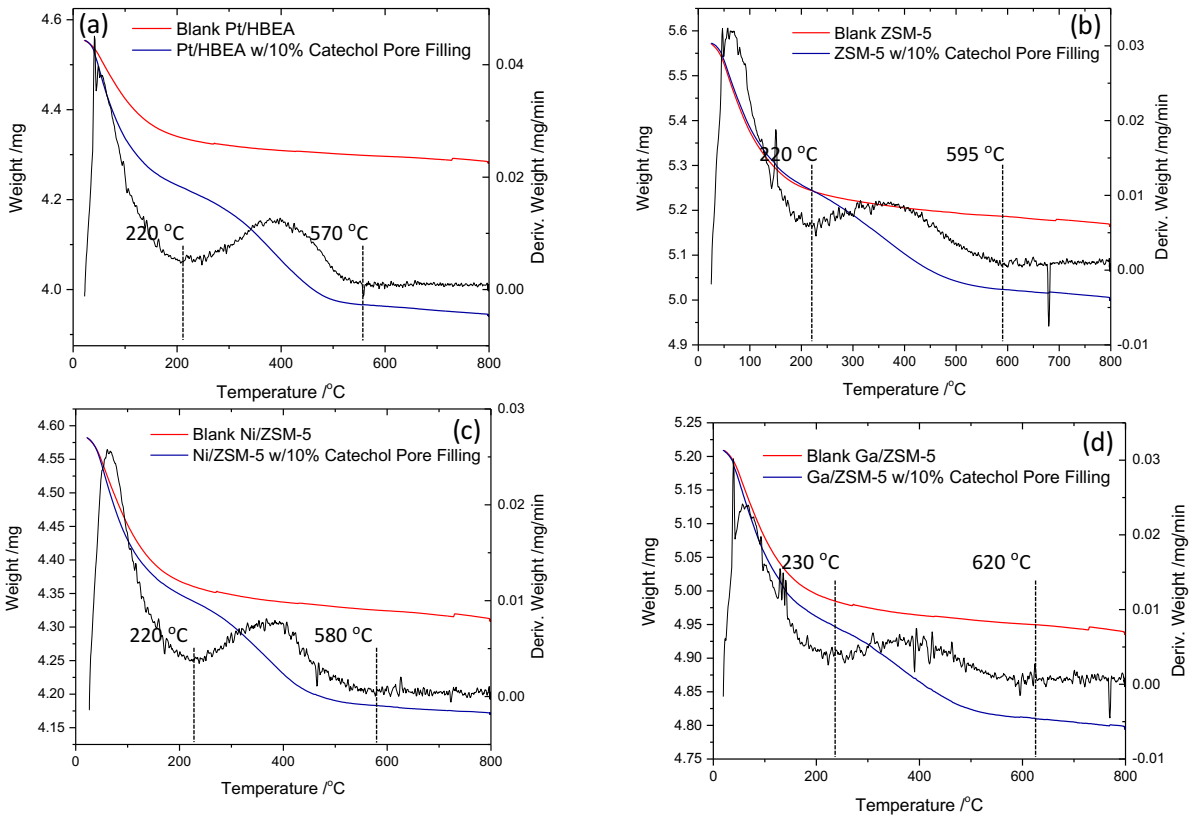

Figure D.1 TGA of blank and roadblocked catalysts in air (a) Pt/HBEA (b) ZSM-5 (c) Ni/ZSM-5 (d) Ga/ZSM-5

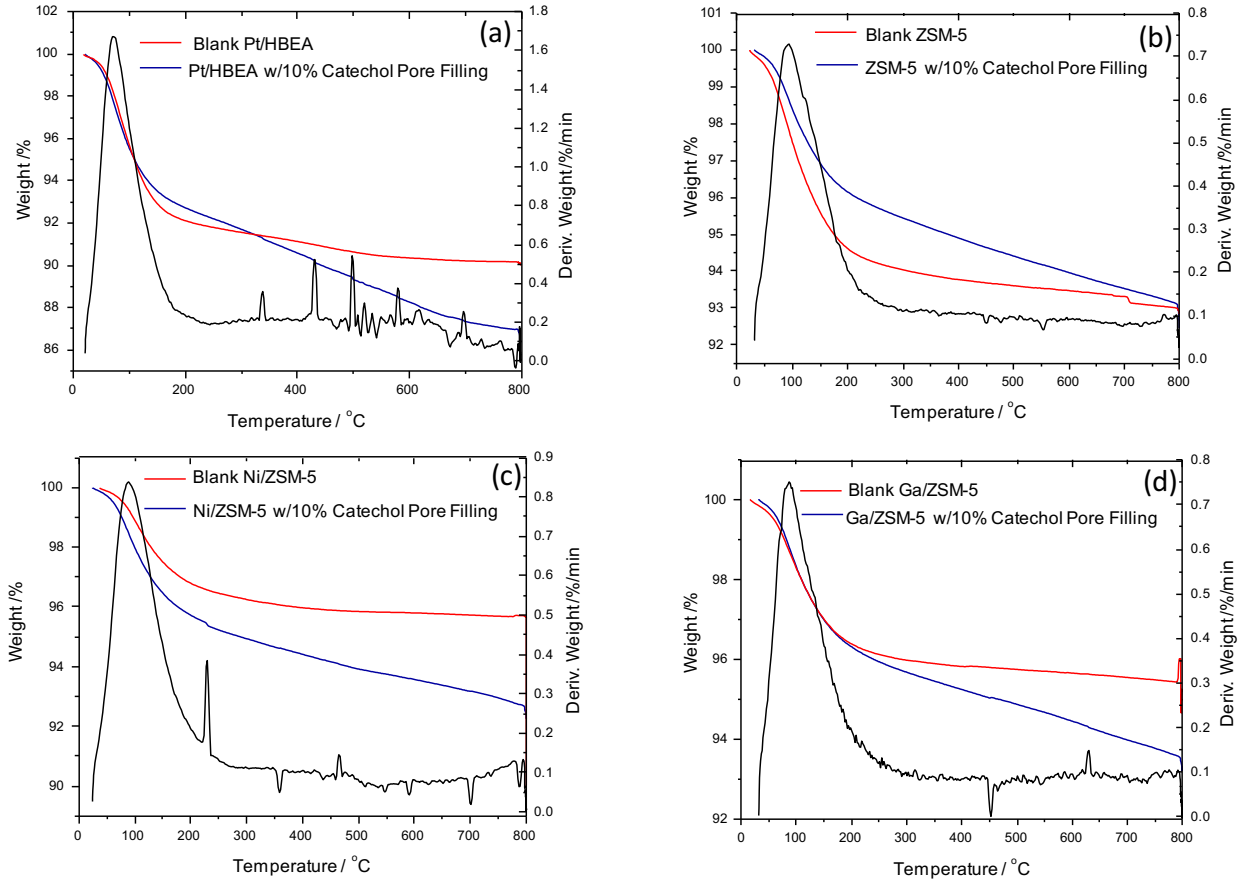

Figure D.2 TGA of blank and roadblocked catalysts in nitrogen (a) Pt/HBEA (b) ZSM-5 (c) Ni/ZSM-5 (d) Ga/ZSM-5

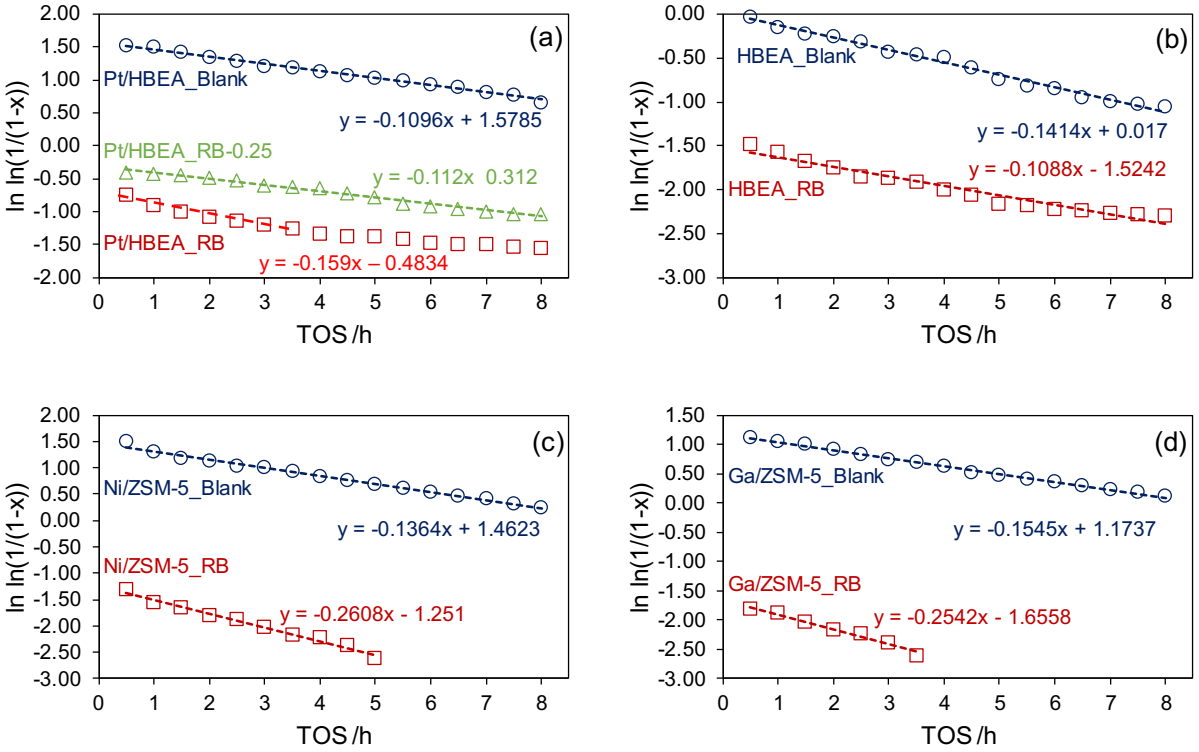

Figure D.3 First order deactivation profile of catalysts during HDO of anisole (a) Pt/HBEA (b) HBEA (c) Ni/ZSM-5 (d) Ga/ZSM-5

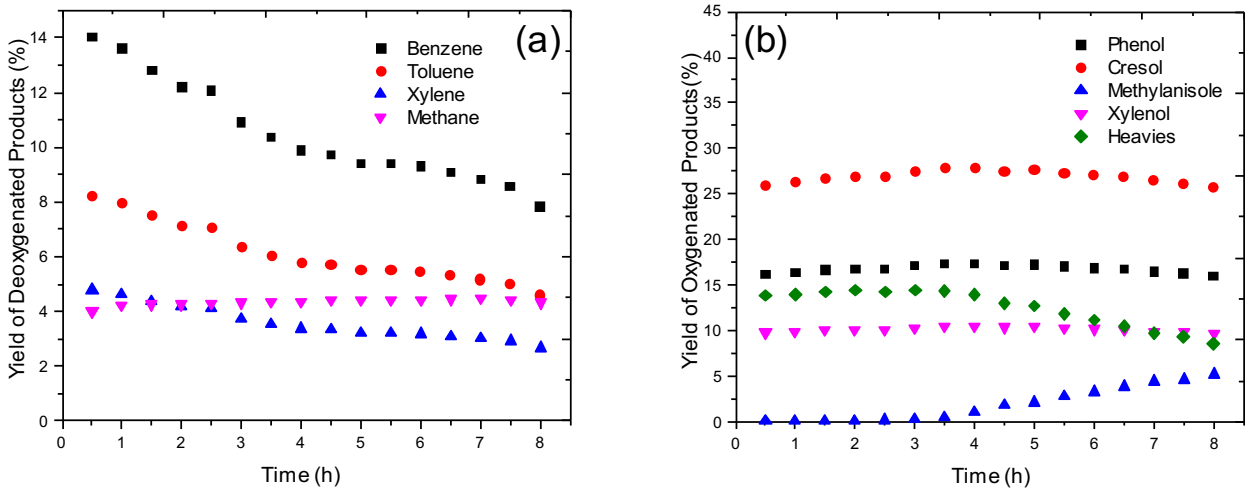

Figure D.4 Yields of products during HDO of anisole over Pt/HBEA_Blank (a) deoxygenated products (b) oxygenated products

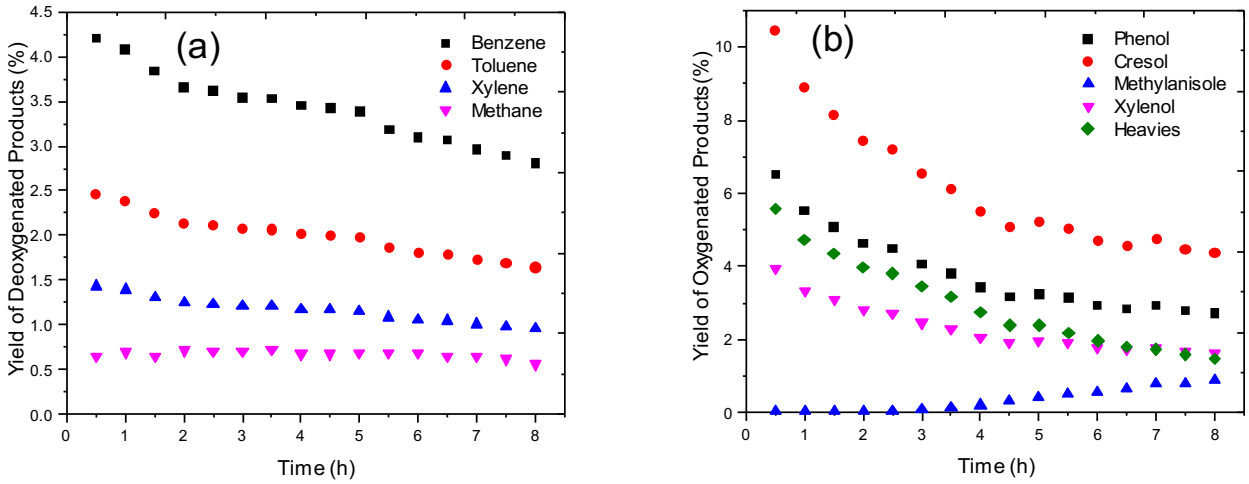

Figure D.5 Yields of products during HDO of anisole over Pt/HBEA_RB (a) deoxygenated products (b) oxygenated products

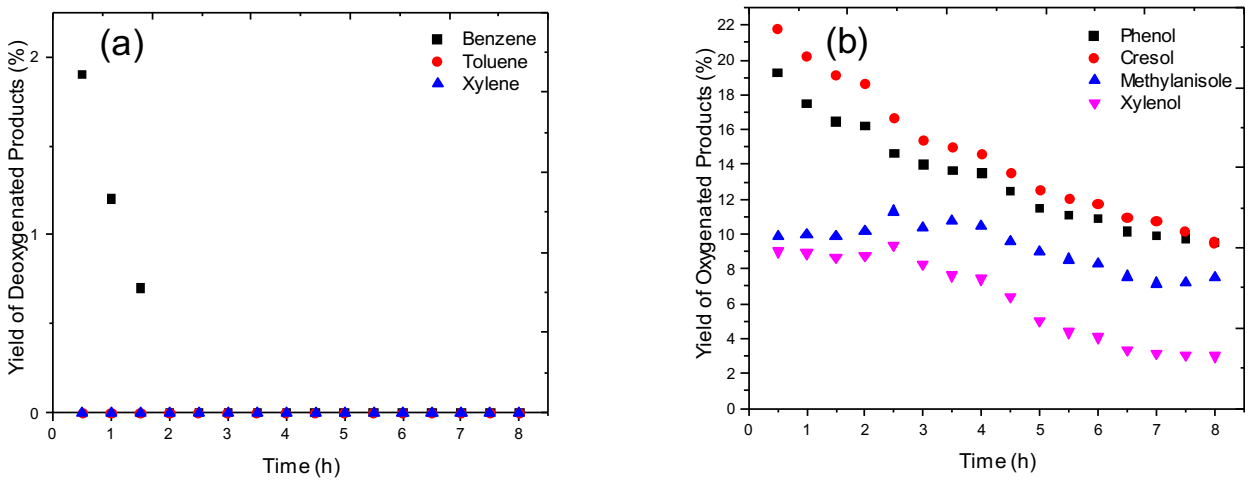

Figure D.6 Yields of products during HDO of anisole over HBEA_Blank (a) deoxygenated products (b) oxygenated products

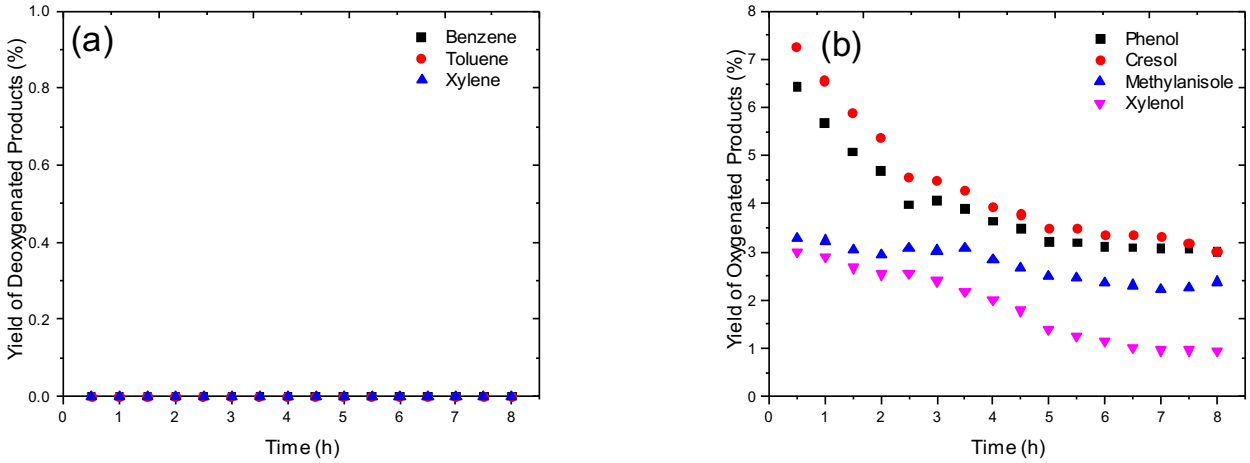

Figure D.7 Yields of products during HDO of anisole over HBEA_RB (a) deoxygenated products (b) oxygenated products

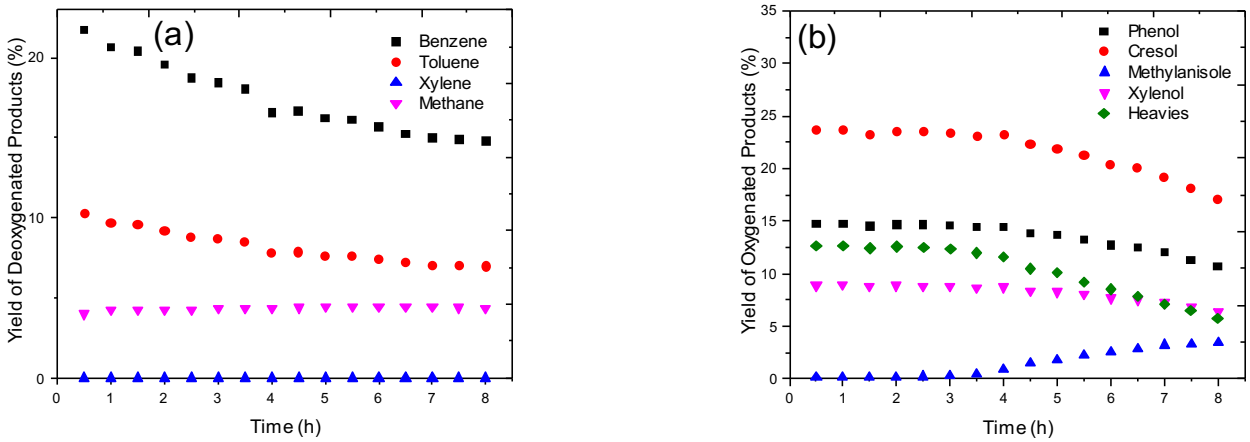

Figure D.8 Yields of products during HDO of anisole over Ni/ZSM-5_Blank (a) deoxygenated products (b) oxygenated products

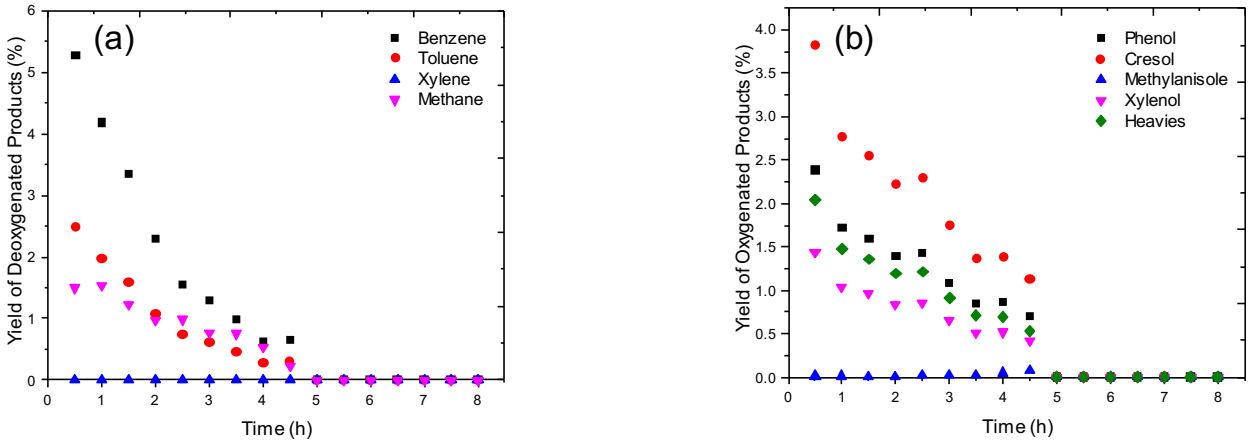

Figure D.9 Yields of products during HDO of anisole over Ni/ZSM-5_RB (a) deoxygenated products (b) oxygenated products

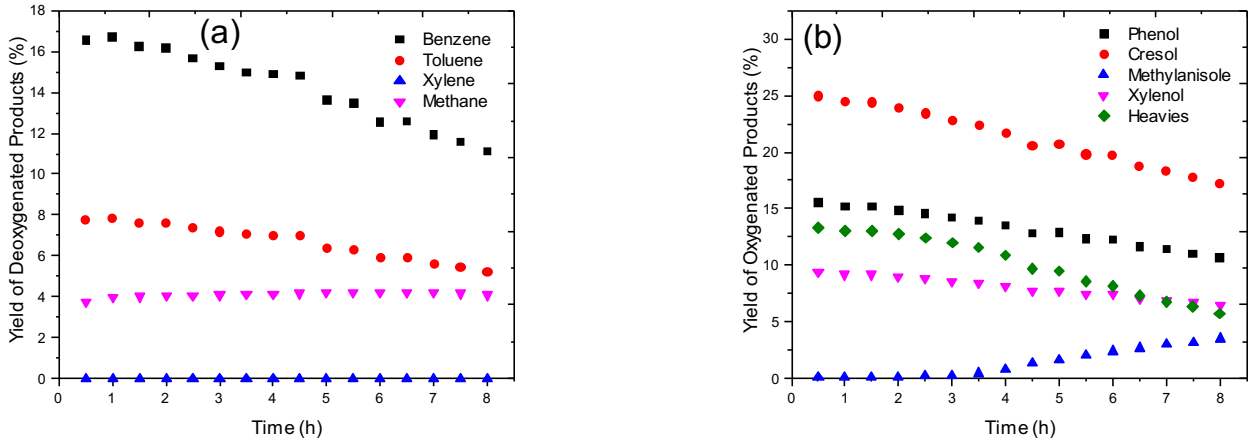

Figure D.10 Yields of products during HDO of anisole over Ga/ZSM-5_Blank (a) deoxygenated products (b) oxygenated products

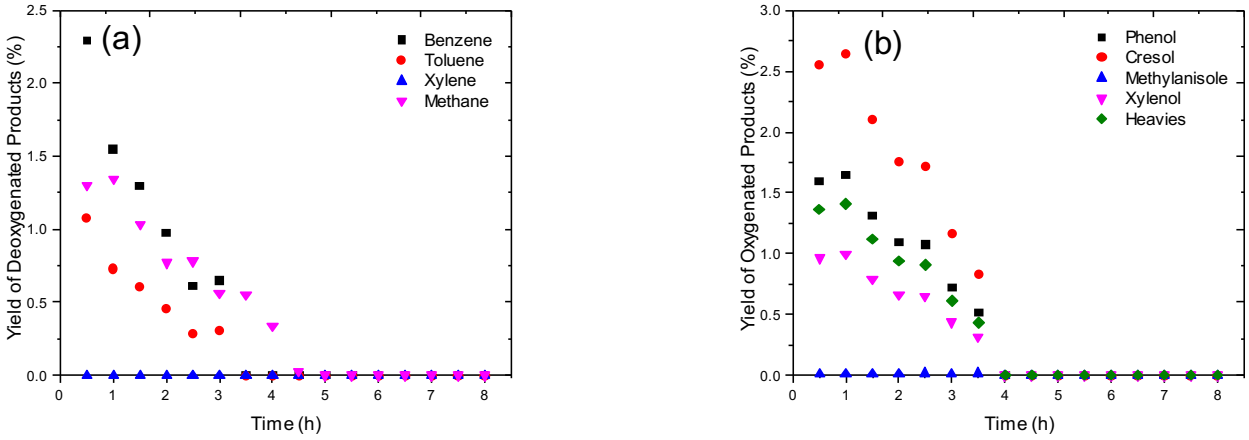

Figure D.11 Yields of products during HDO of anisole over Ga/ZSM-5_RB (a) deoxygenated products (b) oxygenated products

REFERENCES

1. Liu, B. S.; Tian, L.; Li, L.; Au, C. T.; Cheung, A. S. C., Performance of 3%Mo/ZSM-5 Catalyst in the Presence of Water During Methane Aromatization in Supersonic Jet Expansion. *Aiche J* **2011,** *57* (7), 1852-1859.

2. Fan, M. S.; Abdullah, A. Z.; Bhatia, S., Catalytic Technology for Carbon Dioxide Reforming of Methane to Synthesis Gas. *Chemcatchem* **2009,** *1* (2), 192-208.

3. Hickman, D. A.; Schmidt, L. D., Production of Syngas by Direct Catalytic-Oxidation of Methane. *Science* **1993,** *259* (5093), 343-346.

4. Liu, D. P.; Lau, R.; Borgna, A.; Yang, Y. H., Carbon dioxide reforming of methane to synthesis gas over Ni-MCM-41 catalysts. *Appl Catal a-Gen* **2009,** *358* (2), 110-118.

5. Sadykov, V.; Rogov, V.; Ermakov, E.; Arendarsky, D.; Mezentseva, N.; Alikina, G.; Sazonova, N.; Bobin, A.; Pavlova, S.; Schuurman, Y.; Mirodatos, C., Mechanism of CH4 dry reforming by pulse microcalorimetry: Metal nanoparticles on perovskite/fluorite supports with high oxygen mobility. *Thermochim Acta* **2013,** *567*, 27-34.

6. Machocki, A.; Jezior, R., Oxidative coupling of methane over a sodium-calcium oxide catalyst modified with chloride ions. *Chem Eng J* **2008,** *137* (3), 643-652.

7. Yaghobi, N.; Ghoreishy, M. H. R., Oxidative coupling of methane in a fixed bed reactor over perovskite catalyst: A simulation study using experimental kinetic model. *Journal of Natural Gas Chemistry* **2008,** *17* (1), 8-16.

8. Lunsford, J. H., The Catalytic Oxidative Coupling of Methane. *Angewandte Chemie-International Edition in English* **1995,** *34* (9), 970-980.

9. Hammond, C.; Conrad, S.; Hermans, I., Oxidative Methane Upgrading. *Chemsuschem* **2012,** *5* (9), 1668-1686.

10. Guo, X. G.; Fang, G. Z.; Li, G.; Ma, H.; Fan, H. J.; Yu, L.; Ma, C.; Wu, X.; Deng, D. H.; Wei, M. M.; Tan, D. L.; Si, R.; Zhang, S.; Li, J. Q.; Sun, L. T.; Tang, Z. C.; Pan, X. L.; Bao, X. H., Direct, Nonoxidative Conversion of Methane to Ethylene, Aromatics, and Hydrogen. *Science* **2014,** *344* (6184), 616-619.

11. Soulivong, D.; Norsic, S.; Taoufik, M.; Coperet, C.; Thivolle-Cazat, J.; Chakka, S.; Basset, J. M., Non-oxidative coupling reaction of methane to ethane and hydrogen catalyzed by the silica-supported tantalum hydride: (SiO)(2)Ta-H. *J Am Chem Soc* **2008,** *130* (15), 5044-+.

12. Szeto, K. C.; Norsic, S.; Hardou, L.; Le Roux, E.; Chakka, S.; Thivolle-Cazat, J.; Baudouin, A.; Papaioannou, C.; Basset, J. M.; Taoufik, M., Non-oxidative coupling of methane catalysed by supported tungsten hydride onto alumina and silica-alumina in classical and H-2 permeable membrane fixed-bed reactors. *Chem. Commun.* **2010,** *46* (22), 3985-3987.

13. Xu, Y. D.; Bao, X. H.; Lin, L. W., Direct conversion of methane under nonoxidative conditions. *J Catal* **2003,** *216* (1-2), 386-395.

14. Balasubramanian, R.; Smith, S. M.; Rawat, S.; Yatsunyk, L. A.; Stemmler, T. L.; Rosenzweig, A. C., Oxidation of methane by a biological dicopper centre. *Nature* **2010,** *465* (7294), 115-U131.

15. Hammond, C.; Forde, M. M.; Ab Rahim, M. H.; Thetford, A.; He, Q.; Jenkins, R. L.; Dimitratos, N.; Lopez-Sanchez, J. A.; Dummer, N. F.; Murphy, D. M.; Carley, A. F.; Taylor, S. H.; Willock, D. J.; Stangland, E. E.; Kang, J.; Hagen, H.; Kiely, C. J.; Hutchings, G. J., Direct Catalytic Conversion of Methane to Methanol in an Aqueous Medium by using Copper-Promoted Fe-ZSM-5. *Angew Chem Int Edit* **2012,** *51* (21), 5129-5133.

16. M. Shuqi, G. X., Z. Lingxiao, S. Susannah, B. Xinhe, Recent progress in methane dehydroaromatization: From laboratory curiosities to promsing technology. *J Energy Chem* **2013,** *22* (1), 1-20.

17. Girio, F. M.; Fonseca, C.; Carvalheiro, F.; Duarte, L. C.; Marques, S.; Bogel-Lukasik, R., Hemicelluloses for fuel ethanol: A review. *Bioresource Technol* **2010,** *101* (13), 4775-4800.

18. Gnansounou, E.; Dauriat, A., Ethanol fuel from biomass: A review. *J Sci Ind Res India* **2005,** *64* (11), 809-821.

19. Srivastava, N.; Rawat, R.; Oberoi, H. S.; Ramteke, P. W., A Review on Fuel Ethanol Production From Lignocellulosic Biomass. *Int J Green Energy* **2015,** *12* (9), 949-960.

20. Liu, C. J.; Ye, J. Y.; Jiang, J. J.; Pan, Y. X., Progresses in the Preparation of Coke Resistant Ni-based Catalyst for Steam and CO2 Reforming of Methane. *Chemcatchem* **2011,** *3* (3), 529-541.

21. Wood, B. J.; Sancier, K. M., The Mechanism of the Catalytic Gasification of Coal Char - a Critical-Review. *Catal Rev* **1984,** *26* (2), 233-279.

22. Herman, R. G., Advances in catalytic synthesis and utilization of higher alcohols. *Catal Today* **2000,** *55* (3), 233-245.

23. Calverley, E. M.; Smith, K. J., Kinetic-Model for Alcohol Synthesis over a Promoted Cu/Zno/Cr2o3 Catalyst. *Ind Eng Chem Res* **1992,** *31* (3), 792-803.

24. Riva, A.; Trifiro, F.; Vaccari, A.; Busca, G.; Mintchev, L.; Sanfilippo, D.; Manzatti, W., The Promoting Role of Cr and K in Catalysts for High-Pressure and High-Temperature Methanol and Higher-Alcohol Synthesis. *J Chem Soc Farad T 1* **1987,** *83*, 2213-2225.

25. Tronconi, E.; Ferlazzo, N.; Forzatti, P.; Pasquon, I., Synthesis of Alcohols from Carbon Oxides and Hydrogen .4. Lumped Kinetics for the Higher Alcohol Synthesis over a Zn-Cr-K Oxide Catalyst. *Ind Eng Chem Res* **1987,** *26* (10), 2122-2129.

26. Beretta, A.; Sun, Q.; Herman, R. G.; Klier, K., Synthesis of 2-methylpropan-1-ol-methanol mixtures from H-2-CO synthesis gas over double-bed Cs/Cu/ZnO/Cr2O3 and Cs/ZnO/Cr2O3 catalysts. *J Chem Soc Chem Comm* **1995,** (24), 2525-2526.

27. Epling, W. S.; Hoflund, G. B.; Hart, W. M.; Minahan, D. M., Reaction and surface characterization study of higher alcohol synthesis catalysts .2. Cs-promoted commercial Zn/Cr spinel. *J Catal* **1997,** *172* (1), 13-23.

28. Smith, K. J.; Anderson, R. B., The Higher Alcohol Synthesis over Promoted Cu/Zno Catalysts. *Can J Chem Eng* **1983,** *61* (1), 40-45.

29. Smith, K. J.; Anderson, R. B., The Synthesis of Higher Alcohols on Cu/Zno Catalysts Promoted with K2co3. *Abstr Pap Am Chem S* **1984,** *188* (Aug), 68-Fuel.

30. Klier, K.; Herman, R. G.; Young, C. W., Direct Synthesis of 2-Methyl-1-Propanol. *Abstr Pap Am Chem S* **1984,** *188* (Aug), 69-Fuel.

31. Gong, J. L.; Yue, H. R.; Zhao, Y. J.; Zhao, S.; Zhao, L.; Lv, J.; Wang, S. P.; Ma, X. B., Synthesis of Ethanol via Syngas on Cu/SiO2 Catalysts with Balanced Cu-0-Cu+ Sites. *J Am Chem Soc* **2012,** *134* (34), 13922-13925.

32. Baik, M. H.; Newcomb, M.; Friesner, R. A.; Lippard, S. J., Mechanistic studies on the hydroxylation of methane by methane monooxygenase. *Chem Rev* **2003,** *103* (6), 2385-2419.

33. Raja, R.; Ratnasamy, P., Direct conversion of methane to methanol. *Appl Catal a-Gen* **1997,** *158* (1-2), L7-L15.

34. Kudrik, E. V.; Afanasiev, P.; Bouchu, D.; Millet, J. M. M.; Sorokin, A. B., Diiron N-bridged species bearing phthalocyanine ligand catalyzes oxidation of methane, propane and benzene under mild conditions. *J Porphyr Phthalocya* **2008,** *12* (10), 1078-1089.

35. Sorokin, A. B.; Kudrik, E. V.; Bouchu, D., Bio-inspired oxidation of methane in water catalyzed by N-bridged diiron phthalocyanine complex. *Chem. Commun.* **2008,** (22), 2562-2564.

36. Coperet, C., C-H Bond Activation and Organometallic Intermediates on Isolated Metal Centers on Oxide Surfaces. *Chem Rev* **2010,** *110* (2), 656-680.

37. Joubert, J.; Salameh, A.; Krakoviack, V.; Delbecq, F.; Sautet, P.; Coperet, C.; Basset, J. M., Heterolytic splitting of H-2 and CH4 on gamma-alumina as a structural probe for defect sites. *J Phys Chem B* **2006,** *110* (47), 23944-23950.

38. Montini, T.; Melchionna, M.; Monai, M.; Fornasiero, P., Fundamentals and Catalytic Applications of CeO2-Based Materials. *Chem Rev* **2016,** *116* (10), 5987-6041.

39. Descorme, C.; Madier, Y.; Duprez, D., Infrared study of oxygen adsorption and activation on cerium-zirconium mixed oxides. *J Catal* **2000,** *196* (1), 167-173.

40. Shafiee, S.; Topal, E., When will fossil fuel reserves be diminished? *Energ Policy* **2009,** *37* (1), 181-189.

41. A. Bauen, G. B., M. Junginger, M. Londo, F. Vuille. Bioenergy - a Sustainable and Reliable Energy Source 2009.

42. Huber, G. W.; Iborra, S.; Corma, A., Synthesis of transportation fuels from biomass: Chemistry, catalysts, and engineering. *Chem Rev* **2006,** *106* (9), 4044-4098.

43. Venderbosch, R. H.; Prins, W., Fast pyrolysis technology development. *Biofuel Bioprod Bior* **2010,** *4* (2), 178-208.

44. Czernik, S.; Bridgwater, A. V., Overview of applications of biomass fast pyrolysis oil. *Energ Fuel* **2004,** *18* (2), 590-598.

45. Elliott, D. C., Historical developments in hydroprocessing bio-oils. *Energy Fuels* **2007,** *21* (3), 1792-1815.

46. Laurent, E.; Delmon, B., Study of the Hydrodeoxygenation of Carbonyl, Carboxylic and Guaiacyl Groups over Sulfided Como/Gamma-Al2o3 and Nimo/Gamma-Al2o3 Catalyst .2. Influence of Water, Ammonia and Hydrogen-Sulfide. *Appl Catal a-Gen* **1994,** *109* (1), 97-115.

47. Fisk, C. A.; Morgan, T.; Ji, Y. Y.; Crocker, M.; Crofcheck, C.; Lewis, S. A., Bio-oil upgrading over platinum catalysts using in situ generated hydrogen. *Appl Catal a-Gen* **2009,** *358* (2), 150-156.

48. Kubicka, D.; Kaluza, L., Deoxygenation of vegetable oils over sulfided Ni, Mo and NiMo catalysts. *Appl Catal a-Gen* **2010,** *372* (2), 199-208.

49. Lee, E. H.; Park, R. S.; Kim, H.; Park, S. H.; Jung, S. C.; Jeon, J. K.; Kim, S. C.; Park, Y. K., Hydrodeoxygenation of guaiacol over Pt loaded zeolitic materials. *J Ind Eng Chem* **2016,** *37*, 18-21.

50. Hong, D. Y.; Miller, S. J.; Agrawal, P. K.; Jones, C. W., Hydrodeoxygenation and coupling of aqueous phenolics over bifunctional zeolite-supported metal catalysts. *Chem Commun* **2010,** *46* (7), 1038-1040.

51. Zhu, X. L.; Lobban, L. L.; Mallinson, R. G.; Resasco, D. E., Bifunctional transalkylation and hydrodeoxygenation of anisole over a Pt/HBeta catalyst. *J. Catal.* **2011,** *281* (1), 21-29.

52. Horacek, J.; St'avova, G.; Kelbichova, V.; Kubicka, D., Zeolite-Beta-supported platinum catalysts for hydrogenation/hydrodeoxygenation of pyrolysis oil model compounds. *Catal Today* **2013,** *204*, 38-45.

53. Lee, C. R.; Yoon, J. S.; Suh, Y. W.; Choi, J. W.; Ha, J. M.; Suh, D. J.; Park, Y. K., Catalytic roles of metals and supports on hydrodeoxygenation of lignin monomer guaiacol. *Catal Commun* **2012,** *17*, 54-58.

54. Mortensen, P. M.; Grunwaldt, J. D.; Jensen, P. A.; Knudsen, K. G.; Jensen, A. D., A review of catalytic upgrading of bio-oil to engine fuels. *Appl Catal a-Gen* **2011,** *407* (1-2), 1-19.

55. Furimsky, E.; Massoth, F. E., Deactivation of hydroprocessing catalysts. *Catal Today* **1999,** *52* (4), 381-495.

56. Ashcroft, A. T.; Cheetham, A. K.; Foord, J. S.; Green, M. L. H.; Grey, C. P.; Murrell, A. J.; Vernon, P. D. F., Selective Oxidation of Methane to Synthesis Gas-Using Transition-Metal Catalysts. *Nature* **1990,** *344* (6264), 319-321.

57. Bharadwaj, S. S.; Schmidt, L. D., Synthesis Gas-Formation by Catalytic-Oxidation of Methane in Fluidized-Bed Reactors. *J Catal* **1994,** *146* (1), 11-21.

58. Choudhary, V. R.; Rajput, A. M.; Rane, V. H., Low-Temperature Oxidative Conversion of Methane to Synthesis Gas over Co Rare-Earth-Oxide Catalysts. *Catal Lett* **1992,** *16* (3), 269-272.

59. Ito, T.; Lunsford, J. H., Synthesis of Ethylene and Ethane by Partial Oxidation of Methane over Lithium-Doped Magnesium-Oxide. *Nature* **1985,** *314* (6013), 721-722.

60. Kasztelan, S.; Moffat, J. B., Partial Oxidation of Methane by Oxygen over Silica. *J Chem Soc Chem Comm* **1987,** (21), 1663-1664.

61. Lunsford, J. H.; Qiu, P.; Rosynek, M. P.; Yu, Z. Q., Catalytic conversion of methane and ethylene to propylene. *J Phys Chem B* **1998,** *102* (1), 167-173.

62. Pereira, P.; Lee, S. H.; Somorjai, G. A.; Heinemann, H., The Conversion of Methane to Ethylene and Ethane with near Total Selectivity by Low-Temperature (Less-Than 610-Degrees C) Oxydehydrogenation over a Calcium-Nickel-Potassium Oxide Catalyst. *Catal Lett* **1990,** *6* (3-6), 255-262.

63. Periana, R. A.; Taube, D. J.; Evitt, E. R.; Loffler, D. G.; Wentrcek, P. R.; Voss, G.; Masuda, T., A Mercury-Catalyzed, High-Yield System for the Oxidation of Methane to Methanol. *Science* **1993,** *259* (5093), 340-343.

64. Periana, R. A.; Taube, D. J.; Gamble, S.; Taube, H.; Satoh, T.; Fujii, H., Platinum catalysts for the high-yield oxidation of methane to a methanol derivative. *Science* **1998,** *280* (5363), 560-564.

65. Poirier, M. G.; Sanger, A. R.; Smith, K. J., Direct Catalytic Conversion of Methane. *Can J Chem Eng* **1991,** *69* (5), 1027-1035.

66. Rezgui, S.; Liang, A.; Cheung, T. K.; Gates, B. C., Methane conversion to ethane in the presence of iron- and manganese-promoted sulfated zirconia. *Catal Lett* **1998,** *53* (1-2), 1-2.

67. Sigl, M.; Bradford, M. C. J.; Knozinger, H.; Vannice, M. A., CO2 reforming of methane over vanadia-promoted Rh/SiO2 catalysts. *Top Catal* **1999,** *8* (3-4), 211-222.

68. Solymosi, F.; Kutsan, G.; Erdohelyi, A., Catalytic Reaction of Ch4 with Co-2 over Alumina-Supported Pt Metals. *Catal Lett* **1991,** *11* (2), 149-156.

69. Wu, M. C.; Truong, C. M.; Coulter, K.; Goodman, D. W., Investigations of Active-Sites for Methane Activation in the Oxidative Coupling Reaction over Pure and Li-Promoted Mgo Catalysts. *J Catal* **1993,** *140* (2), 344-352.

70. Yamagata, N.; Tanaka, K.; Sasaki, S.; Okazaki, S., Oxidative Coupling of Methane over Bao Mixed with Cao and Mgo. *Chem Lett* **1987,** (1), 81-82.

71. Schanke, D.; Rytter, E.; Jaer, F. O., Scale-up of Statoil's Fischer-Tropsch process. *Natural Gas Conversion Vii* **2004,** *147*, 43-48.

72. T. H. Fleisch, R. A. S., M. D. Briscoe, Emergence of the gas-to-liquids industry: a review of global GTL developments. *Journal of Natural Gas Chemistry* **2002,** *11*, 1-14.

73. Khodakov, A. Y.; Chu, W.; Fongarland, P., Advances in the development of novel cobalt Fischer-Tropsch catalysts for synthesis of long-chain hydrocarbons and clean fuels. *Chem Rev* **2007,** *107* (5), 1692-1744.

74. Lunsford, J. H., The Catalytic Conversion of Methane to Oxygenates and Higher Hydrocarbons. *Studies in Surface Science and Catalysis* **1993,** *75*, 103-126.

75. Gao, J.; Zheng, Y. T.; Jehng, J. M.; Tang, Y. D.; Wachs, I. E.; Podkolzin, S. G., Identification of molybdenum oxide nanostructures on zeolites for natural gas conversion. *Science* **2015,** *348* (6235), 686-690.

76. Koerts, T.; Vansanten, R. A., A Low-Temperature Reaction Sequence for Methane Conversion. *J Chem Soc Chem Comm* **1991,** (18), 1281-1283.

77. Soulivong, D.; Norsic, S.; Taoufik, M.; Coperet, C.; Thivolle-Cazat, J.; Chakka, S.; Basset, J. M., Non-oxidative coupling reaction of methane to ethane and hydrogen catalyzed by the silica-supported tantalum hydride: (SiO)(2)Ta-H. *J. Am. Chem. Soc.* **2008,** *130* (15), 5044-5045.

78. Bailey, B. C.; Fan, H. J.; Baum, E. W.; Huffman, J. C.; Baik, M. H.; Mindiola, D. J., Intermolecular C-H bond activation promoted by a titanium alkylidyne. *J Am Chem Soc* **2005,** *127* (46), 16016-16017.

79. Parkin, G.; Bunel, E.; Burger, B. J.; Trimmer, M. S.; Vanasselt, A.; Bercaw, J. E., Alpha-Migratory and Beta-Migratory Insertion and Elimination Processes for Alkyl Complexes of Permethylscandocene and Permethyltantalocene. *J Mol Catal* **1987,** *41* (1-2), 21-39.

80. Matich, T. Tantalum Price Trends 2015. http://investingnews.com/daily/resource-investing/critical-metals-investing/tantalum-investing/tantalum-price-critical-elements-pilbara-minerals/ (accessed December 20, 2015).

81. Kee, B.; Karakaya, C.; Zhu, H. Y.; DeCaluwe, S.; Kee, R. J., The Influence of Hydrogen-Permeable Membranes and Pressure on Methane Dehydroaromatization in Packed-Bed Catalytic Reactors. *Ind Eng Chem Res* **2017,** *56* (13), 3551-3559.

82. Kumar, P.; Sun, Y.; Idem, R. O., Nickel-based ceria, zirconia, and ceria-zirconia catalytic systems for low-temperature carbon dioxide reforming of methane. *Energ Fuel* **2007,** *21* (6), 3113-3123.

83. Wang, J. B.; Wu, Y. S.; Huang, T. J., Effects of carbon deposition and de-coking treatments on the activation of CH4 and CO2 in CO2 reforming of CH4 over Ni/yttria-doped ceria catalysts. *Appl Catal a-Gen* **2004,** *272* (1-2), 289-298.

84. Zhu, T. L.; Flytzani-Stephanopoulos, M., Catalytic partial oxidation of methane to synthesis gas over Ni-CeO2. *Appl Catal a-Gen* **2001,** *208* (1-2), 403-417.

85. Roh, H. S.; Eum, I. H.; Jeong, D. W., Low temperature steam reforming of methane over Ni-Ce(1-x)Zr(x)O2 catalysts under severe conditions. *Renew Energ* **2012,** *42*, 212-216.

86. Rossignol, S.; Madier, Y.; Duprez, D., Preparation of zirconia-ceria materials by soft chemistry. *Catal Today* **1999,** *50* (2), 261-270.

87. Schimming, S. M.; Foo, G. S.; LaMont, O. D.; Rogers, A. K.; Yung, M. M.; D'Amico, A. D.; Sievers, C., Kinetics of hydrogen activation on ceria-zirconia. *J Catal* **2015,** *329*, 335-347.

88. Espinosa-Alonso, L.; de Jong, K. P.; Weckhuysen, B. M., Effect of the nickel precursor on the impregnation and drying of gamma-Al2O3 catalyst bodies: A UV-vis and IR microspectroscopic study. *J Phys Chem C* **2008,** *112* (18), 7201-7209.

89. Brunauer, S.; Emmett, P. H.; Teller, E., Adsorption of gases in multimolecular layers. *J Am Chem Soc* **1938,** *60*, 309-319.

90. Barrett, E. P.; Joyner, L. G.; Halenda, P. P., The Determination of Pore Volume and Area Distributions in Porous Substances .1. Computations from Nitrogen Isotherms. *J Am Chem Soc* **1951,** *73* (1), 373-380.

91. Tamura, M.; Shimizu, K.; Satsuma, A., Comprehensive IR study on acid/base properties of metal oxides. *Appl Catal a-Gen* **2012,** *433*, 135-145.

92. Tanuma, S.; Powell, C. J.; Penn, D. R., Calculations of Electron Inelastic Mean Free Paths (Imfps) .4. Evaluation of Calculated Imfps and of the Predictive Imfp Formula Tpp-2 for Electron Energies between 50 and 2000 Ev. *Surf Interface Anal* **1993,** *20* (1), 77-89.

93. Wang, J.; Kispersky, V. F.; Delgass, W. N.; Ribeiro, F. H., Determination of the Au active site and surface active species via operando transmission FTIR and isotopic transient experiments on 2.3 wt.% Au/TiO2 for the WGS reaction. *J Catal* **2012,** *289*, 171-178.

94. Rossignol, S.; Gerard, F.; Duprez, D., Effect of the preparation method on the properties of zirconia-ceria materials. *J Mater Chem* **1999,** *9* (7), 1615-1620.

95. Fornasiero, P.; Montini, T.; Graziani, M.; Kaspar, J.; Hungria, A. B.; Martinez-Arias, A.; Conesa, J. C., Effects of thermal pretreatment on the redox behaviour of Ce0.5Zr0.5O2: isotopic and spectroscopic studies. *Phys Chem Chem Phys* **2002,** *4* (1), 149-159.

96. Escribano, V. S.; Lopez, E. F.; Panizza, M.; Resini, C.; Amores, J. M. G.; Busca, G., Characterization of cubic ceria-zirconia powders by X-ray diffraction and vibrational and electronic spectroscopy. *Solid State Sci* **2003,** *5* (10), 1369-1376.

97. Choudhury, B.; Chetri, P.; Choudhury, A., Oxygen defects and formation of Ce3+ affecting the photocatalytic performance of CeO2 nanoparticles. *Rsc Adv* **2014,** *4* (9), 4663-4671.

98. Akhlaghinia, B.; Ebrahimabadi, H.; Goharshadi, E. K.; Samiee, S.; Rezazadeh, S., Ceria nanoparticles as an efficient catalyst for oxidation of benzylic C-H bonds. *J Mol Catal a-Chem* **2012,** *357*, 67-72.

99. Schimming, S. M.; LaMont, O. D.; Konig, M.; Rogers, A. K.; D'Amico, A. D.; Yung, M. M.; Sievers, C., Hydrodeoxygenation of Guaiacol over Ceria-Zirconia Catalysts. *Chemsuschem* **2015,** *8* (12), 2073-2083.

100. Okolie, C.; Belhseine, Y. F.; Lyu, Y.; Yung, M. M.; Engelhard, M. H.; Kovarik, L.; Stavitski, E.; Sievers, C., Conversion of Methane to Methanol and Ethanol over Nickel Oxide on Ceria-Zirconia Catalysts in a Single Reactor. *Angew Chem Int Ed* **2017,** *56*, 13876-13881.

101. Fu, Q.; Saltsburg, H.; Flytzani-Stephanopoulos, M., Active nonmetallic Au and Pt species on ceria-based water-gas shift catalysts. *Science* **2003,** *301* (5635), 935-938.

102. Okolie, C.; Belhseine, Y. F.; Lyu, Y.; Yung, M. M.; Engelhard, M. H.; Kovarik, L.; Stavitski, E.; Sievers, C., Conversion of Methane to Methanol and Ethanol over Nickel Oxide on Ceria–Zirconia Catalysts in a Single Reactor. *Angew Chem Int Ed* **2017,** *56*, 13876-13881.

103. Piao, L. Y.; Li, Y. D.; Chen, J. L.; Chang, L.; Lin, J. Y. S., Methane decomposition to carbon nanotubes and hydrogen on an alumina supported nickel aerogel catalyst. *Catal Today* **2002,** *74* (1-2), 145-155.

104. Takenaka, S.; Ogihara, H.; Yamanaka, I.; Otsuka, K., Decomposition of methane over supported-Ni catalysts: effects of the supports on the catalytic lifetime. *Appl Catal a-Gen* **2001,** *217* (1-2), 101-110.

105. Takenaka, S.; Shigeta, Y.; Tanabe, E.; Otsuka, K., Methane decomposition into hydrogen and carbon nanofibers over supported Pd-Ni catalysts. *J Catal* **2003,** *220* (2), 468-477.

106. Morse, J. K., The structure and dimensions of the benzene ring. *P Natl Acad Sci USA* **1927,** *13*, 789-793.

107. Ohnishi, R.; Liu, S. T.; Dong, Q.; Wang, L.; Ichikawa, M., Catalytic dehydrocondensation of methane with CO and CO2 toward benzene and naphthalene on Mo/HZSM-5 and Fe/Co-modified Mo/HZSM-5. *J Catal* **1999,** *182* (1), 92-103.

108. Long, J. W.; Laskoski, M.; Peterson, G. W.; Keller, T. M.; Pettigrew, K. A.; Schindler, B. J., Metal-catalyzed graphitic nanostructures as sorbents for vapor-phase ammonia. *J Mater Chem* **2011,** *21* (10), 3477-3484.

109. Biniak, S.; Szymanski, G.; Siedlewski, J.; Swiatkowski, A., The characterization of activated carbons with oxygen and nitrogen surface groups. *Carbon* **1997,** *35* (12), 1799-1810.

110. Wang, D. J.; Lunsford, J. H.; Rosynek, M. P., Characterization of a Mo/ZSM-5 catalyst for the conversion of methane to benzene. *J Catal* **1997,** *169* (1), 347-358.

111. Tuinstra, F.; Koenig, J. L., Raman Spectrum of Graphite. *J Chem Phys* **1970,** *53* (3), 1126-1130.

112. Tuinstra, F.; Koenig, J. L., Characterization of Graphite Fiber Surfaces with Raman Spectroscopy. *J Compos Mater* **1970,** *4*, 492-499.

113. Lezanska, M.; Pietrzyk, P.; Sojka, Z., Investigations into the Structure of Nitrogen-Containing CMK-3 and OCM-0.75 Carbon Replicas and the Nature of Surface Functional Groups by Spectroscopic and Sorption Techniques. *J Phys Chem C* **2010,** *114* (2), 1208-1216.

114. Sadezky, A.; Muckenhuber, H.; Grothe, H.; Niessner, R.; Poschl, U., Raman micro spectroscopy of soot and related carbonaceous materials: Spectral analysis and structural information. *Carbon* **2005,** *43* (8), 1731-1742.

115. Socrates, G., *Infrared and Raman Characteristic Group Frequencies*. John Wiley & Sons: West Sussex PO19 8SQ England, 2001; Vol. 3, p 345.

116. Jérôme Joubert; Alain Salameh; Vincent Krakoviack; Françoise Delbecq; Philippe Sautet; Christophe Copéret, a.; Basset‡, J. M., Heterolytic Splitting of H2 and CH4 on γ-Alumina as a Structural Probe for Defect Sites. **2006**.

117. Palumbo, L.; Bonino, F.; Beato, P.; Bjorgen, M.; Zecchina, A.; Bordiga, S., Conversion of methanol to hydrocarbons: Spectroscopic characterization of Carbonaceous species formed over H-ZSM-5. *J Phys Chem C* **2008,** *112* (26), 9710-9716.

118. Park, J. W.; Seo, G., IR study on methanol-to-olefin reaction over zeolites with different pore structures and acidities. *Appl Catal a-Gen* **2009,** *356* (2), 180-188.

119. Deutch, J., The Good News About Gas The Natural Gas Revolution and Its Consequences. *Foreign Aff* **2011,** *90* (1), 82.

120. Rostrup-Nielsen, J. R.; Sehested, J.; Norskov, J. K., Hydrogen and synthesis gas by steam- and CO2 reforming. *Advances in Catalysis, Vol 47* **2002,** *47*, 65-139.

121. P.L. Spath, D. C. D. *Preliminary Screening - Technical and Economic Assessment of Synthesis Gas to Fuels and Chemicals with Emphasis on the Potential for Biomass-Derived Syngas*; NREL: Golden, CO December 2003, 2003; p 160.

122. Jager, B.; Espinoza, R., Advances in Low-Temperature Fischer-Tropsch Synthesis. *Catal Today* **1995,** *23* (1), 17-28.

123. EPA, A. *Inventory of US greenhouse gas emissions and sinks: 1990-2009*; EPA 430-R-11-005: 2011.

124. Gao, J.; Zheng, Y.; Jehng, J.-M.; Tang, Y.; Wachs, I. E.; Podkolzin, S. G., Identification of molybdenum oxide nanostructures on zeolites for natural gas conversion. *Science* **2015,** *348* (6235), 686-690.

125. Ashcroft, A. T.; Cheetham, A. K.; Foord, J. S.; Green, M. L. H.; Grey, C. P.; Murrell, A. J.; Vernon, P. D. F., Selective oxidation of methane to synthesis gas using transition metal catalysts. *Nature* **1990,** *344* (6264), 319-321.

126. Lin, M.; Sen, A., Direct Catalytic Conversion of Methane to Acetic-Acid in an Aqueous-Medium. *Nature* **1994,** *368* (6472), 613-615.

127. Liu, Y. Y.; Murata, K.; Inaba, M.; Takahara, I.; Okabe, K., Mixed alcohols synthesis from syngas over Cs- and Ni-modified Cu/CeO2 catalysts. *Fuel* **2013,** *104*, 62-69.

128. Luk, H. T.; Mondelli, C.; Ferre, D. C.; Stewart, J. A.; Perez-Ramirez, J., Status and prospects in higher alcohols synthesis from syngas. *Chem Soc Rev* **2017,** *46* (5), 1358-1426.

129. Woertink, J. S.; Smeets, P. J.; Groothaert, M. H.; Vance, M. A.; Sels, B. F.; Schoonheydt, R. A.; Solomon, E. I., A Cu_2O (2+) core in Cu-ZSM-5, the active site in the oxidation of methane to methanol. *Proc. Natl. Acad. Sci. U. S. A.* **2009,** *106* (45), 18908-18913.

130. Wulfers, M. J.; Teketel, S.; Ipek, B.; Lobo, R. F., Conversion of methane to methanol on copper-containing small-pore zeolites and zeotypes. *Chem Commun* **2015,** *51* (21), 4447-4450.

131. Starokon, E. V.; Parfenov, M. V.; Arzumanov, S. S.; Pirutko, L. V.; Stepanov, A. G.; Panov, G. I., Oxidation of methane to methanol on the surface of FeZSM-5 zeolite. *J Catal* **2013,** *300*, 47-54.

132. Groothaert, M. H.; Smeets, P. J.; Sels, B. F.; Jacobs, P. A.; Schoonheydt, R. A., Selective oxidation of methane by the bis(mu-oxo)dicopper core stabilized on ZSM-5 and mordenite zeolites. *J. Am. Chem. Soc.* **2005,** *127* (5), 1394-1395.

133. Grundner, S.; Markovits, M. A. C.; Li, G.; Tromp, M.; Pidko, E. A.; Hensen, E. J. M.; Jentys, A.; Sanchez-Sanchez, M.; Lercher, J. A., Single-site trinuclear copper oxygen clusters in mordenite for selective conversion of methane to methanol. *Nat Commun* **2015,** *6*.

134. Narsimhan, K.; Iyoki, K.; Dinh, K.; Roman-Leshkov, Y., Catalytic Oxidation of Methane into Methanol over Copper-Exchanged Zeolites with Oxygen at Low Temperature. *Acs Central Sci* **2016,** *2* (6), 424-429.

135. Panov, G. I.; Uriarte, A. K.; Rodkin, M. A.; Sobolev, V. I., Generation of active oxygen species on solid surfaces. Opportunity for novel oxidation technologies over zeolites. *Catal. Today* **1998,** *41* (4), 365-385.

136. Panov, G. I.; Sobolev, V. I.; Dubkov, K. A.; Parmon, V. N.; Ovanesyan, N. S.; Shilov, A. E.; Shteinman, A. A., Iron complexes in zeolites as a new model of methane monooxygenase. *React. Kinet. Catal. Lett.* **1997,** *61* (2), 251-258.

137. Datka, J.; Turek, A. M.; Jehng, J. M.; Wachs, I. E., Acidic Properties of Supported Niobium Oxide Catalysts - an Infrared-Spectroscopy Investigation. *J Catal* **1992,** *135* (1), 186-199.

138. Colthup, N. B.; Daly, L. H.; Wiberley, S. E., *Introduction to Infrared and Raman spectroscopy*. Academic Press Inc.: San Diego, 1990.

139. Jacobs, G.; Patterson, P. M.; Williams, L.; Chenu, E.; Sparks, D.; Thomas, G.; Davis, B. H., Water-gas shift: in situ spectroscopic studies of noble metal promoted ceria catalysts for CO removal in fuel cell reformers and mechanistic implications. *Appl Catal a-Gen* **2004,** *262* (2), 177-187.

140. Binet, C.; Badri, A.; Lavalley, J. C., A Spectroscopic Characterization of the Reduction of Ceria from Electronic-Transitions of Intrinsic Point-Defects. *J Phys Chem-Us* **1994,** *98* (25), 6392-6398.

141. De Smet, F.; Ruiz, P.; Delmon, B.; Devillers, M., Rationalization of the catalytic behavior of lanthanide oxides and praseodymium molybdates in total and selective oxidation of isobutene. *J Phys Chem B* **2001,** *105* (49), 12355-12363.

142. Yan, Z. G.; Andersson, S. L. T., Catalytic and Spectroscopic Studies of Ag1.2v3ceyo8+X Catalysts for Oxidation of Toluene. *J Catal* **1991,** *131* (2), 350-368.

143. Subramani, V.; Gangwal, S. K., A review of recent literature to search for an efficient catalytic process for the conversion of syngas to ethanol. *Energ Fuel* **2008,** *22* (2), 814-839.

144. Monnerat, B.; Kiwi-Minsker, L.; Renken, A., Hydrogen production by catalytic cracking of methane over nickel gauze under periodic reactor operation. *Chem Eng Sci* **2001,** *56* (2), 633-639.

145. Sperle, T.; Chen, D.; Lodeng, R.; Holmen, A., Pre-reforming of natural gas on a Ni catalyst - Criteria for carbon free operation. *Appl Catal a-Gen* **2005,** *282* (1-2), 195-204.

146. Reis, P. M.; Silva, J. A. L.; Palavra, A. F.; da Silva, J. J. R. F.; Kitamura, T.; Fujiwara, Y.; Pombeiro, A. J. L., Single-pot conversion of methane into acetic acid in the absence of CO and with vanadium catalysts such as amavadine. *Angew Chem Int Edit* **2003,** *42* (7), 821-823.

147. Lunsford, J. H., Catalytic conversion of methane to more useful chemicals and fuels: a challenge for the 21st century. *Catal Today* **2000,** *63* (2-4), 165-174.

148. McFarland, E., Unconventional Chemistry for Unconventional Natural Gas. *Science* **2012,** *338* (6105), 340-342.

149. Podkolzin, S. G.; Stangland, E. E.; Jones, M. E.; Peringer, E.; Lercher, J. A., Methyl chloride production from methane over lanthanum-based catalysts. *J Am Chem Soc* **2007,** *129* (9), 2569-2576.

150. Khalilpour, R.; Karimi, I. A., Evaluation of utilization alternatives for stranded natural gas. *Energy* **2012,** *40* (1), 317-328.

151. Labinger, J. A.; Bercaw, J. E., Understanding and exploiting C-H bond activation. *Nature* **2002,** *417* (6888), 507-514.

152. Singh, A. D.; Krase, N. W., Synthesis of acetic acid from methanol and carbon monoxide. *Ind Eng Chem* **1935,** *27*, 909-914.

153. Hereijgers, B. P. C.; Bleken, F.; Nilsen, M. H.; Svelle, S.; Lillerud, K. P.; Bjorgen, M.; Weckhuysen, B. M.; Olsbye, U., Product shape selectivity dominates the Methanol-to-Olefins (MTO) reaction over H-SAPO-34 catalysts. *J Catal* **2009,** *264* (1), 77-87.

154. Cui, Z. M.; Liu, Q.; Song, W. G.; Wan, L. J., Insights into the mechanism of methanol-to-olefin conversion at zeolites with systematically selected framework structures. *Angew Chem Int Edit* **2006,** *45* (39), 6512-6515.

155. Garbarino, G.; Travi, I.; Pani, M.; Carnasciali, M. M.; Busca, G., Pure vs ultra-pure gamma-alumina: A spectroscopic study and catalysis of ethanol conversion. *Catal Commun* **2015,** *70*, 77-81.

156. Sun, J.; Wang, Y., Recent Advances in Catalytic Conversion of Ethanol to Chemicals. *Acs Catal* **2014,** *4* (4), 1078-1090.

157. Hanspal, S.; Young, Z. D.; Shou, H.; Davis, R. J., Multiproduct Steady-State Isotopic Transient Kinetic Analysis of the Ethanol Coupling Reaction over Hydroxyapatite and Magnesia. *Acs Catal* **2015,** *5* (3), 1737-1746.

158. Kozlowski, J. T.; Davis, R. J., Heterogeneous Catalysts for the Guerbet Coupling of Alcohols. *Acs Catal* **2013,** *3* (7), 1588-1600.

159. James A. Anderson, M. F. G., *Supported Metals in Catalysis*. Imperial College Press: London U.K. , 2005; Vol. 5, p 381.

160. Haber, J.; Block, J. H.; Delmon, B., Manual of Methods and Procedures for Catalyst Characterization. *Pure Appl Chem* **1995,** *67* (8-9), 1257-1306.

161. Ataloglou, T.; Vakros, J.; Bourikas, K.; Fountzoula, C.; Kordulis, C.; Lycourghiotis, A., Influence of the preparation method on the structure-activity of cobalt oxide catalysts supported on alumina for complete benzene oxidation. *Appl Catal B-Environ* **2005,** *57* (4), 299-312.

162. Regalbuto, J. R., CATL 2 - A simple, rational method to prepare supported metal catalysts. *Abstr Pap Am Chem S* **2009,** *237*, 884-884.

163. Agashe, K. B.; Regalbuto, J. R., A revised physical theory for adsorption of metal complexes at oxide surfaces. *J Colloid Interf Sci* **1997,** *185* (1), 174-189.

164. Park, J.; Regalbuto, J. R., Simple, Accurate Determination of Oxide Pzc and the Strong Buffering Effect of Oxide Surfaces at Incipient Wetness. *J Colloid Interf Sci* **1995,** *175* (1), 239-252.

165. Regalbuto, J. R.; Navada, A.; Shadid, S.; Bricker, M. L.; Chen, Q., An experimental verification of the physical nature of Pt adsorption onto alumina. *J Catal* **1999,** *184* (2), 335-348.

166. Hao, X.; Quach, L.; Korah, J.; Spieker, W. A.; Regalbuto, J. R., The control of platinum impregnation by PZC alteration of oxides and carbon. *J Mol Catal a-Chem* **2004,** *219* (1), 97-107.

167. Jiao, L.; Regalbuto, J. R., The synthesis of highly dispersed noble and base metals on silica via strong electrostatic adsorption: I. Amorphous silica. *J Catal* **2008,** *260* (2), 329-341.

168. Miller, J. T.; Schreier, M.; Kropf, A. J.; Regalbuto, J. R., A fundamental study of platinum tetraammine impregnation of silica 2. The effect of method of preparation, loading, and calcination temperature on (reduced) particle size. *J Catal* **2004,** *225* (1), 203-212.

169. Schreier, M.; Regalbuto, J. R., A fundamental study of Pt tetraammine impregnation of silica 1. The electrostatic nature of platinum adsorption. *J Catal* **2004,** *225* (1), 190-202.

170. D'Souza, L.; Jiao, L.; Regalbuto, J. R.; Miller, J. T.; Kropf, A. J., Preparation of silica- and carbon-supported cobalt by electrostatic adsorption of Co(III) hexaammines. *J Catal* **2007,** *248* (2), 165-174.

171. Xu, S.; Wang, X. L., Highly active and coking resistant Ni/CeO2-ZrO2 catalyst for partial oxidation of methane. *Fuel* **2005,** *84* (5), 563-567.

172. Li, G. H.; Hu, L. J.; Hill, J. M., Comparison of reducibility and stability of alumina-supported Ni catalysts prepared by impregnation and co-precipitation. *Appl Catal a-Gen* **2006,** *301* (1), 16-24.

173. Wang, S. B.; Lu, G. Q. M., CO2 reforming of methane on Ni catalysts: Effects of the support phase and preparation technique. *Appl Catal B-Environ* **1998,** *16* (3), 269-277.

174. Haruta, M.; Yamada, N.; Kobayashi, T.; Iijima, S., Gold Catalysts Prepared by Coprecipitation for Low-Temperature Oxidation of Hydrogen and of Carbon-Monoxide. *J Catal* **1989,** *115* (2), 301-309.

175. Wei, J. M.; Xu, B. Q.; Li, J. L.; Cheng, Z. X.; Zhu, Q. M., Highly active and stable Ni/ZrO2 catalyst for syngas production by CO2 reforming of methane. *Appl Catal a-Gen* **2000,** *196* (2), L167-L172.

176. Rossignol, S.; Madier, Y.; Duprez, D., Preparation of zirconia-ceria by soft chemistry. *Catal Today* **1999,** *50* (2), 261-270.

177. Noh, J. S.; Schwarz, J. A., Estimation of the Point of Zero Charge of Simple Oxides by Mass Titration. *J Colloid Interf Sci* **1989,** *130* (1), 157-164.

178. Schreier, M.; Feltes, T. E.; Schaal, M. T.; Regalbuto, J. R., The determination of oxide surface charging parameters for a predictive metal adsorption model. *J Colloid Interf Sci* **2010,** *348* (2), 571-578.

179. Marceau, E.; Che, M.; Cejka, J.; Zukal, A., Nickel(II) Nitrate vs. Acetate: Influence of the Precursor on the Structure and Reducibility of Ni/MCM-41 and Ni/Al-MCM-41 Catalysts. *Chemcatchem* **2010,** *2* (4), 413-422.

180. Deng, J.; Chu, W.; Wang, B.; Yang, W.; Zhao, X. S., Mesoporous Ni/Ce1-xNixO2-y heterostructure as an efficient catalyst for converting greenhouse gas to H-2 and syngas. *Catal Sci Technol* **2016,** *6* (3), 851-862.

181. Du, X. J.; Zhang, D. S.; Shi, L. Y.; Gao, R. H.; Zhang, J. P., Morphology Dependence of Catalytic Properties of Ni/CeO2 Nanostructures for Carbon Dioxide Reforming of Methane. *J Phys Chem C* **2012,** *116* (18), 10009-10016.

182. Odedairo, T.; Chen, J. L.; Zhu, Z. H., Synthesis of Supported Nickel Nanoparticles via a Nonthermal Plasma Approach and Its Application in CO2 Reforming of Methane. *J Phys Chem C* **2013,** *117* (41), 21288-21302.

183. Bond, G. C.; Thompson, D. T., Catalysis by gold. *Catal Rev* **1999,** *41* (3-4), 319-388.

184. Tauster, S. J., Strong Metal-Support Interactions. *Accounts Chem Res* **1987,** *20* (11), 389-394.

185. Carrettin, S.; Concepcion, P.; Corma, A.; Nieto, J. M. L.; Puntes, V. F., Nanocrystalline CeO2 increases the activity of an for CO oxidation by two orders of magnitude. *Angew Chem Int Edit* **2004,** *43* (19), 2538-2540.

186. Odedairo, T.; Chen, J. L.; Zhu, Z. H., Metal-support interface of a novel Ni-CeO2 catalyst for dry reforming of methane. *Catal Commun* **2013,** *31*, 25-31.

187. Chen, L.; Fleming, P.; Morris, V.; Holmes, J. D.; Morris, M. A., Size-Related Lattice Parameter Changes and Surface Defects in Ceria Nanocrystals. *J Phys Chem C* **2010,** *114* (30), 12909-12919.

188. Bear, J. C.; McNaughter, P. D.; Southern, P.; O'Brien, P.; Dunnill, C. W., Nickel-Doped Ceria Nanoparticles: The Effect of Annealing on Room Temperature Ferromagnetism. *Crystals* **2015,** *5* (3), 312-326.

189. Gimenez-Manogil, J.; Garcia-Garcia, A., Identifying the nature of the copper entities over ceria-based supports to promote diesel soot combustion: Synergistic effects. *Appl Catal a-Gen* **2017,** *542*, 226-239.

190. Liu, L. J.; Yao, Z. J.; Liu, B.; Dong, L., Correlation of structural characteristics with catalytic performance of CuO/CexZr1-xO2 catalysts for NO reduction by CO. *J Catal* **2010,** *275* (1), 45-60.

191. Rogers, J. L.; Mangarella, M. C.; D'Amico, A. D.; Gallagher, J. R.; Dutzer, M. R.; Stavitski, E.; Miller, J. T.; Sievers, C., Differences in the Nature of Active Sites for Methane Dry Reforming and Methane Steam Reforming over Nickel Aluminate Catalysts. *Acs Catal* **2016,** *6* (9), 5873-5886.

192. Ewbank, J. L.; Kovarik, L.; Diallo, F. Z.; Sievers, C., Effect of metal-support interactions in Ni/Al2O3 catalysts with low metal loading for methane dry reforming. *Appl Catal a-Gen* **2015,** *494*, 57-67.

193. Ewbank, J. L.; Kovarik, L.; Kenvin, C. C.; Sievers, C., Effect of preparation methods on the performance of Co/Al2O3 catalysts for dry reforming of methane. *Green Chem* **2014,** *16* (2), 885-896.

194. Ioelovich, M., Recent Findings and the Energetic Potential of Plant Biomass as a Renewable Source of Biofuels - A Review. *Bioresources* **2015,** *10* (1), 1879-1914.

195. Donovan, C. W., *Renewable Energy Finance: Powering the Future*. Imperial College Press: London WC2H 9HE, 2015.

196. Rosillo-Calle, F., A review of biomass energy-shortcomings and concerns. *J Chem Technol Biot* **2016,** *91* (7), 1933-1945.

197. Si, Z.; Zhang, X. H.; Wang, C. G.; Ma, L. L.; Dong, R. J., An Overview on Catalytic Hydrodeoxygenation of Pyrolysis Oil and Its Model Compounds. *Catalysts* **2017,** *7* (6).

198. Nakagawa, Y.; Liu, S. B.; Tamura, M.; Tomishige, K., Catalytic Total Hydrodeoxygenation of Biomass-Derived Polyfunctionalized Substrates to Alkanes. *Chemsuschem* **2015,** *8* (7), 1114-1132.

199. Brunet, S.; Mey, D.; Perot, G.; Bouchy, C.; Diehl, F., On the hydrodesulfurization of FCC gasoline: a review. *Appl Catal a-Gen* **2005,** *278* (2), 143-172.

200. Mochida, I.; Choi, K. H., An overview of hydrodesulfurization and hydrodenitrogenation. *J Jpn Petrol Inst* **2004,** *47* (3), 145-163.

201. Laurent, E.; Delmon, B., Study of the Hydrodeoxygenation of Carbonyl, Carboxylic and Guaiacyl Groups over Sulfided Como/Gamma-Al2o3 and Nimo/Gamma-Al2o3 Catalysts .1. Catalytic Reaction Schemes. *Appl Catal a-Gen* **1994,** *109* (1), 77-96.

202. Laurent, E.; Delmon, B., Deactivation of a Sulfided Nimo/Gamma-Al2o3 during the Hydrodeoxygenation of Bio-Oils - Influence of a High Water-Pressure. *Catalyst Deactivation 1994* **1994,** *88*, 459-466.

203. Lin, Y. C.; Li, C. L.; Wan, H. P.; Lee, H. T.; Liu, C. F., Catalytic Hydrodeoxygenation of Guaiacol on Rh-Based and Sulfided CoMo and NiMo Catalysts. *Energ Fuel* **2011,** *25* (3), 890-896.

204. Furimsky, E., Catalytic hydrodeoxygenation. *Appl Catal a-Gen* **2000,** *199* (2), 147-190.

205. Wildschut, J.; Mahfud, F. H.; Venderbosch, R. H.; Heeres, H. J., Hydrotreatment of Fast Pyrolysis Oil Using Heterogeneous Noble-Metal Catalysts. *Ind Eng Chem Res* **2009,** *48* (23), 10324-10334.

206. Wildschut, J.; Iqbal, M.; Mahfud, F. H.; Melian-Cabrera, I.; Venderbosch, R. H.; Heeres, H. J., Insights in the hydrotreatment of fast pyrolysis oil using a ruthenium on carbon catalyst. *Energ Environ Sci* **2010,** *3* (7), 962-970.

207. Zhao, C.; Kou, Y.; Lemonidou, A. A.; Li, X. B.; Lercher, J. A., Highly Selective Catalytic Conversion of Phenolic Bio-Oil to Alkanes. *Angew Chem Int Edit* **2009,** *48* (22), 3987-3990.

208. Zhao, C.; Kou, Y.; Lemonidou, A. A.; Li, X. B.; Lercher, J. A., Hydrodeoxygenation of bio-derived phenols to hydrocarbons using RANEY (R) Ni and Nafion/SiO2 catalysts. *Chem Commun* **2010,** *46* (3), 412-414.

209. Zhao, C.; Lercher, J. A., Upgrading Pyrolysis Oil over Ni/HZSM-5 by Cascade Reactions. *Angew Chem Int Edit* **2012,** *51* (24), 5935-5940.

210. Zhao, C.; Song, W. J.; Lercher, J. A., Aqueous Phase Hydroalkylation and Hydrodeoxygenation of Phenol by Dual Functional Catalysts Comprised of Pd/C and H/La-BEA. *Acs Catal* **2012,** *2* (12), 2714-2723.

211. Zhao, C.; Lercher, J. A., Selective Hydrodeoxygenation of Lignin-Derived Phenolic Monomers and Dimers to Cycloalkanes on Pd/C and HZSM-5 Catalysts. *Chemcatchem* **2012,** *4* (1), 64-68.

212. Sitthisa, S.; Resasco, D. E., Hydrodeoxygenation of Furfural Over Supported Metal Catalysts: A Comparative Study of Cu, Pd and Ni. *Catal Lett* **2011,** *141* (6), 784-791.

213. Sitthisa, S.; Sooknoi, T.; Ma, Y. G.; Balbuena, P. B.; Resasco, D. E., Kinetics and mechanism of hydrogenation of furfural on Cu/SiO2 catalysts. *J Catal* **2011,** *277* (1), 1-13.

214. Ausavasukhi, A.; Huang, Y.; To, A. T.; Sooknoi, T.; Resasco, D. E., Hydrodeoxygenation of m-cresol over gallium-modified beta zeolite catalysts. *J Catal* **2012,** *290*, 90-100.

215. Nie, L.; Resasco, D. E., Kinetics and mechanism of m-cresol hydrodeoxygenation on a Pt/SiO2 catalyst. *J Catal* **2014,** *317*, 22-29.

216. Zhu, X. L.; Nie, L.; Lobban, L. L.; Mallinson, R. G.; Resasco, D. E., Efficient Conversion of m-Cresol to Aromatics on a Bifunctional Pt/HBeta Catalyst. *Energ Fuel* **2014,** *28* (6), 4104-4111.

217. Gonzalez-Borja, M. A.; Resasco, D. E., Anisole and Guaiacol Hydrodeoxygenation over Monolithic Pt-Sn Catalysts. *Energy Fuels* **2011,** *25* (9), 4155-4162.

218. Khromova, S. A.; Smirnov, A. A.; Bulavchenko, O. A.; Saraev, A. A.; Kaichev, V. V.; Reshetnikov, S. I.; Yakovlev, V. A., Anisole hydrodeoxygenation over Ni-Cu bimetallic catalysts: The effect of Ni/Cu ratio on selectivity. *Appl Catal a-Gen* **2014,** *470*, 261-270.

219. Gutierrez, A.; Kaila, R. K.; Honkela, M. L.; Slioor, R.; Krause, A. O. I., Hydrodeoxygenation of guaiacol on noble metal catalysts. *Catal Today* **2009,** *147* (3-4), 239-246.

220. Sun, J. M.; Karim, A. M.; Zhang, H.; Kovarik, L.; Li, X. H. S.; Hensley, A. J.; McEwen, J. S.; Wang, Y., Carbon-supported bimetallic Pd-Fe catalysts for vapor-phase hydrodeoxygenation of guaiacol. *J Catal* **2013,** *306*, 47-57.

221. Rensel, D. J.; Rouvimov, S.; Gin, M. E.; Hicks, J. C., Highly selective bimetallic FeMoP catalyst for C-O bond cleavage of aryl ethers. *J Catal* **2013,** *305*, 256-263.

222. Foo, G. S.; Rogers, A. K.; Yung, M. M.; Sievers, C., Steric Effect and Evolution of Surface Species in the Hydrodeoxygenation of Bio-Oil Model Compounds over Pt/HBEA. *Acs Catal* **2016,** *6* (2), 1292-1307.

223. Yung, M. M.; Stanton, A. R.; Iisa, K.; French, R. J.; Orton, K. A.; Magrini, K. A., Multiscale Evaluation of Catalytic Upgrading of Biomass Pyrolysis Vapors on Ni- and Ga-Modified ZSM-5. *Energ Fuel* **2016,** *30* (11), 9471-9479.

224. Mu, W.; Ben, H. X.; Du, X. T.; Zhang, X. D.; Hu, F.; Liu, W.; Ragauskas, A. J.; Deng, Y. L., Noble metal catalyzed aqueous phase hydrogenation and hydrodeoxygenation of lignin-derived pyrolysis oil and related model compounds. *Bioresource Technol* **2014,** *173*, 6-10.

225. Li, Y.; Zhang, C. S.; Liu, Y. G.; Hou, X. X.; Zhang, R. Q.; Tang, X. Y., Coke Deposition on Ni/HZSM-5 in Bio-oil Hydrodeoxygenation Processing. *Energ Fuel* **2015,** *29* (3), 1722-1728.

226. Popov, A.; Kondratieva, E.; Goupil, J. M.; Mariey, L.; Bazin, P.; Gilson, J. P.; Travert, A.; Mauge, F., Bio-oils Hydrodeoxygenation: Adsorption of Phenolic Molecules on Oxidic Catalyst Supports. *J. Phys. Chem. C* **2010,** *114* (37), 15661-15670.

227. Popov, A.; Kondratieva, E.; Gilson, J. P.; Mariey, L.; Travert, A.; Mauge, F., IR study of the interaction of phenol with oxides and sulfided CoMo catalysts for bio-fuel hydrodeoxygenation. *Catal Today* **2011,** *172* (1), 132-135.

228. Popov, A.; Kondratieva, E.; Mariey, L.; Goupil, J. M.; El Fallah, J.; Gilson, J. P.; Travert, A.; Mauge, F., Bio-oil hydrodeoxygenation: Adsorption of phenolic compounds on sulfided (Co)Mo catalysts. *J Catal* **2013,** *297*, 176-186.

229. Prasomsri, T.; Shetty, M.; Murugappan, K.; Roman-Leshkov, Y., Insights into the catalytic activity and surface modification of MoO3 during the hydrodeoxygenation of lignin-derived model compounds into aromatic hydrocarbons under low hydrogen pressures. *Energ Environ Sci* **2014,** *7* (8), 2660-2669.

230. Rane, N.; Kersbulck, M.; van Santen, R. A.; Hensen, E. J. M., Cracking of n-heptane over Bronsted acid sites and Lewis acid Ga sites in ZSM-5 zeolite. *Micropor Mesopor Mat* **2008,** *110* (2-3), 279-291.

231. Saito, A.; Foley, H. C., High-Resolution Nitrogen and Argon Adsorption on Zsm-5 Zeolites - Effects of Cation-Exchange and Si/Al Ratio. *Microporous Mater* **1995,** *3* (4-5), 543-556.

232. Saito, A.; Foley, H. C., Argon Porosimetry of Selected Molecular-Sieves - Experiments and Examination of the Adapted Horvath-Kawazoe Model. *Microporous Mater* **1995,** *3* (4-5), 531-542.

233. Groen, J. C.; Peffer, L. A. A.; Perez-Ramirez, J., Pore size determination in modified micro- and mesoporous materials. Pitfalls and limitations in gas adsorption data analysis. *Micropor Mesopor Mat* **2003,** *60* (1-3), 1-17.

234. Perez-Ramirez, J.; Garcia-Cortes, J. M.; Kapteijn, F.; Mul, G.; Moulijn, J. A.; de Lecea, C. S. M., Characterization and performance of Pt-USY in the SCR of NOx with hydrocarbons under lean-burn conditions. *Appl Catal B-Environ* **2001,** *29* (4), 285-298.

235. Wang, H. T.; Wang, Z. B.; Huang, L. M.; Mitra, A.; Holmberg, B.; Yan, Y. S., High-surface-area zeolitic silica with mesoporosity. *J Mater Chem* **2001,** *11* (9), 2307-2310.

236. Higgins, J. B.; Lapierre, R. B.; Schlenker, J. L.; Rohrman, A. C.; Wood, J. D.; Kerr, G. T.; Rohrbaugh, W. J., The Framework Topology of Zeolite-Beta. *Zeolites* **1988,** *8* (6), 446-452.

237. Kokotailo, G. T.; Lawton, S. L.; Olson, D. H.; Olson, D. H.; Meier, W. M., Structure of Synthetic Zeolite Zsm-5. *Nature* **1978,** *272* (5652), 437-438.

238. Kwak, J. H.; Hu, J. Z.; Mei, D.; Yi, C. W.; Kim, D. H.; Peden, C. H. F.; Allard, L. F.; Szanyi, J., Coordinatively Unsaturated Al3+ Centers as Binding Sites for Active Catalyst Phases of Platinum on gamma-Al2O3. *Science* **2009,** *325* (5948), 1670-1673.

239. Pujari, S. P.; Scheres, L.; Marcelis, A. T. M.; Zuilhof, H., Covalent Surface Modification of Oxide Surfaces. *Angew Chem Int Edit* **2014,** *53* (25), 6322-6356.

240. Yang, Y. L.; Yan, W.; Jing, C. Y., Dynamic Adsorption of Catechol at the Goethite/Aqueous Solution Interface: A Molecular-Scale Study. *Langmuir* **2012,** *28* (41), 14588-14597.

241. Lee, N.; Hummer, D. R.; Sverjensky, D. A.; Rajh, T.; Hazen, R. M.; Steele, A.; Cody, G. D., Speciation of L-DOPA on Nanorutile as a Function of pH and Surface Coverage Using Surface-Enhanced Raman Spectroscopy (SERS). *Langmuir* **2012,** *28* (50), 17322-17330.

242. Socrates, G., *Infrared and Raman Characteristic Group Frequencies*. 3rd ed.; Wiley: Chichester, England, 2001.

243. Kotrel, S.; Lunsford, J. H.; Knozinger, H., Characterizing zeolite acidity by spectroscopic and catalytic means: A comparison. *J Phys Chem B* **2001,** *105* (18), 3917-3921.

244. Simon-Masseron, A.; Marques, J. P.; Lopes, J. M.; Ribeiro, F. R.; Gener, I.; Guisnet, M., Influence of the Si/Al ratio and crystal size on the acidity and activity of HBEA zeolites. *Appl Catal a-Gen* **2007,** *316* (1), 75-82.

245. Vimont, A.; Thibault-Starzyk, F.; Lavalley, J. C., Infrared spectroscopic study of the acidobasic properties of beta zeolite. *J Phys Chem B* **2000,** *104* (2), 286-291.

246. Nobukawa, T.; Yoshida, M.; Kameoka, S.; Ito, S.; Tomishige, K.; Kunimori, K., In-situ observation of reaction intermediate in the selective catalytic reduction of N2O with CH4 over Fe ion-exchanged BEA zeolite catalyst for the elucidation of its reaction mechanism using FTIR. *J Phys Chem B* **2004,** *108* (13), 4071-4079.

247. Sobalik, Z.; Belhekar, A. A.; Tvaruzkova, Z.; Wichterlova, B., Metal ligand complexes in CoH-BEA relevant to ethane ammoxidation to acetonitrile: an FTIR study. *Appl Catal a-Gen* **1999,** *188* (1-2), 175-186.

248. Gora-Marek, K.; Datka, J.; Dzwigaj, S.; Che, M., Influence of V content on the nature and strength of acidic sites in VSi beta zeolite evidenced by IR spectroscopy. *J Phys Chem B* **2006,** *110* (13), 6763-6767.

249. Montanari, T.; Bevilacqua, M.; Busca, G., Use of nitriles as probe molecules for the accessibility of the active sites and the detection of complex interactions in zeolites through IR spectroscopy. *Appl Catal a-Gen* **2006,** *307* (1), 21-29.

250. Penkova, A.; Dzwigaj, S.; Kefirov, R.; Hadjiivanov, K.; Che, M., Effect of the preparation method on the state of nickel ions in BEA zeolites. A study by Fourier transform infrared spectroscopy of adsorbed CO and NO, temperature-programmed reduction, and X-ray diffraction. *J Phys Chem C* **2007,** *111* (24), 8623-8631.

251. Zecchina, A.; Arean, C. O., Diatomic molecular probes for mid-IR studies of zeolites. *Chem Soc Rev* **1996,** *25* (3), 187-+.

252. Wang, Y.; Zhitomirsky, I., Bio-inspired catechol chemistry for electrophoretic nanotechnology of oxide films. *J Colloid Interf Sci* **2012,** *380*, 8-15.

253. Copeland, J. R.; Santillan, I. A.; Schimming, S. M.; Ewbank, J. L.; Sievers, C., Surface Interactions of Glycerol with Acidic and Basic Metal Oxides. *J Phys Chem C* **2013,** *117* (41), 21413-21425.

254. Copeland, J. R.; Shi, X. R.; Sholl, D. S.; Sievers, C., Surface Interactions of C-2 and C-3 Polyols with gamma-Al2O3 and the Role of Coadsorbed Water. *Langmuir* **2013,** *29* (2), 581-593.

255. Foo, G. S.; Wei, D.; Sholl, D. S.; Sievers, C., Role of Lewis and Bronsted Acid Sites in the Dehydration of Glycerol over Niobia. *ACS Catalysis* **2014,** *4* (9), 3180-3192.

256. Jongerius, A. L.; Copeland, J. R.; Foo, G. S.; Hofmann, J. P.; Bruijnincx, P. C. A.; Sievers, C.; Weckhuysen, B. M., Stability of Pt/gamma-Al2O3 Catalysts in Lignin and Lignin Model Compound Solutions under Liquid Phase Reforming Reaction Conditions. *Acs Catal* **2013,** *3* (3), 464-473.

257. Ravenelle, R. M.; Copeland, J. R.; Van Pelt, A. H.; Crittenden, J. C.; Sievers, C., Stability of Pt/gamma-Al2O3 Catalysts in Model Biomass Solutions. *Top Catal* **2012,** *55* (3-4), 162-174.

258. Ennaert, T.; Van Aelst, J.; Dijkmans, J.; De Clercq, R.; Schutyser, W.; Dusselier, M.; Verboekend, D.; Sels, B. F., Potential and challenges of zeolite chemistry in the catalytic conversion of biomass. *Chem Soc Rev* **2016,** *45* (3), 584-611.

259. Carlson, T. R.; Vispute, T. R.; Huber, G. W., Green gasoline by catalytic fast pyrolysis of solid biomass derived compounds. *Chemsuschem* **2008,** *1* (5), 397-400.

260. Carlson, T. R.; Tompsett, G. A.; Conner, W. C.; Huber, G. W., Aromatic Production from Catalytic Fast Pyrolysis of Biomass-Derived Feedstocks. *Top Catal* **2009,** *52* (3), 241-252.

261. Rivallan, M.; Thomas, S.; Lepage, M.; Takagi, N.; Hirata, H.; Thibault-Starzyk, F., Evolution of Platinum Particles Dispersed on Zeolite upon Oxidation Catalysis and Ageing. *Chemcatchem* **2010,** *2* (12), 1599-1605.

262. Stakheev, A. Y.; Shpiro, E. S.; Tkachenko, O. P.; Jaeger, N. I.; SchulzEkloff, G., Evidence for monatomic platinum species in H-ZSM-5 from FTIR spectroscopy of chemisorbed CO. *J Catal* **1997,** *169* (1), 382-388.

263. Kubanek, P.; Schmidt, H. W.; Spliethoff, B.; Scuth, F., Parallel IR spectroscopic characterization of CO chemisorption on Pt loaded zeolites. *Micropor Mesopor Mat* **2005,** *77* (1), 89-96.

264. Zholobenko, V. L.; Lei, G. D.; Carvill, B. T.; Lerner, B. A.; Sachtler, W. M. H., Identification of Isolated Pt Atoms in H-Mordenite. *J Chem Soc Faraday T* **1994,** *90* (1), 233-238.

265. Brown, C. J., Crystal Structure of Catechol. *Acta Crystallogr* **1966,** *21*, 170-&.

266. Dib, E.; Grand, J.; Mintova, S.; Fernandez, C., Structure-Directing Agent Governs the Location of Silanol Defects in Zeolites. *Chem Mater* **2015,** *27* (22), 7577-7579.

267. Foster, M. D.; Rivin, I.; Treacy, M. M. J.; Friedrichs, O. D., A geometric solution to the largest-free-sphere problem in zeolite frameworks. *Micropor Mesopor Mat* **2006,** *90* (1-3), 32-38.

268. Jae, J.; Tompsett, G. A.; Foster, A. J.; Hammond, K. D.; Auerbach, S. M.; Lobo, R. F.; Huber, G. W., Investigation into the shape selectivity of zeolite catalysts for biomass conversion. *J Catal* **2011,** *279* (2), 257-268.

269. Olson, D. H.; Kokotailo, G. T.; Lawton, S. L.; Meier, W. M., Crystal-Structure and Structure-Related Properties of Zsm-5. *J Phys Chem-Us* **1981,** *85* (15), 2238-2243.

270. Newsam, J. M.; Treacy, M. M. J.; Koetsier, W. T.; Degruyter, C. B., Structural Characterization of Zeolite-Beta. *P Roy Soc Lond a Mat* **1988,** *420* (1859), 375-&.

271. Laurent, E.; Delmon, B., Influence of Water in the Deactivation of a Sulfided Nimo Gamma-Al2o3 Catalyst during Hydrodeoxygenation. *J Catal* **1994,** *146* (1), 281-291.

272. Saidi, M.; Rostami, P.; Rahimpour, H. R.; Fallah, M. A. R.; Rahimpour, M. R.; Gates, B. C.; Raeissi, S., Kinetics of Upgrading of Anisole with Hydrogen Catalyzed by Platinum Supported on Alumina. *Energ Fuel* **2015,** *29* (8), 4990-4997.

273. Saidi, M.; Rostami, P.; Rahimpour, M. R.; Gates, B. C.; Raeissi, S., Upgrading of Lignin-Derived Bio-oil Components Catalyzed by Pt/gamma-Al2O3: Kinetics and Reaction Pathways Characterizing Conversion of Cyclohexanone with H-2. *Energ Fuel* **2015,** *29* (1), 191-199.

274. Hemelsoet, K.; Van Speybroeck, V.; Waroquier, M., A DFT-Based Investigation of Hydrogen Abstraction Reactions from Methylated Polycyclic Aromatic Hydrocarbons. *Chemphyschem* **2008,** *9* (16), 2349-2358.

275. Zheng, B.; Hua, W. M.; Yue, Y. H.; Gao, Z., Dehydrogenation of propane to propene over different polymorphs of gallium oxide. *J Catal* **2005,** *232* (1), 143-151.

276. Shao, C. T.; Lang, W. Z.; Yan, X.; Guo, Y. J., Catalytic performance of gallium oxide based-catalysts for the propane dehydrogenation reaction: effects of support and loading amount. *Rsc Adv* **2017,** *7* (8), 4710-4723.

277. Kelkar, S.; Saffron, C. M.; Li, Z. L.; Kim, S. S.; Pinnavaia, T. J.; Miller, D. J.; Kriegel, R., Aromatics from biomass pyrolysis vapour using a bifunctional mesoporous catalyst. *Green Chem* **2014,** *16* (2), 803-812.

278. Neumann, G. T.; Hicks, J. C., Novel Hierarchical Cerium-Incorporated MFI Zeolite Catalysts for the Catalytic Fast Pyrolysis of Lignocellulosic Biomass. *Acs Catal* **2012,** *2* (4), 642-646.

279. Xu, W. Y.; Miller, S. J.; Agrawal, P. K.; Jones, C. W., Positive Effect of Water on Zeolite BEA Catalyzed Alkylation of Phenol with Propylene. *Catal Lett* **2014,** *144* (3), 434-438.

280. Zhao, C.; Camaioni, D. M.; Lercher, J. A., Selective catalytic hydroalkylation and deoxygenation of substituted phenols to bicycloalkanes. *J Catal* **2012,** *288*, 92-103.

281. Zapata, P. A.; Faria, J.; Ruiz, M. P.; Jentoft, R. E.; Resasco, D. E., Hydrophobic Zeolites for Biofuel Upgrading Reactions at the Liquid-Liquid Interface in Water/Oil Emulsions. *J Am Chem Soc* **2012,** *134* (20), 8570-8578.

282. Verboekend, D.; Liao, Y. H.; Schutyser, W.; Sels, B. F., Alkylphenols to phenol and olefins by zeolite catalysis: a pathway to valorize raw and fossilized lignocellulose. *Green Chem* **2016,** *18* (1), 297-306.

283. N.B. Colthup, L. H. D., S.E. Wiberley, *Introduction to Infrared and Raman Spectroscopy*. 3rd ed.; Academic Press: Waltham, MA, 1990; p 261.

284. Rozwadowski, M.; Lezanska, M.; Wloch, J.; Erdmann, K.; Golembiewski, R.; Kornatowski, J., Investigation of coke deposits on Al-MCM-41. *Chem Mater* **2001,** *13* (5), 1609-1616.

VITA

CHUKWUEMEKA OKOLIE

Chukwuemeka hails from Delta state in the southern part of Nigeria. He moved to the United States in 2009 to pursue a bachelor's degree in Chemical Engineering at Howard University in Washington DC. Upon graduation from Howard University, Chukwuemeka moved to Atlanta, Georgia in 2013 to pursue a Ph.D. in Chemical Engineering at Georgia Tech doing research in catalysis with Dr. Sievers' research group. When not conducting research, Chukwuemeka enjoys running, working out, reading Nigerian folktales and spending time with family and friends.